

---

Doctoral Dissertations

Student Theses and Dissertations

---

Summer 2019

## Nanomorphology dependent optical and mechanical properties of aerogels

Chandana Mandal

Follow this and additional works at: [https://scholarsmine.mst.edu/doctoral\\_dissertations](https://scholarsmine.mst.edu/doctoral_dissertations)

 Part of the [Materials Science and Engineering Commons](#), and the [Polymer Chemistry Commons](#)  
Department: Chemistry

---

### Recommended Citation

Mandal, Chandana, "Nanomorphology dependent optical and mechanical properties of aerogels" (2019).  
*Doctoral Dissertations*. 2810.  
[https://scholarsmine.mst.edu/doctoral\\_dissertations/2810](https://scholarsmine.mst.edu/doctoral_dissertations/2810)

This thesis is brought to you by Scholars' Mine, a service of the Missouri S&T Library and Learning Resources. This work is protected by U. S. Copyright Law. Unauthorized use including reproduction for redistribution requires the permission of the copyright holder. For more information, please contact [scholarsmine@mst.edu](mailto:scholarsmine@mst.edu).

NANOMORPHOLOGY DEPENDENT OPTICAL AND MECHANICAL  
PROPERTIES OF AEROGELS

by

CHANDANA MANDAL

A DISSERTATION

Presented to the Faculty of the Graduate School of the  
MISSOURI UNIVERSITY OF SCIENCE AND TECHNOLOGY

In Partial Fulfillment of the Requirements for the Degree

DOCTOR OF PHILOSOPHY

in

CHEMISTRY

2019

Approved by:

Dr. Nicholas Leventis, Advisor  
Dr. Chariklia Sotiriou-Leventis, Co-Advisor  
Dr. Manashi Nath  
Dr. Garry S Grubbs II  
Dr. K. Chandrashekhara

© 2019

Chandana Mandal

All Rights Reserved

**DEDICATED TO**

MY PARENTS

Shri. MADHUSUDAN MANDAL

Smt. MADHURI MANDAL

&

MY BELOVED HUSBAND

SURAJ DONTHULA

## PUBLICATION DISSERTATION OPTION

This dissertation consists of the following three manuscripts that have been published or submitted for publication:

Paper I, pages 44-80, was published in *Journal of Sol-Gel Science and Technology*.

Paper II, pages 81-120, was submitted in *Journal of Sol-Gel Science and Technology*.

Paper III, pages 121-170, was submitted in *Journal of Sol-Gel Science and Technology*.

Paper IV, pages 171-196, is intended to submit in *ACS Nano*.

## ABSTRACT

Aerogels are very low density, light weight open pore materials. A hypothesis that is under intense current investigation by the scientific community states that the mechanical properties of nanostructured polymers depend on their nanomorphology. Aerogels are nanostructured ultra-lightweight nanoporous materials with skeletal frameworks that can display a wide range of nanomorphologies. Thereby aerogels comprise a suitable platform for testing not only that hypothesis but also a wide range of other properties such as light scattering for applications, for example, in thermally insulating windows.

To study the mechanical properties of nanostructured matter as a function of nanomorphology, various shape-memory polyurethane aerogels were prepared with identical density, porosity, and chemical composition, but with vastly different nanostructures. Based on 5 different catalysts at 5 different concentrations each, the elastic modulus of all materials followed a well-defined trend whereas, all other factors being equal, bicontinuous structures were by several times stiffer than spheroidal nanostructures.

In order to develop silica aerogels as thermal insulators for windows, one must achieve a balance of clarity, strength, and thermal insulation value. Light scattering (haze) was studied with an integrating sphere, thermal conductivity with the hot plate method and mechanical strength with uniaxial compression. Delamination of wet-gels from glass substrates during drying into aerogels was traced to the nature mass fractal of the secondary particles that allows them to merge with one another.

## ACKNOWLEDGEMENTS

I would like to express my sincere gratitude to my advisor, Prof. Nicholas Leventis and co-advisor Prof. Chariklia Sotiriou-Leventis for their support, patience, and encouragement throughout my graduate studies. Prof. Nicholas Leventis is someone you will instantly love with his good grace and spontaneity.

I would like to thank Dr. M. Nath, Dr. G. S. Grubbs, and Dr. K. Chandrashekhara for serving on my PhD thesis committee and providing me their valuable suggestions throughout the completion of this dissertation. I thank the Department of Chemistry, Missouri S&T for providing financial assistance and resources. I want to thank my past group members, Adnan and Suraj for their assistance during my research work and my present group members Hojat, Tara, Parwani, Rushi, Shaheen, Saidulu, Vaibhav and all my friends for their great help.

I would especially like to thank my parents, Mr. Madhusudan Mandal and Mrs. Madhuri Mandal for their belief on me. Without their support and encouragement, I wouldn't have been able to achieve this. I would also like to thank my brother Mr. Koushik Mandal for motivating and being beside me always. Also, special thanks to my father in law, Mr. Suresh Donthula, my mother in law, Mrs. Uma Devi Donthula and my sister in laws, Tirna Mandal and Sushmitha Donthula, for their affection towards me. Finally, I would like to deeply thank my husband Suraj Donthula for his unconditional love, continued support and encouragement in my research and for standing beside me as a partner and as a senior to help me get to this point.

## TABLE OF CONTENTS

	Page
PUBLICATION DISSERTATION OPTION .....	iv
ABSTRACT.....	v
ACKNOWLEDGEMENTS .....	vi
LIST OF FIGURES .....	xiii
LIST OF SCHEMES.....	xviii
LIST OF TABLES .....	xix
 SECTION	
1. INTRODUCTION .....	1
1.1. NANOMORPHOLOGY .....	1
1.2. AEROGELS – BRIEF HISTORY .....	3
1.3. SILICA AEROGELS.....	5
1.4. HAZE IN SILICA AEROGELS .....	9
1.5. ADDRESSING THE FRAGILITY OF SILICA AEROGELS - CROSSLINKED SILICA AEROGELS (X-AEROGELS) .....	14
1.6. APPLICATIONS IN WINDOWS .....	17
1.7. DRYING SHRINKAGE IN SILICA AEROGELS .....	22
1.8. THE ISOCYANATE CHEMISTRY .....	25
1.8.1. Reaction of Isocyanates with Alcohols.....	27
1.8.2. Urethanes by Base-Catalysis. ....	27
1.8.3. Urethanes by Acid-Catalysis. ....	29
1.8.4. Polyurethanes (PU).....	30
1.8.4.1. Thermoplastic polyurethanes.....	32

1.8.4.2. Rigid PU foams. ....	32
1.8.4.3. Flexible PU foams. ....	33
1.8.4.4. Polyurethane ionomers. ....	34
1.8.4.5. Waterborne polyurethanes. ....	34
1.8.5. Shape Memory Polymers (SMP). ....	35
1.8.6. Shape Memory Poly (urethane-isocyanurate) Aerogels. ....	38
1.8.6.1. Characterization of shape memory aerogels. ....	39
1.8.6.2. Quantification and possible explanation for SME. ....	39
1.8.6.3. Applications of shape memory aerogels. ....	41

## PAPER

I. LIGHT SCATTERING AND HAZE IN TMOS-CO-APTES SILICA AEROGELS. ....	44
ABSTRACT .....	44
1. INTRODUCTION .....	46
2. EXPERIMENTAL .....	48
2.1. MATERIALS .....	48
2.1.1. Synthesis of Variable-Density, Amine-Modified Silica Aerogels (TMOS-co-APTES) .....	49
2.2. METHODS .....	51
2.2.1. Chemical Characterization .....	51
2.2.2. Physical Characterization of Aerogels .....	51
2.2.3. Structural Characterization of Aerogels. ....	52
2.2.4. Haze Measurements of Wet-gels and Aerogels. ....	53
3. RESULTS AND DISCUSSION .....	53
3.1. SYNTHESIS AND MATERIALS CHARACTERIZATION OF TMOS-CO-APTES AEROGELS .....	53

3.2. OPTICAL PROPERTIES OF TMOS-CO-APTES WET-GELS AND AEROGELS .....	59
3.2.1. Haze. ....	59
3.2.2. Haze and the Scatterer Size. ....	60
4. CONCLUSION.....	60
SUPPORTING INFORMATION .....	76
REFERENCES .....	78
II. OPTIMIZED TRANSPARENT, MECHANICALLY STRONG, THERMALLY INSULATING CROSSLINKED SILICA AEROGELS FOR ENERGY-EFFICIENT WINDOWS .....	81
ABSTRACT .....	81
1. INTRODUCTION .....	82
2. RESULTS AND DISCUSSION.....	86
2.1. SYNTHESIS AND MATERIALS CHARACTERIZATION OF TMOS-CO-APTES AEROGELS.....	86
2.2. CHEMICAL CHARACTERIZATION OF NATIVE AND CROSSLINKED AEROGELS.....	88
2.3. STRUCTURAL CHARACTERIZATION OF NATIVE AND CROSSLINKED SILICA AEROGELS.....	89
2.4. MECHANICAL CHARACTERIZATION OF NATIVE AND CROSSLINKED SILICA AEROGELS.....	90
2.5. THERMAL CONDUCTIVITIES OF NATIVE AND CROSSLINKED SILICA AEROGELS.....	91
2.6. OPTICAL PROPERTIES OF NATIVE AND CROSSLINKED SILICA AEROGELS.....	92
3. EXPERIMENTAL.....	95
3.1. MATERIALS.....	95
3.1.1. Synthesis of Amine-Modified Silica Wet-gels.....	96

3.1.2. Synthesis of Native and Crosslinked Amine-Modified Silica Aerogels.....	97
3.2. METHODS .....	98
3.2.1. Chemical Characterization.....	98
3.2.2. Physical Characterization of Aerogels.....	99
3.2.3. Structural Characterization of Aerogels. ....	99
3.2.4. Mechanical Characterization. ....	100
3.2.5. Thermal Characterization. ....	100
3.2.6. Haze Measurements of Native and Cross-linked Aerogels. ....	102
4. CONCLUSIONS .....	102
SUPPORTING INFORMATION .....	116
REFERENCES.....	118
III. EXPERIMENTAL DECONVOLUTION OF DEPRESSURIZATION FROM CAPILLARY SHRINKAGE DURING DRYING OF SILICA WET-GELS WITH SCF CO <sub>2</sub> . WHY AEROGELS SHRINK?.....	121
ABSTRACT .....	122
1. INTRODUCTION .....	123
2. RESULTS .....	128
2.1. PREPARATION AND PROCESSING OF SILICA WET-GEL AND AEROGELS.....	128
2.2. CHARACTERIZATION OF AEROGELS FROM THE DIFFERENT PROCESSING ROUTES.....	131
2.2.1. Chemical Characterization.....	131
2.2.2. Structural Characterization. ....	134
3. EXPERIMENTAL.....	141
3.1. MATERIALS.....	141

3.1.1. Preparation of Silica Aerogels. ....	141
3.2. METHODS .....	143
3.2.1. Chemical Characterization of Wet-gels and Aerogels.....	143
3.2.2. Physical Characterization of Wet-gels and Aerogels. ....	144
3.2.3. Structural Characterization of Wet-gels and Aerogels. ....	145
4. DISCUSSION.....	146
5. CONCLUSION.....	149
ACKNOWLEDGEMENTS .....	149
SUPPORTING INFORMATION .....	166
REFERENCES.....	167
IV. NANOMORPHOLOGY DEPENDENT MECHANICAL PROPERTIES: A CASE STUDY BASED ON POLYURETHANE AEROGELS.. .....	171
ABSTRACT .....	171
1. INTRODUCTION .....	172
2. RESULTS AND DISCUSSION.....	175
2.1. SYNTHESIS.....	175
2.2. CHARACTERIZATION OF PU WET-GEL.....	176
2.2.1. Material Characterization of PU Aerogels.....	178
2.2.2. Chemical Characterization of PU Aerogels.....	178
2.2.3. Structural Characterization of PU Aerogels. ....	178
2.2.4. Thermomechanical Characterization of PU Aerogels .....	179
3. EXPERIMENTAL.....	181
3.1. MATERIALS.....	181
3.2. PREPARATION OF THE CATALYST STOCK SOLUTIONS.....	182

3.3. SYNTHESIS OF SHAPE MEMORY POLY(ISOCYANURATE-URETHANE) AEROGELS .....	182
3.4. METHODS .....	183
3.4.1. Drying.....	183
3.4.2. Chemical Characterization.....	183
3.4.3. Physical Characterization. ....	184
3.4.4. Structural Characterization. ....	184
3.4.5. Thermomechanical Characterization. ....	185
4. CONCLUSIONS .....	187
SUPPORTING INFORMATION .....	194
REFERENCES.....	195
SECTION	
2. CONCLUSIONS .....	197
BIBLIOGRAPHY .....	200
VITA.....	212

## LIST OF FIGURES

SECTION	Page
Figure 1.1. Classes of porous materials and their properties.....	1
Figure 1.2. Morphology of aerogels .....	4
Figure 1.3. The typical nanostructure of a silica aerogel (left) and its macroscopic appearance (right) .....	5
Figure 1.4. Preparation of aerogel via the sol-gel process .....	8
Figure 1.5. Representation of haze and clarity .....	10
Figure 1.6. Scattering of light upon interaction with non-uniformities in the object.....	11
Figure 1.7. Scatterer in silica network.....	12
Figure 1.8. Change in the type of scattering due to increase in scatterer size.....	13
Figure 1.9. Scattering in silica wet-gels with decrease in silane concentration .....	13
Figure 1.10. A thin polymer layer is formed conformally on the skeletal silica nanoparticles .....	15
Figure 1.11. Comparison of compressive strength of X-silica aerogels w.r.t. other strong materials.....	16
Figure 1.12. Preparation of X-silica aerogel .....	17
Figure 1.13. Silica aerogels for insulating window applications .....	18
Figure 1.14. Cause of delamination of silica wet-gel from clean plate.....	19
Figure 1.15. Picture comparing the clarity through a clean glass plate (left) and silica sol-gel coated glass plate (right).....	20
Figure 1.16. Picture showing silica wet-gel sticking to the glass plate.....	20
Figure 1.17. Delamination of silica gel during supercritical drying. ....	21
Figure 1.18. Types of PU and their common applications.....	31

Figure 1.19.	Shape memory aerogels showing superelastic and shape memory properties .....	36
Figure 1.20.	Relationship between elastic modulus (thermodynamic property) and shape memory recovery rate (kinetic property) .....	37
Figure 1.21.	Metal chlorides tested for catalytic activity of polyurethane aerogel synthesis .....	39
Figure 1.22.	SEM images of $\text{CuCl}_2$ catalyzed SMPU aerogels with increasing catalyst concentration from A. 1/20 $\times$ , (B) 1/10 $\times$ , and (C) 4 $\times$ .....	40
Figure 1.23.	Experiment demonstrating shape memory effect .....	41
Figure 1.24.	Application of shape memory aerogels in orthopedics.....	42
<b>PAPER I</b>		
Figure 1.	(A) Photograph of TMOS-co-APTES wet-gels showing an increase in haze with decreasing silane concentration (K to K/32). (B) Same as in (A) with gels prepared in flat cells (13.49 mm thick), used later (Figure 8) for measuring haze .....	66
Figure 2.	(A) Photograph of a K and a K/2 aerogel monolith in front of text. (B) An aerogel monolith of standard formulation (K) in front of landscape.....	67
Figure 3.	Typical solid-state $^{29}\text{Si}$ NMR spectra of K aerogels under direct and cross-polarization .....	68
Figure 4.	SEM images of TMOS-co-APTES aerogels as shown.....	69
Figure 5.	$\text{N}_2$ -sorption data. ....	70
Figure 6.	Representative Hg-intrusion porosimetry data of K and K/2 aerogels. ....	71
Figure 7.	Typical SAXS data (sample shown: K aerogel) fitted into two regions.....	71
Figure 8.	Typical percent haze data for wet-gels as a function of wavelength from 380 nm to 800 nm. ....	72
Figure 9.	Photograph of three small K/8 aerogel monoliths ( $\rho_b = 0.032 \text{ g cm}^{-3}$ ) on a black surface with a white background demonstrating Rayleigh scattering by showing transmitted yellow/orange light and reflected bluish light. ....	72

Figure 10.	Plots according to Eq 8 of wet-gels (solid lines) and aerogels (dashed lines). .....	73
 PAPER II		
Figure 1.	Formulations according to a three-level, two-variable full-factorial design of experiments (DoE) statistical method (dark circles) enhanced with for additional star points. ....	104
Figure 2.	Representative N <sub>2</sub> -sorption data of 0.5K, 0.5K-3%, 0.5K-6%. ....	105
Figure 3.	Solid-state NMR of native and cross-linked (X-) TMOS-co-APTES aerogels. ....	106
Figure 4.	Representative high resolution SEM images (200×) of native and crosslinked silica aerogels across the design space of Figure 1. ....	107
Figure 5.	Basic material properties of native and cross-linked TMOS-co-APTES aerogels as a function of the two explanatory variables as shown. ....	108
Figure 6.	Material properties of interest to application of TMOS-co-APTES aerogels in windows as a function of the two explanatory variables of this study. ....	109
Figure 7.	Particle radii as a function of the two explanatory variables of this study. ....	110
Figure 8.	Haze as a function of thickness of native TMOS-co-APTES aerogel samples prepared with the 0.875K formulation molded with Teflon tape coated glass plates. ....	111
Figure 9.	Unobstructed view and view through a cross-linked TMOS-co-APTES aerogel sample fabricated with the formulation shown with an arrow in Figure 6. ....	111
 PAPER III		
Figure 1.	(A) Photograph from two perspectives of an aged and acetone-washed silica wet-gel cast between two glass plates (glass side-spacers had been removed). (B) After drying with SCF CO <sub>2</sub> the aerogel delaminated from both glass facers. ....	150
Figure 2.	Rheology of a TMOS sol during gelation at 23°C, according to the procedure described in the experimental section. ....	151

Figure 3.	Liquid $^{29}\text{Si}$ NMR of a TMOS sol up to two hours after mixing the sol. ....	152
Figure 4.	(A) Linear shrinkages of wet-gels and aerogels along processing. (B) Linear shrinkage of aerogels obtained by drying acetone wet-gels aged for different time periods as shown .....	153
Figure 5.	Linear shrinkages of wet-gels and aerogels at different processing stages for (A) 2h-aged, (B) 24h-aged samples.....	154
Figure 6.	Top: Representative ATR-FTIR spectra of 24h-aged wet-gel and aerogel samples solvent-exchanged with toluene as shown. Bottom: The 2500 $\text{cm}^{-1}$ to 4000 $\text{cm}^{-1}$ region of the spectra shown on top. ....	155
Figure 7.	Direct polarization solid-state $^{29}\text{Si}$ NMR data of aerogels prepared from wet-gels aged for 2h or 24h as shown on top, and solvent-exchanged prior to drying with the solvents shown on the left .....	156
Figure 8.	SEM images of 24h-aged aerogel samples processed from (A) acetone, (B) toluene, and (C) xylene.....	157
Figure 9.	$\text{N}_2$ -sorption data of aerogel samples solvent-exchanged prior to drying as shown. ....	158
Figure 10.	(A) Hg-intrusion porosimetry data of 24h-aged aerogels. (B) Pore size distributions. (C) Plots of $\text{Ln}(-dV_{\text{cumulative}}/dR)$ vs $\text{Ln } R$ used for the determination of the fractal dimensions of the porous networks probed by Hg-intrusion .....	159
Figure 11.	Small angle X-ray scattering (SAXS) data for 24h-aged aerogel samples solvent-exchanged prior to drying in acetone (A), toluene (B), and xylene (C).....	160
Figure 12.	Deconvoluted particle-size distribution curves by fitting into Gaussians the volume distribution functions obtained from SAXS data of 24h-aged wet-gels and of the corresponding aerogels in acetone, toluene, and xylene as shown .....	161
 PAPER IV		
Figure 1.	Different metal salts used as catalysts for the synthesis of shape memory polyurethane aerogels .....	187
Figure 2.	Reaction for the synthesis of PU aerogel.....	188

Figure 3.	Solid-state $^{13}\text{C}$ NMR of PU aerogels catalyzed by different metal salts.....	189
Figure 4.	Rheology of the PU sol at 23°C, according to the procedure described in the experimental section .....	190
Figure 5.	Gelation times for different metal salts that catalyze PU reaction.....	191
Figure 6.	Storage ( $G'$ ), loss ( $G''$ ) moduli and $\tan \delta (=G''/G')$ curves of a representative sample catalyzed by DBTDL as a function of temperature .....	191
Figure 7.	Typical 3D representation of shape memory experiment with temperature, strain, and stress on X, Y, and Z axes respectively .....	192
Figure 8.	Relationship between Log [E] and Log [gelation time] for different samples .....	192

## LIST OF SCHEMES

SECTION	Page
Scheme 1.1. Formation of silica network from the hydrolysis and condensation of TMOS .....	7
Scheme 1.2. Synthesis of crosslinked silica .....	15
Scheme 1.3. Structural reorganization of silica wet-gels during drying .....	24
Scheme 1.4. The isocyanate group .....	25
Scheme 1.5. Nucleophilic attack on the isocyanate group .....	25
Scheme 1.6. The chemistry of isocyanates with different nucleophiles.....	26
Scheme 1.7. Formation of urethanes from isocyanates and alcohols .....	27
Scheme 1.8. Formation of urethanes according to Baker et. al. ....	28
Scheme 1.9. Formation of urethanes from isocyanates and alcohols by base catalysis.....	28
Scheme 1.10. Formation of urethanes from isocyanates and alcohols by acid catalysis.....	30
 PAPER I	
Scheme 1. Configurations of the integrating sphere for measuring haze.....	73
 PAPER II	
Scheme 1. Synthesis and crosslinking of silica wet-gels.....	112
Scheme 2. Configurations of the integrating sphere for measuring haze.....	112
 PAPER III	
Scheme 1. Processing of 2h- and 24h-aged wet-gels in different solvents .....	162
Scheme 2. Summary of processes that lead to shrinkage of silica wet-gels.....	163
 PAPER IV	
Scheme 1. Synthesis of SMPU aerogels using different catalysts .....	193

## LIST OF TABLES

PAPER I		Page
Table 1.	General materials characterization data for the TMOS-co-APTES aerogels prepared with decreasing total silane (TMOS+APTES) concentration.....	74
Table 2.	SAXS data for TMOS-co-APTES aerogels prepared with different silane concentrations.....	75
Table 3.	Average haze and scatterer diameter for TMOS-co-APTES gels .....	75
 PAPER II		
Table 1.	General materials characterization data for the crosslinked TMOS-co-APTES aerogels .....	113
Table 2.	SAXS data for TMOS-co-APTES aerogels .....	114
Table 3.	Mechanical characterization of all silica aerogels .....	114
Table 4.	Thermal conductivities of native and crosslinked silica aerogels.....	115
Table 5.	Average haze for native and crosslinked silica aerogels .....	115
 PAPER III		
Table 1.	Rheology data during base-catalyzed gelation of TMOS sols in methanol.....	163
Table 2.	General materials characterization data for silica aerogels.....	164
Table 3.	Data from deconvolution of direct-polarization solid-state <sup>29</sup> Si NMR spectra of aerogels as shown.....	165
Table 4.	Data from Hg-intrusion porosimetry .....	165
Table 5.	SAXS data for 24h-aged silica aerogels, and processed in three different solvents.....	165
Table 6.	Particle size distribution of 24h aged gels from SAXS .....	166
 PAPER IV		
Table 1.	Rheology data for the gelation of polyurethane sol .....	193

# 1. INTRODUCTION

## 1.1. NANOMORPHOLOGY

The study of morphology of nanostructured materials is termed as nanomorphology. Nano-structured materials with different nanomorphologies have various applications and therefore studying the nanomorphology is important. Based upon the nanomorphology of the porous materials, they have different properties and different applications and can be classified by their degree of long-range order and their intermolecular bond strengths as shown in Figure 1.1.<sup>1</sup>

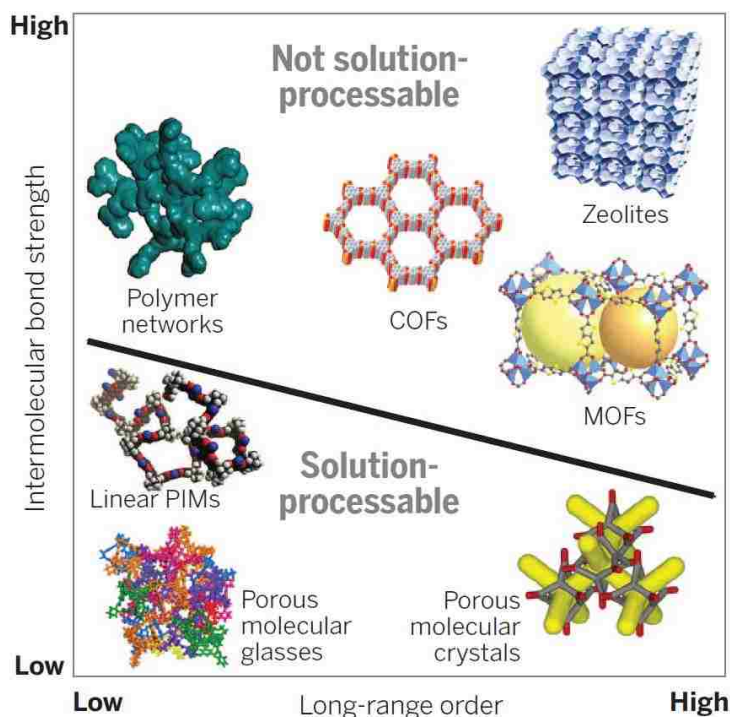


Figure 1.1. Classes of porous materials and their properties

For example, by varying the morphology even at the single particle scale, the material's catalytic activity changes due to change in the number and nature of the active sites.<sup>2,3,4</sup> The wetting property of the matter changes with change in the morphology of the material.<sup>4,5</sup> The nanomorphology of polyurea aerogels can be quantified using a predicting tool termed as K-index.<sup>5</sup> Therefore, synthesis of new polymeric materials with nanomorphology engineering is one of the emerging topics.<sup>6-11</sup> Other properties such as the mechanical strength, thermal conductivity, surface area, gas sorption properties of porous materials strongly also depend on the nanomorphology that is controlled by the composition.<sup>6,12-14</sup>

This dissertation deals with the mechanical and optical properties of aerogels based upon their nanomorphologies. In order to study the dependence of nanomorphology on mechanical properties, shape memory aerogels were prepared that can remember and recover back to its initial shape when triggered by external stimulus like temperature. Different morphologies of shape memory polyurethane aerogels were prepared by varying the type and concentration of the catalyst and their mechanical properties were studied as a function of their morphologies. For studying the dependence of nanomorphology on the optical properties of aerogels, silica aerogels with different morphologies were prepared by varying the silane concentration in the silica sol. In order to use the transparent silica aerogels for applications in thermally insulating windows, the fragility issue, thermal conductivity and transparency were studied. Moreover, the reason for the drying shrinkage in silica aerogels that hinders their application in windows was also studied.

## 1.2. AEROGELS – BRIEF HISTORY

Aerogels are very low-density open pore, lightweight and highly porous solids in which the dispersed phase is a gas.<sup>15</sup> These aerogels comprise of different properties such as high surface areas, low thermal conductivities, good elastic properties, acoustic attenuation, and possibilities for easy surface modification.<sup>16</sup> Thereby, they can be used as absorbents,<sup>17</sup> aerospace applications,<sup>18</sup> sensors,<sup>19,20</sup> capacitors,<sup>21</sup> catalyst supports,<sup>22-24</sup> clothing and thermal insulation blankets,<sup>25</sup> dielectrics,<sup>26,27</sup> energy storage materials,<sup>28,29</sup> thermal insulators,<sup>30</sup> templates for solar cells,<sup>31</sup> and insulating windows. However, all porous materials are not aerogels. For example, metal organic frameworks (MOFs), microporous materials like zeolites, etc. are not aerogels. Different authors have defined aerogels by different terminology. The first definition was given by S. S. Kistler, the inventor of aerogels who reported that aerogels are the gels in which the pore filling liquid has been replaced by air without compromising the shrinkage and volume of the gel is retained.<sup>32</sup> Later aerogels were defined aerogels as “highly porous nanostructured solid materials derived from gels, in which the pores filling phase is a gas and whose properties/structures are not significantly affected by the removal of swelling agents regardless of the drying approach used”.<sup>33</sup> The above definitions explain the “aero” part of the aerogels but do not address the “gel” part. Later a more complete definition of the term “aerogel” has been proposed by Leventis that also differentiates them from closed-cell foam one from xerogels: “an open non-fluid colloidal network or polymer network that is expanded throughout its whole volume by a gas, and is formed by the removal of all swelling agents from a gel without substantial volume reduction or network compaction”.<sup>34</sup> Aerogels are derived from wet-gels where the pore-filling solvent is replaced by a

supercritical fluid and then is vented off as a gas. That process preserves the porous skeletal framework of the wet-gel into the final solid object with a minimum volume compromise (shrinkage).

Microscopically aerogels comprise of porous secondary particles that can be as small as 20 to 40 nm resulting in particulate morphology or they can also comprise of large spheres in the micrometer range to give spheroidal morphologies or can comprise of fuse spheres with early phase separation resulting in bicontinuous structures (Figure 1.2). Apart from spheroidal and bicontinuous structures, polymeric aerogels can also comprise of fibrous and cocoon morphologies.<sup>5</sup> Therefore, aerogels comprise a convenient platform to study the properties of the nano-structured matter.

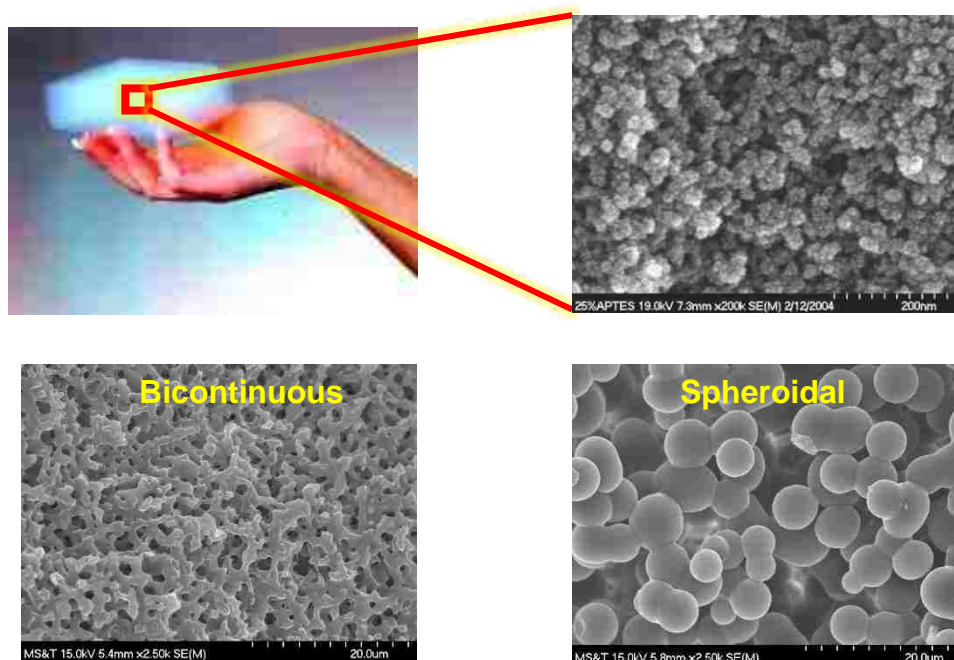


Figure 1.2. Morphology of aerogels

### 1.3. SILICA AEROGELS

Silica aerogels were first synthesized by S. S. Kistler in the 1930s.<sup>32</sup> By converting the liquid into a supercritical fluid (SCF), he replaced the pore-filling solvent of wet-gels with air without destroying the gel structure. As with any porous materials, the size and shape of the pores influences the bulk physical properties. Figure 1.3 shows the typical solid network structure of silica aerogels. The solid network consists of a complex hierarchical structure comprising aggregation of smaller non-porous primary particles in the range of 2 to 5 nm to fractal porous secondary particles. These porous secondary particles eventually agglomerate to a pearl-necklace like structure to form hierarchical assemblies of particles (Figure 1.3) thereby forming the gel network. The generation and agglomeration of particles is controlled by the sol-gel process. The physical properties of aerogels are effectively derived from the shape and size of pores in the solid network.<sup>7</sup> Consequently, a significant effort has been directed towards understanding and controlling the nanoporous structure.

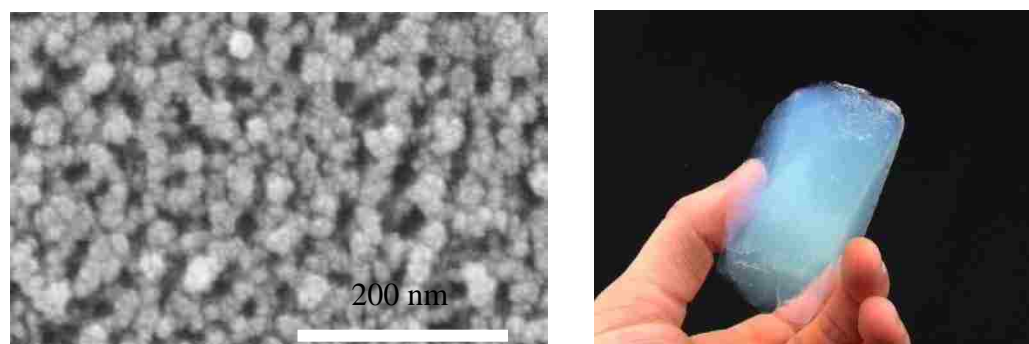


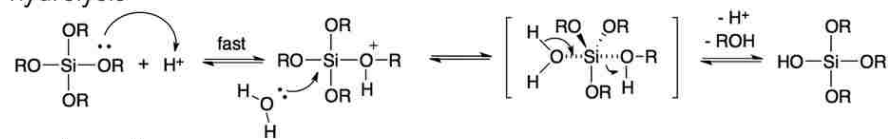
Figure 1.3. The typical nanostructure of a silica aerogel (left) and its macroscopic appearance (right)<sup>35</sup>

Kistler realized the potential economic significance of aerogels and commercialized the first silica aerogels through Monsanto Chemical Company. The main drawback of Kistler's method for the preparation of silica aerogels was the time-consuming gelation and solvent exchange process. In 1966 Peri introduced a new process for synthesizing aerogels using alkoxides as precursors.<sup>3</sup> Preparation of aerogels involves formation of three dimensional (3D) porous assemblies of nanoparticles. According to sol-gel chemistry, aerogels are prepared by mixing the two chemical precursors, one containing the monomer and other containing the catalyst to form a colloidal solution of primary particles termed as sol. Typical alkoxy silane precursors used for the synthesis of silica aerogels include tetramethylorthosilicate ( $\text{Si}(\text{OCH}_3)_4$ , abbreviated as TMOS) or tetraethylorthosilicate ( $\text{Si}(\text{OC}_2\text{H}_5)_4$ , abbreviated as TEOS) dissolved in their respective alcohol e.g., methanol or ethanol that acts as a co-solvent for the silane and water needed for hydrolysis. As a catalyst, ammonium hydroxide ( $\text{NH}_4\text{OH}$ ) can be used by mixing it with water and solvent. The first step of the process is either an acid- or a base-catalyzed hydrolysis where the alkoxy group of TMOS or TEOS hydrolyze to form silanols. These silanol groups undergoes *in situ* condensation reaction to form Si-O-Si linkages that results in the formation of silica gel network as shown in Scheme 1.1.<sup>36</sup>

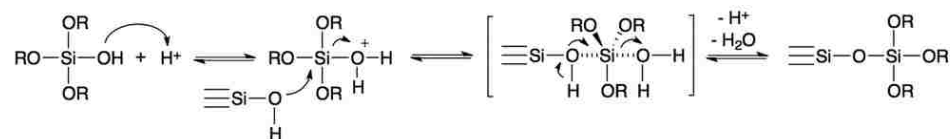
The linkages grow in 3D and the polymer phase separates into tiny non-porous primary silica particles. When enough primary nanoparticles are formed, they are connected to one another to form mass-fractal secondary particles. These secondary particles agglomerate into higher mass-fractal aggregates until the percolation threshold is reached, and a continuous network of particles is formed that is referred to as a wet-gel (Figure 1.4).

### a) acid-catalyzed - pH < 2

hydrolysis

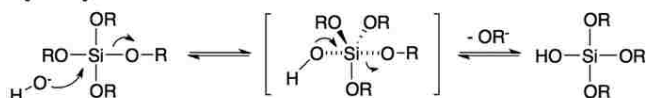


condensation

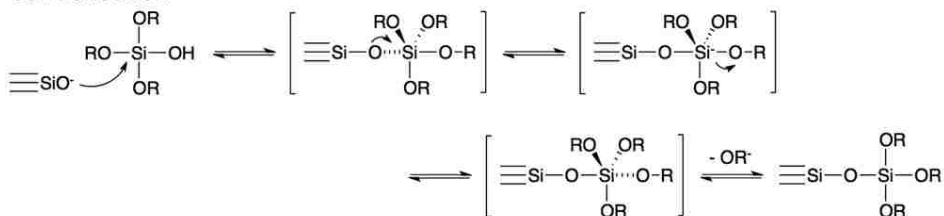


### b) base-catalyzed - pH > 2

hydrolysis



condensation



Scheme 1.1. Formation of silica network from the hydrolysis and condensation of TMOS

The wet-gels are then aged in their molds for the completion of reaction in order to gain mechanical stability. During aging, silica dissolves from the surface of the primary particles and reprecipitates at the interparticle necks rendering necks wider, which enhances the mechanical strength of the network. The resulting solvent-filled wet-gels are solvent-exchanged with alcohol to remove water from the network before drying.

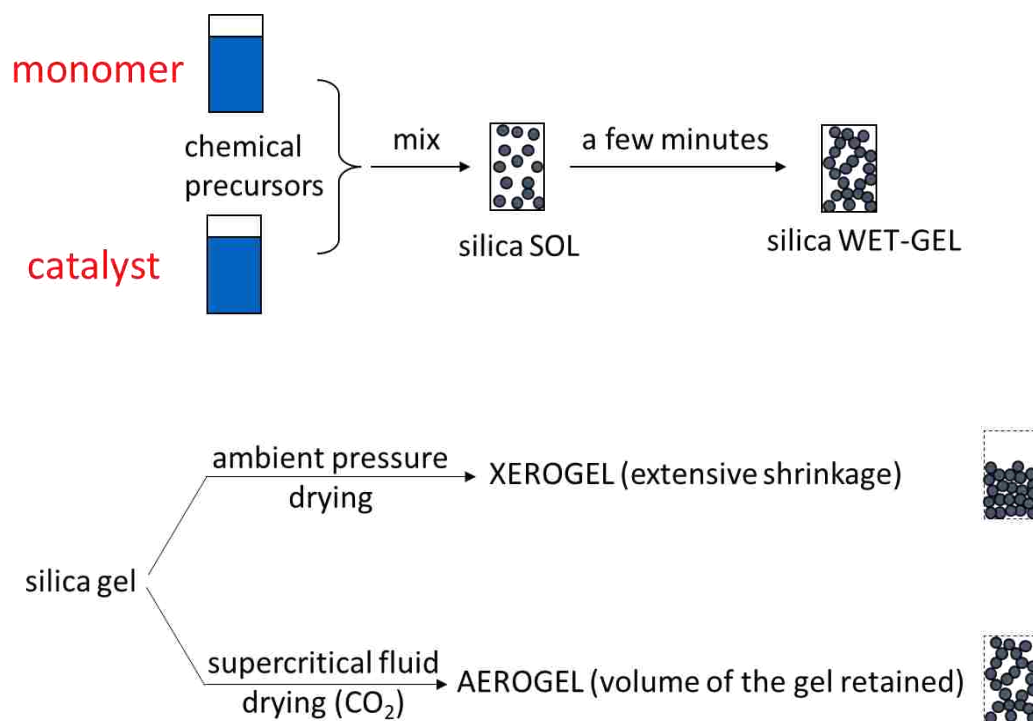


Figure 1.4. Preparation of aerogel via the sol-gel process

Silica wet-gels can be dried in two different ways: (a) by allowing entrapped solvent to evaporate at atmospheric pressure to form a collapsed porous structure with extensive shrinkage; the resulting materials are referred to as xerogels; or, (b) by using a SCF such as  $\text{CO}_2$  to form an aerogel whereas the volume and the porous structure of the original wet-gel are retained. In practice, supercritical drying involves use of an autoclave to replace the gelation solvent with liquid  $\text{CO}_2$ , which is then converted to SCF and vented off isothermally (critical point of  $\text{CO}_2$ :  $31.1\text{ }^\circ\text{C}$  at 1072 psi).

Silica aerogels have been considered for many applications. Flexible aerogels can be used for insulation applications in subsea systems, insole for shoes, industrial buildings and refrigerators.<sup>37</sup> Fiber reinforced aerogel composite blankets are commercially available from Aspen aerogels which can be bent and rolled over.<sup>38-42</sup>

However, silica aerogels have been actually used only in specialized environments, such as Cerenkov radiation detectors in certain nuclear reactors, aboard spacecraft as collectors for cosmic particles (NASA's Stardust program),<sup>43,44</sup> and for thermal insulation in planetary vehicles on Mars. Different properties, underlying concerns, and process development of silica aerogels for their applications in windows are discussed below.

Due to the small particle size of silica aerogels, they are transparent. However, these silica aerogels are highly fragile due to small interparticle neck thereby limiting their applications in various fields. Therefore, using silica aerogels as a replacement for mechanically strong and transparent silica aerogels for application in insulating windows is hindered. The major drawbacks for that application are making silica aerogels transparent and mechanically strong. In order to improve the transparency of silica aerogels, the cause of haze must be understood.

#### **1.4. HAZE IN SILICA AEROGELS**

Properties of silica aerogels have made them a versatile candidate for many applications. Combination of low thermal conductivity with high optical transparency serves silica aerogels as a good candidate for applications in thermally insulating windows and daylighting.<sup>45-49</sup> Though silica aerogels have good transparency, they still appear hazy restricting their use in windows. When light interacts with a sample, some of the light is reflected, some is absorbed, and rest of the light is transmitted. Reflection doesn't involve much loss in light in case of silica aerogels and neither they absorb light in the visible range.<sup>50</sup> Therefore, the loss of clarity and hence the appearance of haze is due to scattering. The transmitted light from the object can follow different paths. Firstly, the transmitted

light might not deviate from the normal and is parallel to the normal incident beam. In other case, the transmitted light might deviate from the normal by a certain angle. When that deviation is in between  $0^\circ$  to  $90^\circ$  from the normal, that is termed as scattered light. Deviation beyond  $90^\circ$  from the normal corresponds to reflection. The scattered light was further categorized into two parts. In the first part, when scattered light is deviated by  $\pm 2.5^\circ$  from the normal, it is called “clarity”.<sup>51</sup> On the other hand, the scattered light that deviates beyond  $2.5^\circ$  to  $90^\circ$  is called as “haze” (Figure 1.5).

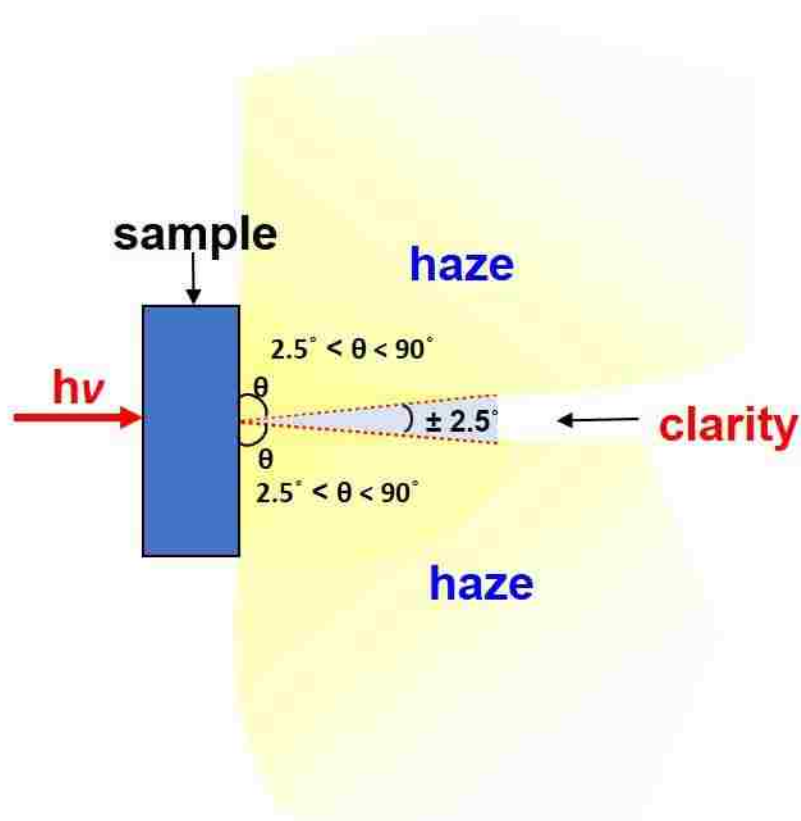


Figure 1.5. Representation of haze and clarity

As mentioned above, the haze induced in silica aerogels is due to scattering. That scattering can be of three types namely Rayleigh scattering,<sup>49,52</sup> Mie scattering and surface scattering. When sunlight interacts with the air molecule in the atmosphere, it scatters thereby the sky appearing blue. Silica aerogels in front of light appears bluish upon reflection and yellowish orange upon transmittance. That can be explained by Rayleigh's theory, which in turn is valid when the scatterer size is less than the one tenth (0.1) of the wavelength of the light. Rayleigh scattering is elastic scattering of light from particles with one-tenth of the wavelength of light.

The blue color of the sky is due to Rayleigh's scattering occurring due to the scattering of sunlight from the air particles in the atmosphere. According to this theory, the wavelength of light has inverse relationship to the fourth power of the intensity of the light. When the electromagnetic waves of light interact with the non-uniformities along the optical path of the sample, it deviates as shown in Figure 1.6. Those non-uniformities are termed as scatterers.

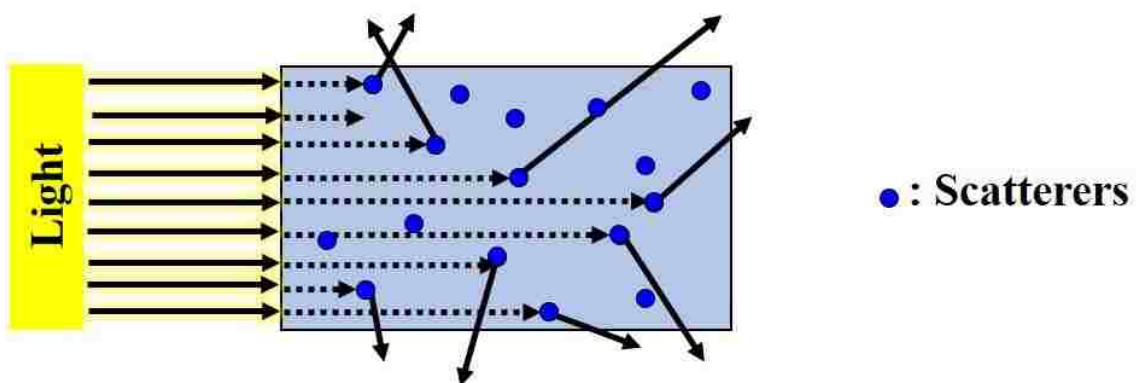


Figure 1.6. Scattering of light upon interaction with non-uniformities in the object

Those scatterers can be either particles or even the pores.<sup>53</sup> Owing to the small sizes of scatterers, skeletal silica particles (typically < 10 nm) can be considered as an obvious choice. However, the mesopores of silica aerogels also fulfill the condition for Rayleigh scattering, and they can also act as the primary scatterers (Figure 1.7). In addition to the scattering from the particles and/or pores, surface scattering in silica aerogels were also studied since it decreases the transparency and hence restricts their applications in windows.

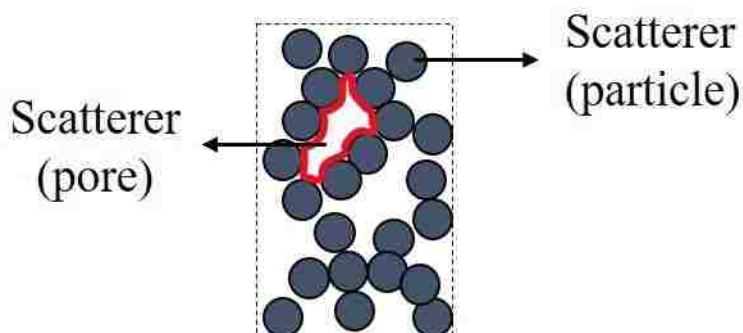


Figure 1.7. Scatterer in silica network

As the scatterer size increase, scattering is expected to increase due to the change in scattering type from Rayleigh to Mie scattering (Figure 1.8).<sup>54</sup> Apart from Rayleigh and Mie scattering, surface scattering also causes haze in silica aerogels.<sup>55</sup>

It was observed that scattering in silica wet-gels increases with decrease in silane concentration (Figure 1.9).<sup>56</sup> The reason for this increase in haze in silica wet-gels was studied. Since silica aerogels are very fragile therefore, they are very prone to surface

scratches and hence haze increases in silica aerogels. Therefore, addressing the fragility of silica aerogels was important to control the haze due to surface scattering.

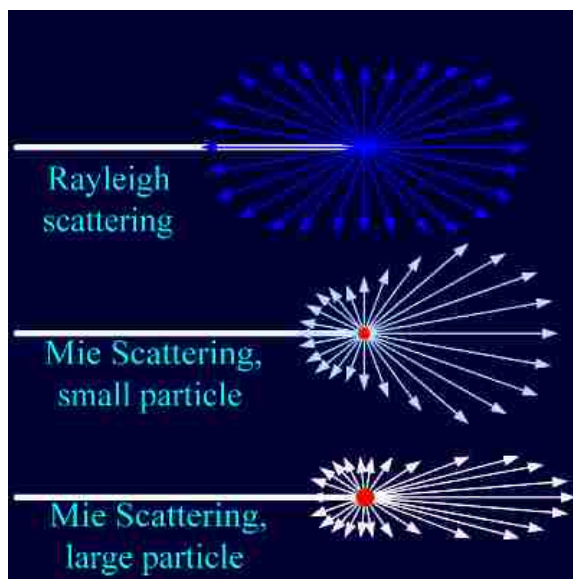


Figure 1.8. Change in the type of scattering due to increase in scatterer size

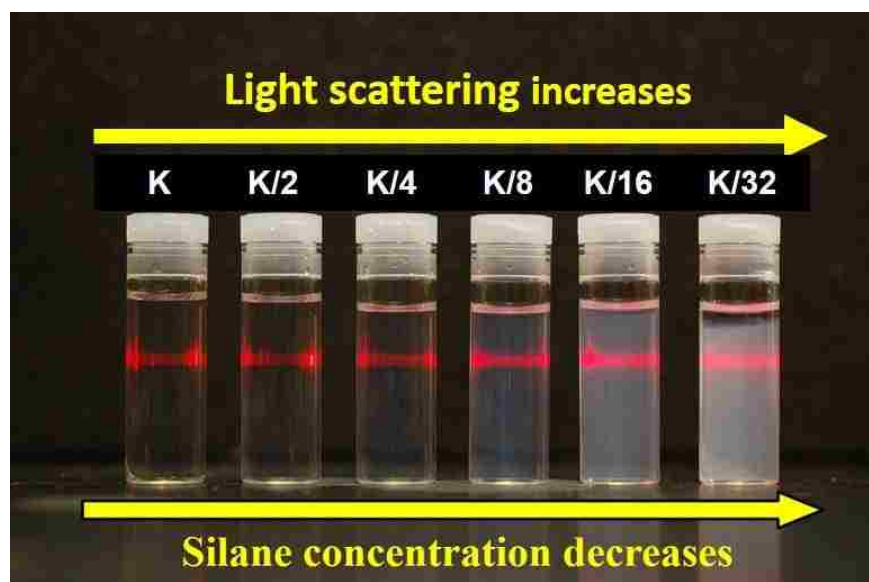
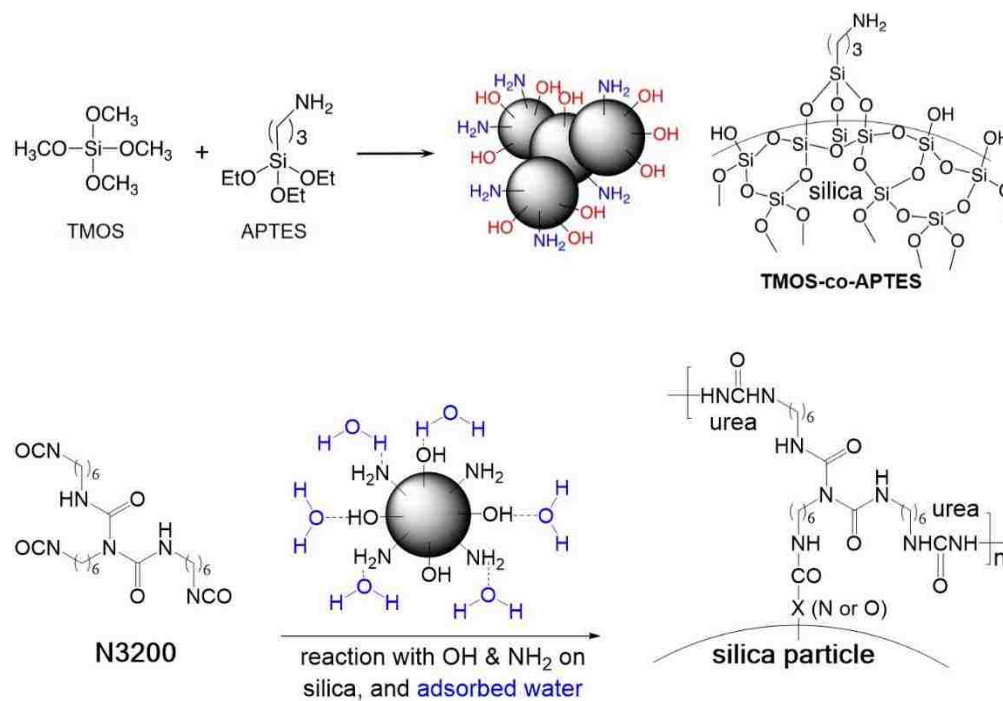


Figure 1.9. Scattering in silica wet-gels with decrease in silane concentration

### **1.5. ADDRESSING THE FRAGILITY OF SILICA AEROGELS - CROSSLINKED SILICA AEROGELS (X-AEROGELS)**

The fragility issue of silica aerogels has limited their use in certain types of thermal insulation,<sup>41, 42</sup> catalyst supports and space exploration for example in capturing cosmic dust in outer space (refer to NASA's Stardust program).<sup>43, 44</sup> Silica aerogels consists of small particles and well defined narrow interparticle necks. The poor mechanical properties of silica aerogels due to narrow interparticle connections hinders the commercialization of silica aerogels. Aging of silica wet-gels results in dissolution from the surface of particles and reprecipitation of silica on the interparticle necks of silica particles. This phenomenon is termed as Ostwald ripening. Due to Ostwald ripening, the interparticle necks becomes thick thereby increasing the strength of the silica backbone. Different types of aging can be done to reinforce the silica network for e.g. thermal aging, aging of silica wet-gels in water, aging of silica wet-gels in methanol/water mixture, aging in silica precursor solution etc. However, strengthening silica network by aging is a long-term process. Finally, the fragility issue of silica aerogels has been resolved by crosslinking them.<sup>57-61</sup> Both multistep and one-pot crosslinking can improve the mechanical properties of silica aerogels.<sup>62-70</sup> Taking the advantage of the isocyanate chemistry for the formation of polyurea, the silica aerogels were crosslinked with polyisocyanate.<sup>70</sup> The skeletal silica nanoparticles possess surface amino/silanol groups, that can react with polyisocyanates to form polyurethane/urea tethers that bridge the nanoparticles chemically, reinforcing the interparticle necks (Scheme 1.2).



Scheme 1.2. Synthesis of crosslinked silica

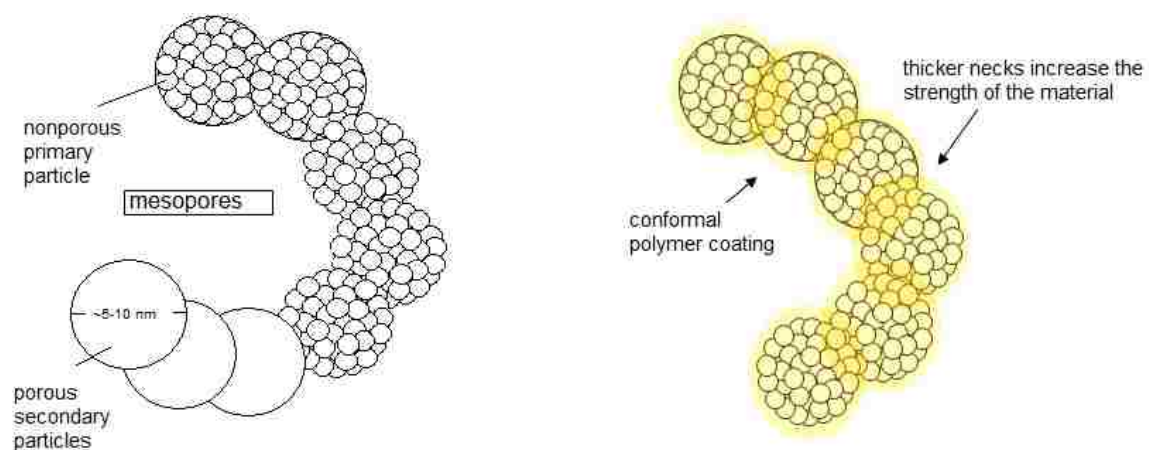


Figure 1.10. A thin polymer layer is formed conformally on the skeletal silica nanoparticles

Due to the formation of the polymer layer on the silica particle, the narrow interparticle necks becomes thicker and hence the strength of crosslinked silica aerogels increases (Figure 1.10).

Thus, the entire skeletal framework is coated conformally with a polymer, while the open porosity is preserved. The resulting materials have been referred to as polymer-crosslinked aerogels (X-aerogels). The bulk properties of X-aerogels are not compromised significantly by crosslinking where an increase in the bulk density by a factor of  $3\times$  leads to a  $300\times$  increase in the flexural strength of typical X-aerogel monoliths. X-aerogels are exceptionally strong in comparison not only with their non-crosslinked counterparts (native aerogels), but also with other materials that are usually considered strong, such as steel, Kevlar, and silicon carbide (Figure 1.11).<sup>16</sup> In order to crosslink silica wet-gels, the silica sol is prepared and casted in the sols. Figure 1.12 shows the procedure for preparing crosslinked silica aerogels.

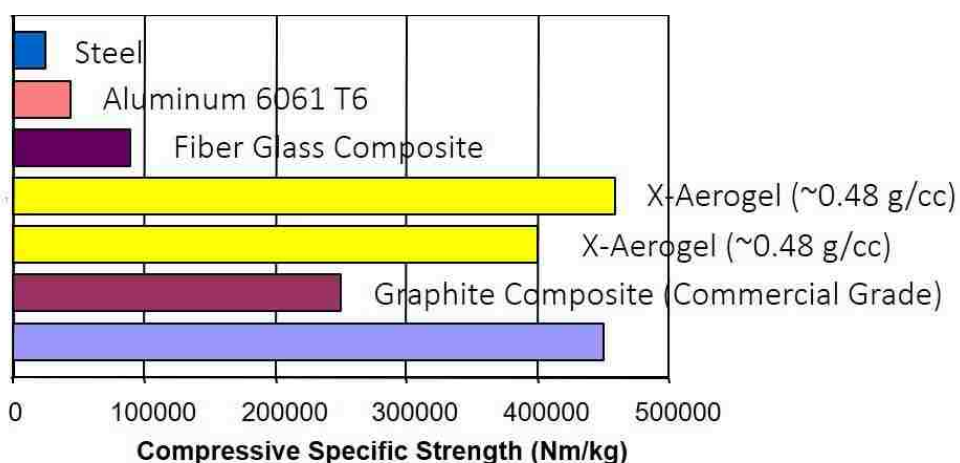


Figure 1.11. Comparison of compressive strength of X-silica aerogels w.r.t. other strong materials

The resulting wet-gels are then added to the crosslinking solution and heated at higher temperature for completion of the polyurea/urethane reaction. The resulting X-silica aerogels can be dried to form X-silica aerogels. Due to the increase in the strength of X-silica aerogels, they can also be dried at ambient pressure thereby reducing the costly supercritical drying.<sup>61,71,72</sup>

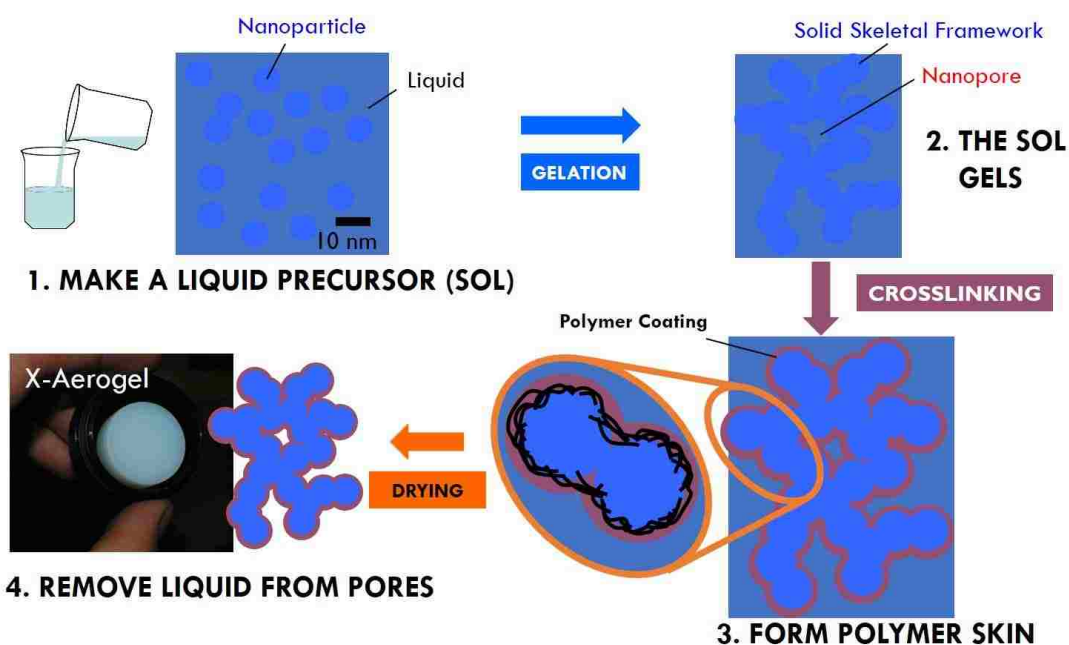


Figure 1.12. Preparation of X-silica aerogel

## 1.6. APPLICATIONS IN WINDOWS

Silica aerogels, due to their good optical and thermal insulating can be used for applications in thermally insulating windows. For that application, silica aerogel can be sandwiched between the two glasses of the window as shown in Figure 1.13. The resulting

window glass with aerogel sandwiched between them will result in the decrease the overall thermal conductivity.

The best approach to better contact with the glass facers is to cast the silica sol in a glass sandwich mold as shown in Figure 1.14. The problem however is that silica wet-gels do not stick to the glass plates and slides off easily. That is because the surface of silica gel is nano-rough while the surface of the cleaned glass plate is smooth. When silica gel comes in contact with the glass plate, it is not able to make enough points of contact and therefore slides off easily.

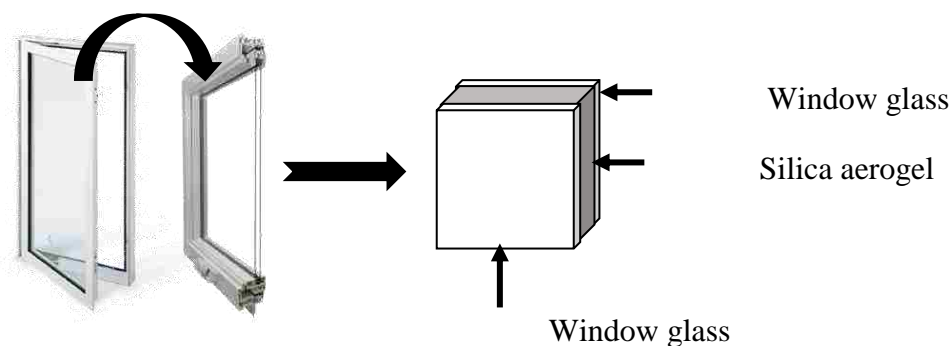


Figure 1.13. Silica aerogels for insulating window applications

In order to avoid the sliding of the silica gel, the glass plate is needed to be nano-modified. When the silica gel comes in contact with the nano-modified glass plate, it sticks due to the roughness of the glass plate and silica surface as shown in Figure 1.14. That roughness can be introduced by sol-gel method by coating the surface of the glass plate with silica sol and then let it dry to form a thin film of silica sol-gel film on glass. The resulting sol-gel coated glass plate were as transparent as non-coated glass plate as can be

seen in Figure 1.15. The nano-modified glass plate was used to make the mold and silica gel stuck to the glass plate as shown in Figure 1.16. After the gelation of the silica sol in the glass mold, the spacers were removed, and the assembly was washed with the solvent and was dried supercritically from supercritical fluid CO<sub>2</sub>. The silica wet-gel sticks to the glass plate due roughness of the nano-modified glass plate. Figure 1.18 shows the picture of silica wet-gel sticking to the from both surfaces of the wet-gel.

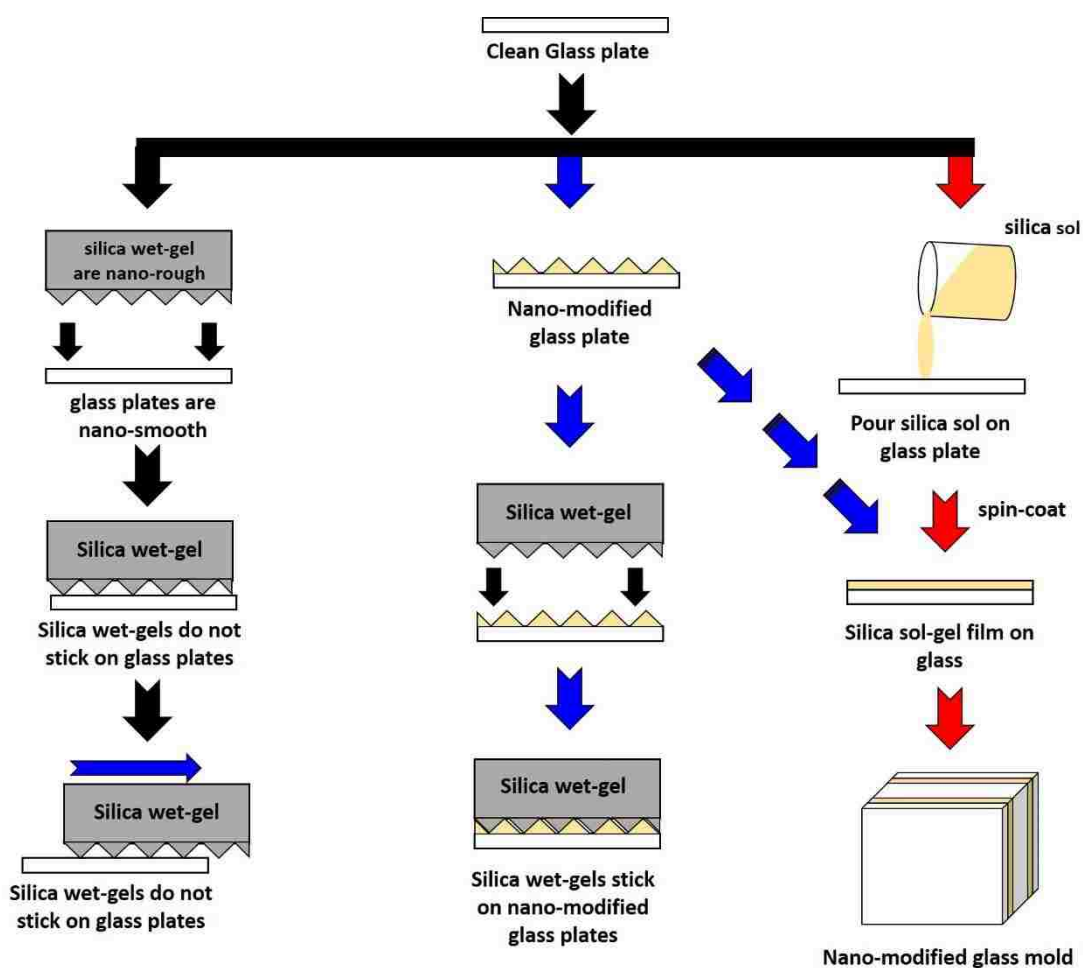


Figure 1.14. Cause of delamination of silica wet-gel from clean plate

After drying, the silica aerogel delaminated from the glass plates thereby rendering its application in windows by this method as shown in Figure 1.17.



Figure 1.15. Picture comparing the clarity through a clean glass plate (left) and silica sol-gel coated glass plate (right)



Figure 1.16. Picture showing silica wet-gel sticking to the glass plate

In order to use silica aerogels for windows applications by this method, it was important to understand the cause of delamination. It was proposed that the delamination of silica aerogel from the glass plate during drying was due to the drying shrinkage. When silica wet-gels are dried, they shrink. That shrinkage creates stress between the silica aerogel and glass surface. The generated stress was strong enough to delaminate the silica aerogel from the glass plate. Therefore, the third part focuses on why silica aerogels shrink during drying by studying the structural reorganization of silica wet-gels during processing.

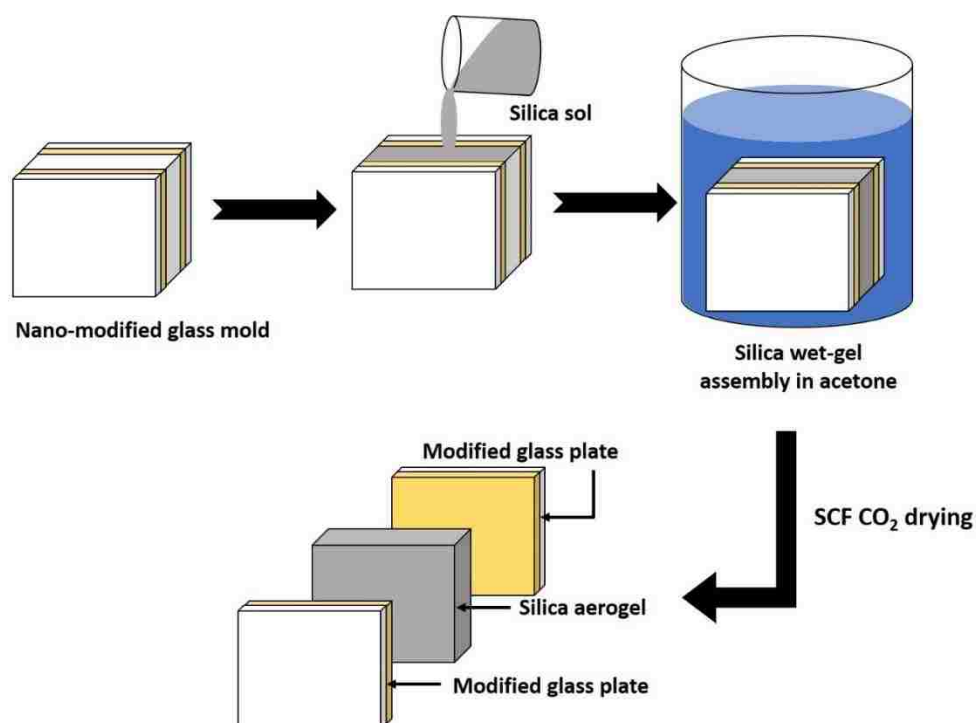


Figure 1.17. Delamination of silica gel during supercritical drying

## 1.7. DRYING SHRINKAGE IN SILICA AEROGELS

Drying of wet-gels can be done by three different techniques. The first one is by ambient pressure drying where the gels are dried under atmospheric pressure and the pore filling solvent is removed by evaporation. The evaporation can either be done at room temperature or at higher temperature. Silica wet-gels cracks during the ambient pressure drying. The resulting dried gels are termed as xerogels. Those xerogels undergoes extensive shrinkage and cracks due to the stress generated from capillary pressure during ambient drying.<sup>73,74</sup>

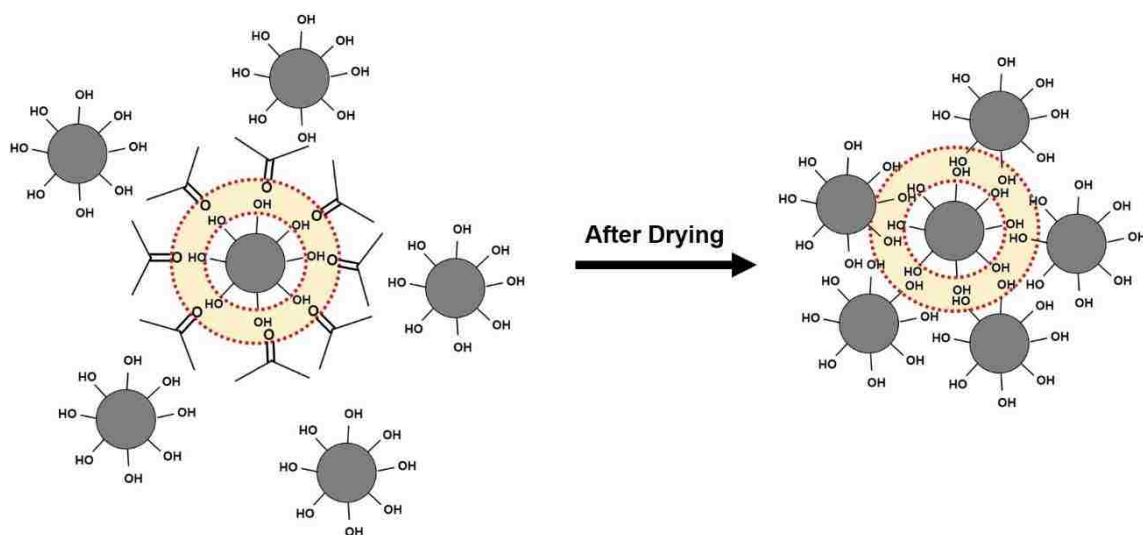
Moreover, since silica aerogels are mostly mesoporous, the small pore sizes increase the capillary pressure and therefore silica wet-gels crack upon ambient pressure drying. In order to control the stress due to the capillary pressure, the surface tension can be changed by drying from different solvents or  $\cos\theta$  can be decreased. Introducing supercritical drying eliminates the capillary pressure due to elimination of  $\cos\theta$ . Therefore, aerogels are synthesized by supercritically drying the wet-gels where the volume of the gel is retained. In supercritical drying, the pore filling solvent is taken to critical point where it will be converted into gas. Then that gas is vented off and replaced by air and is termed as aerogel. The supercritical drying can be of two types, one is by heating the pore filling solvent (methanol or ethanol) to its critical point in order to convert into gas. Achieving that critical point of the solvents need high temperature. When the wet-gels are heated at high temperatures to attain the critical point of the solvent, Ostwald ripening accelerates and due to this accelerated syneresis, aerogels shrink. Moreover, heating the solvents to such a high temperature during this process is dangerous. Therefore, the second way of supercritical drying is by exchanging the pore filling solvent with supercritical fluid CO<sub>2</sub>.

That can be done at room temperature and higher pressure. Once the pore filling solvent is replaced by the supercritical fluid CO<sub>2</sub>, it can be converted into gas at 33 °C and vented off as gas resulting in aerogel. At critical point, since the  $\cos\theta$  term is zero, the capillary pressure becomes zero. However, it was reported in literature that even after supercritical drying, aerogels shrink, and that shrinkage is termed as drying shrinkage.

The drying shrinkage was also observed when the silica wet-gel assembly stuck to the glass plates (Figure 1.17) was dried supercritical, they delaminated. Different methods were used in literature to control the drying shrinkage of silica aerogels for example making silica aerogels hydrophobic that decreases the surface tension of the pore filling solvent.<sup>74</sup> Aging silica wet-gels in gelation solvent, water, mixture of water and ethanol,<sup>75</sup> silica precursors, thermal aging, etc.<sup>76-80</sup> Crosslinking can also decrease the shrinkage by mechanically reinforcing the silica network.<sup>81</sup> The collapse of the network is dependent on the rate at which the liquid escapes from the gel. Since liquid CO<sub>2</sub> have low permeabilities with low viscosity, therefore, the network can relax at a faster rate, hence the shrinkage.<sup>79</sup> Moreover, during the replacement of pore filling solvent with liquid CO<sub>2</sub>, incomplete diffusion might lead to existence of the residual solvent in the pores. When the wet-gel with incomplete diffusion is subjected to the critical point of CO<sub>2</sub>, shrinkage takes place. Rangarajan et.al. reported that maximum shrinkage occurs during depressurization. That is because at wet-gel stage, the adsorbed liquid in the small pores exert forces. During depressurization, when the CO<sub>2</sub> is desorbed, the stress due to adsorption decreases resulting in compression and hence explains the drying shrinkage.<sup>79</sup>

It was also reported that during drying, the particle or clusters come closer leading to shrinkage.<sup>76</sup> Silica primary particles consist of surface silanol groups. In the wet-gel

stage, silica particles are surrounded by the solvent for e.g., acetone. At that stage, the surface silanol groups can establish H-bonding interaction with the solvent. Therefore, the silica particles stay in dispersed state. However, after drying, the solvent is lost. At that stage, the H-bonding of surface silanol groups are also lost. Therefore, in order to establish H-bonding, adjacent primary particles come closer and undergoes H-bonding with adjacent primary particles as shown in Scheme 1.3.



Scheme 1.3. Structural reorganization of silica wet-gels during drying

During this rearrangement, particles come closer and squeeze into another particle. In order to one particle squeeze into another, the silica particles need to have enough space to accommodate the adjacent particle. When the drying conditions were duplicated at wet-gel stage the stage of shrinkage stage changes. In absence of H-bonding solvent, shrinkage occurred during wet-gel stage. Finally, all the aerogels showed similar shrinkage with different stages of shrinkage.

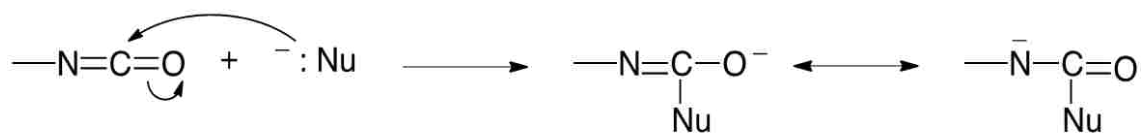
### 1.8. THE ISOCYANATE CHEMISTRY

The isocyanate,  $\text{-N=C=O}$ , is one of the most reactive organic groups, due to the presence of partial positive charge on the carbon atom induced by the electron withdrawing abilities of both the nitrogen and oxygen atoms. Therefore, the isocyanate group acts as an electrophile (Scheme 1.4) and is susceptible to nucleophilic attack as shown in Scheme 1.2. However due to the presence of the substituents on the N, its reactivity towards nucleophile.



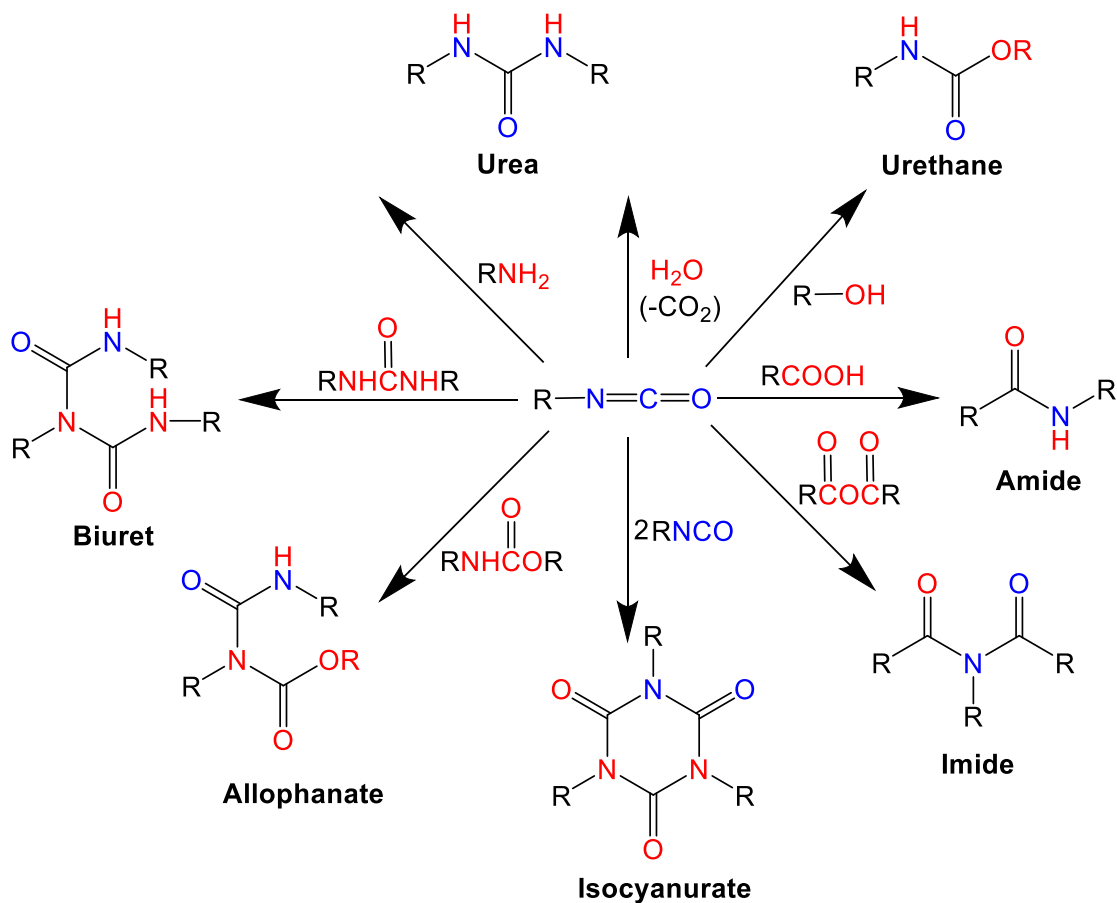
Scheme 1.4. The isocyanate group

Scheme 1.5 shows the nucleophilic attack on the isocyanate group. The isocyanate can react with different kinds of nucleophiles like alcohols ( $\text{R-OH}$ ), amines ( $\text{R-NH}_2$ ), carboxylic acids ( $\text{R-COOH}$ ), isocyanate ( $\text{R-NCO}$ ),  $\text{H}_2\text{O}$  etc. Isocyanates when react with alcohol, they produce urethane linkage as shown in Scheme 1.6.<sup>82</sup>



Scheme 1.5. Nucleophilic attack on the isocyanate group

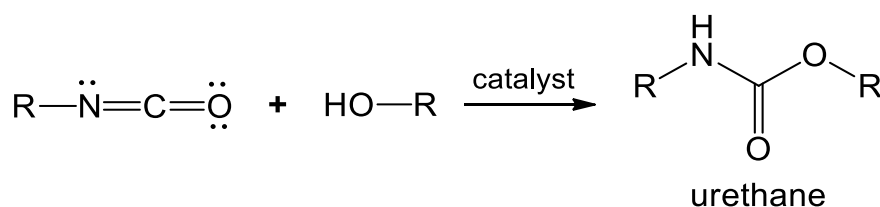
Substitution of the aliphatic group with aromatic group in the isocyanate increases the reactivity of isocyanates. That increase in the reactivity is due to the increase in positive charge on the carbon atom due to resonance with the aromatic ring. Therefore, the carbon atom of the aromatic isocyanate groups can act as better electrophile than carbon atom of aliphatic isocyanates. In addition to that, the electropositive character is more pronounced when any electron-withdrawing substitution group is present on the aromatic ring. Due to the addition of the electron-withdrawing group, the positive charge density on the C-atom further increases thereby increasing the reactivity of isocyanate.<sup>82-85</sup>



Scheme 1.6. The chemistry of isocyanates with different nucleophiles

Part of this dissertation is based on the reaction of isocyanate with alcohols to polyurethanes and therefore, those reactions are discussed in more detail below.

**1.8.1. Reaction of Isocyanates with Alcohols.** When the isocyanate reacts with alcohols, addition reaction takes place leading to the formation of urethane. The stoichiometry of the reaction is shown in Scheme 1.7.<sup>24</sup>

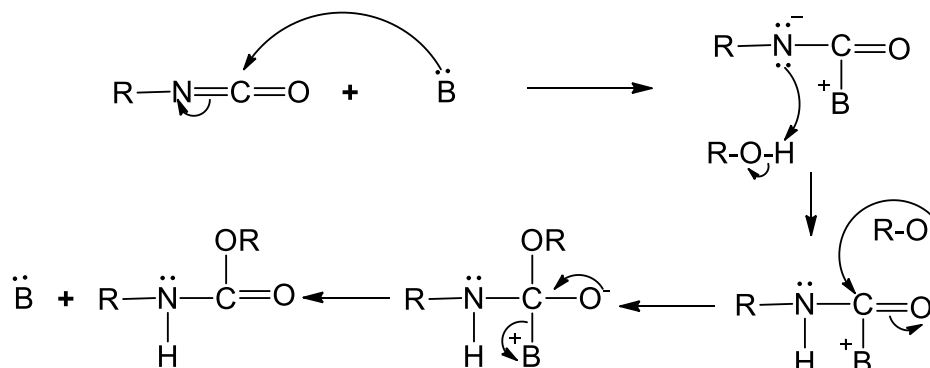


Scheme 1.7. Formation of urethanes from isocyanates and alcohols

Unlike aromatic isocyanates, aromatic alcohols are less reactive than aliphatic alcohols. Due to resonance, delocalization of the electron pair on oxygen to the aromatic ring takes place and the positive charge density on the O-atom increases. Since the alcohol acts as a nucleophile, therefore, its ability to donate electrons decreases when aromatic group is attached to it thereby making it less reactive than aliphatic alcohol. Moreover, with increase in the alcohol chain length of aliphatic alcohols, the reactivity further decreases due to steric reasons. Since the reactivity of alcohols with isocyanates to form urethane is low, the reaction is typically catalyzed with Lewis acids or bases.

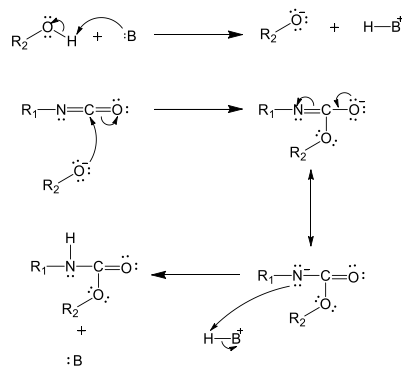
**1.8.2. Urethanes by Base-Catalysis.** Formation of urethanes by base catalysis was assumed to be nucleophilic catalysis. Initially, tertiary amine (B) was used as the base

catalyst for urethane formation. The base acts as a nucleophile and activates the isocyanate carbon as shown in Scheme 1.8.<sup>144</sup>



Scheme 1.8. Formation of urethanes according to Baker et. al.

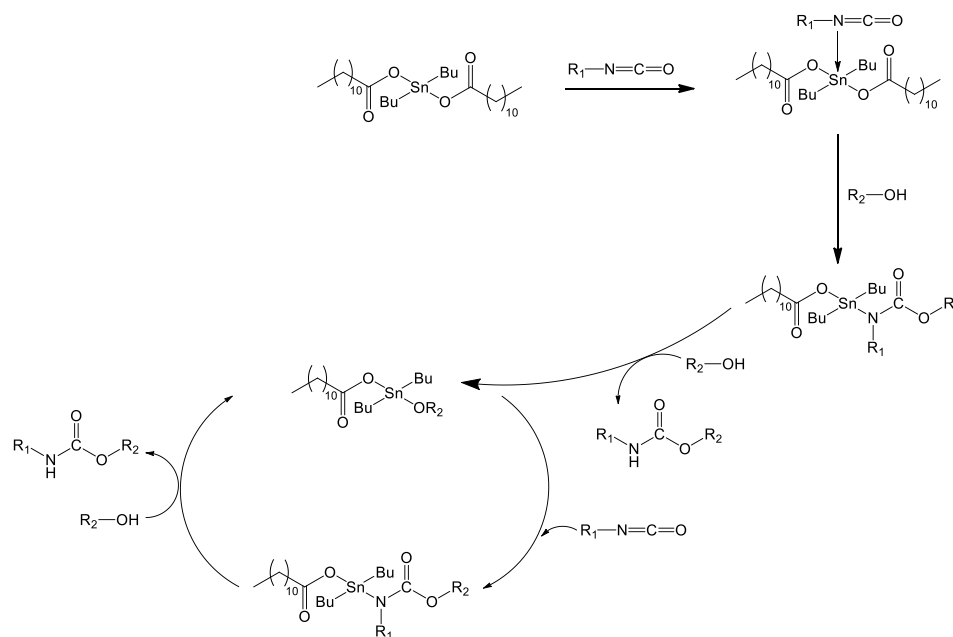
Due to many contradictions, the above mechanism was not valid. However, for an acidic alcohol such as phenol the base extracts the acidic proton of the alcohol thereby forming alkoxide. That alkoxide attacks the isocyanate carbon leading to the adding of the alcohol to the isocyanate (Scheme 1.9).<sup>145</sup>



Scheme 1.9. Formation of urethanes from isocyanates and alcohols by base catalysis

**1.8.3. Urethanes by Acid-Catalysis.** Acid catalyzed urethanes prepared using organotin compounds are widely used for foam processing. Borkent et al. reported that the formation of urethane in polar solvents such as DMF is proportional to the square root of dibutyltin dilaurate concentration.<sup>146</sup> Lead-2-ethylhexoate, lead benzoate, lead oleate, sodium trichlorophenate, sodium propionate, lithium acetate, potassium oleate can also be used as trimerization catalysts. Tin catalyst such as dibutyltin dioctoate, dibutyltin dilaurate, stannous oleate and stannous octoate are many times more powerful for the isocyanate-hydroxyl reaction than tertiary amines, but they are not strong catalysts for the isocyanate-water reaction to yield urea (foam system). Apart from organotin compounds, many metallic compounds were effective catalyst for the isocyanate-hydroxyl reaction and gelation was studied gelation at 70 °C in polyether solvent with a NCO/OH ratio of 1.0.<sup>147</sup> The catalytic activity decreases as follows: Bi, Pb, Sn, DABCO, strong bases, Ti, Fe, Sb, U, Cd, Co, Th, Al, Hg Zn, Ni, trialkylamines, Ce, Mo, Va, Cu, Mn, Zr and trialkyl phosphines. It was reported that urethanes prepared by metal catalyst activates both the reactants involved by means of ternary complex.<sup>148</sup>

Houghton et.al. reported that the activity of the metal salts depends on their ability to form a complex in which the two reacting groups are held in their optimum position for reaction.<sup>149</sup> According to the above mechanism, the catalyst coordinates by the N-coordination of the isocyanate. The tin alkoxide shown in Scheme 1.10 is formed by the alcoholysis of the starting tin compound (Scheme 1.10). Dibutyltin dilaurate (DBTDL) is a typical acid catalyst favored by many researchers.



Scheme 1.10. Formation of urethanes from isocyanates and alcohols by acid catalysis

**1.8.4. Polyurethanes (PU).** Polyurethanes were discovered in 1937 by Otto Bayer and his coworkers through the reaction of diisocyanates and polyester diols.<sup>45,86</sup> Commercialization of polyurethanes started in the year 1952. Soon after polyester polyols were replaced by polyether polyols due to their advantages such as low cost, ease of handling, and improved hydrolytic stability. Tetrahydrofuran was the first commercially available polyether polyol that was first introduced in 1956 by DuPont. Based upon the structure of the original reactants, including the structure and molar mass, number of reactive functional group per molecule of the alcohol and isocyanate, the mechanical, biological, physical and chemical properties of polyurethanes can be varied. For example, soft elastic polyurethanes can be obtained from flexible long segments of polyol, while, short polyol segments yield rigid polymers due to extensive crosslinking. Moreover, by varying the chain length and degree of crosslinking of the polyols, different properties like

stretchy, hard, foamy, etc. of polyurethane can be obtained. Therefore, by tuning the synthetic conditions for preparation of polyurethanes, they can be used for various applications such as in construction, transportation, textiles, fibers, adhesives, foams, bedding and electronic appliances.<sup>87-90</sup> Because of easy modification of the polymer properties, such as mechanical strength and elastic modulus, polyurethanes have been used as a replacement for other plastics, rubber, and metals.<sup>91-94</sup> Depending upon the change in their properties, their application changes and can be used in different types as shown in Figure 1.18.<sup>46</sup>

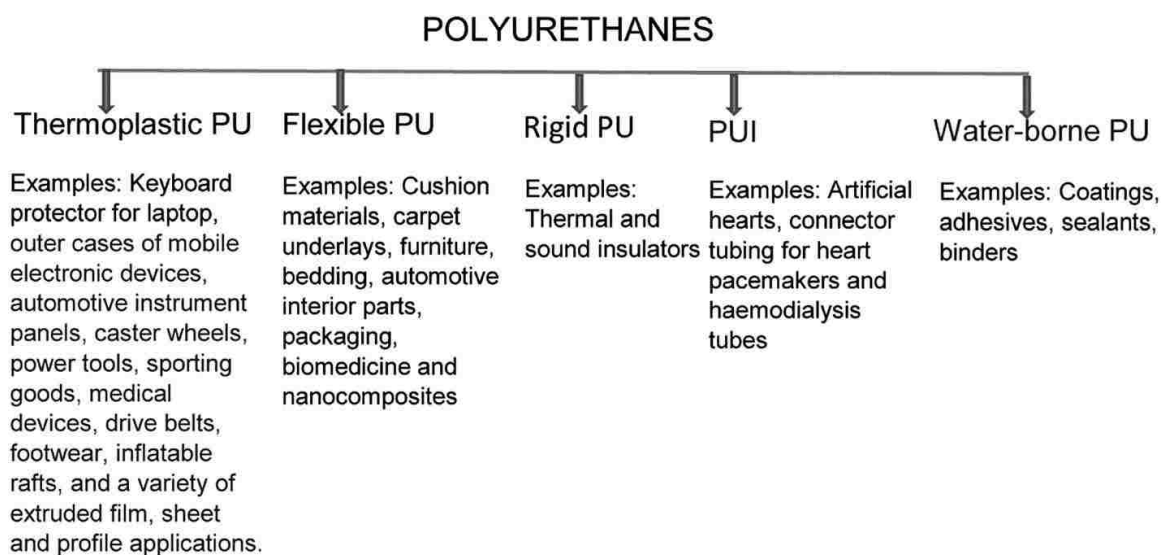


Figure 1.18. Types of PU and their common applications

Based upon the common applications of polyurethanes, they were classified into five categories as: thermoplastic polyurethane, rigid polyurethane, flexible polyurethane, polyurethane ionomers (PUI), and waterborne polyurethane dispersion.<sup>53</sup>

**1.8.4.1. Thermoplastic polyurethanes.** Thermoplastic polyurethanes (TPUs) have many applications such as in footwear, automotive and construction.<sup>95,96</sup> Moreover, due to the non-ionic, water insoluble and inert properties of TPUs, they can be used in medical tubing.<sup>97,98</sup> TPUs are flexible and elastic with impact resistant properties that makes them applicable for various purposes. Like other elastomers, TPUs are processed from heat (melt-processable polymers). They can also be prepared by extrusion, blow, compression and injection-moulding equipment.

**1.8.4.2. Rigid PU foams.** These foams can be used mostly as energy saving insulation materials and can also impart structural strength to the appliances and vehicles.<sup>99,100</sup> Due to their effective insulation properties, they have been applied in windows applications as well as barrier sealants. They can be prepared from petroleum based or bio-based polyols. The properties of the resulting PU foam depend on the type of polyol used. Several studies have been done to replace the petroleum-based polyols with other polyols such as vegetable-based polyols. PU foams derived from soybean oil show high flame-retardant properties.<sup>150</sup> Incorporation of nanoclays increases the thermal stability of PU foam with light weight, increased compressive strength and good flame-retardant properties. Incorporation of polyisocyanurate (PIR) in the rigid PU foams can be used to insulate buildings.<sup>101,102,103</sup> They are synthesized from the trimerization of aliphatic or aromatic isocyanates upon heating whose forward reaction is more favored than the backward reaction. Due to high crosslinking, the rigid foams have closed pores and hence trapped solvents in the pores. Therefore, the solvents with low thermal conductivities are preferred for the synthesis of rigid foam.<sup>104</sup>

**1.8.4.3. Flexible PU foams.** Flexible polyurethane foams are synthesized by three separate and consecutive processes: blowing, polymerization and crosslinking process. In the blowing process, CO<sub>2</sub> and urea are formed by the reaction of isocyanate with water that gets entrapped by the reaction mixture while the urethane linkages are formed by the reaction of isocyanate and alcohols. The CO<sub>2</sub> evolved acts as blowing agent. Apart from CO<sub>2</sub>, other blowing agents such as methylene chloride, chlorofluorocarbon, etc. These blowing agents does not change the chemical composition and are only used to expand the foam by vaporization.

(1) Gas Formation, Foaming



immediately followed by:



(2) Chain Formation:



(3) Crosslink Formation:



In the second step, the isocyanate reacts with diols to form polyurethanes. From the third step i.e., the crosslinking step, the morphology and microstructure are varied. Flexible PU foams consists of block copolymers of two or more segments and their flexibility is controlled by the phase separations of the soft segment and the hard segment.<sup>111</sup> By varying the proportion of the soft and hard segments, the flexibility of these foams can be adjusted. Applications of flexible PU foams include cushion materials, carpets, furniture, packaging,

biomedicine and nanocomposites.<sup>105-109</sup> Flexibility can be enhanced by using lower crosslinking, lower NCO:OH ratio, and longer chain length of the monomers. Using longer chain length for monomers, the glass transition of the flexible PU decreases. The most commonly used isocyanates for foams are 2,4 and 2,6-toluene diisocyanate, while the alcohols are polyether polyols with the general formula  $H-(CHOH)_m-CH_2O-(C_2H_5O)_n-H$ , that is, typical polyols are polyethers from active hydrogen compounds like glycerol, sorbitol, sucrose etc. Though flexible PU are crosslinked, they have weak tensile and tear properties. To overcome the mechanical issue, flexible PU can be reinforced with textile-based fibers of carbon, basalt and aramids.<sup>110</sup>

**1.8.4.4. Polyurethane ionomers.** Polyurethane ionomers are the polyurethanes that consists of ionic groups in the polyurethane backbone chain. Polyurethane ionomers can be prepared from ionic alcohols or diisocyanates containing ionic groups. Due to the presence of those ionic groups, they have better dispersion in polar medium with enhanced mechanical and thermal properties. The biocompatibility of these polymers makes them useful for many medical applications like artificial hearts, connector tubing for heart pacemakers and haemodialysis.<sup>112-128</sup> The presence of the ionic groups in the polyurethane backbone changes the glass transition temperatures for polyurethanes.

**1.8.4.5. Waterborne polyurethanes.** Due to excellent mechanical, chemical and physical properties, waterborne PUs find vast applications as coatings, adhesives, sealants and elastomers.<sup>129,130</sup> For using PUs in coatings, they need to possess good adhesive properties, low temperature flexibility, high chemical resistivity, excellent drying, and adequate scratch resistivity.<sup>131-134</sup> However, PUs has poor impact resistance and degrades under UV rendering their applications as coatings. In order to overcome those problems

several authors have synthesized PUs with enhanced properties.<sup>135-138</sup> PUs can be used as elastomers in shoe soles, household items, surfboats etc.<sup>139,140</sup> They are lighter than metals and can recover back after extreme deformation. However, they have weak elastic properties that can be addressed by incorporating graphene oxide in the PU foam.

**1.8.5. Shape Memory Polymers (SMP).** SMPs belongs to the special class of polymers which can remember and recover back to its original shape when triggered by any external stimulus such as temperature, light, electric or magnetic fields (Figure 1.19). A necessary condition for shape memory effect is superelasticity. Superelasticity is the property of the material to recover back to its original shape after extreme deformation. Superelasticity and shape memory effects are mostly associated with alloys. Many shape memory alloys have been reported in literature. In 1932, Au-Cd alloy was discovered to show superelastic behavior by Olander. Then in 1938, shape memory effect in Cu-Zn alloy was reported. Again in 1951, Au-Cd alloy that had been reported as superelastic, also showed shape memory effect. Then in 1963, very commonly used Ni-Ti alloy, commonly known as nitinol was reported to show shape memory effect. Finally, in 1986, the mechanism of the shape memory effect in alloys was explained by Otsuka and Shimizu. These shape memory materials can exist in two stable phases: austenitic phase (at higher temperature) and a martensitic phase (at lower temperature or under stress). Under stress these materials are converted to a martensitic phase at higher temperature and then upon cooling, it fixes itself at that phase in the deformed shape. Upon heating, the material returns to austenitic phase, and the object recovers back to its original shape. Apart from SMAs, Shape memory polymers are also reported in literature.<sup>141,142</sup> First Shape memory polymers were reported by Vernon et.al. These shape memory polymers can be used as

dental materials. Then in 1960, covalently crosslinked polyethylene in the form of heat shrinkage tubing was reported. In 1990, significant interest in SMP have been accelerated. SMPs are differentiated from SMAs by their high tolerance for strains, low density, and low stresses. Here, superelasticity is usually referred to as “rubber-like elasticity,” or simply as a “memory effect”. Thereby, shape memory polymers are elastomers that have rigid crosslinking nodes between stretchable polymeric strands. In order to be stretchable, polymeric strands must be free to move and should be amorphous above their glass transition ( $T_g$ ). Shape memory aerogels have extra advantages of low thermal conductivity over the shape memory polymers.

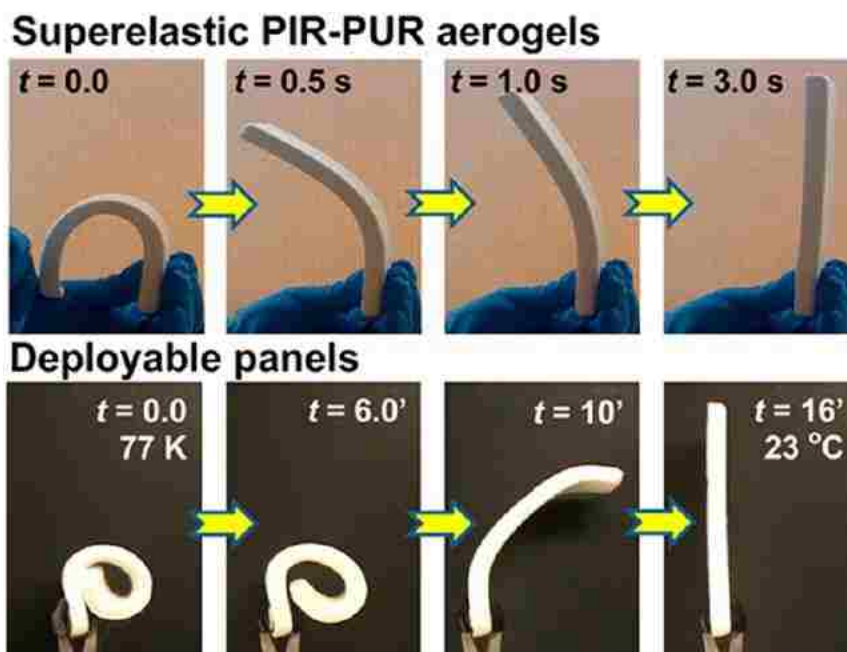


Figure 1.19. Shape memory aerogels showing superelastic and shape memory properties

Preparation of shape memory aerogels was reported from thiol-ene networks of 1,6-hexanedithiol, pentaerythritol tetrakis (3-mercaptopropionate), and triallyl-1,3,5-triazine-2,4,6,-trione. They possessed  $T_g$  values in the range of 42-64 °C which assists in the shape recovery process. Samples were characterized using compression testing for five cycles.<sup>94</sup> In 2017, Donthula et.al, reported the synthesis of shape memory polyisocyanurate-polyurethane aerogels using isocyanurate-based triisocyanate and ethylene glycol-based diols (ethylene glycol, diethylene glycol, triethylene glycol, and tetraethylene glycol). The formation of polyurethane was catalysed using Sn based Dibutyltindilaurate (DBTDL) as catalyst.<sup>14,151</sup>

Thermodynamic and kinetic properties of shape memory aerogels similar to Marcus type relationship were correlated as shown in Figure 1.20 by Donthula, S et al.

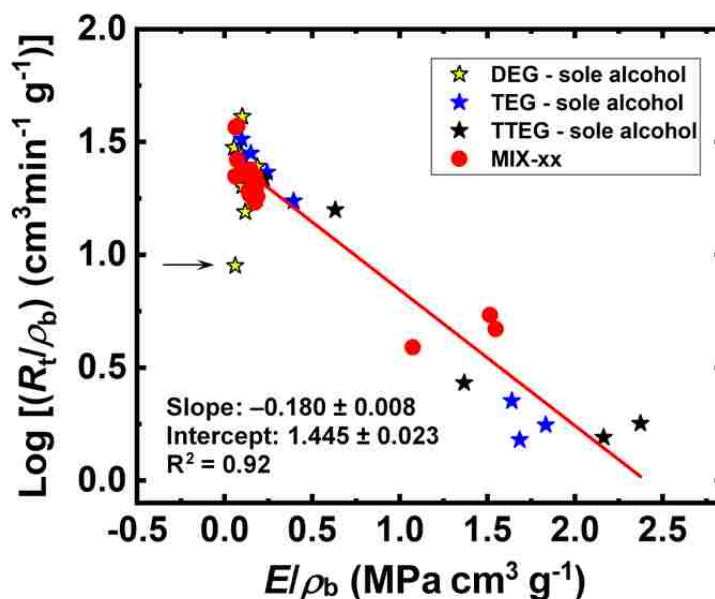


Figure 1.20. Relationship between elastic modulus (thermodynamic property) and shape memory recovery rate (kinetic property)

That was achieved by preparing aerogels from N3300A and mixture of alcohols. An inverse relationship was observed between elastic modulus (thermodynamic property) and shape memory recovery rate (kinetic property).<sup>14,151</sup>

**1.8.6. Shape Memory Poly (urethane-isocyanurate) Aerogels.** Synthesis of poly(urethane-isocyanurate) aerogels have been reported from commercially available aliphatic triisocyanate (N3300A) and triethylene glycol in acetonitrile. The monomer concentration and alcohol mole fraction was varied in order to prepare SMAs with varying morphologies including fused spheroidal morphology consisting of micrometer sized particles fused together, bicontinuous structures which is formed due to early phase separation, and spheroidal morphologies with individual spheres. The factors that led to the formation of those morphologies were gelation kinetics, that was controlled by varying the monomer concentration. Higher monomer concentration gives faster gelation and chances for early phase separation resulting in bicontinuous structures. However, increasing the monomer concentration beyond certain limit results in collapse of the aerogel network. Another factor that influences the morphology of SMPUs is the solubility of the polymer which is dependent on the mixture of the alcohol. With increase in the alcohol chain length, polymer solubility increases resulting in late phase separation. Moreover, the solvents used for the synthesis also effects the morphology of SMPUs. Part of the thesis is on preparing SMPUs with different morphologies with similar material properties that was obtained by controlling the gelation kinetics. In order to do that, the synthesis of SMPU was catalyzed using different metal chloride salts from the periodic table as shown in Figure 1.21. Various metal chlorides showed the catalytic activity. Different morphologies were obtained from



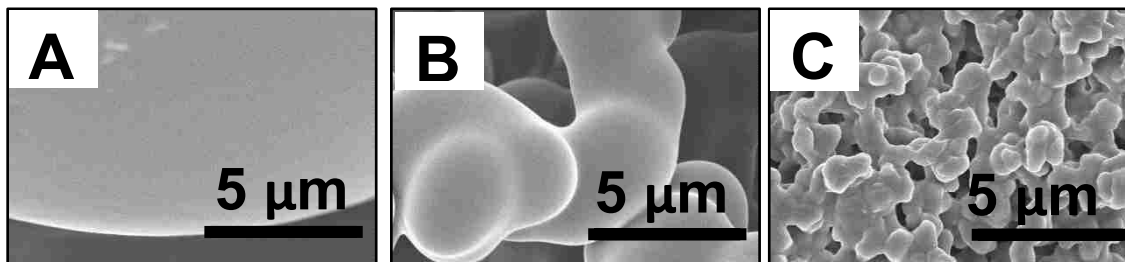


Figure 1.22. SEM images of  $\text{CuCl}_2$  catalyzed SMPU aerogels with increasing catalyst concentration from A. 1/20 $\times$ , (B) 1/10 $\times$ , and (C) 4 $\times$

Then the temperature was decreased to fixation temperature ( $T_f$ ) by keeping the force constant. At this point, the sample becomes stiff with a slight increase in strain (Step 2). Then the stress was removed by keeping the temperature constant. The sample relaxes slightly and slight decrease in strain was observed. At this point, the sample becomes stiff and attains a fixed temporary shape (step 3). Then finally the temperature was increase to the recovery temperature ( $T_r$ ) with a constant heating rate, where the sample recovers back to its original shape leaving behind some residual strain. The residual strain was observed only after the first cycle and was attributed to the settling in the sample at the molecular level.<sup>14</sup> The process was repeated for 5 times in order to how robust its shape memory behavior was. In order to define the three temperatures ( $T_d$ ,  $T_f$ , and  $T_r$ ) used during the shape memory experiment, glass transition temperature ( $T_g$ ) was measured and the three temperatures were defined w.r.t. the glass transition temperature. The deformation temperature was  $T_g+10$  °C, fixation temperature was  $T_g-40$  °C, and recovery temperature was same as the deformation temperature i.e.,  $T_g+10$  °C.  $T_g$  values were obtained from single frequency strain oscillation experiments while ramping the temperature from -150 °C to 150 °C using a Dynamic Mechanical Analyzer.

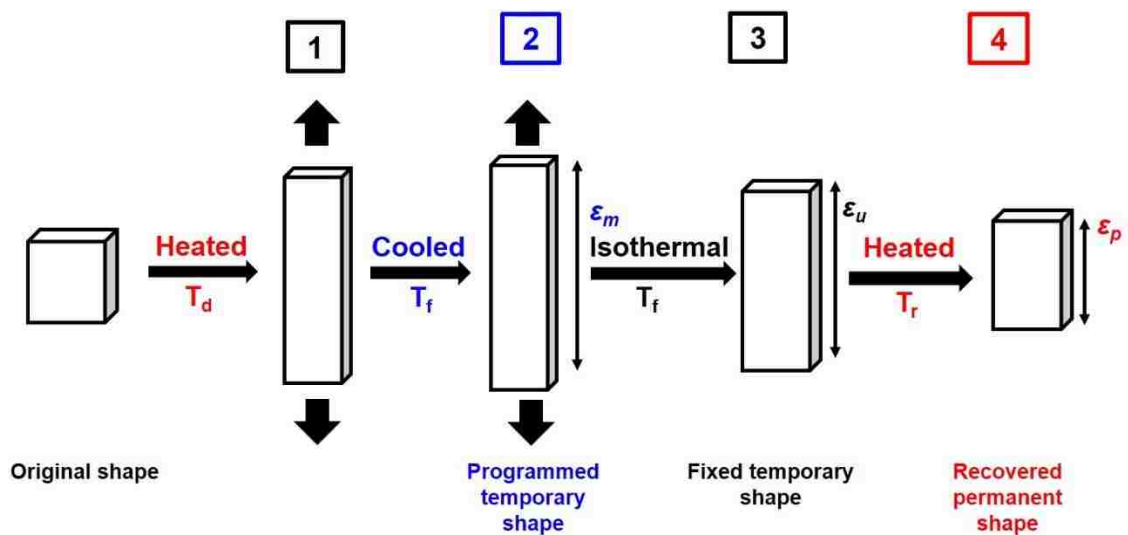


Figure 1.23. Experiment demonstrating shape memory effect

**1.8.6.3. Applications of shape memory aerogels.** The shape memory aerogels can be used in orthopedics as a plaster for fractured bones. Consider a shape memory aerogel prepared in the form of hollow cylindrical as shown in Figure 1.24. The sample when heated above glass transition, it can be deformed to a temporary shape. Then it can be cooled and used in hospitals. When the sample will be heated above glass transition, it will recover back to its original shape thereby wrapping around and holding the limb firmly. Previously, these shape memory aerogels have been shown to bio mimic the muscle coordination of a human hand grabbing a pen.<sup>14</sup>

In this paper, the origin of drying shrinkage in silica aerogels was investigated by employing silica wet-gels formed via base-catalyzed hydrolysis and polycondensation of tetramethylorthosilicate (TMOS). Typically, as-prepared silica wet-gels are aged (e.g., for 24 h) in order to reinforce their skeletal framework, and it is well-known that shrinkage

observed during that period (syneresis) is due to dissolution and reprecipitation of silica (Ostwald ripening).

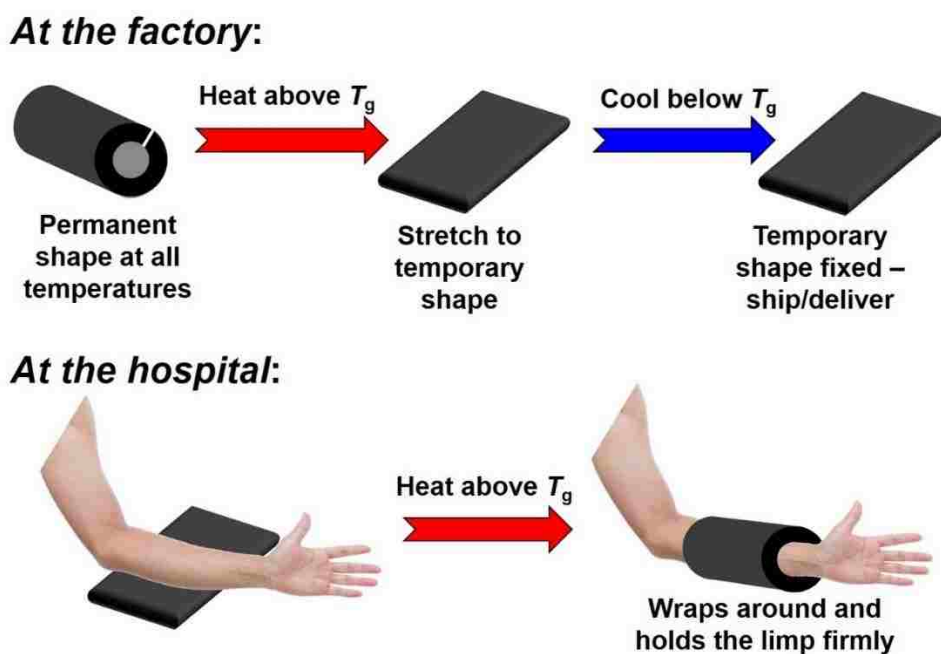


Figure 1.24. Application of shape memory aerogels in orthopedics

For this study, the sol-gel process was monitored with liquid  $^{29}\text{Si}$  NMR. Subsequently, in order to deconvolute drying shrinkage from syneresis, wet-gels were processed into aerogels at seven different stages during aging (2, 4, 8, 12, 16, 20 and 24 h). Importantly, we were able to emulate the drying shrinkage effect in the wet-gel stage by exchanging pore-filling gelation solvents with non-H-bonding solvents like toluene and xylene. The final aerogels were chemically characterized using solid state  $^{13}\text{C}$ ,  $^{29}\text{Si}$  NMR, and FTIR. Physical characterization to study the pore structure, particle size and morphology were done using  $\text{N}_2$  sorption, Hg intrusion porosimetry, small angle X-ray

scattering (SAXS) and Scanning electron microscopy (SEM). Liquid state  $^{29}\text{Si}$  NMR was employed to study the progress of the reaction of TMOS sol. Rheology was used to monitor the viscoelastic properties during gelation of the TMOS sol in order to calculate the rheological gelation time.

**PAPER****I. LIGHT SCATTERING AND HAZE IN TMOS-CO-APTES SILICA AEROGELS**

Chandana Mandal<sup>1</sup>, Suraj Donthula<sup>1</sup>, Rushi Soni<sup>1</sup>, Massimo Bertino<sup>2</sup>, Chariklia Sotiriou-Leventis<sup>1</sup>, Nicholas Leventis<sup>\*,1</sup>

<sup>1</sup> Department of Chemistry, Missouri University of Science and Technology, Rolla, MO 65409, U.S.A.

<sup>2</sup> Department of Physics, Virginia Commonwealth University, Richmond, VA 23284, U.S.A.

\* Correspondence: Tel.: 573-341-4391; E-mail: [leventis@mst.edu](mailto:leventis@mst.edu)

Published in *Journal of Sol-Gel Science and Technology*

**ABSTRACT**

TMOS-co-APTES wet-gels have been used as templates for polymer crosslinked aerogels, which in turn have been used as strong materials and as starting materials for ceramic aerogels. Such wet-gels are prepared in acetonitrile (CH<sub>3</sub>CN) via co-gelation of tetramethylorthosilicate (TMOS) and 3-aminopropyl silane (APTES) in a 3:1 v/v ratio. Qualitatively, native monolithic TMOS-co-APTES aerogels appear more clear than the corresponding straight TMOS-derived materials, suggesting applications in thermally insulating daylighting. For that application, it is important to understand and minimize haze. Haze from the bulk of silica aerogels may be due to scattering from particles or pores, but study of its origin may be complicated by scattering and reflections from the surface of the monolith. In this report, using wet-gels as proxy materials for aerogels, haze from

TMOS-co-APTES was investigated as a function of density, which is controlled by the amount of TMOS+APTES in the sol. The wet-gel approach to the study of haze of aerogels has the advantages of eliminating surface scattering issues from aerogel monoliths, and owing to better refractive index matching between the skeletal framework and the surrounding medium (CH<sub>3</sub>CN), bulk scattering is also reduced, facilitating study of lower-density materials. Haze from the bulk was traced to Rayleigh scattering down to 0.017 g cm<sup>-3</sup> aerogels. The opacity of even lower-density samples (down to 0.006 g cm<sup>-3</sup>) was attributed to Mie scattering. The scatterer size was obtained via Rayleigh's law and matched the secondary particle sizes of silica. The size of those particles increased as the density decreased, producing higher haze. Results suggest that in order to keep haze low at lower densities, one must keep the particle size low, for example, by increasing the rate of gelation.

Keywords: Haze, Clarity, Rayleigh scattering, TMOS, APTES, Aerogels, Wet-gels

Highlights:

- The haze of the title silica aerogels increases as their density decreases.
- Wet-gels are good proxy materials for measuring haze in lower-density silica aerogels.
- Wet-gels do not have surface scattering issues, and better index matching reduces haze, allowing measurements at lower densities.
- The haze of the title silica aerogels was traced to Rayleigh scattering from secondary skeletal silica particles to densities as low as 0.017 g cm<sup>-3</sup>.
- Increased haze at lower densities was attributed to increasing particle size.

## 1. INTRODUCTION

Silica aerogels are highly porous, low-density, usually optically transparent nanostructured solids. They were first prepared in the 1930s via acid-catalyzed gelation of aqueous sodium silicate solutions followed by conversion of the pore-filling solvent into a supercritical fluid that was vented off like a gas [1]. Currently, most silica aerogels are prepared via the sol-gel method that was introduced in the 1960s and is based on polycondensation of silicon alkoxides in methanol [2]. Exceptionally low thermal conductivities (around  $0.014 \text{ mW m}^{-1}\text{K}^{-1}$  [3, 4]) have become the point of departure for applications of silica aerogels in thermal superinsulation [5]. Along those lines, combination of low thermal conductivity with high optical transparency renders silica aerogels good candidates for applications in thermally insulating windows and daylighting [6, 7]. Optimization for that application though is confronted by two conflicting requirements. Lowering the density reduces thermal conductivity, primarily because of reduction of the through-solid conduction. By the same token, however, silica aerogels become hazy [8]. Therefore, controlling haze in silica aerogels as density decreases is of pivotal importance for applications in windows and skylights. In that regard, this study focuses on haze as a function of density in silica aerogels prepared by copolymerization of tetramethylorthosilicate (TMOS) and 3-aminopropyltriethoxy silane (APTES) [9, 10]. The resulting materials are abbreviated as TMOS-co-APTES. The choice of TMOS-co-APTES over conventional TMOS-derived silica was based on the fact that optically those materials seem to be clearer than the later.

Silica aerogels do not absorb light in the visible part of the electromagnetic spectrum [11], therefore, loss of clarity is due to light scattering. Clarity is defined as the light that does not deviate more than  $\pm 2.5^\circ$  from the incident beam [12]. All light that is not confined within that angle contributes to haze [12]. Elastic light scattering is caused by interactions of electromagnetic waves with electrons around finite non-uniformities along the optical path [13]. Such non-uniformities can be particles, or pores. In silica aerogels scattering can be caused by either or both [14].

It is well known that silica aerogels appear bluish in ‘reflection,’ and yellowish-orange in transmission [15]. That has been explained by Rayleigh’s theory, which in turn is valid when the scatterer size is less than the one tenth (0.1) of the wavelength of light. In that theory, the intensity of the transmitted light has an inverse relationship with the fourth power of the wavelength, therefore short wavelengths are scattered more, hence the bluish hue of silica aerogels. Owing to their small sizes, primary skeletal silica particles (typically <10 nm) have been considered as an obvious choice [16, 7]. However, since pores in several silica aerogel formulations fall in the medium-to-low part of the mesopore range (2-50 nm) they also fulfill the condition for Rayleigh scattering, and they have been also proposed as the primary scatterers [14].

In addition to scattering by the bulk, the clarity of silica aerogel monoliths can be compromised further by surface defects, e.g., scratches from handling and storage [17]. While the bulk radiation properties of silica aerogels (such as Rayleigh scattering) are intrinsic material properties, and therefore independent of the sample geometry [6], surface scattering from handling depends on the history of the sample and is independent of wavelength [18]. The effect of such surface defects may become quite severe and, due to

the fragility of silica aerogels, it is magnified as density decreases. In practice, controlling surface scattering is quite a challenge.

In this study, haze was quantified with an integrating sphere [12]. Data were related to the scatterer size, which in turn was again related to the size of particles and pores. The particle size was quantified with N<sub>2</sub>-sorption porosimetry and small angle X-ray scattering (SAXS), while pore sizes were quantified with N<sub>2</sub>-sorption and Hg-intrusion porosimetry. In order to eliminate surface scattering effects, and also resolve issues associated with preparation of fragile low-density monolithic aerogels of appropriate size for optical measurements, the main body of haze measurements was carried out with wet-gels serving as proxies for the corresponding aerogels. That approach had also the advantage that due to better refractive index matching between silica and the matrix (the solvent, CH<sub>3</sub>CN), it reduced overall bulk scattering too, and facilitated probing the scatterer size in lower-density materials. Based on those data, scattering and haze were tracked to Rayleigh scattering from secondary skeletal particles down to 0.017 g cm<sup>-3</sup>. Reducing the density even lower (0.006 g cm<sup>-3</sup>) resulted in Mie scattering from pores with sizes in the wavelength range of the visible spectrum.

## **2. EXPERIMENTAL**

### **2.1. MATERIALS**

All reagents and solvents were used as received unless noted otherwise. Tetramethylorthosilicate (TMOS) and anhydrous acetonitrile (99.8%) were purchased from Sigma Aldrich. 3-Aminopropyltriethoxysilane (APTES) and ACS Grade acetonitrile

were purchased from Alfa-Aesar. Siphon grade CO<sub>2</sub> was obtained from Ozark Gas, Rolla, MO.

**2.1.1. Synthesis of Variable-Density, Amine-Modified Silica Aerogels (TMOS-co-APTES).** In a typical procedure for what is referred to herewith as the standard formulation of TMOS-co-APTES gels (and symbolized as K) [9], two solutions, solution A containing TMOS (2.887 mL, 0.0194 mol), APTES (0.963 mL, 0.0041 mol) and anhydrous acetonitrile (4.5 mL), and solution B containing water (1.5 mL, 0.0833 mol) and anhydrous acetonitrile (4.5 mL) were first cooled in dry-ice, then they were allowed to thaw, and as soon as “ice” melted, the two solutions were mixed together. The resulting sol was agitated vigorously and was poured into molds where it was allowed to gel. Aerogels intended for typical material characterization were molded with cylindrical Polypropylene Scintillation Vials, 6.5 mL, Sigma-Aldrich Catalog No. Z376825, 12.56 mm inner diameter. (Molding of wet-gels and aerogels intended for haze measurements was different - see below.) Wet-gels were aged in their molds for 24 h or 4× the gelation time, whichever was longer. After aging, wet-gels were removed from the molds, they were washed with acetonitrile (4×8 h each time), and were dried in an autoclave with liquid CO<sub>2</sub> taken out at the end as a supercritical fluid (SCF). While the volume ratio of TMOS:APTES was kept constant (3:1 v/v), the total mass of silane (TMOS+APTES ) was varied from 1/2, 1/4, 1/8, 1/16 and 1/32 with respect to the total mass used in the standard formulation as just described above (refer to Table S.1, Appendix I in Supporting Information). (The mass of H<sub>2</sub>O used in the sol followed the reduction in mass of the total silane.) Sols below 1/32 of the standard formulation did not gel.

In order to measure haze (H) of wet-gels, we constructed special rectangular glass molds with microscope slides (3'' × 1'' × 1 mm, Fisher Scientific, Catalog No. 12-544-1). First, the microscope slides were cleaned by submerging them in water containing 3-5 drops of Micro-90 cleaning solution (Cole-Parmer, Item # SK-18100-05). Glass pipettes were placed between slides in order to avoid sticking of one microscope slide to another. The cleaning solution with the slides in it was heated to boil. As soon as the cleaning solution started boiling it was decanted, glass slides were washed thoroughly with copious amounts of distilled water, and were dried in an oven at 150 °C for 12 h. Molds were prepared by using epoxy glue to join two such pre-cleaned and dried glass slides together with suitable spacers fixed along the two long sides of the slides. The thickness of the resulting rectangular glass containers (13.49 mm) was determined by the thickness of the spacers. The spacers were narrow borosilicate glass stripes cut at a glass shop. Epoxy was cured in an oven at 150 °C for 12 h.

In order to prepare aerogels for haze measurements, glass molds were prepared by holding two pre-cleaned and dried (see above) 3''×3'' glass plates parallel to one another with a circular spacer in between. The spacer was constructed by cutting a ~10 mm ring off a 1'' diameter plastic container using a band saw. The spacer was attached to the glass plates by applying a small amount of high vacuum grease along its outer edges. (High vacuum grease is not soluble in the sol and prevented leaking.) The assembly of the two glass plates with the spacer in between was wrapped tightly with Parafilm™. The mold was filled with the sol through a very small portion of the ring spacer that had been previously cut off with a knife. That opening was sealed with Parafilm™ once the sol gelled.

## 2.2. METHODS

Drying of wet-gels was carried out in an autoclave (SPIDRY Jumbo Supercritical Point Dryer, SPI Supplies, Inc. West Chester, PA, or Spe-edSFE System, Applied Separations, Allentown, PA). Wet-gels submerged in acetonitrile were loaded into the autoclave at room temperature. The pressure vessel was closed, and liquid CO<sub>2</sub> was allowed in at room temperature. Acetonitrile was drained out from the pressure vessel every 20 min, while more liquid CO<sub>2</sub> was allowed in. The cycle was repeated several times until all acetonitrile had been extracted out of the pores of the samples. Subsequently, the temperature of the autoclave was raised to 40 °C, and that condition was maintained for two hours. Finally, SCF CO<sub>2</sub> was vented off as a gas.

**2.2.1. Chemical Characterization.** Solid-state <sup>29</sup>Si NMR spectra were obtained on the Bruker Avance III 400 MHz spectrometer using a 7 mm Bruker MAS probe and magic angle spinning at 5 kHz with a 59.624 MHz silicon frequency. <sup>29</sup>Si NMR spectra of one of the sample were obtained using both cross-polarization (CPMAS pulse sequence) and direct polarization. All spectra were referenced externally to neat tetramethylsilane (TMS, 0 ppm). The relaxation delay was set at 5 s in both experiments. The number of scans for the CPMAS experiment was set at 8,192 with a contact time of 3,000 μs, while the number of scans for the direct polarization experiment was set at 16,384.

**2.2.2. Physical Characterization of Aerogels.** Bulk densities ( $\rho_b$ ) were calculated from the weight and the physical dimensions of aerogel monolith directly after removing the samples from the drier. Skeletal densities ( $\rho_s$ ) were determined with helium pycnometry using a Micromeritics AccuPyc II 1340 instrument. Samples for skeletal density were degassed for 24 h at 80 °C under vacuum. Percent porosities of aerogels,  $\Pi$ , were

determined from the  $\rho_b$  and  $\rho_s$  values via  $\Pi = 100 \times (\rho_s - \rho_b) / \rho_s$ . Linear shrinkages were calculated from the physical dimensions of the samples.

**2.2.3. Structural Characterization of Aerogels.** BET surface areas, fractal dimensions and pore size distributions for pore sizes in the range of 1.7–300 nm were determined with N<sub>2</sub>-sorption porosimetry at 77 K using a Micromeritics ASAP 2020 surface area and porosity analyzer. Pore size distributions of the standard sample, standard/2, /4 and /8 (referred to as K, K/2, K/4 and K/8) were also determined with Hg-intrusion porosimetry using a Micromeritics AutoPore IV 9500 instrument.

Scanning electron microscopy (SEM) was conducted with Au/Pd (80/20) coated samples on a Hitachi Model S-4700 field-emission microscope. A single-sided sticky Cu-tape was attached on a double-sided sticky carbon dot placed on the stub, and the sample was stuck on the sticky-side of the Cu-tape. Then, thin Cu-strips were cut and placed on top of the samples leaving some area open for observation.

Small-angle X-ray scattering (SAXS) was carried out with a PANalytical X'PertPro Multipurpose Diffractometer (MPD) configured for SAXS, using Cu K $\alpha$  radiation ( $\lambda = 1.54$  Å), a 1/32° SAXS slit together with a 1/16° antiscatter slit on the incident beam side, and a 0.1 mm antiscatter slit and a Ni 0.125 mm automatic beam attenuator on the diffracted beam side. Aerogels were placed in circular holders between thin Mylar sheets, and the scattering intensities were measured with a point detector in the transmission geometry using  $2\theta$  scans ranging from  $-0.1^\circ$  up to  $5^\circ$ . SAXS intensity data are reported in arbitrary units as a function of  $Q$ , the momentum transferred during a scattering event ( $Q = 4\pi \times n \times \sin \theta / \lambda$ , where  $n$  is the refractive index of the medium. For air  $n = 1$ ). Data analysis

was conducted with the Irena SAS tool for modeling and analysis of small-angle scattering within the commercial Igor Pro software package (WaveMetrics, Inc. Lake Oswego, OR).

**2.2.4. Haze Measurements of Wet-gels and Aerogels.** Haze (H) measurements of wet-gels were carried out directly in their rectangular glass molds (see above) using a Cary 5000 UV-Vis Spectrophotometer Model # G9825A equipped with an integrating sphere (S/N # MY 1744 0002). Transmittance was recorded from 380 nm to 800 nm. Samples were referenced against similar glass molds filled with CH<sub>3</sub>CN. Experiments were carried out according to the ASTM D1003-13 (see next section). Haze measurements of aerogels were carried out similarly, with one notable difference: The integrating sphere was referenced to open air, and therefore haze measurements included both bulk and surface haze.

### 3. RESULTS AND DISCUSSION

#### 3.1. SYNTHESIS AND MATERIALS CHARACTERIZATION OF TMOS-CO-APTES AEROGELS

TMOS-co-APTES wet-gels were prepared with different silane (TMOS+APTES) concentrations in the sol while the TMOS:APTES volume ratio was kept constant at 3:1 v/v as described in the Experimental section. The standard formulation was the one used in reference [9], and the corresponding wet-gels and aerogels are referred to as K (from the name of the first author in reference [9]). Subsequently, samples were prepared by decreasing the mass of total silane in the sol to K/2, K/4, K/8, K/16 and K/32. The reaction is autocatalytic, namely the –NH<sub>2</sub> groups of APTES provide the base environment needed for gelation. Owing to the high concentration of APTES in K, the sol needed cooling in dry

ice in order to allow time to be cast in the molds. Gelation of that cold solution took about 2 min. Gelation time progressively increased and the process did not require cooling. K/32 gelled in about 13 h at room temperature (refer to Table S.1 of Appendix I in Supporting Information). Wet-gels appeared progressively more hazy as the monomer concentration decreased (Figure 1). K/32 wet-gels were milky-white allowing only diffused light to go through. All wet-gels were washed (solvent exchanged) with the gelation solvent ( $\text{CH}_3\text{CN}$ ) and were dried to aerogels according to standard procedures. Aerogels appeared much more hazy than the corresponding wet-gels. Figure 2A shows K and K/2 aerogels in front of text, and Figure 2B in front of landscape. The clarity of those samples was high, however it was compromised by some surface defects from handling and storage (Figure 2B). K/8 to K/32 aerogels were extremely fragile. Diffuse light could still go through K/8 and K/16, but K/32 aerogels were completely opaque white.

The average skeletal density ( $\rho_s$ ) of K to K/32 aerogels was  $1.728 \pm 0.009 \text{ g cm}^{-3}$  suggesting an identical chemical composition and absence of closed pores. The identical chemical composition was confirmed with  $^{29}\text{SiNMR}$  spectra taken both under direct and under cross polarization. The two sets of spectra were internally identical for all samples. A typical spectrum (for the K aerogel) is shown in Figure 3. The  $\text{T}_3$  and  $\text{T}_2$  silicon atoms of APTES appeared at -66 ppm and -59 ppm, respectively. The shoulder at -92 ppm and the peaks at -101 ppm and at -110 ppm correspond to the  $\text{Q}_2$ ,  $\text{Q}_3$  and  $\text{Q}_4$  silicon atoms of TMOS, respectively. The intensification of the T-group and the  $\text{Q}_3$  resonance under cross polarization was due to the vicinity of silicon atoms to hydrogens from the propyl group of APTES and OH, respectively [19].

Material characterization data for the aerogels are summarized in Table 1. Most samples shrunk around 8 to 12 % in linear dimensions during processing (solvent exchange and drying) except for K/16 and K/32, which shrunk around 19 % and 42 %, respectively (mostly during drying). Despite shrinkage, bulk densities ( $\rho_b$ ) were found as low as 0.017 g cm<sup>-3</sup> and 0.006 g cm<sup>-3</sup> for K/16 and K/32, respectively. At the other end, bulk densities of K and K/2 were as high as 0.214 g cm<sup>-3</sup> and 0.119 g cm<sup>-3</sup>, respectively. Correspondingly, percent porosities,  $\Pi$ , calculated via  $\Pi=100\times(\rho_s-\rho_b)/\rho_s$ , increased from 87.6% v/v for K, to 99.7% for K/32.

Microscopically (SEM – Figure 4), all samples consisted of particles. As reported before [9,20], the tiniest building blocks of the K formulation of TMOS-co-APTES aerogels appeared to form small aggregates, which in turn appeared to be distributed randomly in the 3D space. As bulk density decreased, we noticed: (a) a progressive slight but definite increase in the size of the particles discernible in SEM, and (b) an arrangement of the secondary aggregates into strings. Short strings are already visible in K/2, and by K/32 strings of beads dominate the structure. We also notice a very large increase in pore size with decreasing silane concentration. Pores moved from the mesopore/small macropore domain in K (30-50 nm) to large macropores in K/32 (>500 nm).

The porous structure and the skeletal framework were probed further with N<sub>2</sub>-sorption and Hg-intrusion porosimetry as well as with small angle X-ray scattering. Those techniques are complimentary in scope (e.g., probing pores vs particles), and in size-regime: they were selected in order to compare particle and pore sizes with the sizes of scattering entities (from Haze measurements), and thus identify the origin of haze.

The N<sub>2</sub>-sorption isotherms of K and K/2 aerogels were clearly of Type IV (Figure 5A), they reached saturation and showed broad hysteresis loops characteristic of mesoporous materials. The two samples uptook the same amounts of N<sub>2</sub> as partial pressure approached unity ( $P/P_o \rightarrow 1$ ). From K/4 and beyond, samples uptook progressively much less N<sub>2</sub>, the hysteresis loops became narrower, and the overall isotherms tended towards Type II, typical of macroporous materials (Figure 5B). The specific pore volumes in the range of 1.7-300 nm ( $V_{1.7-300\text{-nm}}$ , Table 1) of K aerogel samples, was about equal to the total specific pore volume calculated from bulk and skeletal density data (via  $V_{\text{Total}} = (1/\rho_b) - (1/\rho_s)$ ) meaning that we are dealing with mostly a mesoporous material (refer to the pore size discussion below); in K/2  $V_{1.7-300\text{-nm}}$  was a little over half ( $4.5 \text{ cm}^3 \text{ g}^{-1}$ ) of  $V_{\text{Total}}$  ( $7.8 \text{ cm}^3 \text{ g}^{-1}$ ); and, in K/32  $V_{1.7-300\text{-nm}}$  decreased to a tiny fraction of  $V_{\text{Total}}$  indicating macroporous materials. Specific surface areas,  $\sigma$ , were calculated via the BET equation and decreased from  $960 \text{ m}^2 \text{ g}^{-1}$  in K to  $148 \text{ m}^2 \text{ g}^{-1}$  in K/32, consistent with the increase in particle size noted in SEM. Primary particle radii,  $r$ , were calculated from skeletal density and surface area data via  $r = 3/(\rho_s \times \sigma)$ , and increased from 1.79 nm in K aerogels to 5.34 nm in K/8 to 9.54 nm in K/16, and to 11.7 in K/32 (Table 1). The aggregates of those particles that were visible in SEM were mass fractals, and their fractal dimensions,  $D_f$ , were calculated from the slopes of  $\text{Ln}(V)$  versus  $\text{Ln}\{\text{Ln}(P_o/P)\}$  plots according to Eq 1 [21], where,  $V$  is the volume of N<sub>2</sub> adsorbed at each equilibrium pressure  $P$ ,  $V_m$  is the volume of N<sub>2</sub> adsorbed in a monolayer, and  $P_o$

$$\text{Ln}\left(\frac{V}{V_m}\right) = (D_f - 3) \left[ \text{Ln}\left\{ \text{Ln}\left(\frac{P_o}{P}\right) \right\} \right] + \text{constant} \quad (1)$$

is the saturation pressure. The mass fractal dimensions of all samples, K to K/32, ranged from 2.57 to 2.70 in no particular order (Table 1). Fractal assembly of primary particles indicates that in spite of samples turning macroporous with decreasing density, there was always a certain amount of small pores, in the mesopore range, that persisted the mesoporous-to-macroporous transition – hence explaining the very narrow but persisting hysteresis loops in Figure 5B.

Pore diameters were calculated from N<sub>2</sub>-sorption data using the  $4 \times V/\sigma$  method. Pore diameters were compared by setting  $V = V_{\text{Total}} = (1/\rho_b) - (1/\rho_s)$  versus  $V = V_{1.7\_300\_nm}$  (Table 1). The two values converged for K aerogels (17.1 nm vs 19.6 nm, respectively), but they started diverging immediately after that: for example, by setting  $V = V_{1.7\_300\_nm}$ , the average pore diameter of K/2 was about equal to that of K (19.9 nm), but it was found higher by setting  $V = V_{\text{Total}}$  (34.9 nm). At any rate, both ways of applying the  $4 \times V/\sigma$  method indicated that K and K/2 were mesoporous materials. In agreement to that, the pore size distributions calculated by the BJH method (see inset in Figure 5A) were narrow and the maxima agreed reasonably well to the values calculated by setting  $V = V_{1.7\_300\_nm}$ . Beyond K/2, average pore diameters calculated by setting  $V = V_{1.7\_300\_nm}$  *decreased* and remained all in the range of 4.3-7.6 nm. On the other hand, by setting  $V = V_{\text{Total}}$ , average pore diameters kept on *increasing* from 34.9 nm in K/2, to 75 nm in K/4, up to 4.5  $\mu\text{m}$  in K/32, reflecting the increasing porosity as the amount of matter getting into the materials decreased. The two facts, namely that: (a) by setting  $V = V_{1.7\_300\_nm}$ , pore diameters decreased, and (b) after the K/4 sample pore diameters remained within a narrow range, agree with the mass fractal assembly of primary particles, as discussed above. Mass fractal secondary particles include, percentage wise, a large amount of empty space [22].

The porous structures of K, K/2, K/4 and K/8 aerogels were also probed with Hg-intrusion porosimetry. Beyond those samples, K/16 and K/32 were mechanically too weak to withstand any significant pressure and collapsed early. The Hg-intrusion isotherms of K and K/2 samples are shown in Figure 6. Calculated average pore diameters are included in Table 1. Hg-intrusion is capable of probing pores larger than the 1.7-300 nm range that is probed by N<sub>2</sub>-sorption, and in that respect it confirms the increasing trend in pore sizes noted with the  $4 \times V/\sigma$  method when  $V$  considers the entire pore volume, namely by setting  $V = V_{\text{Total}} = (1/\rho_b) - (1/\rho_s)$ .

Small angle X-ray scattering (SAXS) of all aerogels of this study was conducted in order to probe and quantify the solid framework further in terms of particle sizes. Figure 7 shows typical data for the scattering intensity vs. the scattering vector,  $Q$ . Data were analyzed with the Beaucage Unified Model [23, 24], and results are summarized in Table 2.

All X-ray scattering profiles for all samples could be fitted in only 2 regions (e.g., see Figure 7). The power-law, high- $Q$  region (Region I) had a slope of about 4.0, thus obeying Porod's law [25]. That slope confirms that scattering from the upper  $Q$  range came from the smallest particles. The curvature of the profiles at lower  $Q$ s (Guinier knee – Region II) gave the radii of gyration of the scattering particles,  $R_G$ , which were related to the actual radii,  $R$ , via  $R_G = 0.77 \times R$ . It is noted that those  $R$  values from SAXS were larger than the  $r$  values of primary particles via N<sub>2</sub>-sorption (Table 1). In that regard, considering: (a) the relative sizes of the primary particles ( $r$  in Table 1) and the particles identified via SAXS ( $R$  in Table 2), and (b) the fact that primary particles aggregate (via SEM) into mass fractals (via N<sub>2</sub>-sorption), the particles identified via SAXS were assigned to secondary particles.

The fact that primary particles were not observed in SAXS was attributed to their small size (small radii of gyration), in combination with the scatter of data (i.e., the noise) in the high- $Q$  region. This nanoscopic picture emerging from the N<sub>2</sub>-sorption/SAXS data agrees with SEM, according to which there is a match between the smallest discernible aggregates (pointed at by circles and arrows) and the particle sizes identified with SAXS.

### **3.2. OPTICAL PROPERTIES OF TMOS-CO-APTES WET-GELS AND AEROGELS**

**3.2.1. Haze.** The Haze ( $H$ ) of all wet-gels as well as of K and K/2 aerogels was measured from 380 nm to 800 nm using an integrating sphere according to ASTM D1003-13 (Scheme 1) [12]. Wet-gels were prepared and sealed in thin flat cells (see Figure 1B) that were constructed with clean microscope slides and suitable spacers as described in the Experimental section. Referring to Scheme 1, each cell containing a wet-gel was placed in front of the transmittance port of the integrating sphere and transmittance was recorded from 380 nm to 800 nm under two different configurations: (a) the total light that passed through the sample (total transmittance of sample,  $T_2$ ) was recorded by placing the cover on the reflectance port of the integrating sphere so that no light could escape the sphere; and, (b) only the scattered light (sample scatter,  $T_4$ ) was captured by removing the cover from the reflectance port.

In order to correct the data for stray light, as well as for scattering and reflectance from the cell, parallel measurements were carried out by placing a CH<sub>3</sub>CN-filled cell, similar to those that contained the wet-gels, in the transmittance port of the integrating sphere with the cover of the reflectance port in place (reference radiant spectrum,  $T_1$ ), and also with the cover removed (reference scatter,  $T_3$ ). In the case of aerogels, we used the

samples shown in Figure 2A (for the  $T_2$  and  $T_4$  measurements), while the instrument radiant ( $T_1$ ) and instrument scatter ( $T_3$ ) measurements were obtained without placing anything in front of the transmittance port. Using the above four transmittance values,  $T_1$  to  $T_4$ , the percent haze ( $\%H$ ) was calculated via Eq 2.

$$\%H = 100 \times \left( \frac{T_4}{T_2} - \frac{T_3}{T_1} \right) \quad (2)$$

In all samples, haze increased from 800 nm to 380 nm (Figure 8). The average percent haze over all wavelengths for all wet-gels as well as for K and K/2 aerogels were calculated from the integrals underneath the spectra (shaded area in Figure 8) divided by the width of the wavelength domain (= 800 nm – 380 nm = 420 nm). The minimum haze was observed for K wet-gels with an average value of 2.75 %. Consistent with Figure 1, haze increased with decreasing total silane concentration in the sol (Figure 8 – inset). The average haze of K and K/2 aerogels was about 2.5 times higher than the haze of the corresponding wet-gels. Results are summarized in Table 3.

**3.2.2. Haze and the Scatterer Size.** As mentioned in the Introduction, Haze ( $H$ ) is defined as light that is scattered at angles larger than ( $\pm 2.5^\circ$ ) from the direction of a collimated incident beam [12]. Light that remains within that interval is defined as clarity,  $C$  [12]. With data corrected for scattering and reflection from the cell (as the case is here with wet-gels - see section 3.b.1 above), and when a material has negligible light absorption, then the sum of haze and clarity is equal to the total transmittance:  $H + C = T$ . In our case, wet-gels and aerogels do not absorb light in the 380 nm to 800 nm range, therefore  $T = 1$ , and the same holds true for the sum of  $H + C$ :

$$H + C = 1 \quad (3)$$

Now, loss of clarity due to haze, is mathematically analogous, to loss of transmittance due to absorbance. Therefore, by analogy to Beer's law, it can be shown that [26]:

$$-\ln(C) = \sigma_{\text{scatterer}} c_{\text{scatterer}} l \quad (4)$$

where  $\sigma_{\text{scatterer}}$  is the scattering cross-section per scattering entity,  $c_{\text{scatterer}}$  is the number-average concentration of scatterers per unit volume, and  $l$  is the thickness of the sample (in all wet-gels  $l = 13.49$  mm; for the K/2-aerogel,  $l = 9.81$  mm; and, for the K-aerogel,  $l = 9.88$  mm).

As it could be demonstrated readily with fairly hazy K/8 aerogels, white light reflected off those samples looked bluish, and transmitted light was yellowish (Figure 9). This is classic behavior attributed to Rayleigh scattering. The same phenomenon was observed visually with K/16 aerogels, but because of their increased opacity the transmitted light was too weak to be captured easily in a photograph as with K/8 in Figure 9. As noted above, K/32 aerogels were opaque-white. Therefore, it is safe to assume that haze, at least down to K/16, was mainly due to Rayleigh scattering. In Rayleigh scattering the scatterer cross-section is given by Eq 5 [27],

$$S_{\text{scatterer}} = \frac{2\rho^5 d^6}{3l^4} \left( \frac{n^2 - 1}{n^2 + 2} \right)^2 \quad (5)$$

where  $d$  is the scatterer diameter,  $\lambda$  is the wavelength of the incident light, and  $n$  is the relative refractive index of the scatterer versus the surrounding medium (matrix):  $n = n_{\text{scatterer}} / n_{\text{matrix}}$ .

For Rayleigh scattering to occur (as in Figure 9) the scatterer size should be at least  $10\times$  smaller than the wavelength of light ( $d \leq 0.1\lambda$ ) [11]. As we saw above, all K to K/32

aerogels may have both particles and pores that fulfill that constrain. It is reminded, however, that in K/4 to K/32 aerogels the pore size that could cause Rayleigh scattering remained about the same (4.3-7.6 nm in diameter – Table 1), while the number of the pores decreased (refer to the values of  $V_{1.7-300\_nm}$  relative to  $V_{Total}$  in Table 1). The latter is because those tiny pores were located between primary particles, and the number of those particles decreased both because primary particles became larger towards the K/32 end of the range, and because the total amount of matter in the samples decreased. Thereby, if Rayleigh scattering (as of Figure 9) was due to tiny pores, the scattering intensity should decrease with density, not increase, as observed experimentally. Therefore, Rayleigh scattering was caused by particles, not by pores.

Having established the skeletal TMOS-co-APTES silica particles as the most probable cause for scattering and haze, their number-average concentration per unit volume,  $c_{scatterer}$ , is given by Eq 6, where  $\Pi$  is the sample porosity. For aerogels,  $\Pi_{aerogel}$  was calculated directly from bulk

$$c_{scatterer} = \frac{6(1 - P)}{\rho d^3} \quad (6)$$

and skeletal density data (Table 1). For wet-gels,  $\Pi_{wet-gel}$  was calculated from the bulk and skeletal densities of the corresponding aerogels, and the corresponding shrinkage data (Table 1) via Eq 7 (for the derivation of Eq 7, refer to Appendix II in Supporting Information).

$$P_{wet-gel} = \frac{r_{s\_of\_silica} - \left(1 - \frac{\%shrinkage}{100}\right)^3 \times r_{b\_of\_aerogel}}{r_{s\_of\_silica}} \quad (7)$$

Substituting Eq.s 3, 5 and 6 into Eq 4 we obtain Eq 8, in which the scatterer is silica and the matrix is either CH<sub>3</sub>CN or air.

$$-Ln(1 - H) = \frac{4(1 - P)\rho^4 d^3 \left(\frac{n^2 - 1}{n^2 + 2}\right)^2}{l^4} l \quad (8)$$

Therefore, for wet-gels  $n_{\text{wet-gel}} = n_{\text{silica}}/n_{\text{CH}_3\text{CN}} = 1.462/1.346=1.086$ , and for aerogels  $n_{\text{aerogel}} = n_{\text{silica}} / n_{\text{air}} = 1.462$ . (The  $n$  values used for those calculations were those reported for fused silica and CH<sub>3</sub>CN at 500 nm [28].) Correspondingly, for wet-gels the  $[(n^2 - 1)/(n^2 + 2)]^2$  term of Eq 8 was calculated equal to 0.003, while for aerogels that term was equal to 0.076. Clearly, wet-gels will scatter significantly less than the corresponding aerogels, and therefore their clarity will be higher, as observed experimentally (compare Figure 1 and Figure 2 and refer to Table 3).

Primary haze data for all wet-gels and aerogels (as those in the main frame of Figure 8) were plotted versus  $1/\lambda^4$  according to Eq 8 (Figure 10). For wet-gels, deviations from linearity started with K/8 and became more pronounced in K/16. The relationship of Eq 8 was not valid for K/32, nevertheless an attempt was still made to fit the K/32 data to that equation. The scatterer size of wet-gels was calculated from the slopes of the curves in Figure 10 and data are included in Table 3. (For K/8 and K/16 we used only the linear part of the plots in Figure 10 for calculating slopes, although that did not change the scatter size dramatically, <5%.) Table 3 also includes the secondary particle diameters from the SAXS data ( $2 \times R$ , Table 2). With the exception of the K/32 wet-gel, there was a remarkably good agreement between the scatterer size in wet-gels calculated from Rayleigh's law, and the secondary particle size of silica aerogels. What is particularly interesting in the cases of K and K/2 wet-gels, in which (as inferred from the corresponding aerogels) not only the sizes

of the secondary particles (Tables 2 & 3), but also the sizes of the pores (Table 1) were within range for Rayleigh scattering, the size of the secondary particles matched much better than the size of the pores with the size of the scatterers. Scattering from K/32 wet-gels, which looked opaque-white and did not follow Rayleigh's law, was probably due to Mie scattering from the fraction of the pores whose size was in the same range as the wavelengths of visible light (refer to SEM: Figure 4) [29].

As summarized in Table 3, the average haze of K and K/2 aerogels was about 2.5 times higher than the haze of the corresponding wet-gels. That was not due to the thickness of the samples, which, in fact, were thinner than the corresponding wet-gels (see footnotes of Table 3).

Thereby, higher haze from aerogels was attributed partly to  $n_{\text{aerogel}} > n_{\text{wet-gel}}$ , and partly to surface defects from handling (for example, refer to the area pointed at by the yellow arrow in Figure 2B). Such surface scratches cause reflection and scattering of the incident beam *before* it enters the sample. The slopes of the  $-\ln(1-H)$  vs  $1/\lambda^4$  plots of the K and K/2 aerogels (Figure 10, dashed lines) were also higher than the slopes from the corresponding wet-gels. Not being affected by surface scattering, those slopes depended (via Eq 8) on the sample porosity, thickness, relative refractive index of the skeletal framework, and the scatterer diameter. The latter were calculated to be about 50% of the scatterer size in the corresponding wet-gels (refer to Table 3), and they fell in the range between the sizes of the primary (Table 1) and secondary particles (Tables 2 or 3), suggesting that both of those particles contributed to the scattering and haze of native aerogels.

#### 4. CONCLUSION

Using TMOS-co-APTES silica wet-gels as proxies for the optical properties of the corresponding aerogels, it has been shown that haze increases as the sol concentration decreases. Haze was traced to Rayleigh scattering down to sol compositions that yield aerogels with bulk densities as low as  $0.017 \text{ g cm}^{-3}$ . Haze in those wet-gel samples was attributed to light scattering from silica particles rather than pores. The scatterer size calculated via Rayleigh's law matched well with the size of the secondary silica particles (SAXS). That was not the case of the most dilute sols of this study, i.e., those that yield aerogels with bulk densities as low as  $0.006 \text{ g cm}^{-3}$ . In those sols, haziness was attributed to Mie scattering from pores with sizes in the visible part of the electromagnetic spectrum. Wet-gels were definitely much more clear than the corresponding aerogels. Unfortunately, however, larger wet-gels monoliths survived processing and yielded monolithic aerogels suitable for optical measurements only from the upper end of sol concentrations (K and K/2). Indeed, the haze of those aerogel samples was significantly higher than that of the corresponding wet-gels, and was partly attributed to their higher relative refractive index, and partly to surface defects (e.g., roughness from handling or storage). Overall, it is noted that since the dependence of the scattering cross-section on the particle size is to the sixth power (Eq 5), small apparent increases in skeletal particle size end up to disproportional increase in haze. That explains the difficulty to make transparent polymeric aerogels, while in terms of materials design, for silica aerogels with lower densities and high clarity one would need to accelerate the nucleation and growth process at lower sol concentrations [30]. The later could be accomplished, for instance, by using high catalyst concentrations

(comparable to the APTES concentration in the K formulation of TMOS-co-APTES sols of this study).

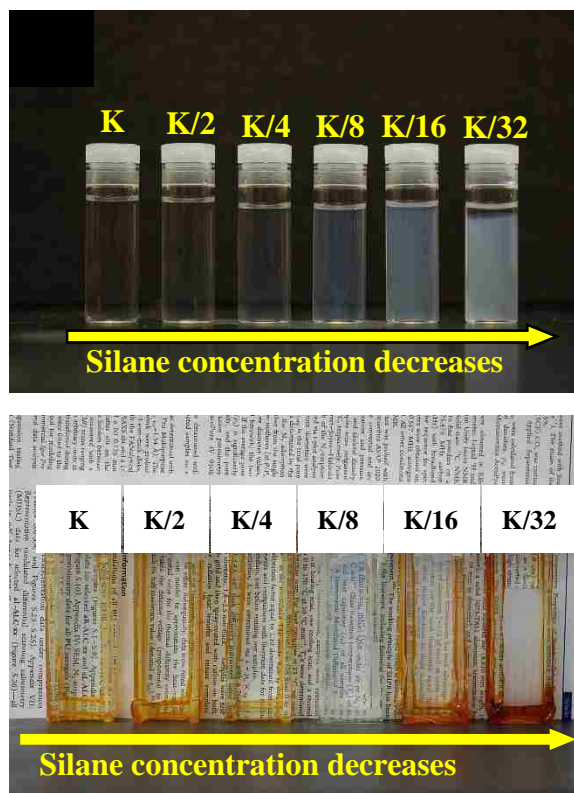


Figure 1. (A) Photograph of TMOS-co-APTES wet-gels showing an increase in haze with decreasing silane concentration (K to K/32). (B) Same as in (A) with gels prepared in flat cells (13.49 mm thick), used later (Figure 8) for measuring haze

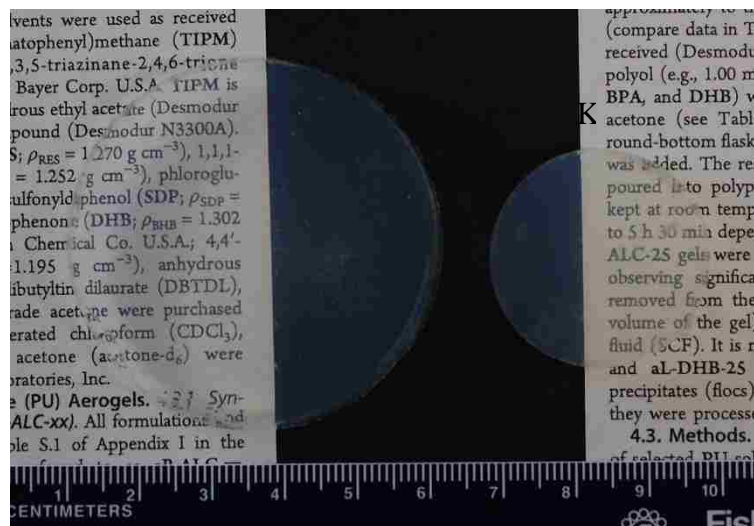


Figure 2. (A) Photograph of a K and a K/2 aerogel monolith in front of text. (B) An aerogel monolith of standard formulation (K) in front of landscape. Slight lensing is due to the curved surface of the monolith that was created by the meniscus of the sol. Yellow arrow points to surface scratches caused by handling

Direct Polarization

Cross Polarization

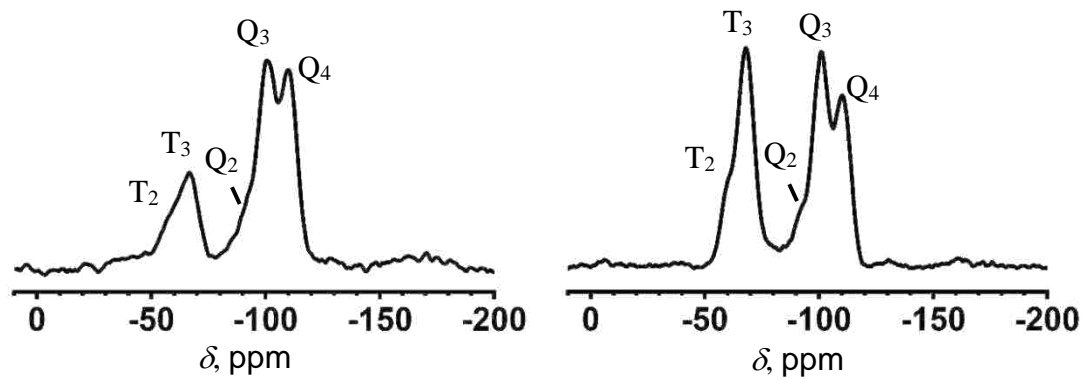


Figure 3. Typical solid-state  $^{29}\text{Si}$  NMR spectra of K aerogels under direct and cross-polarization

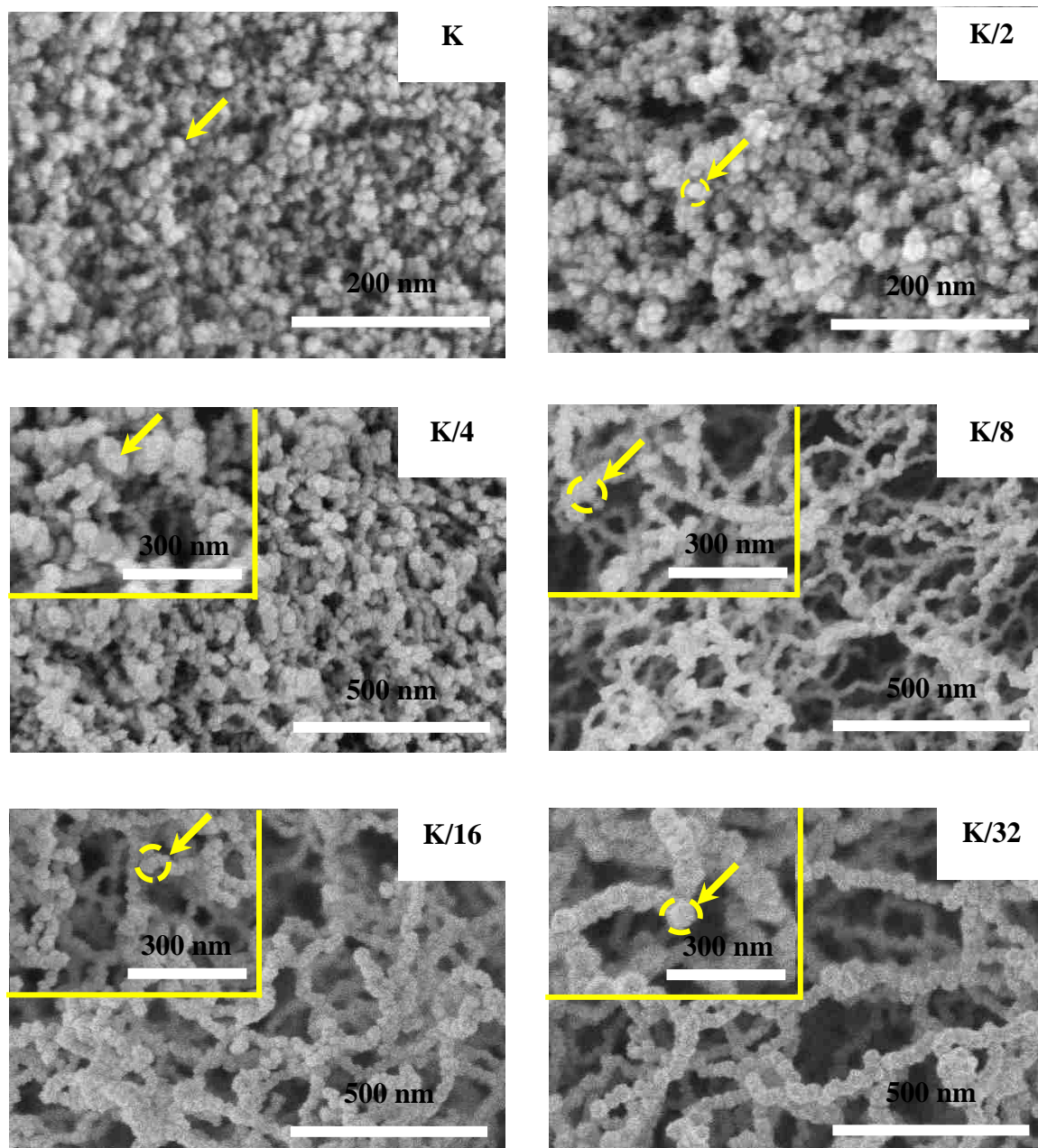


Figure 4. SEM images of TMOS-co-APTES aerogels as shown. (For other material properties refer to Table 1.) Dashed circles and arrows point to secondary particles

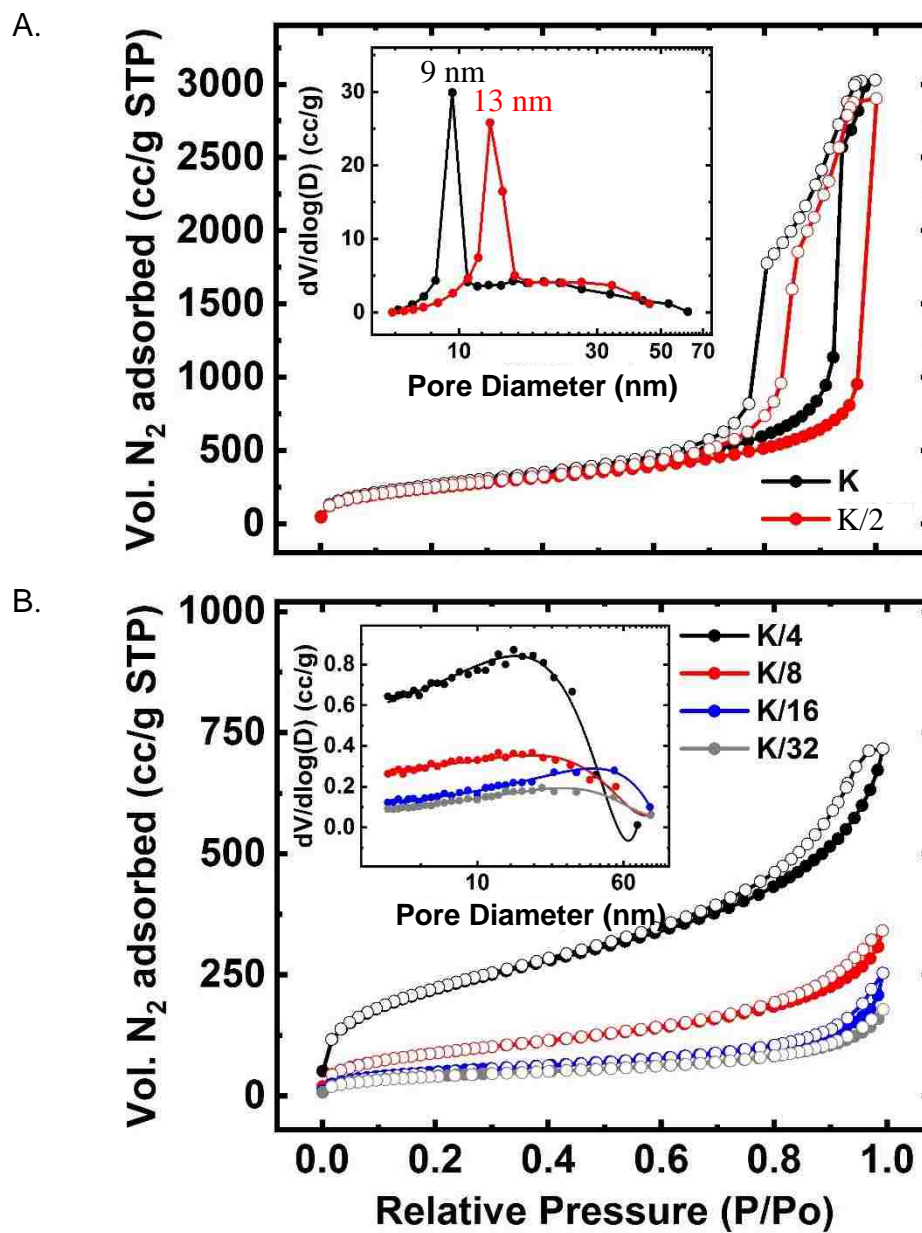


Figure 5. N<sub>2</sub>-sorption data. (A) K and K/2 aerogels. (B) K/4, K/8, K/16, and K/32 aerogels. Insets: Corresponding pore size distributions by the BJH desorption method

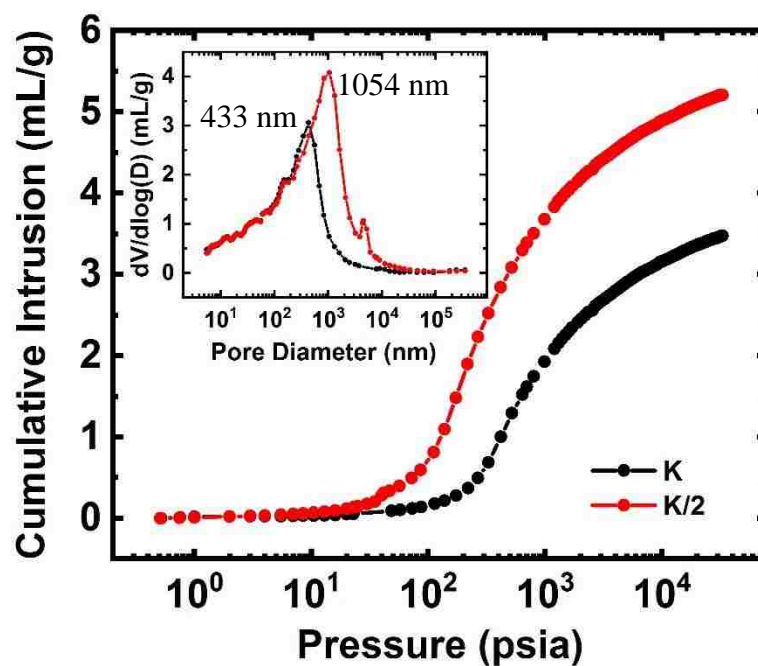


Figure 6. Representative Hg-intrusion porosimetry data of K and K/2 aerogels. Inset: Pore size distributions

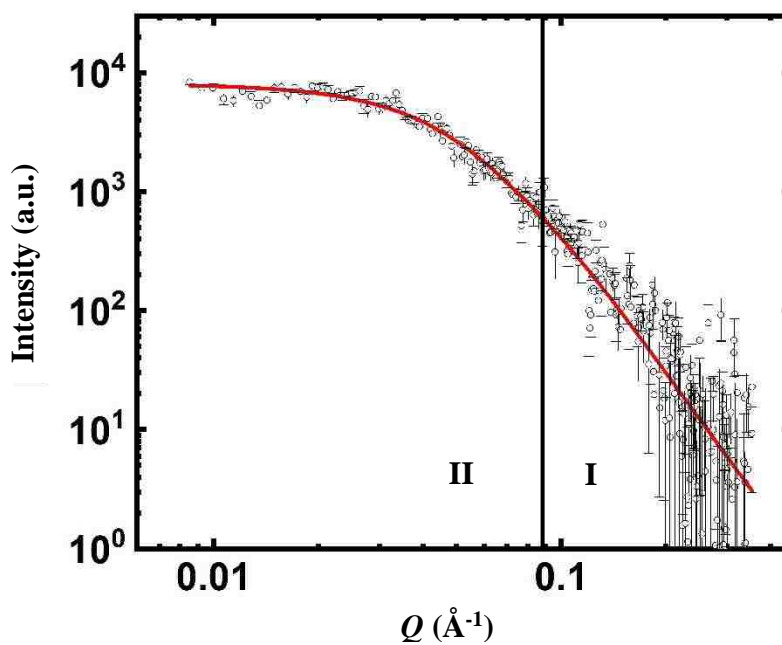


Figure 7. Typical SAXS data (sample shown: K aerogel) fitted into two regions: Region I, Porod's Law; Region II, Guinier knee

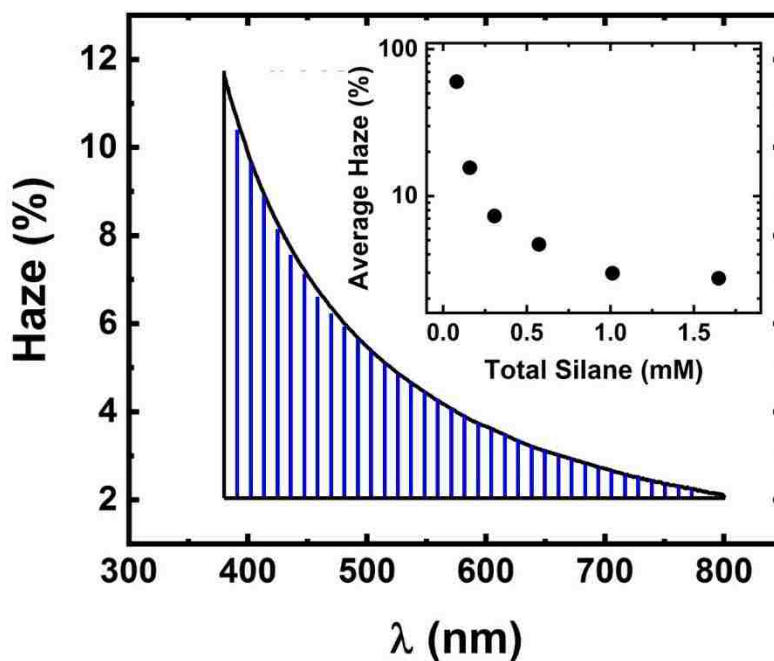


Figure 8. Typical percent haze data for wet-gels as a function of wavelength from 380 nm to 800 nm (sample shown: K/4 wet-gel – see Figure 1). Average haze was calculated by integrating the shaded area. Inset: Average percent haze of all wet-gels of this study

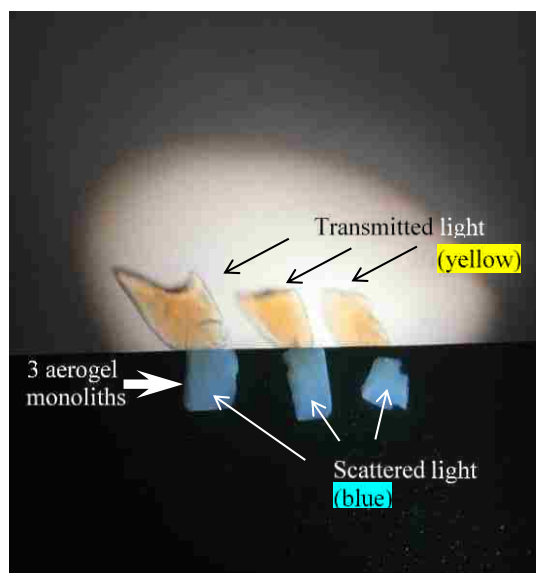


Figure 9. Photograph of three small K/8 aerogel monoliths ( $\rho_b = 0.032 \text{ g cm}^{-3}$ ) on a black surface with a white background demonstrating Rayleigh scattering by showing transmitted yellow/orange light and reflected bluish light. Samples were illuminated with a white light source from the front

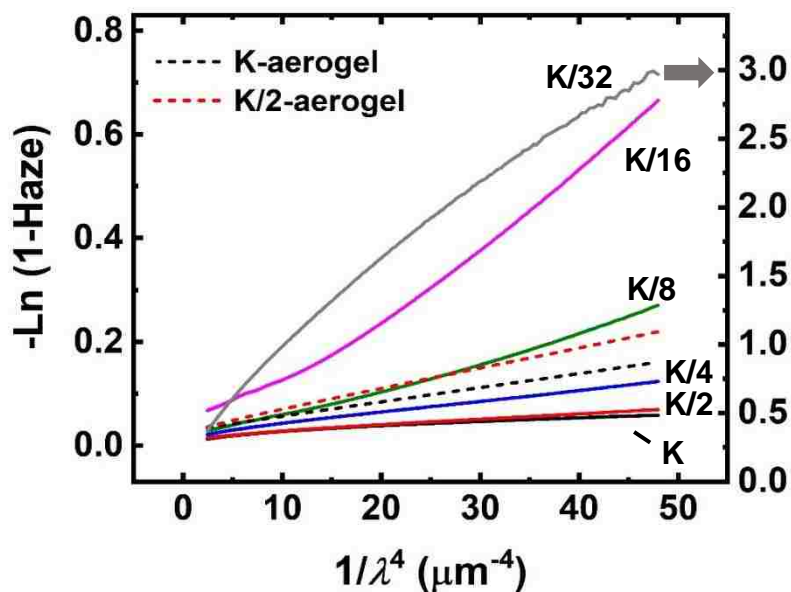
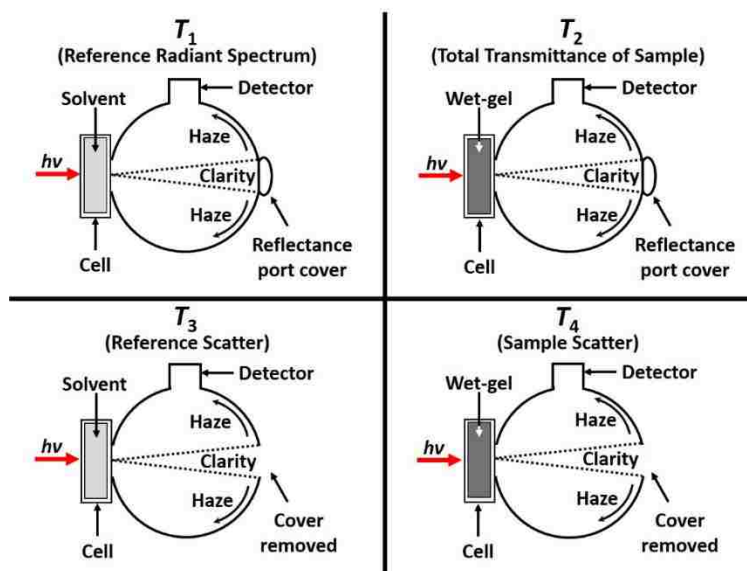


Figure 10. Plots according to Eq 8 of wet-gels (solid lines) and aerogels (dashed lines). Linear dependence of  $-\text{Ln}(1-\text{Haze})$  versus  $1/\lambda^4$  indicates Rayleigh scattering



Scheme 1. Configurations of the integrating sphere for measuring haze

Table 1. General materials characterization data for the TMOS-co-APTES aerogels prepared with decreasing total silane (TMOS+APTES) concentration

sample	shrinkage (%) <sup>a,b</sup>	bulk density ( $\rho_b$ , g cm <sup>-3</sup> ) <sub>b</sub>	skeletal density ( $\rho_s$ , g cm <sup>-3</sup> ) <sub>c</sub>	$\Pi$ (% v/v) <sup>d</sup>	specific pore volume (cm <sup>3</sup> g <sup>-1</sup> )			BET surface area ( $\sigma$ , m <sup>2</sup> g <sup>-1</sup> )	average pore diameter (4V/ $\sigma$ , nm) <sup>h</sup>	pore diameter by Hg-intrusion (nm) <sup>i</sup>	particle radius (r, nm) <sub>j</sub>	fractal dimension (D <sub>m</sub> ) <sub>n</sub>
					V <sub>Total</sub> <sup>e</sup>	V <sub>1.7-300 nm</sub> <sup>f</sup>	V <sub>&gt;300 nm</sub> <sup>g</sup>					
K	12.31 ± 1.35	0.214 ± 0.002	1.742 ± 0.003	87.7	4.099	4.697	-	960	17.08 [19.6]	59	1.79	2.57
K/2	10.41 ± 0.73	0.119 ± 0.003	1.725 ± 0.007	93.1	7.824	4.468	3.356	897	34.89 [19.9]	87	1.94	2.68
K/4	10.46 ± 0.97	0.064 ± 0.003	1.718 ± 0.004	96.3	15.04	0.855	14.19	802	75.03 [4.26]	263	2.18	2.70
K/8	8.93 ± 0.64	0.032 ± 0.005	1.728 ± 0.009	98.1	30.67	0.433	30.24	325	377.5 [5.33]	460	5.34	2.68
K/16	18.83 ± 1.47	0.017 ± 0.007	1.728 ± 0.009	99.0	58.25	0.344	57.90	182	1280 [7.56]	-	9.54	2.66
K/32	42.08 ± 0.89	0.006 ± 0.003	1.728 ± 0.009	99.7	166.1	0.233	165.9	148	4489 [6.30]	-	11.7	2.67

<sup>a</sup> Shrinkage =  $100 \times (\text{mold diameter} - \text{sample diameter}) / (\text{mold diameter})$ . <sup>b</sup> Average of 3 samples. <sup>c</sup> Single sample, average of 50 measurements. K, K/2 and K/4 were measured directly. Owing to the low density of K/8 to K/32, there was not enough material for accurate measurement, and the value reported is the average of the  $\rho_s$  values of K to K/4. <sup>d</sup> Percent porosity,  $\Pi = 100 \times (\rho_s - \rho_b) / \rho_s$ . <sup>e</sup> Calculated via  $V_{\text{Total}} = (1/\rho_b) - (1/\rho_s)$ . <sup>f</sup> Cumulative volume of pores between 1.7 and 300 nm from N<sub>2</sub>-sorption data and the BJH desorption method. <sup>g</sup>  $V_{>300 \text{ nm}} = V_{\text{Total}} - V_{1.7-300 \text{ nm}}$ . <sup>h</sup> For the first number, V was taken equal to  $V_{\text{Total}} = (1/\rho_b) - (1/\rho_s)$ ; for the number in [brackets], V was set equal to the total volume probed by N<sub>2</sub>-sorption (=  $V_{1.7-300 \text{ nm}}$ ) up to  $P/P_0 \rightarrow 1.0$ . <sup>i</sup> Average pore diameters from Hg-intrusion porosimetry. Samples K/16 to K/32 were too weak mechanically and collapsed under small pressures. <sup>j</sup>  $r = 3/(\rho_s \times \sigma)$ .

Table 2. SAXS data for TMOS-co-APTES aerogels prepared with different silane concentrations

Sample	high- $Q$ slope <sup>a</sup>	$R_G$ <sup>b</sup> (nm)	$R$ <sup>c</sup> (nm)
K	$4.00 \pm 0.08$	$3.76 \pm 0.06$	$4.88 \pm 0.08$
1/2 K	$4.00 \pm 0.04$	$5.64 \pm 0.15$	$7.32 \pm 0.19$
1/4 K	$4.00 \pm 0.03$	$8.73 \pm 0.10$	$11.34 \pm 0.13$
1/8 K	$4.00 \pm 0.02$	$15.50 \pm 0.23$	$20.13 \pm 0.30$
1/16 K	$3.86 \pm 0.04$	$19.04 \pm 0.35$	$24.73 \pm 0.45$
1/32 K	$4.20 \pm 0.08$	$24.29 \pm 0.63$	$31.55 \pm 0.82$

<sup>a</sup> Referring to Figure 7: From power law Region I. <sup>b</sup> From Guinier Region II. <sup>c</sup> Particle radius,  $R = R_G/0.77$ .

Table 3. Average haze and scatterer diameter for TMOS-co-APTES gels

Sample	wet-gel		aerogel		
	average % Haze <sup>a</sup>	scatterer diameter ( $d$ , nm)	average % Haze	scatterer diameter ( $d$ , nm)	secondary particle diameter ( $2 \times R$ , nm) <sup>d</sup>
K	2.75	9.25	$6.42$ <sup>b</sup>	4.43	$9.76 \pm 0.16$
K/2	2.98	11.27	$8.06$ <sup>c</sup>	6.14	$14.64 \pm 0.39$
K/4	4.68	16.94	<sup>e</sup>	-	$22.68 \pm 0.26$
K/8	7.30	28.61	<sup>e</sup>	-	$40.26 \pm 0.60$
K/16	15.57	55.85	<sup>e</sup>	-	$49.46 \pm 0.90$
K/32	60.15	169.36	<sup>e</sup>	-	$63.10 \pm 1.64$

<sup>a</sup> Thickness of all wet gels,  $l = 13.49$  mm. <sup>b</sup> Thickness of K aerogel,  $l = 9.88$  mm. <sup>c</sup> Thickness of K/2-aerogel,  $l = 9.81$  mm. <sup>d</sup> Reproduced from Table 2. <sup>e</sup> Too weak to handle.

## SUPPORTING INFORMATION

Appendix I. Formulations of TMOS-co-APTES sols and gelation times.

Appendix II. Derivation of porosity of wet-gels from the porosity of aerogels (Eq 7).

Appendix I. Formulations of TMOS-co-APTES sols and gelation times

Table S1. Synthesis of different concentration of TMOS-co-APTES wet-gels

Sample	TMOS, mL [mmol]	APTES, mL [mmol]	H <sub>2</sub> O, mL [mmol]	Acetonitrile [mL]	Total Silane concentration [mM]	Gelation time
K	2.887 [19.535]	0.963 [4.115]	1.500 [83.333]	9	1.648	2 min
K/2	1.444 [9.771]	0.481 [2.055]	0.750 [41.667]	9	1.013	3 min
K/4	0.721 [4.879]	0.241 [1.030]	0.375 [20.833]	9	0.572	9 min
K/8	0.361, [2.443]	0.120 [0.514]	0.188 [10.417]	9	0.306	58 min
K/16	0.181 [1.225]	0.060 [0.256]	0.094 [5.222]	9	0.159	3 h 45 min
K/32	0.090 [0.609]	0.030 [0.128]	0.047 [2.611]	9	0.080	13 h 15 min

Appendix II. Derivation of the porosity of wet-gels from the porosity of aerogels

The decimal porosity of an aerogel is given by:

$$\Pi_{aerogel} = \frac{\rho_{s\_of\_silica} - \rho_{b\_of\_aerogel}}{\rho_{s\_of\_silica}}$$

Since, the skeletal densities for an aerogel and its wet-gel precursor are equal, therefore, the porosity of the wet-gel is given by:

$$\Pi_{wet-gel} = \frac{\rho_{s\_of\_silica} - \rho_{b\_of\_wet-gel}}{\rho_{s\_of\_silica}}$$

The bulk density of an aerogel and a wet-gel are given by:

$$\rho_{b\_of\_aerogel} = \frac{M_{aerogel}}{V_{aerogel}}$$

$$\rho_{b\_of\_wet-gel} = \frac{M_{wet-gel}}{V_{wet-gel}}$$

Assuming, for example, that the aerogel and the wet-gel are cylindrical in shape:

$$V_{aerogel} = \pi r_{aerogel}^2 h_{aerogel}$$

$$V_{wet-gel} = \pi r_{wet-gel}^2 h_{wet-gel}$$

$$r_{wet-gel} = \frac{r_{aerogel}}{(1-s)}$$

$$h_{wet-gel} = \frac{h_{aerogel}}{(1-s)}$$

Where,

$$s = \frac{\%shrinkage}{100}$$

Therefore,

$$V_{wet-gel} = \pi \times \frac{r_{aerogel}^2}{(1-s)^2} \times \frac{h_{aerogel}}{(1-s)}$$

$$V_{wet-gel} = \frac{V_{aerogel}}{(1-s)^3}$$

Since mass, M, corresponds to the mass of skeletal network, therefore,  $M_{aerogel}$  and  $M_{wet-gel}$  are equal:

$$\rho_{b\_of\_wet-gel} = (1-s)^3 \times \frac{M_{aerogel}}{V_{aerogel}}$$

$$\rho_{b\_of\_wet-gel} = (1-s)^3 \times \rho_{b\_aerogel}$$

And the porosity expression becomes:

$$\Pi_{wet-gel} = \frac{\rho_{s\_of\_silica} - [(1 - s)^3 \times \rho_{b\_of\_aerogel}]}{\rho_{s\_of\_silica}}$$

Or:

$$\Pi_{wet-gel} = \frac{\rho_{s\_of\_silica} - \left[ \left( 1 - \frac{\%shrinkage}{100} \right)^3 \times \rho_{b\_of\_aerogel} \right]}{\rho_{s\_of\_silica}}$$

## REFERENCES

1. Kistler SS (1931) Nature 127:741.
2. Nicolaon GA, Teichner SJ (1968) Bull Soc Chim Fr 5:1900-1906.
3. Fricke J, Arduini-Schuster MC, Buttner D, Ebert H-P, Heinemann U, Hetfleisch J, Hummer E, Kuhn J, Lu X (1990) In: Cremers CJ, Fine HA (eds) Thermal Conductivity 21. Plenum Press, New York, pp 235-245.
4. Pierre AC, Rigacci A (2011) In: Aegerter M, Leventis N, Koebel M, (eds) Aerogels Handbook - Advances in Sol-Gel Derived Materials and Technologies. Springer, New York , Chapter 2, pp 21-45, DOI: 10.1007/978-1-4419-7589-8\_2.
5. <http://www.aerogel.com/products-and-solutions/all-insulation-products/> (Accessed 28 May 2018).
6. Zhao L, Yang S, Bhatia B, Strobach E, Wang EN (2016) AIP Adv 6:025123-1-8.
7. Rubin M, Lampert CM (1983) Sol Energy Mater 7:393-400.
8. Beck A, Gelsen O, Wang P, Fricke J (1989) J Phys Colloques 50:C4-203-C4-208.
9. Katti A, Shimpi N, Roy S, Lu H, Fabrizio EF, Das A, Capadona LA, Leventis N (2006) Chem Mater 18:285-296.
10. Leventis N (2007) Acc Chem Res 40:874-884.
11. Pajonk G (1998) J Non-Cryst Solids 225:307-314.

12. ASTM D1003-13, Standard Test Method for Haze and Luminous Transmittance of Transparent Plastics, ASTM International, West Conshohocken, PA, 2013, [www.astm.org](http://www.astm.org)
13. Hunt AJ, Ayers MR (2001) *J Non-Cryst Solids* 285:162-166.
14. Boonstra AH, Meeuwssen TPM, Baken JME, Aben GVA (1989) *J Non-Cryst Solids* 109:153-163.
15. Kistler SS (1932) *J Phys Chem* 36:52-64.
16. Kerker, M. The scattering of the light and other electromagnetic radiation, Chapter 3; Clarkson College of Technology: Potsdam, NY, 1969.
17. Wang P, Korner W, Emmerling A, Beck A, Kuhn J, Fricke J (1992) *J Non-Cryst Solids* 145:141-145.
18. Emmerling A, Petricevic R, Beck A, Wang P, Scheller H, Frickey J (1995) *J Non-Cryst Solids* 185:240-248.
19. Rewatkar PM, Taghvaei T, Saeed AM, Donthula S, Mandal C, Chandrasekaran N, Leventis T, Shruthi TK, Sotiriou-Leventis C, Leventis N (2018) *Chem Mater* 30:1635-1647.
20. Mohite DP, Larimore ZJ, Lu H, Mans JT, Sotiriou-Leventis C, Leventis N (2012) *Chem Mater* 24:3434-3448.
21. Wu MK (1996) *Aerosol Sci Technol* 25:392-398.
22. Banerji A, Ghosh I (2009) *PLoS One* 4:e7361-1-13.
23. Beaucage G (1996) *J Appl Crystallogr* 29:134-146.
24. Mang JT, Son SF, Hjelm RP, Peterson PD, Jorgensen BS (2007) *J Mater Res* 22:1907-1920.
25. Porod G (1951) *Kolloid Z* 124:83-114.
26. <http://life.nthu.edu.tw/~labcjw/BioPhyChem/Spectroscopy/beerslaw.htm> (Accessed 28 May 2018.)
27. Howell JR, Siegel R, Mengüç MP (2010) In: *Thermal Radiation Heat Transfer*, 5th edn. CRC Press, Florida Chapter 15, p 764.
28. Polyanskiy MN Refractive Index Database. <https://refractiveindex.info>. (Accessed 22 May 2018).

29. Howell JR, Siegel R, Mengüç MP (2010) In: Thermal Radiation Heat Transfer, 5th edn. CRC Press, Florida, Chapter 15, p 767.
30. Tillotson TM, Hrubesh LW (1992) J Non-Cryst Solids 145:44-50.

## II. OPTIMIZED TRANSPARENT, MECHANICALLY STRONG, THERMALLY INSULATING CROSSLINKED SILICA AEROGELS FOR ENERGY-EFFICIENT WINDOWS

Chandana Mandal, Suraj Donthula, Hojat Majedi Far, Adnan Malik Saeed, Chariklia Sotiriou-Leventis, Nicholas Leventis\*

Department of Chemistry, Missouri University of Science and Technology, Rolla, MO 65409, U.S.A.

\* Correspondence: Tel.: 573-341-4391; E-mail: [n.leventis@yahoo.com](mailto:n.leventis@yahoo.com)

Was submitted in *Journal of Sol-Gel Science and Technology*

### ABSTRACT

TMOS-co-APTES wet-gels have been used as templates for polymer crosslinked aerogels, which in turn have been used as strong materials and as starting materials for ceramic aerogels. Such wet-gels are prepared in acetonitrile (CH<sub>3</sub>CN) via co-gelation of tetramethylorthosilicate (TMOS) and 3-aminopropyl silane (APTES) in a 3:1 v/v ratio. Qualitatively, native monolithic TMOS-co-APTES aerogels appear more clear than the corresponding straight TMOS-derived materials, suggesting applications in thermally insulating daylighting. For that application, it is important to understand and minimize haze. Haze from the bulk of silica aerogels may be due to scattering from particles or pores, but study of its origin may be complicated by scattering and reflections from the surface of the monolith. In this report, using wet-gels as proxy materials for aerogels, haze from TMOS-co-APTES was investigated as a function of density, which is controlled by the amount of TMOS+APTES in the sol. The wet-gel approach to the study of haze of aerogels has the advantages of eliminating surface scattering issues from aerogel monoliths, and

owing to better refractive index matching between the skeletal framework and the surrounding medium ( $\text{CH}_3\text{CN}$ ), bulk scattering is also reduced, facilitating study of lower-density materials. Haze from the bulk was traced to Rayleigh scattering down to  $0.017 \text{ g cm}^{-3}$  aerogels. The opacity of even lower-density samples (down to  $0.006 \text{ g cm}^{-3}$ ) was attributed to Mie scattering. The scatterer size was obtained via Rayleigh's law and matched the secondary particle sizes of silica. The size of those particles increased as the density decreased, producing higher haze. Results suggest that in order to keep haze low at lower densities, one must keep the particle size low, for example, by increasing the rate of gelation.

## 1. INTRODUCTION

The main reason for the slow commercialization of silica aerogels is their fragility and poor mechanical properties. The poor mechanical properties of silica aerogels are generally attributed to the well-defined narrow interparticle necks.<sup>14</sup> The fragility issue of those silica aerogels has been resolved by crosslinking aerogels with organic polymers.<sup>15</sup> Briefly, it was realized that skeletal silica nanoparticles possess surface silanol groups, that can react with polyisocyanates to form polyurethane tethers that bridge the nanoparticles chemically, reinforcing the interparticle necks. Thus, the entire skeletal framework is coated conformally with a polymer, while the open porosity is preserved. The resulting materials have been referred to as polymer-crosslinked aerogels (X-aerogels). All the other bulk properties of X-aerogels are not compromised significantly by crosslinking where an increase in the bulk density by a factor of  $3\times$  leads to a  $300\times$  increase in the flexural strength

of typical X-aerogel monoliths. X-aerogels are exceptionally strong in comparison not only with their non-crosslinked counterparts (native aerogels), but also with other materials that are usually considered strong, such as steel, Kevlar, and silicon carbide.<sup>16</sup> In X-linked aerogels, the silica nanoparticle framework serves as a template for the accumulation of polymer, which covalently connects the skeletal particles.

The cost-effectiveness of ambient pressure drying has led to the synthesis of many crosslinked silica xerogels.<sup>17-20</sup> In 2018, xerogels were used for synthesis of highly porous SiC and Si<sub>3</sub>N<sub>4</sub>.<sup>21</sup> The ambient pressure drying is safe and cost-effective compared to supercritical fluid drying (SCD). Moreover, crosslinking improves the mechanical strength that can support the silica skeleton to withstand capillary forces during drying.<sup>17,22-24,</sup>

Various multi-step crosslinking of polymer-reinforced silica aerogels were done to improve their mechanical properties.<sup>25,26</sup> Since one-pot synthesis has few advantages over the multistep crosslinking, RF and polyurethane-urea crosslinked aerogels were synthesized *via* one-pot route in order to increase the mechanical strength of silica aerogels<sup>27,28</sup>. In 2010, the synthesis of monolithic porous SiC ceramic from crosslinked Si-PAN aerogels prepared from one pot synthesis was reported.<sup>29</sup> Since Si-AIBN is a bidentate ligand, it can attach itself to silica from both ends. That provides the advantage of binding the polymer produced by the thermal or photochemical reaction to the silica surface and hence rendering the post-crosslinking washes. One pot synthesis of polyimide crosslinked silica aerogels was also synthesized using different silica precursors for improved mechanical strength with good acoustic performance.<sup>30-32</sup> In 2010, Meador et al. prepared epoxy crosslinked aerogels using the ionic process for crosslinking with higher activation energy obtained through heating. The fundamental difference in properties (for

e.g., porosity, density and mechanical) between the one pot and multistep diffusion process were reported. The one pot synthesis for preparing crosslinked silica aerogels not only shortens the process by eliminating the monomer diffusion step but also polymer reinforcement becomes more efficient and uniform. In 2014, mechanical reinforcing by one-pot polymer crosslinking was achieved using alkyl and aryl bridges of bis-silane precursors along with crosslinking of the silica surface functionality with tri-methacrylate crosslinker.<sup>33</sup> Introduction of aryl bridges of 1,4-bis(triethoxysilyl)benzene (BTESB) precursor in the reinforced BTESB derived aerogels showed larger mesopores accounting for further improvement in thermal insulating properties even with higher crosslinking. In 2018, it was reported that, in polymer crosslinked aerogels, the polymer (TIPM in this case) engages both  $-NH_2$  groups and dangling  $-SiOH$  groups in crosslinking that was explained based on  $^{29}Si$  NMR.<sup>21</sup> Photoinduced polymer crosslinked aerogels were prepared by irradiating a liquid mixture containing an alkoxy silane, a monomer and a photoinitiator that results in instantaneous polymerization and gelation.<sup>34</sup> Though crosslinking of silica aerogels enhances its mechanical properties, it results in a decrease of porosity and surface area.<sup>35</sup> Therefore in order to understand the exact location of the polymer in the silica structure and how much of polymer is required to enhance the mechanical properties with minimal compromise in the porosity.<sup>36</sup> Surface functionalization of silica particles in order to attach the polymer was done using Si-NAD that can be considered as an APTES derivative. It was reported that at a higher degree of crosslinking, polymer is filled in the secondary particles thereby decreasing the porosity. Moreover, only small amount of polymer that coats the primary particles was enough to increase the stiffness by a factor of 20× with minimal compromise in the porosity and surface areas. Beyond that

concentration, when the additional polymer accumulates in the space around the primary particle, the porosity and surface area gradually decrease without any noticeable improvement in mechanical properties. When the secondary particles are almost filled, the mechanical properties improved drastically.

Though one-pot synthesis is fast, and diffusion is not a limiting factor, however the increase in bulk density and decrease in porosity is very drastic thereby limiting the one-step crosslinking procedure for the synthesis of mechanically strong but thermally insulating and transparent silica aerogels. Moreover, to optimize the mechanical properties with minimum sacrifice in porosity, a statistical approach was done using DOE.<sup>37</sup> Reinforcement of silica aerogels by controlled deposition process preserves the porosity and low density of silica aerogels.<sup>38</sup> Mechanically reinforced silica aerogels were prepared without compromising its porosity by forming a thin crust on the surface of the aerogel while the core retains the features of native aerogel.<sup>39</sup> Higher thermal stability compared to polymer-reinforced aerogels was achieved due to the ceramic nature of the reinforcement. Mechanical reinforcement of silica aerogels was achieved by various processes including Ostwald ripening, polymer crosslinking and chemical vapor deposition.<sup>17,40</sup> In 2010, mechanically reinforced silica aerogels were prepared by controlled growth of grafted polymer using surface-initiated atom transfer radical polymerization (SI-ATRP).<sup>41</sup> Introducing ethylene glycol dimethacrylate (EGDMA) along with MMA in the ATRP monomer solution increased the mechanical strength of the resulting composite to around 44%.<sup>42</sup> In 2015, Maleki et al. introduced the optimal mechanical reinforcement of silica aerogels using surface-initiated reversible addition-fragmentation chain transfer (SI-RAFT).<sup>43</sup>

## 2. RESULTS AND DISCUSSION

### 2.1. SYNTHESIS AND MATERIALS CHARACTERIZATION OF TMOS-CO-APTES AEROGELS

TMOS-co-APTES wet-gels were prepared with different silane (TMOS+APTES) concentrations in the sol while the TMOS:APTES volume ratio was kept constant at 3:1 v/v as described in the Experimental section. Design-of-Experiments statistical method based on a Central Composite Full Factorial (CCF) design model was used in order to locate the best combination of transparency, thermal conductivity, and mechanical strength. Extra points were added (denoted by red star) to the CCF design in order to increase confidence (Figure 1). The exploratory variables were the silane concentration (TMOS+APTES) for the formation of silica, and the triisocyanate concentration for crosslinking the skeletal framework. The central point of the design was repeated twice. The total % w/w of crosslinker in the crosslinking bath was varied between 0 % and 6 % w/w. The ranges of the silane concentration were based on the % haze results of native silica wet-gels reported in Mandal et. al. in which low silane concentrations wet-gels were studied for haze.<sup>1</sup> Based upon the haze results of that paper, silane concentration was varied from 0.5 to 1 w.r.t the standard silane concentration reported in Katti et al.<sup>2</sup> The reaction is autocatalytic, namely the  $-NH_2$  groups of APTES provide the base environment needed for gelation. Owing to the high concentration of APTES in K, the sol needed cooling in dry ice in order to allow time to be cast in the molds. Gelation of that cold solution took about 2 min. Gelation times for all the sols were around 2-3 minutes.

All wet-gels were washed (solvent exchanged) with the gelation solvent ( $CH_3CN$ ) and were crosslinked with isocyanate solution and dried to aerogels according to standard

procedures. Scheme 1 shows the synthesis and crosslinking of silica wet-gel. Crosslinked aerogels appeared hazier than the corresponding native gels and all aerogels appeared more hazy than the corresponding wet-gels.

Material characterization data for all native and crosslinked aerogels are summarized in Table 1 and Figure 5. The skeletal densities ( $\rho_s$ ) of all native samples ranged from  $1.742 \pm 0.003 \text{ g cm}^{-3}$  to  $1.718 \pm 0.004 \text{ g cm}^{-3}$  suggesting that the physical structure of those samples was identical and absence of closed pores. Upon crosslinking, the skeletal densities decreased and were in the range of  $1.335 \pm 0.002 \text{ g cm}^{-3}$  to  $1.444 \pm 0.002 \text{ g cm}^{-3}$ . The decrease in skeletal density from native to crosslinked samples is due to the increase in carbon content from the polyurea coating around the silica particles upon crosslinking. That also confirmed the uptake of the isocyanate.

The bulk densities of native silica aerogels decreased as the silane concentration decreased due to decrease in the solid content. The bulk densities of the native samples were in the range of  $0.177 \pm 0.001 \text{ g cm}^{-3}$  to  $0.220 \pm 0.004 \text{ g cm}^{-3}$ . With increase in silane concentration of the native samples, bulk density increased due to increase in solid content. Moreover, the bulk density increased upon crosslinking. Higher the degree of crosslinking, higher was the bulk density.

The bulk densities of the crosslinked silica aerogels were in the range of  $0.186 \pm 0.002 \text{ g cm}^{-3}$  to  $0.405 \pm 0.003 \text{ g cm}^{-3}$ . That increase in bulk density was due to the increase in the solid content. As the crosslinking concentration increases, the polyurea coating on silica particles increases and therefore the solid content increases upon crosslinking. Correspondingly, percent porosities,  $\Pi$  were calculated via  $\Pi=100 \times (\rho_s - \rho_b) / \rho_s$ . For native samples, the porosity increased from 87 % to 90 % upon decrease in silane concentration

from K to 0.5 K. After crosslinking, the porosity decreased indicating the uptake of the polymer. The porosities for the crosslinked samples were in the range of 70 % to 87 % that decreased with increase in crosslinking. Due to crosslinking, the particle necks becomes thicker and therefore the porosity decreases.

The porous and skeletal framework was probed with N<sub>2</sub> sorption. As can be seen from Figure 2, the N<sub>2</sub> sorption isotherms for all the samples follow a typical Type IV isotherm. At higher pressure, a saturation is achieved along with hysteresis indicating the presence of mesopores. The average pore diameters were calculated via the  $4 \times V_{\text{Total}}/\sigma$  ( $\sigma$ : BET surface area, see Table 1). Here  $V_{\text{Total}}$  was either calculated via  $V_{\text{Total}} = (1/\rho_b) - (1/\rho_s)$  or from the the maximum volume adsorped along the N<sub>2</sub>-sorption isotherm (at  $P/P_0 \sim 1$ ). The average pore diameter gradually increased with increasing crosslinking and was in the range of 17.89 nm for K to 53.45 nm for 0.5K-3% N3200. The total pore volume ( $V_{\text{total}}$ ) for native samples decreased with decreasing silane concentration. The pore volume also decreased for crosslinked ssamples compared to the native samples. Moreover, the pore volume decreased upon increasing the degree of crosslinking since the polymer started filling the pores there by decreasing the pore volume. The BET surface area decreased with increase in the degree of crosslinking.

## **2.2. CHEMICAL CHARACTERIZATION OF NATIVE AND CROSSLINKED AEROGELS**

All the samples from DOE were analyzed for the polymer content using TGA. The amount of C in native aerogel was considered zero because the C content in native silica is from the aminopropyl group of APTES. % polymer content was calculated with respect to

the native sample and is tabulated in Table 1. The % polymer increased with increase in crosslinking concentration indicating the uptake of the triisocyanate upon crosslinking.

Attachment of the polymer to the silica backbone was further confirmed from  $^{29}\text{Si}$  solid-state NMR. The  $^{29}\text{Si}$  cross-polarization experiment in Figure 3 showed that the intensity ratio of Q4:Q3 and T3:T2 decreased from silica aerogel to X- silica aerogel. That was because the peak intensities in cross polarization experiment resulted from the abundance of protons in the close proximity of Si atom. When silica was crosslinked, the  $-\text{CH}_2$  groups of the triisocyanate attaches itself from the  $\text{NH}_2$  and OH ends, thereby, increasing the proton abundance in that area and the peak intensities increases.

### **2.3. STRUCTURAL CHARACTERIZATION OF NATIVE AND CROSSLINKED SILICA AEROGELS**

The 3D arrangement of the skeletal framework in the porous space for all the aerogels were investigated using SEM in order to study the changes in morphology with increasing degree of crosslinking. All aerogels consisted of strings of particles. As the silane concentration was decreased from K to 0.5 K, not much change in morphology was observed. However, for crosslinked samples, the particle size increased as the degree of crosslinking increased. Figure 4 shows the representative SEMs of all the aerogels at two different magnifications.

Small angle X-ray scattering was performed to study the solid frameworks in terms of its elementary building blocks. All the data were analyzed with Beaucage Unified Model<sup>3,4,5</sup> and the results are shown in Table 2. All samples showed a power law region with slope  $< -4.0$  in the high Q range indicating the presence of primary particles with fuzzy interfaces.

At low Q values beside this region, those samples showed a Guineir knee from where the radius of gyration ( $R_G$ ) of primary particles were calculated. From  $R_G$ , the actual radius (R) of primary particles was calculated using  $R_G = 0.77 \times R$  (Figure 7). The radii of primary particles gradually increased with increase in crosslinking indicating formation of a conformal coating on the primary particles. The aggregation of primary particles of n-TMOS-co-APTES to form secondary particles couldn't be analyzed as it was beyond the Q-range of our SAXS capability.

#### **2.4. MECHANICAL CHARACTERIZATION OF NATIVE AND CROSSLINKED SILICA AEROGELS**

All the native and crosslinked aerogels were tested for their mechanical properties by compressing the sample at 2.5 mm/min strain rate according to ASTM 1621-04a procedure using cylindrical specimens of length:diameter ratio of 1:1. The typical stress-strain curves obtained are shown in Figure 6. The stress-strain curves of all samples showed an initial linear elastic region upto around 4 % strain followed by plastic deformation and finally inelastic hardening or densification. All the mechanical testing data is tabulated in Table 3.

The highest ultimate compressive strength obtained was  $375.25 \pm 4.53$  MPa for 0.5K-6 % N3200. The 0.5 K aerogel was very fragile and shattered into pieces with low compressive strength ( $1.52 \pm 1.20$  MPa). Young's modulus was calculated for all the native and crosslinked samples from the slope of the intial linear part of stress-strain curve. The native silica aerogels were fragile with low Young's modulus that increased upon crosslinking. For native 0.75K aerogel, the Youngs modulus was  $9.39 \pm 1.09$  MPa that increased to  $46.85 \pm 0.60$  MPa for crosslinked 0.75K-6% N3200.

The increase in Young's modulus for all the samples was around 5 to 8 times as the degree of crosslinking increased from 0 % to 6 %. The highest Young's modulus obtained was  $119.21 \pm 12.43$  for K-6% N3200. The yield strength increased with increase in silane and crosslinking concentration. The minimum yield strength was  $0.071 \pm 0.004$  MPa for 0.5K and maximum yield strength was  $2.672 \pm 0.270$  MPa for K-6% N3200. Strain at yield was calculated and was in the range of  $0.039 \pm 0.003$  mm/mm to  $0.151 \pm 0.009$  mm/mm that decreased as silane and crosslinking concentration increased. Stress at yield was calculated from the stress value at the yield point with a minimum value of  $0.222 \pm 0.029$  MPa for 0.5 K and a maximum value of  $4.607 \pm 0.280$  MPa for K-6% N3200.

## **2.5. THERMAL CONDUCTIVITIES OF NATIVE AND CROSSLINKED SILICA AEROGELS**

The thermal conductivities of all aerogel samples were measured using the hot-plate method where panels of the various silica aerogel samples and a NIST standard were used to construct layered structures between an aluminum block heated at  $37.5$  °C and a bucket of ice/water ( $0$  °C). The heat flux through the layered structure was determined by measuring the temperatures at the interfaces of the layered structure using suitably placed thermal couples (see Experimental section). Thermal conductivity increased with both the total silane concentration in the sol, and the concentration of the triisocyanate in the crosslinking bath (Table 3). The minimum thermal conductivity value ( $0.0127 \pm 0.0004$  W  $m^{-1}$   $K^{-1}$ ) was obtained with the lowest-silane concentration native samples (0.5K), while the highest one ( $0.0299 \pm 0.0009$  W  $m^{-1}$   $K^{-1}$ ) was obtained with K and [N3200]<sub>in\_the\_X-linking\_bath</sub> = 6% w/w. In fact, the variation of the thermal conductivity as a function of the explanatory variables (Figure 6A) follows the variation in bulk density (compare with

Figure 5A), pointing that the heat conduction through the gas filling the pores had been suppressed effectively by the small size of the pores in all samples, and heat conduction was dominated by heat transfer through the solid framework.

## **2.6. OPTICAL PROPERTIES OF NATIVE AND CROSSLINKED SILICA AEROGELS**

Haziness is defined as the fraction of the transmitted light that falls outside an angle of  $\pm 2.5^\circ$  from the incident beam; the fraction of light that falls within that range is defined as clarity. Haziness is due to light scattering and it has two contributors: bulk scattering and surface scattering. Bulk scattering may depend on the wavelength (e.g., refer to Rayleigh scattering) while haze due to surface scattering is independent of the wavelength. In order to remove surface scattering from being a factor, in a recent study of the haziness of TMOS-co-APTES aerogels as a function of their density (i.e., total silane concentration in the sol) we used wet gels in specially constructed molds as a proxy of the aerogels. In this study here, however, haze from surface scattering is an issue that has to be reckoned with.

Haze of all samples (Figure 1) was measured according to ASTM D1003-13 using an integrating sphere as described recently (see Experimental section). To minimize reflection losses of transparency, all samples were prepared using molds constructed with Teflon tape-coated glass plates facing and held parallel to each other with circular spacers of constant width (see Experimental). The thickness of all aerogels was 7mm. Average haze in the 400-800 nm range was calculated by integrating the primary haze vs wavelength data. and reported Average haze data for all samples are given in Table S2 of the Supporting Information. The haze of the native samples increased from 17.4% (K aerogels)

to 23.2% (0.5K). The average haze of the crosslinked samples was significantly higher, reaching 45.6%. It was noted though that the haze of the K and 0.5K aerogels was significantly higher than the haze of the corresponding wet-gels (17.4% and 23.2%, respectively). The difference could not be reconciled by the difference in the refractive index of the pore-filling fluid in the case of wet-gels and aerogels (acetonitrile vs air, respectively). Thereby, it was concluded that the haze of aerogels had a significant contribution from surface scattering. We set out to measure the latter by adopting the analytical technique referred to as the Method of Standard Additions. For this we prepared several native aerogel samples with variable thickness based on the 0.857K formulation, measured their average haze and extrapolated to zero thickness (Figure 8). Surface haze was given by the intercept (14.41%).

Subsequently, with the understanding that surface haze comes from surface roughness carried over from the molding surfaces (Teflon tape), or random scratches introduced from the contact of the wet-gels with the containers during agitation and solvent exchanges, we considered that value of surface haze (14.41%) as representative for all samples (native and crosslinked) and it was subtracted from all data, thus yielding the bulk haze of each 7 mm thick sample (see Table S2).

Owing to the fragility of native wet-gels, our experimental technique did not allow fabrication of aerogels less than 7 mm thick. However, for application of these aerogels as a see-through thermally insulating layer in double-pane windows, the target thickness of the aerogel layer is 3 mm. The bulk haze of those samples was calculated using Eq 1, which is in effect Beer's Law applied to transmission loss due to bulk haze caused by Rayleigh

scattering, as is the case here. The calculated bulk average haze values for 3 mm samples are plotted vs the explanatory variables in Figure 6C (blue surface).

As our next level of refinement, we fabricated native TMOS-co-APTES aerogels at the K, 0.75K and 0.5K formulations, each one at different thicknesses, and we calculated (Method of standard additions) the surface haze. For those samples we did not use teflon tape on the molding plates and we minimized agitation during solvent exchange. The surface haze of K, 0.75K and 0.5K were found equal to 2.48%, 4.38% and 6.27%, respectively. The upward trend of surface haze from K to 0.5K is attributed to the deterioration of mechanical properties as density decreases. Nevertheless, haze was measured according to the procedure described in ASTM D1003-13. The aerogel sample was placed at the transmittance port of the integrating sphere and the transmittance was recorded. When light passes through the sample, it scatters due to the inhomogeneity in the sample. Two transmittances were recorded for each sample. In first case, the total light that passes through the sample termed as total transmittance of sample ( $T_2$ ) was recorded by placing the spectralon reference puck on the reflectance port of the integrating sphere and collecting the spectrum. In second case, only the scattered light was captured by removing the spectralon reference puck. That transmittance value was termed as sample scatter ( $T_4$ ). In order to eliminate the scattering from the instrument, similar experiments were done without placing any sample in the transmittance port of the integrating sphere with the spectralon reference puck on the reflectance port termed as instrument radiant spectra ( $T_1$ ) and without the spectralon reference puck on the reflectance port termed as instrument scatter ( $T_3$ ). Scheme 2 shows the configuration of the integrating sphere for measuring haze

in aerogels. Using the above four transmittance values, haze (H) was calculated according to equation 1.

$$\% H = \left( \frac{T_4}{T_2} - \frac{T_3}{T_1} \right) \times 100 \quad (1)$$

The total transmittance decreased with increase in sample scattering as silane concentration was decreased. Minimum haze was observed for K aerogels with average haze of 15 % and increased with decrease in silane concentration and increase in degree of crosslinking. When a silica sample is crosslinked, a thin conformal coating of polymer layer occurs on the surface of particles. Therefore, the particle size of crosslinked samples increased upon crosslinking. Those particles act as scatterers and hence due to increase in scatterer size, scattering increases there by making the crosslinked samples appear hazier than the native samples. Moreover, scattering further increased with change in refractive index from silica particle to conformal polymer layer to air. Average haze for all the samples is tabulated in Table 5.

Figure 6 shows the combined plot of Young's modulus, thermal conductivity and %Average Haze. 0.875K-4.5% N3200 was the the near optimal sample with  $E = 70.29 \pm 2.94$  MPa,  $\lambda = 22.5 \pm 0.8$  mW m<sup>-1</sup> K<sup>-1</sup>, and  $H = 16.2\%$ .

### 3. EXPERIMENTAL

#### 3.1. MATERIALS

All reagents and solvents were used as received unless noted otherwise. Tetramethylorthosilicate (TMOS) and anhydrous acetonitrile (99.8%) were purchased

from Sigma Aldrich. 3-Aminopropyltriethoxysilane (APTES) and ACS Grade acetonitrile were purchased from Alfa-Aesar. Siphon grade CO<sub>2</sub> was obtained from Ozark Gas, Rolla, MO. The tri-isocyanate Desmodur N3200A was donated from Covestro LLC.

**3.1.1. Synthesis of Amine-Modified Silica Wet-gels.** Silica aerogels were prepared according to the standard formulation (denoted as K) [Katti] where two solutions, Solution A containing TMOS (2.887 mL, 0.0194 mol), APTES (0.963 mL, 0.0041 mol) and anhydrous acetonitrile (4.5 mL), and solution B containing water (1.5 mL, 0.0833 mol) and anhydrous acetonitrile (4.5 mL) were first cooled in dry-ice, then, they were allowed to thaw followed by mixing the two solutions. While the volume ratio of TMOS:APTES was kept constant (3:1 v/v), the total mass of silane (TMOS+APTES) was varied from K, 0.875 K, 0.75 K, 0.625 K and 0.5 K with respect to the total mass used in the standard formulation as just described above. (The mass of H<sub>2</sub>O used in the sol followed the reduction in mass of the total silane.) The resulting sol was mixed for few seconds and then was poured into the molds and allowed to gel. (Molding of the aerogels intended for haze measurements was different - see below.) After aging for 24 h, all the wet-gels were removed from the molds and were washed with ACS grade acetonitrile (2×8 h each time) followed by washes with anhydrous acetonitrile (2×8 h each time). The resulting wet-gels were then processed for crosslinking.

In order to measure haze (H) of wet-gels, special rectangular glass molds were constructed with borosilicate glass plates (2'' ×2'' ×1 mm). First, the glass plate slides were cleaned by submerging them in water containing 3-5 drops of Micro-90 cleaning solution (Cole-Parmer, Item # SK-18100-05). Glass pipettes were placed between slides in order to avoid sticking of one microscope slide to another. The cleaning solution with the slides in

it was heated to boil. As soon as the cleaning solution started boiling, it was decanted, glass plates were washed thoroughly with copious amounts of distilled water and were dried in an oven at 150 °C for 12 h. Once the glass plates were dried and ready, one of the surfaces of each glass plates were covered with high density PTFE Teflon tape (Taegatech, Catalog No. Mil-T-27730A) uniformly. The glass molds were prepared by holding two pre-cleaned and dried (see above) 3"×3" teflon covered glass plates parallel to one another with a circular spacer in between. The spacer was constructed by cutting a ~10 mm ring off a 1" diameter plastic container using a band saw. The spacer was attached to the glass plates by applying a small amount of high vacuum grease along its outer edges. (High vacuum grease is not soluble in the sol and prevented leaking.) The assembly of the two glass plates with the spacer in between was wrapped tightly with Parafilm™ (Fisher, Catalog No. S37440). The mold was filled with the sol through a very small portion of the ring spacer that had been previously cut off with a knife. That opening was sealed with Parafilm™ once the sol gelled. Sol was poured in those molds and allowed to gel and age. The resulting wet-gels were processed similarly as mentioned above and were subjected to crosslinking as described below.

### **3.1.2. Synthesis of Native and Crosslinked Amine-Modified Silica Aerogels.**

All the wet-gels in anhydrous acetonitrile were crosslinked with different concentrations of the triisocyanate, Desmudur N3200A. Depending on the percentage of crosslinker, weighed amount of Desmudur N3200A was dissolved in anhydrous acetonitrile. The total volume of the N3200A mixture in acetonitrile was 8× the volume of gel. The wet-gels that were in acetonitrile were added to the isocyanate solution in acetonitrile under N<sub>2</sub> atmosphere and were sealed with Parafilm™. The set up was left for 24 hours at room

temperature for the isocyanate to diffuse inside the wet-gel with occasional and slow swirling. After 24 h, the solvent was decanted and fresh anhydrous acetonitrile was added to the gels under N<sub>2</sub> atmosphere. The containers were then sealed with teflon and heated in oven at 70 °C for 3 days for complete crosslinking. After 3 days, the containers were removed from the oven and allowed to reach room temperature after which the gels were washed with anhydrous acetonitrile (2×8 h) followed by washes with ACS grade acetonitrile (2×8 h). The final cross-linked wet-gels obtained were dried in an autoclave with liquid CO<sub>2</sub> taken out at the end as a supercritical fluid (SCF).

### 3.2. METHODS

Drying of wet-gels was carried out in an autoclave (SPIDRY Jumbo Supercritical Point Dryer, SPI Supplies, Inc. West Chester, PA, or Spe-edSFE System, Applied Separations, Allentown, PA). Wet-gels submerged in acetonitrile were loaded into the autoclave at room temperature. The pressure vessel was closed, and liquid CO<sub>2</sub> was allowed in at room temperature. Acetonitrile was drained out from the pressure vessel every 20 min, while more liquid CO<sub>2</sub> was allowed in. The cycle was repeated several times until all acetonitrile had been extracted out of the pores of the samples. Subsequently, the temperature of the autoclave was raised to 40 °C, and that condition was maintained for two hours. Finally, SCF CO<sub>2</sub> trapped in the pores was vented off as a gas to result in aerogels.

**3.2.1. Chemical Characterization.** Solid-state <sup>29</sup>Si NMR spectra were obtained on the Bruker Avance III 400 MHz spectrometer using a 7 mm Bruker MAS probe and magic angle spinning at 5 kHz with a 59.624 MHz silicon frequency. <sup>29</sup>Si NMR spectra of

one of the samples were obtained using both cross-polarization (CPMAS pulse sequence) and direct polarization. All spectra were referenced externally to neat tetramethylsilane (TMS, 0 ppm). The relaxation delay was set at 5 s in both experiments. The number of scans for the CPMAS experiment was set at 8,192 with a contact time of 3,000  $\mu$ s, while the number of scans for the direct polarization experiment was set at 16,384.

**3.2.2. Physical Characterization of Aerogels.** Bulk densities ( $\rho_b$ ) were calculated from the weight and the physical dimensions of aerogel monolith directly after removing the samples from the drier. Skeletal densities ( $\rho_s$ ) were determined with helium pycnometry using a Micromeritics AccuPyc II 1340 instrument. Samples for skeletal density were degassed for 24 h at 80 °C under vacuum. Percent porosities of aerogels,  $II$ , were determined from the  $\rho_b$  and  $\rho_s$  values via  $II = 100 \times (\rho_s - \rho_b) / \rho_s$ . Linear shrinkages were calculated from the physical dimensions of the samples.

**3.2.3. Structural Characterization of Aerogels.** BET surface areas, fractal dimensions and pore size distributions for pore sizes in the range of 1.7–300 nm were determined with N<sub>2</sub>-sorption porosimetry at 77 K using a Micromeritics ASAP 2020 surface area and porosity analyzer.

Scanning electron microscopy (SEM) was conducted with Au/Pd (80/20) coated samples on a Hitachi Model S-4700 field-emission microscope. Samples were mounted on the stub as follows: A single-sided sticky Cu-tape was attached on a double-sided sticky carbon dot placed on the stub, and the sample was stuck on the sticky-side of the Cu-tape. Then, thin Cu-strips were cut and placed on top of the samples leaving some area open for observation.

Small-angle X-ray scattering (SAXS) was carried out with a PANalytical X'PertPro Multipurpose Diffractometer (MPD) configured for SAXS, using Cu K $\alpha$  radiation ( $\lambda = 1.54$  Å), a 1/32° SAXS slit together with a 1/16° antiscatter slit on the incident beam side, and a 0.1 mm antiscatter slit and a Ni 0.125 mm automatic beam attenuator on the diffracted beam side. Aerogels were placed in circular holders between thin Mylar sheets, and the scattering intensities were measured with a point detector in the transmission geometry using  $2\theta$  scans ranging from  $-0.1^\circ$  up to  $5^\circ$ . SAXS intensity data are reported in arbitrary units as a function of  $Q$ , the momentum transferred during a scattering event ( $Q = 4\pi \times n \times \sin \theta / \lambda$ , where  $n$  is the refractive index of the medium. For air  $n = 1$ ). Data analysis was conducted with the Irena SAS tool for modeling and analysis of small-angle scattering within the commercial Igor Pro software package (WaveMetrics, Inc. Lake Oswego, OR).

**3.2.4. Mechanical Characterization.** Mechanical testing was done under quasistatic compression using an Instron 4469 universal testing machine with 50 kN load cell, following the testing procedures and specimen length (2.0 cm) to diameter (2.0 cm) ratio specified in ASTM D1621-04a (Standard Test Method for Compressive Properties of Rigid Cellular Plastics).

**3.2.5. Thermal Characterization.** Thermogravimetric analysis (TGA) was conducted under N<sub>2</sub> with a TA Instruments Model TGA Q50 thermogravimetric analyzer, using a heating rate of 5 °C min<sup>-1</sup>. The thermal conductivity of aerogel samples was measured according to ASTM Standard No. C177 (Standard Test Method for Steady-State Heat Flux Measurements and Thermal Transmission Properties by Means of the Guarded Hot Plate Apparatus) using a thermal conductivity analyzer donated generously by Aerogel Technologies LLC (Boston, MA) consisting of a 4''×4'' aluminum block heated from the

inside with three cartridge heaters (No. 3618K26, McMaster-Carr), and the temperature on the upper surface was maintained at 37.5 °C using a temperature controller (Part No. CN7833, Omega Engineering, INC.). The temperature-controlled surface of the aluminum block was covered with the aerogel sample. Subsequently, a 4''×4''×0.5'' reference sample (NIST standard SRM 1453, Expanded Polystyrene Board – closed cell,  $\lambda_{\text{NIST\_standard}} = 0.033 \text{ W m}^{-1} \text{ K}^{-1}$ ) with two thermocouples attached near the centers of the two opposite faces, was placed over the aerogel sample. An aluminum bucket with crushed ice was supported by two screw-jacks (Product No. 11210-08, Ace Glass INC.) on two opposite sides, and was placed on top of the reference sample in such a way that the entire top (4''×4'') surface of the reference sample was in contact with the base surface of the ice bucket. To ensure good contact between the ice-cold bucket and the NIST standard, the height of the screw-jacks was adjusted based on the thickness of the aerogel sample (thickness minus 5%). A fourth thermocouple was also placed deep in the crushed ice to monitor its temperature. A 4-channel handheld data logger thermometer (Part No. HH378, Omega Engineering, INC.) was used to record the temperature at the four different places in the setup, as just described: at the bottom of the sample (in contact with the aluminum block at 37.5 °C), at the top of the sample, at the top of the reference sample, and in the ice water. Once the setup was thermally equilibrated (about an hour), the readings of the four thermocouples were recorded six times in 15 minute intervals. The thermal conductivity was calculated based on the fact that the same amount of heat flows through both the sample and the reference sample. The apparatus was calibrated with (a) a second 4''×4''×0.5'' piece of the NIST standard run as an unknown; and, (b) several 4''×4''×0.4'' pieces of commercially available Aspen Aerogel blankets [REF]. REF.

<http://www.aerogel.com/products-and-solutions/all-insulation-products/> Because the aerogel samples were not applied as single monoliths, but rather as two pieces tightly fit side-by-side, the apparatus was also calibrated with two NIST standard samples (10.2×10.2×1.3 cm and 10.2×7.6×1.3 cm) fitted likewise, side-by-side. That arrangement made no statistically significant difference. All calibration and crosscheck data are provided in the Supporting Information of reference.

**3.2.6. Haze Measurements of Native and Cross-linked Aerogels.** Haze (*H*) measurements of all aerogels were carried out using a Cary 5000 UV-Vis Spectrophotometer Model # G9825A equipped with an integrating sphere (S/N # MY 1744 0002). Experiments were carried out according to the ASTM D1003-13. Transmittance was recorded from 380 nm to 800 nm. Samples were prepared with flat parallel surfaces (see above), and were referenced to open air; therefore haze measurements included both bulk and surface haze. The latter was estimated for selected native TMOS-co-APTES aerogels with a series of samples with variable thickness by an adaptation of the Method of Standard Additions.

## 4. CONCLUSIONS

Using DOE, different polymer crosslinked silica aerogels at different silane concentrations were prepared, and their mechanical, thermal and optical properties were studied. Polymer uptake by crosslinking was confirmed from TGA and <sup>29</sup>Si NMR. Mechanical properties and thermal conductivity increased with increasing silane and crosslinking concentration. Increase in mechanical strength was due to the conformal

polymer coating that strengthened the silica backbone by making the interparticle necks thicker. On the other hand, increase in thermal conductivity with increase in silane and crosslinking concentration was due to the increase in through solid conduction. However, haze decreased with increase in silane concentration due to slight increase in particle size that acts as scatterer. Haze also increased with increase in crosslinking concentration due to two factors, firstly the particle size acting as scatterer increases upon crosslinking that increases the scattering. And secondly, due to the refractive index mismatch from air to silica to the polymer layer, scattering increases. By the same token, the wet-gels are clearer than corresponding aerogels since the change in refractive index in wet-gel from acetonitrile to silica to polymer is not as pronounced as in aerogel. The way of handling the wet-gels and aerogels resulted in surface scattering that further increased the haze. Near optimal samples combined a density of  $0.329 \pm 0.003 \text{ g cm}^{-3}$ , a Young's modulus of  $71 \pm 3 \text{ MPa}$ , thermal conductivity of  $0.023 \pm 0.001 \text{ W m}^{-1} \text{ K}^{-1}$ , and haziness of 16.2 % using a 3 mm thick sample.

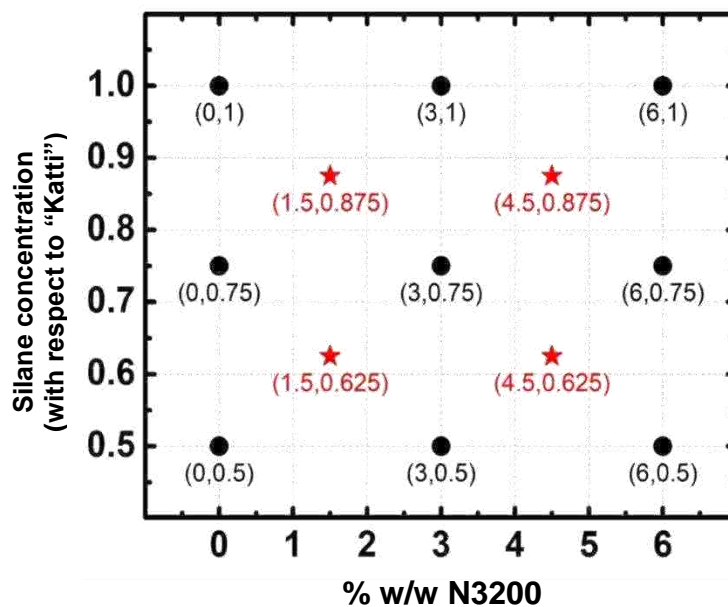


Figure 1. Formulations according to a three-level, two-variable full-factorial design of experiments (DoE) statistical method (dark circles) enhanced with for additional star points. Numbers in parentheses: values of the explanatory variables at each point of the design as follows: (weight percent of Desmodur N3200 in the crosslinking bath, total silane concentration with respect to the Standard referred to as "K")

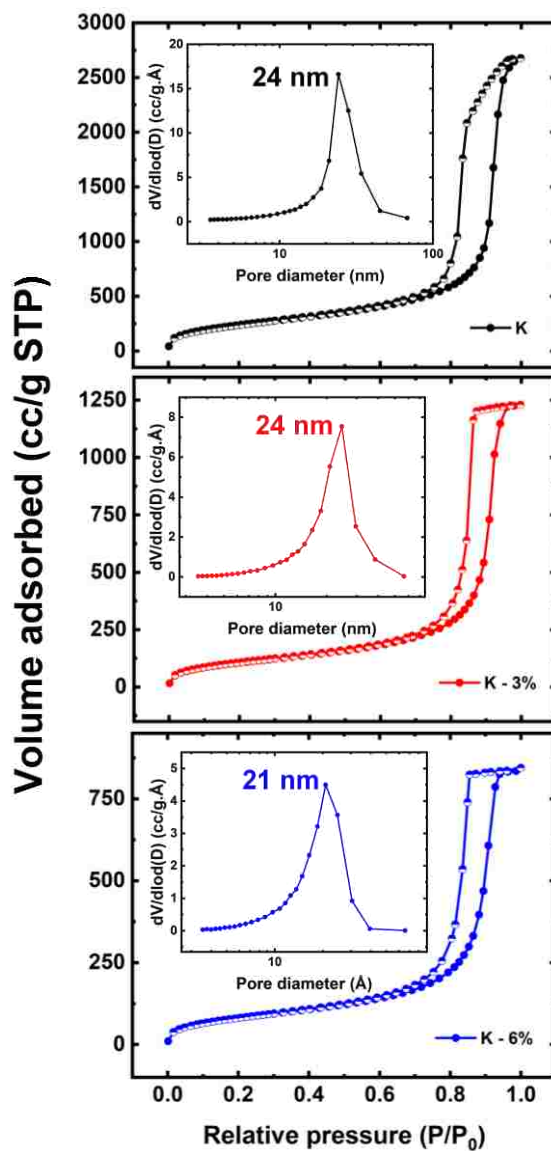


Figure 2. Representative N<sub>2</sub>-sorption data of 0.5K, 0.5K-3%, 0.5K-6%. Insets: BJH pore size distribution plots

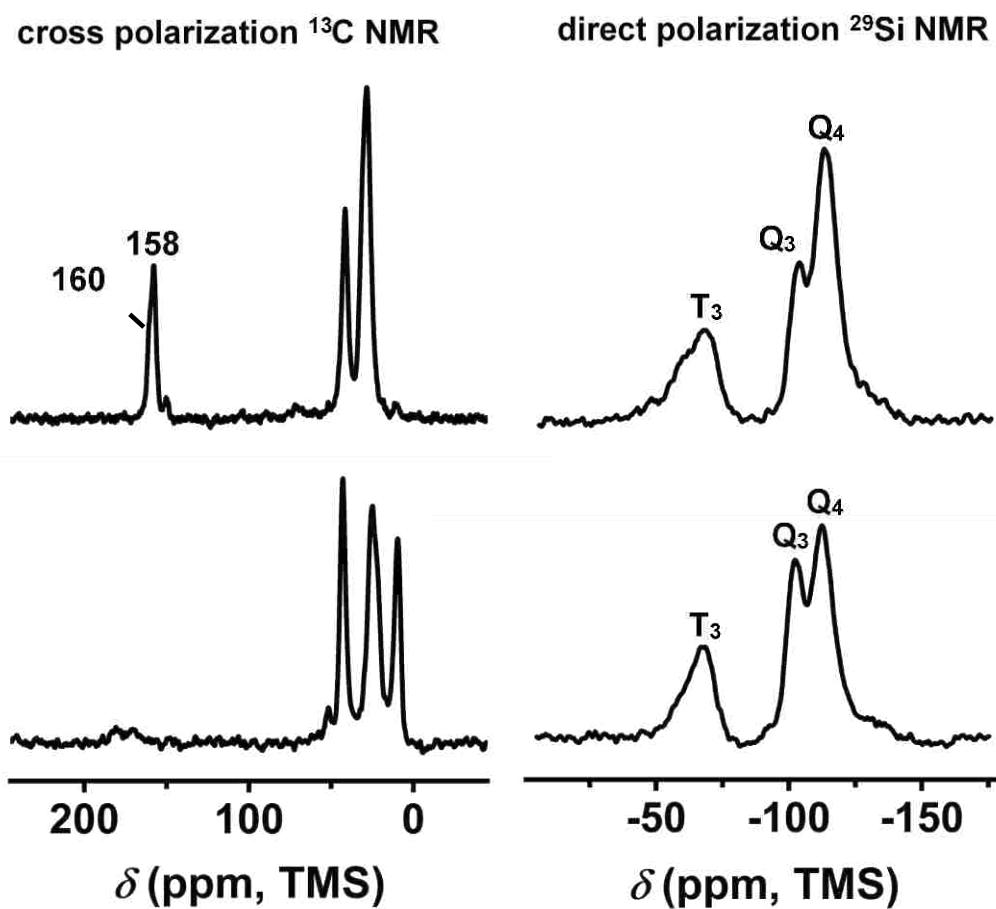


Figure 3. Solid-state NMR of native and cross-linked (X-) TMOS-co-APTES aerogels.  
(A)  $^{13}\text{C}$  CPMAS NMR. (B) Direct polarization  $^{29}\text{Si}$  MAS NMR

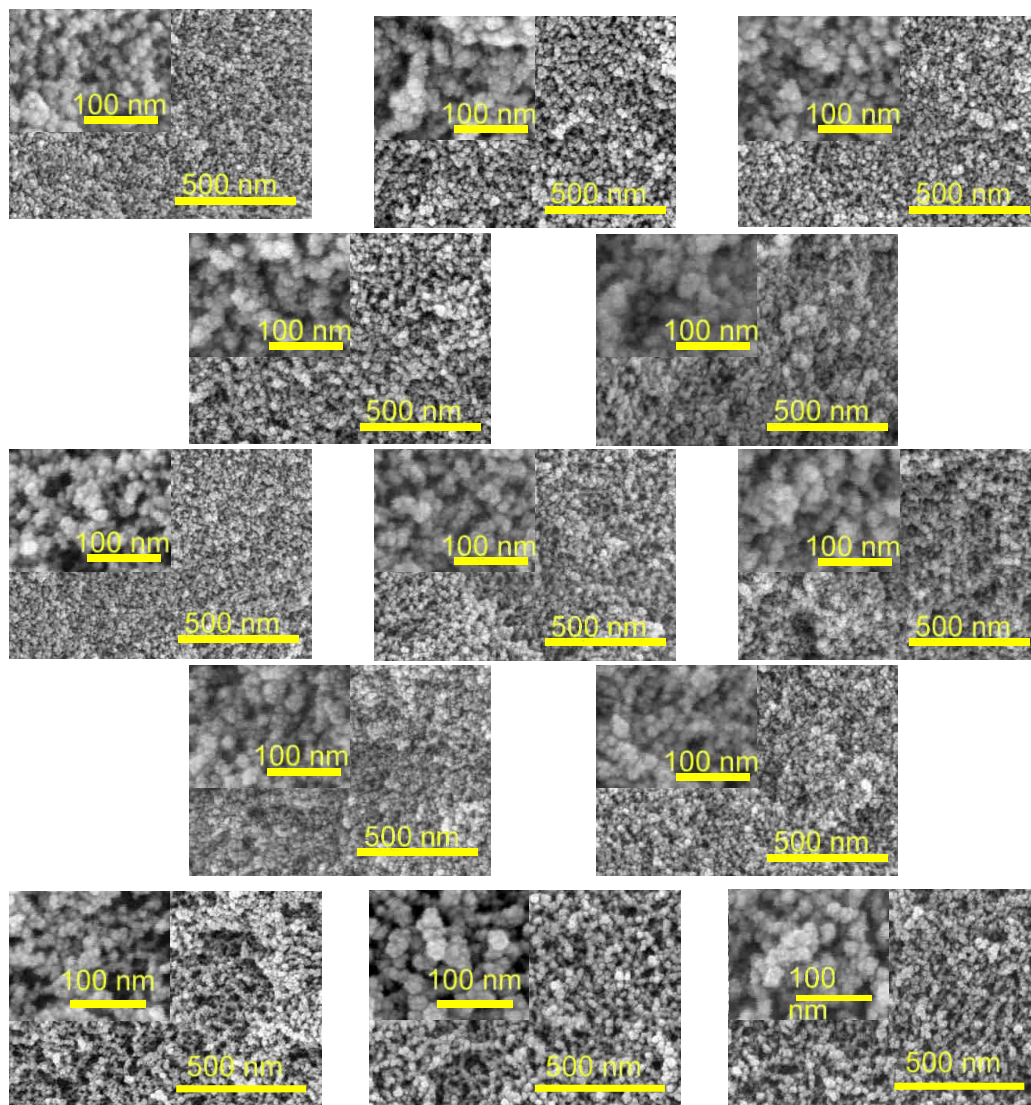


Figure 4. Representative high resolution SEM images (200 $\times$ ) of native and crosslinked silica aerogels across the design space of Figure 1

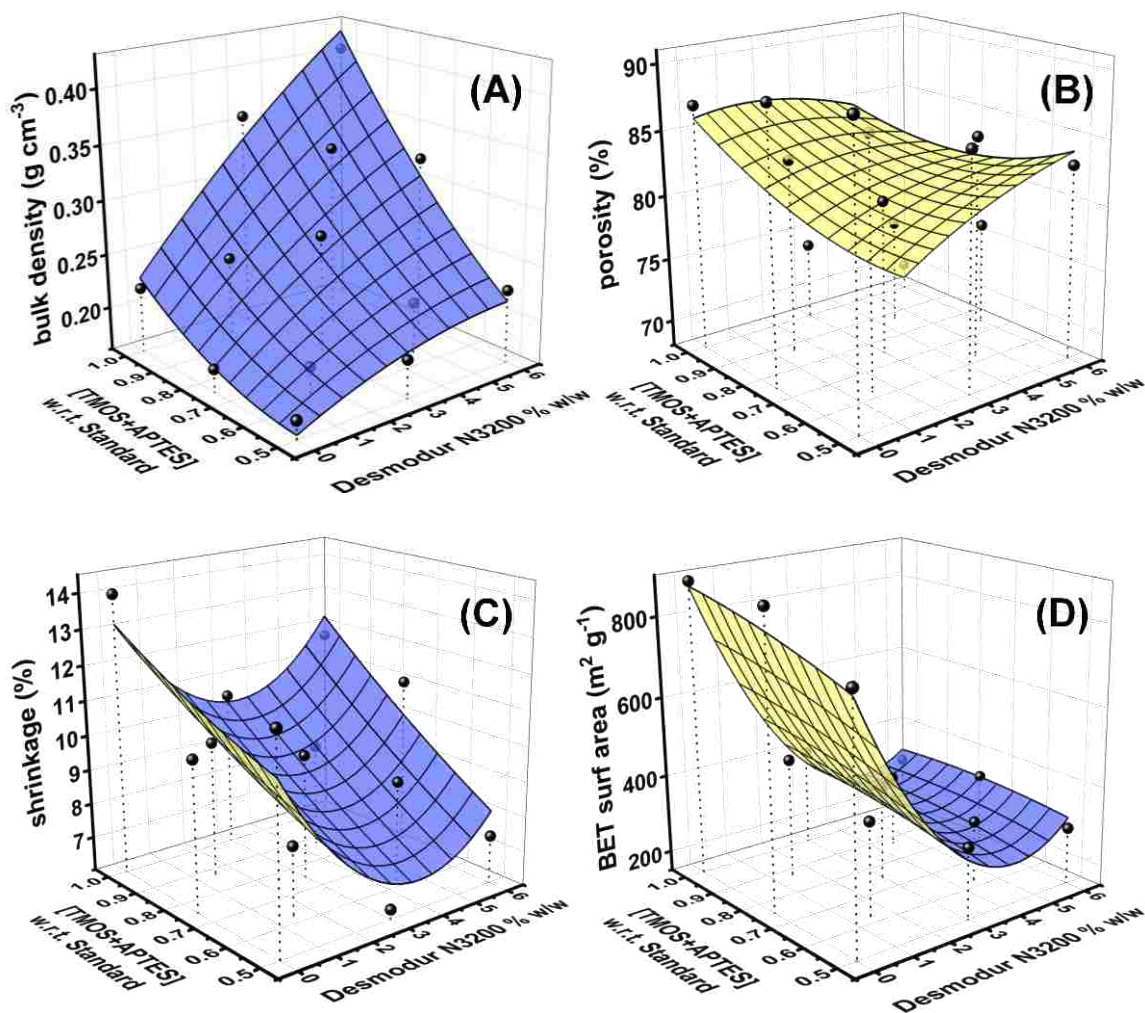


Figure 5. Basic material properties of native and cross-linked TMOS-co-APTES aerogels as a function of the two explanatory variables as shown. (A) Bulk density ( $\rho_b$ ). (B) Porosity ( $\mathcal{P}$ ). (C) Linear shrinkage. (D) BET surface area ( $\sigma$ )

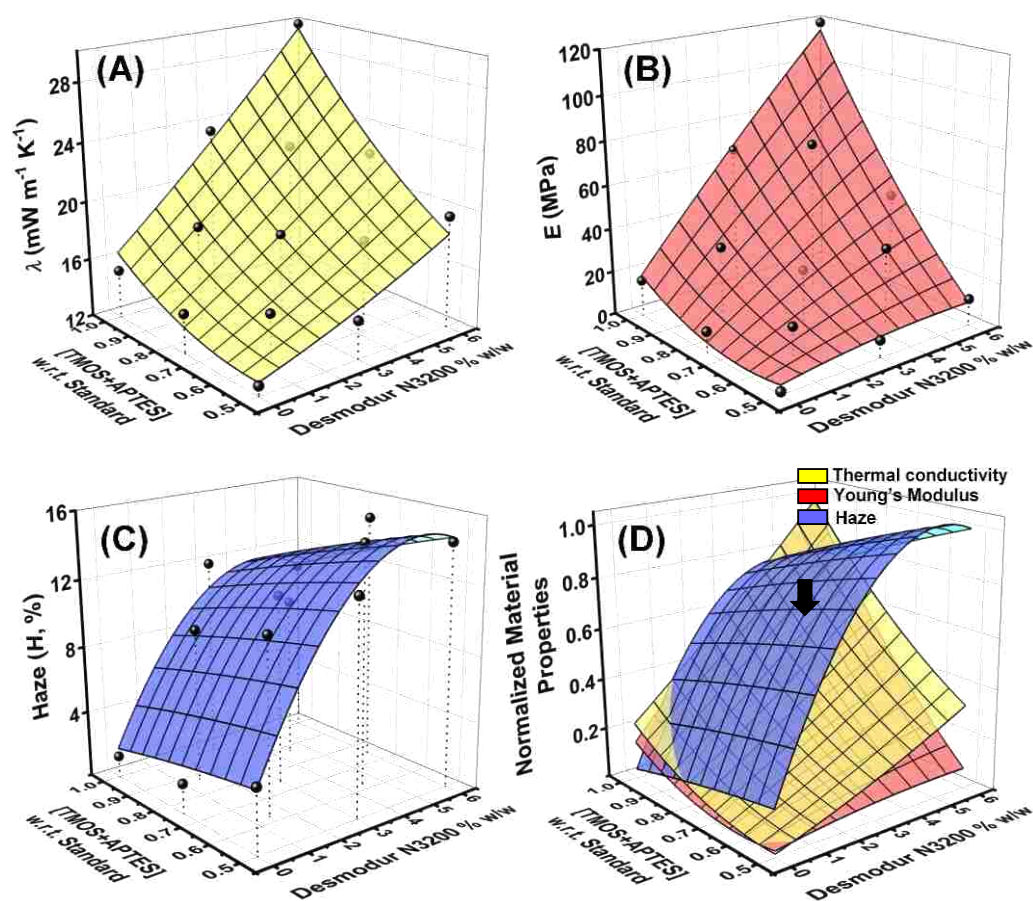


Figure 6. Material properties of interest to application of TMOS-co-APTES aerogels in windows as a function of the two explanatory variables of this study (see Figure 1). (A) Thermal conductivity ( $\lambda$ ). (B) Young's modulus ( $E$ ). Inset: representative stress-strain curves. (C) Haze ( $H$ ) calculated for 3mm-thick samples. (D) Combined all three properties ( $\lambda$ ,  $E$ , and bulk  $H$ ), normalized to their respective highest values, and plotted together. Arrow shows the composition of the panel shown in Figure 9

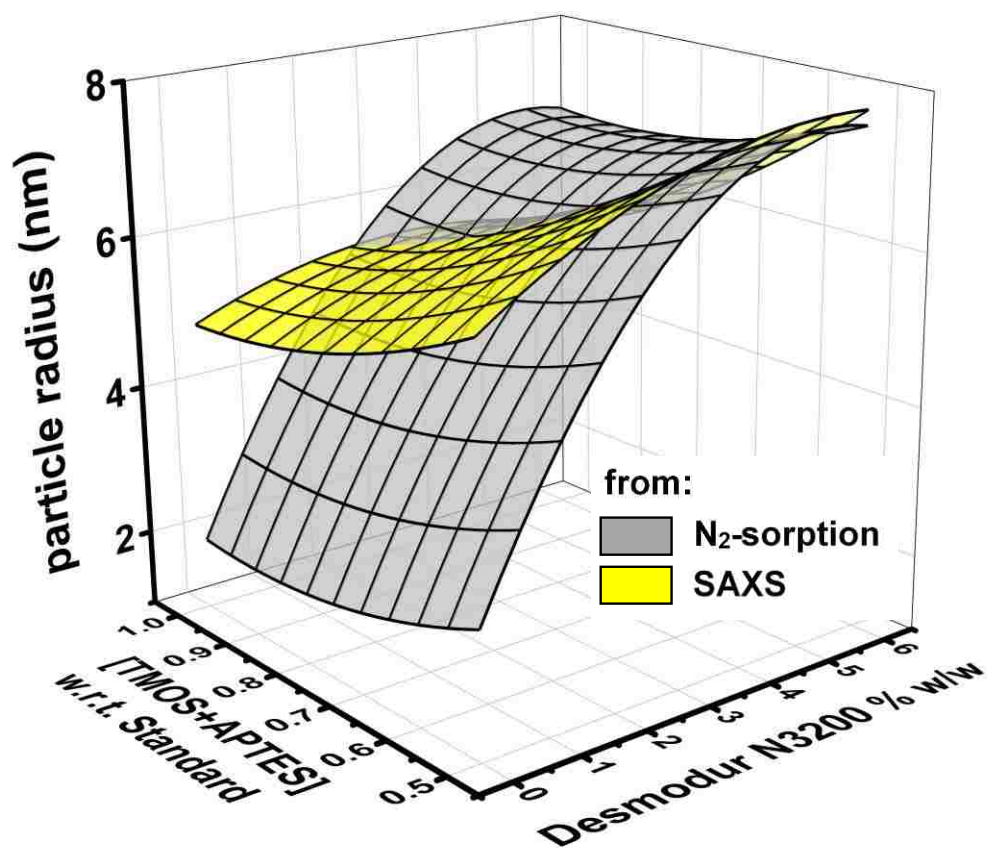


Figure 7. Particle radii as a function of the two explanatory variables of this study (see Figure 1). Grey surface: radius,  $r$ , from N<sub>2</sub>-sorption and skeletal density data via  $r = 3/(\rho_s \times \sigma)$ . Yellow surface: Radius,  $R$ , from SAXS data. (All data from Table 2)

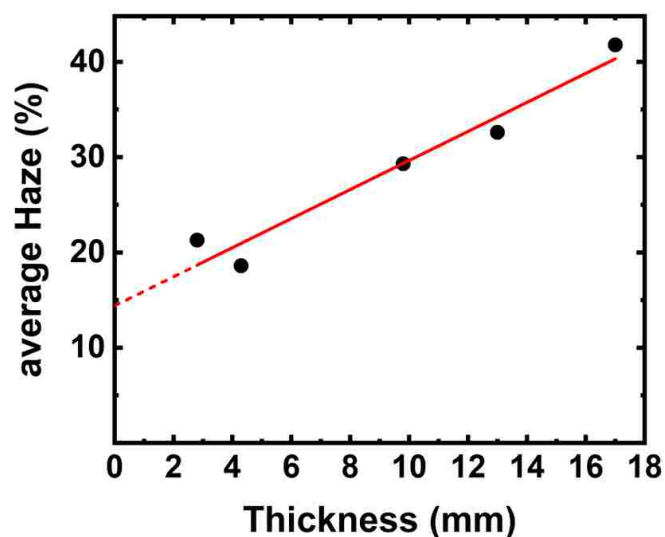


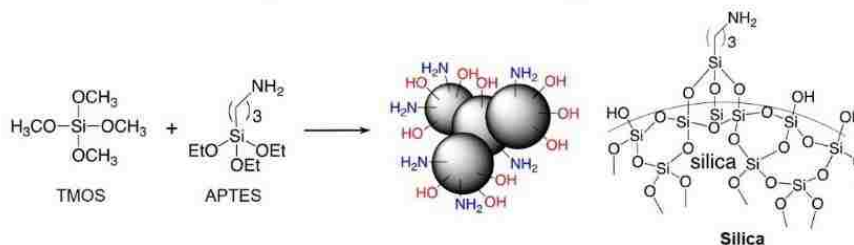
Figure 8. Haze as a function of thickness of native TMOS-co-APTES aerogel samples prepared with the 0.875K formulation molded with Teflon tape coated glass plates. Haze from surface scattering (14.41 %) was obtained by intrapolation to zero thickness. (The value was subtracted from the total haze of each sample measured experimentally, and the remainder was the bulk haze due to Rayleigh scattering)



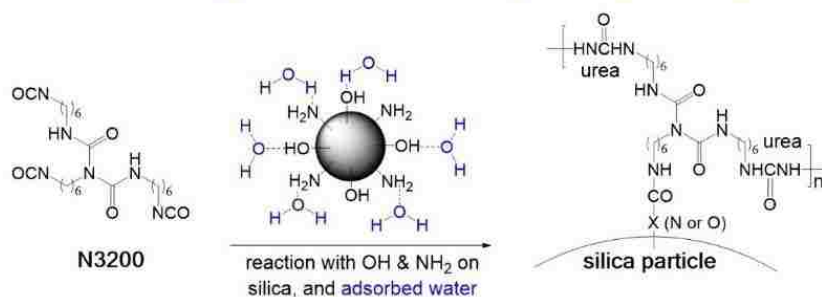
Figure 9. Unobstructed view and view through a cross-linked TMOS-co-APTES aerogel sample fabricated with the formulation shown with an arrow in Figure 6 (0.875,4.5).

Other properties:  $\rho_b = 0.329 \text{ g cm}^{-3}$ ;  $\Pi = 76 \text{ \% v/v}$

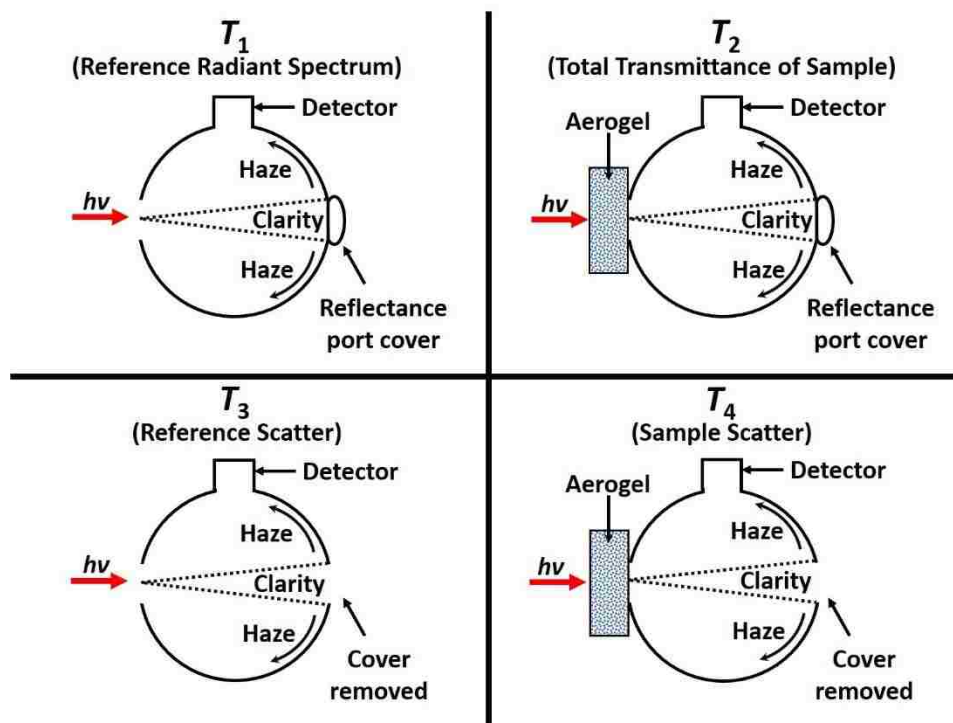
### Synthesis of silica wet-gels



### Crosslinking silica with a triisocyanate (X-Silica)



Scheme 1. Synthesis and crosslinking of silica wet-gels



Scheme 2. Configurations of the integrating sphere for measuring haze

Table 1. General materials characterization data for the crosslinked TMOS-co-APTES aerogels

sample	bulk density ( $\rho_b$ , g cm <sup>-3</sup> ) <sub>b</sub>	skeletal density ( $\rho_s$ , g cm <sup>-3</sup> ) <sup>c</sup>	$\Pi$ (% v/v) <sup>d</sup>	specific pore volume (cm <sup>3</sup> g <sup>-1</sup> )			BET surface area ( $\sigma$ , m <sup>2</sup> g <sup>-1</sup> )	average pore diameter ( $4V/\sigma$ , nm) <sup>h</sup>	particle radius ( $r$ , nm) <sup>i</sup>	% polymer (from TGA)
				$V_{\text{Total}}$ <sup>e</sup>	$V_{1.7-300}$ nm <sup>f</sup>	$V_{>300}$ nm <sup>g</sup>				
Katti	0.220 ± 0.004	1.742 ± 0.003	87	3.971	4.150	0	888	17.89 [18.65]	1.94	N/A
Katti-3% N3200	0.358 ± 0.001	1.385 ± 0.001	74	2.071	1.907	0.164	395	20.97 [19.26]	5.48	47
Katti-6% N3200	0.405 ± 0.003	1.361 ± 0.002	70	1.734	1.301	0.433	303	22.90 [17.05]	7.27	55
0.875 K-1.5 % N3200	0.250 ± 0.004	1.444 ± 0.002	83	3.307	2.729	0.578	450	29.40 [24.22]	4.62	42
0.875 K-4.5 % N3200	0.329 ± 0.003	1.363 ± 0.002	76	2.306	1.869	0.437	330	27.95 [22.38]	6.67	53
0.75 K	0.181 ± 0.003	1.718 ± 0.004	89	4.943	4.257	0.686	882	22.42 [19.25]	1.98	N/A
0.75 K-3% N3200	0.273 ± 0.004	1.389 ± 0.002	80	2.943	2.248	0.695	386	30.50 [23.27]	5.60	50
0.75 K-6% N3200	0.321 ± 0.003	1.362 ± 0.001	76	2.381	2.121	0.260	340	28.01 [23.15]	6.48	51
0.625 K-1.5% N3200	0.186 ± 0.002	1.444 ± 0.002	87	4.684	0.969	3.715	386	48.54 [7.92]	5.38	42
0.625 K-4.5 % N3200	0.213 ± 0.004	1.389 ± 0.004	85	3.975	1.107	2.868	303	52.48 [12.36]	7.13	53
0.5 K	0.177 ± 0.001	1.725 ± 0.007	90	5.070	1.695	3.375	766	26.48 [8.57]	2.27	N/A
0.5 K-3% N3200	0.195 ± 0.002	1.366 ± 0.002	86	4.396	0.637	3.759	329	53.45 [8.14]	6.68	50
0.5 K-6% N3200	0.227 ± 0.003	1.335 ± 0.002	83	3.656	2.828	0.828	293	49.91 [37.98]	7.67	56

<sup>a</sup> Shrinkage =  $100 \times (\text{mold diameter} - \text{sample diameter}) / (\text{mold diameter})$ . <sup>b</sup> Average of 3 samples. <sup>c</sup> Single sample, average of 50 measurements. K, K/2 and K/4 were measured directly. Owing to the low density of K/8 to K/32, there was not enough material for accurate measurement, and the value reported is the average of the  $\rho_s$  values of K to K/4. <sup>d</sup> Percent porosity,  $\Pi = 100 \times (\rho_s - \rho_b) / \rho_s$ . <sup>e</sup> Calculated via  $V_{\text{Total}} = (1/\rho_b) - (1/\rho_s)$ . <sup>f</sup> Cumulative volume of pores between 1.7 and 300 nm from N<sub>2</sub>-sorption data and the BJH desorption method. <sup>g</sup>  $V_{>300 \text{ nm}} = V_{\text{Total}} - V_{1.7-300 \text{ nm}}$ . <sup>h</sup> For the first number,  $V$  was taken equal to  $V_{\text{Total}} = (1/\rho_b) - (1/\rho_s)$ ; for the number in [brackets],  $V$  was set equal to the total volume probed by N<sub>2</sub>-sorption (=  $V_{1.7-300 \text{ nm}}$ ) up to  $P/P_0 \rightarrow 1.0$ . <sup>i</sup>  $r = 3/(\rho_s \times \sigma)$ .

Table 2. SAXS data for TMOS-co-APTES aerogels

Sample	high-Q slope <sup>a</sup>	R <sub>g</sub> (1) <sup>b</sup> (nm)	R <sub>1</sub> <sup>c</sup> (nm)
Katti	-4.21 ± 0.08	3.79 ± 0.07	4.92 ± 0.09
Katti-3% N3200	-4.21 ± 0.11	4.07 ± 0.03	5.29 ± 0.04
Katti-6% N3200	-4.21 ± 0.11	4.25 ± 0.03	5.52 ± 0.04
0.875 K-1.5 % N3200	-4.21 ± 0.09	4.11 ± 0.04	5.34 ± 0.05
0.875 K-4.5 % N3200	-4.21 ± 0.14	4.43 ± 0.03	5.75 ± 0.04
0.75 K	-4.03 ± 0.13	4.27 ± 0.10	5.55 ± 0.13
0.75 K-3% N3200	-4.21 ± 0.08	4.49 ± 0.03	5.83 ± 0.04
0.75 K-6% N3200	-4.21 ± 0.12	4.60 ± 0.02	5.97 ± 0.03
0.625 K-1.5% N3200	-4.21 ± 0.06	5.25 ± 0.06	6.82 ± 0.08
0.625 K-4.5 % N3200	-4.21 ± 0.08	5.35 ± 0.04	6.95 ± 0.05
0.5 K	-4.15 ± 0.08	4.30 ± 0.07	5.58 ± 0.09
0.5 K-3% N3200	-4.21 ± 0.06	5.99 ± 0.04	7.78 ± 0.05
0.5 K-6% N3200	-4.21 ± 0.08	5.92 ± 0.03	7.69 ± 0.04

<sup>a</sup> Referring to Figure 4: From power law Region I. <sup>b</sup> From Guinier Region II. <sup>c</sup> Particle radius = R<sub>g</sub>/0.77.

Table 3. Mechanical characterization of all silica aerogels

Sample	Young's modulus, (MPa) <sup>a</sup>	E	Strain (ε <sub>y</sub> ) at Yield (mm/mm) <sup>a</sup>	Stress (σ <sub>y</sub> ) at Yield (MPa) <sup>a</sup>	Stress (σ <sub>0.2</sub> ) at 0.2 % Strain (MPa) <sup>a</sup>	Ultimate Strength, UCS, (MPa) <sup>a</sup>
Katti	16.60 ± 0.98		0.079 ± 0.004	1.306 ± 0.014	0.596 ± 0.042	170.17 ± 4.16
Katti-3 %	67.05 ± 2.66		0.041 ± 0.003	2.721 ± 0.263	1.476 ± 0.168	68.73 ± 15.13
Katti-6 %	119.21 ± 12.43		0.039 ± 0.003	4.607 ± 0.280	2.672 ± 0.270	111.72 ± 20.74
0.875 K-1.5 %	33.14 ± 4.45		0.060 ± 0.002	1.979 ± 0.182	1.036 ± 0.077	11.39 ± 2.88
0.875 K-4.5 %	70.29 ± 2.94		0.047 ± 0.001	3.311 ± 0.179	1.721 ± 0.133	105.31 ± 10.37
0.75 K	9.39 ± 1.09		0.094 ± 0.003	0.879 ± 0.082	0.370 ± 0.047	183.35 ± 1.68
0.75 K-3 %	23.52 ± 0.71		0.060 ± 0.003	1.403 ± 0.038	0.800 ± 0.022	173.86 ± 41.99
0.75 K-6 %	46.85 ± 0.60		0.051 ± 0.002	2.346 ± 0.086	1.356 ± 0.083	213.67 ± 36.58
0.625 K-1.5 %	12.86 ± 0.67		0.065 ± 0.002	0.832 ± 0.069	0.371 ± 0.039	26.26 ± 8.48
0.625 K-4.5 %	34.51 ± 2.01		0.061 ± 0.002	2.109 ± 0.079	1.066 ± 0.029	97.28 ± 8.93
0.5 K	1.48 ± 0.28		0.151 ± 0.009	0.222 ± 0.029	0.071 ± 0.004	1.52 ± 1.20
0.5 K-3 %	7.93 ± 1.17		0.074 ± 0.010	0.583 ± 0.010	0.294 ± 0.004	372.04 ± 0.00
0.5 K-6 %	12.16 ± 0.69		0.066 ± 0.001	0.805 ± 0.061	0.426 ± 0.045	375.25 ± 4.53

<sup>a</sup> Average of 3 samples.

Table 4. Thermal conductivities of native and crosslinked silica aerogels

Sample	Thermal Conductivity, $\lambda$ (mW m <sup>-1</sup> K <sup>-1</sup> )
Katti	15.3 ± 0.6
Katti-3% N3200	23.5 ± 0.9
Katti-6% N3200	29.9 ± 0.9
0.875 K-1.5 % N3200	18.5 ± 0.7
0.875 K-4.5 % N3200	22.5 ± 0.8
0.75 K	14.7 ± 0.5
0.75 K-3% N3200	18.1 ± 0.6
0.75 K-6% N3200	22.1 ± 0.8
0.625 K-1.5% N3200	14.9 ± 0.5
0.625 K-4.5 % N3200	17.8 ± 0.7
0.5 K	12.7 ± 0.4
0.5 K-3% N3200	14.6 ± 0.5
0.5 K-6% N3200	19.6 ± 0.7

Table 5. Average haze for native and crosslinked silica aerogels

Sample	average % Haze <sup>a</sup>
Katti	7.4
Katti-3% N3200	18.7
Katti-6% N3200	17.3
0.875 K-1.5 % N3200	15.8
0.875 K-4.5 % N3200	16.2
0.75 K	7.9
0.75 K-3% N3200	18.1
0.75 K-6% N3200	21.9
0.625 K-1.5% N3200	17.2
0.625 K-4.5 % N3200	21.4
0.5 K	10.2
0.5 K-3% N3200	19.6
0.5 K-6% N3200	21.6

<sup>a</sup> Thickness of all aerogel,  $l = 3$  mm.

## SUPPORTING INFORMATION

Table S1. Synthesis of different concentration of TMOS-co-APTES wet-gels

Sample	TMOS, mL [mmol]	APTES, mL [mmol]	H <sub>2</sub> O, mL [mmol]	Acetonitrile [mL]	Total Silane concentration [mM]	Gelation time
K	2.887 [19.571]	0.962 [4.113]	1.500 [83.300]	9	1.651	2 min
0.875 K	2.526 [17.124]	0.842 [3.599]	1.31 [72.888]	9	1.515	2 min
0.75 K	2.165 [14.678]	0.722 [3.085]	1.12 [62.475]	9	1.365	2 min
0.625 K	1.805 [12.232]	0.602 [2.570]	0.94 [52.063]	9	1.199	2 min
0.5 K	1.444 [9.785]	0.481 [2.056]	0.75 [41.650]	9	1.014	3 min

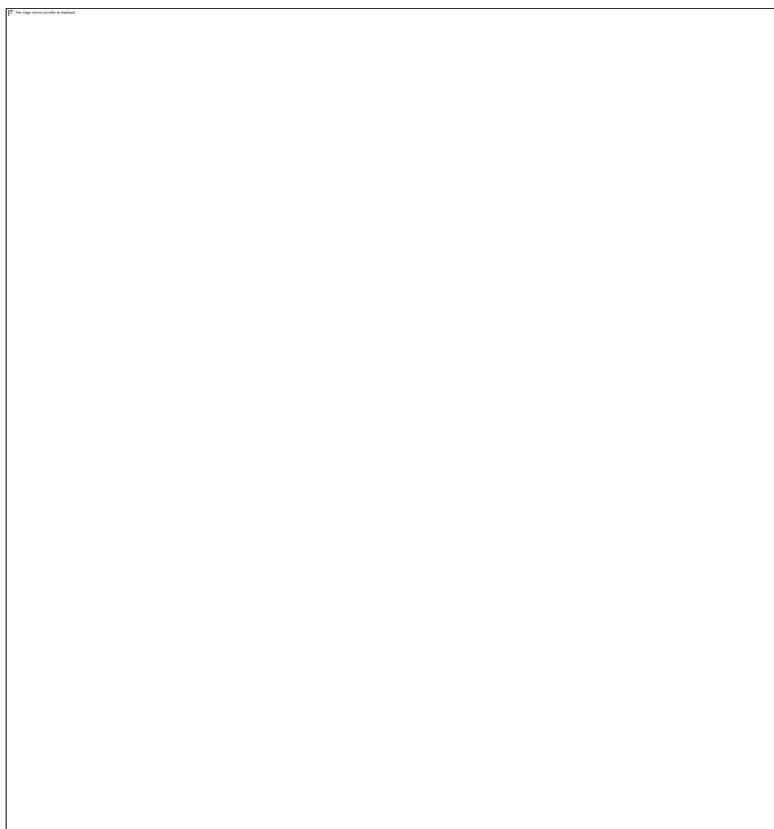


Figure S1. Mechanical characterization of native and crosslinked TMOS-co-APTES aerogels

Table S2. Mechanical characterization of native and crosslinked TMOS-co-APTES aerogels

Sample	Young's modulus, E (MPa) <sup>a</sup>	Strain ( $\epsilon_y$ ) at Yield (mm/mm) <sup>a</sup>	Stress ( $\sigma_y$ ) at Yield (MPa) <sup>a</sup>	Stress ( $\sigma_{0.2}$ ) at 0.2 % Strain (MPa) <sup>a</sup>	Ultimate Strength, UCS, (MPa) <sup>a</sup>
Katti	16.60 ± 0.98	0.079 ± 0.004	1.306 ± 0.014	0.596 ± 0.042	170.17 ± 4.16
Katti-3 %	67.05 ± 2.66	0.041 ± 0.003	2.721 ± 0.263	1.476 ± 0.168	68.73 ± 15.13
Katti-6 %	119.21 ± 12.43	0.039 ± 0.003	4.607 ± 0.280	2.672 ± 0.270	111.72 ± 20.74
0.875 K-1.5 %	33.14 ± 4.45	0.060 ± 0.002	1.979 ± 0.182	1.036 ± 0.077	11.39 ± 2.88
0.875 K-4.5 %	70.29 ± 2.94	0.047 ± 0.001	3.311 ± 0.179	1.721 ± 0.133	105.31 ± 10.37
0.75 K	9.39 ± 1.09	0.094 ± 0.003	0.879 ± 0.082	0.370 ± 0.047	183.35 ± 1.68
0.75 K-3 %	23.52 ± 0.71	0.060 ± 0.003	1.403 ± 0.038	0.800 ± 0.022	173.86 ± 41.99
0.75 K-6 %	46.85 ± 0.60	0.051 ± 0.002	2.346 ± 0.086	1.356 ± 0.083	213.67 ± 36.58
0.625 K-1.5 %	12.86 ± 0.67	0.065 ± 0.002	0.832 ± 0.069	0.371 ± 0.039	26.26 ± 8.48
0.625 K-4.5 %	34.51 ± 2.01	0.061 ± 0.002	2.109 ± 0.079	1.066 ± 0.029	97.28 ± 8.93
0.5 K	1.48 ± 0.28	0.151 ± 0.009	0.222 ± 0.029	0.071 ± 0.004	1.52 ± 1.20
0.5 K-3 %	7.93 ± 1.17	0.074 ± 0.010	0.583 ± 0.010	0.294 ± 0.004	372.04 ± 0.00
0.5 K-6 %	12.16 ± 0.69	0.066 ± 0.001	0.805 ± 0.061	0.426 ± 0.045	375.25 ± 4.53

<sup>a</sup> All values are average of 3 samples. <sup>b</sup> K, 0.875K, 0.75K, 0.625K and 0.5K refer to the “Standard” sol formulation, K, and the corresponding fractions of the total silane concentration [TMOS+APTES]; the percent numerical values that follow in the sample names refer to the concentration of Desmodur N3200A in the crosslinking bath ([N3200A]<sub>in\_the\_X-linking\_bath</sub>).

Table S3. Average haze for native and crosslinked silica aerogels

sample	average haze @ 7 mm (%) <sup>a</sup>	average haze @ 7 mm after surface haze correction (%) <sup>b</sup>	average haze @ 3 mm after surface haze correction (%) <sup>c</sup>	average haze @ 3 mm after adding surface haze (%) <sup>d</sup>
K	17.4	3.0	1.3	3.8
K-3	40.1	25.7	11.9	14.4
K-6	37.4	23.0	10.6	13.1
0-875K-1.5	34.5	20.1	9.2	12.6
0-875K-4.5	35.4	21.0	9.6	13.0
0-75K	18.5	4.1	1.8	6.2
0-75K-3	38.9	24.5	11.3	15.7
0-75K-6	45.6	31.2	14.8	19.2
0-625K-1.5	37.2	22.8	10.5	15.8
0-625K-4.5	44.9	30.5	14.4	19.8
0-5K	23.2	8.8	3.9	10.1
0-5K-3	41.6	27.2	12.7	19.0
0-5K-6	45.1	30.7	14.5	20.8

<sup>a</sup>average haze obtained experimentally using UV-visible spectrophotometer with an integrating sphere. <sup>b</sup>average haze calculated by subtracting the surface haze of 0.875K-native from the experimental haze of 7 mm samples. <sup>c</sup>average haze of 3mm thick sample calculated by using equation 2. <sup>d</sup>average haze of 3mm thick sample after adding the surface haze of the native samples.

$$H_2 = 1 - e^{\left[\frac{l_2}{l_1} \times \{Ln(1-H_1)\}\right]} \quad (2)$$

## REFERENCES

1. Maleki, H.; Duraes, L.; Portugal, A. Development of Mechanically Strong Ambient Pressure Dried Silica Aerogels with Optimized Properties. *J. Phys. Chem.* **2015**, *119*, 7689-7703.
2. Wang, Q.; Feng, J.; Wei, W.; Xie, J.; Xia, C.; Zhu, J.; Jiang, D. Synthesis, Characterization, and Adsorption Properties of Silica Aerogels Crosslinked with Diisocyanate Under Ambient Drying. *J. Mater. Sci.* **2016**, *51*, 9472-9483.
3. Shao, Z.; Wu, G.; Cheng, X.; Zhang, Y. Rapid Synthesis of Amine Crosslinked Epoxy and Methyl co-Modified Silica Aerogels by Ambient Pressure Drying. *J. Non-Cryst. Solids.* **2012**, *358*, 2612-2615.

4. Rewatkar, P. M.; Taghvaei, T.; Saeed, A. M.; Donthula, S.; Mandal, C., Chandrasekaran, N.; Leventis, T.; Shruthi, T. K.; Sotiriou-Leventis, C.; Leventis, N. Sturdy, Monolithic SiC and Si<sub>3</sub>N<sub>4</sub> Aerogels from Compressed Polymer-Crosslinked Silica Xerogel Powders. *Chem. Mater.* **2018**, *30*, 1635-1647.
5. Yang, H.; Kong, X.; Zhang, Y.; Wu, C.; Cao, E. Mechanical Properties of Polymer-Modified Silica Aerogels dried Under Ambient Pressure. *J. Non-Cryst. Solids* **2011**, *357*, 3447-3453.
6. Mohite, D. P.; Larimore, Z. J.; Lu, H.; Mang, J. T.; Sotiriou-Leventis, C.; Leventis, N. Monolithic Hierarchical Fractal Assemblies of Silica Nanoparticles Crosslinked with Polynorbornene via ROMP: A Structure–Property Correlation from Molecular to Bulk through Nano. *Chem. Mater.* **2012**, *24*, 3434-3448.
7. Nguyen, B. N.; Meador, M. A. B.; Medoro, A.; Arendt, V.; Randall, J.; McCorkle, L.; Shonkwiler, B. Elastic Behavior of Methyltrimethoxysilane Based Aerogels Reinforced with Tri-Isocyanate. *ACS Appl. Mater. Interfaces* **2010**, *2*, 1430-1443.
8. Chen, K.; Bao, Z.; Du, Ai; Zhu, X.; Shen, J.; Wu, G.; Zhang, Z.; Zhou, B. One-pot Synthesis, Characterization, and Properties of Acid-Catalyzed RF Crosslinked Silica Aerogels and Their Conversion to Hierarchical Porous Carbon Monoliths. *J. Sol-Gel Sci. Technol.* **2012**, *62*, 294-303.
9. Duan, Y.; Jana, S. C.; Lama, B.; Espe, M. P. Self-Crosslinkable Poly(Urethane Urea)-Reinforced Silica Aerogels. *RSC Adv.* **2015**, *5*, 71551-71558.
10. Guo, H.; Meador, M. A. B.; McCorkle, L.; Quade, D. J.; Guo, J.; Hamilton, B.; Cakmak, M.; Sprowl, G. Polyimide Aerogels Crosslinked Through Amine Functionalized Polyoligomeric Silsesquioxane. *ACS Appl. Mater. Interfaces* **2011**, *3*, 546-552.
11. Yan, P.; Zhou, B.; Du, A. Synthesis of Polyimide Crosslinked Silica Aerogels with Good Acoustic Performance. *RSC Adv.* **2014**, *4*, 58252-58259.
12. Fei, Z.; Yang, Z.; Chen, G. Li, K. Preparation of Tetraethoxysilane-Based Silica Aerogels with Polyimide Crosslinking From 3, 3', 4, 4'-biphenyl tetracarboxylic dianhydride and 4, 4'-oxydianiline. *J. Sol-Gel Sci. Technol.* **2018**, *85*, 506-513.
13. Saeed, S.; Al-Sobaihi, R. M.; Bertino, m. F.; White, L. S. Saoud, K. M. Laser Induced Instantaneous Gelation: Aerogels for 3D Printing. *J. Mater. Chem. A* **2015**, *3*, 17606-17611.
14. Maleki, H.; Duraes, L.; Portugal, A. An Overview on Silica Aerogels Synthesis and Different Mechanical Reinforcing Strategies. *J. Non-Cryst. Solids* **2014**, *385*, 55-74.

15. Randall, J. P.; Meador, M. A. B.; Jana, S. C. Tailoring Mechanical Properties of Aerogels for Aerospace Applications. *ACS Appl. Mater. Interfaces* **2011**, *3*, 613-626
16. Obrey, K. A. D.; Wilson, K. V.; Loy, D. A. Enhancing Mechanical Properties of Silica Aerogels. *J. Non-Cryst. Solids* **2011**, *357*, 3435-3441
17. Franzel, L.; Wingfield, C.; Bertino, M. F.; Mahadik-Khanolkar, S.; Leventis, N. Regioselective Crosslinking of Silica Aerogels with Magnesium Silicate Ceramics. *J. Mater. Chem. A*, **2013**, *1*, 6021-6029
18. Leventis, N.; Sadekar, A.; Chandrasekaran, N.; Sotiriou-Leventis, C.; Click Synthesis of Monolithic Silicon Carbide Aerogels from Polyacrylonitrile-Coated 3D Silica Networks. *Chem. Mater.* **2010**, *22*, 2790-2803
19. Meador, M. A. B.; Scherzer, C. M.; Vivod, S. L.; Quade, D.; Nguyen, B. N. Epoxy Reinforced Aerogels Made Using a Streamlined Process. *ACS Appl. Mater. Interfaces* **2010**, *7*, 2162-2168
20. Maleki, H.; Duraes, L.; Portugal, A. Synthesis of Lightweight Polymer-Reinforced Silica Aerogels with Improved Mechanical and Thermal Insulation Properties for Space Applications. *Microporous Mesoporous Mater.* **2014**, *197*, 116-129
21. Boday, D. J.; Keng, P. Y.; Muriithi, B.; Pyun, J.; Loy, D. A. Mechanically Reinforced Silica Aerogel Nanocomposites via Surface Initiated Atom Transfer Radical Polymerizations. *J. Mater. Chem.* **2010**, *20*, 6863-6865
22. Boday, D. J.; Loy, D. A. Strengthening Silica Aerogels with Surface Initiated ATRP Crosslinked poly(methyl methacrylate). *J. Non-Cryst. Solids* **2015**, *427*, 114-119
23. Maleki, H.; Duraes, L.; Portugal, A. Synthesis of Mechanically Reinforced Silica Aerogels via Surface-Initiated Reversible Addition-Fragmentation Chain Transfer (RAFT) Polymerization. *J. Mater. Chem. A* **2015**, *3*, 1594-1600
24. Li, Z.; Gong, L.; Cheng, X.; He, S.; Li, C.; Zhang, H. Flexible Silica Aerogel Composites Strengthened with Aramid Fibers and Their Thermal Behavior. *Mater. Des.* **2016**, *99*, 349-355
25. Li, S.; Zhang, L.; Li, J.; Wu, Z.; Yang, C. Silica Nanowires Reinforced Self-Hydrophobic Silica Aerogel Derived from Crosslinking of Propyltriethoxysilane and Tetraethoxysilane. *J. Sol-Gel. Technol.* **2017**, *83*, 545-554
26. Matias, T.; Varino, C.; de Sousa, H. C.; Braga, M. E. M.; Portugal, A.; Coelho, J. F. J.; Duraes, L. Novel Flexible, Hybrid Aerogels with Vinyl-and Methyltrimethoxysilane in the Underlying Silica Structure. *J. Mater. Sci.* **2016**, *55*, 6781-6792.

### III. EXPERIMENTAL DECONVOLUTION OF DEPRESSURIZATION FROM CAPILLARY SHRINKAGE DURING DRYING OF SILICA WET-GELS WITH SCF CO<sub>2</sub>. WHY AEROGELS SHRINK?

Chandana Mandal<sup>1</sup>, Suraj Donthula<sup>1</sup>, Parwani M. Rewatkar<sup>1</sup>, Chariklia Sotiriou-Leventis<sup>1</sup>, Nicholas Leventis<sup>\*,1</sup>

<sup>1</sup>Department of Chemistry, Missouri University of Science and Technology, Rolla, MO 65409, U.S.A.

Was submitted in *Journal of Sol-Gel Science and Technology*

#### Highlights:

- The major part of the shrinkage during drying silica wet-gels to aerogels with SCF CO<sub>2</sub> is associated with the depressurization phase of the drying process.
- A part of the shrinkage equal to that reported as depressurization shrinkage (70-75%) has been transferred to the wet-gel phase of processing.
- The remaining part of the drying shrinkage has been assigned to interfacial tension.
- The practical significance of those findings is related to the fact that it is easier to control shrinkage at the wet-gel phase of processing.
- From a theoretical perspective, drying with SCF CO<sub>2</sub> is a two-stage moving boundary problem.

Keywords: silica, wet-gel, aerogel, shrinkage, solvent exchange, toluene, xylene

## ABSTRACT

Silica aerogels are prepared by drying wet-gels under conditions that eliminate surface tension forces, typically by exchanging the pore-filling solvent with liquid or supercritical fluid (SCF) CO<sub>2</sub> that is vented off like a gas. Thereby, silica wet-gels should not shrink during drying, but they do. According to the literature, most shrinkage (~71%) happens during depressurization of the autoclave. Here, based on prior literature, and working with wet-gels obtained via base-catalyzed gelation of tetramethylorthosilicate (TMOS), the basic hypothesis was that depressurization shrinkage takes place at the primary/secondary particle level. For this to happen there has to be available space to accommodate merging secondary particles, and a driving force. Secondary particles are mass fractals (by SAXS) and their empty space can accommodate primary particles from neighboring assemblies. The driving force was assumed to be H-bonding developing between surface silanols as soon as all fluids are removed from the pores. That hypothesis was put to test by replacing gelation solvents with non-hydrogen bonding toluene or xylene. Indeed, while the total drying shrinkage of toluene- or xylene-filled wet-gels was equal to that observed with aerogels obtained from acetone-filled wet-gels (~8-9%), the major part of that shrinkage (~74%) was transferred to the wet-gel stage. The remaining shrinkage (~26%) was assigned to interfacial tension forces between the pore-filling solvent and liquid or SCF CO<sub>2</sub>. Having transferred the major part of drying shrinkage to the wet-gel stage has technological implications, because it is easier to manipulate gels at that stage. Furthermore, our results underline that optimization of the drying process should

take into account the fact that drying of silica wet-gels into aerogels is a two-stage moving boundary problem.

## 1. INTRODUCTION

Silica aerogels are low-density, highly porous solids with high internal surface area, low thermal conductivity, and high acoustic impedance [1]. They were first prepared by S. S. Kistler in 1931 by drying wet-gels in a way that prevents shrinkage by eliminating the capillary pressure that would be exerted by the residing meniscus of an evaporating pore-filling solvent on the pore walls – i.e., the skeletal framework of the wet-gel [2]. The capillary pressure is given by the Young-Laplace equation (Eq 1) [3]:

$$P_c = -\frac{2\gamma_{lv}\cos\theta}{r_h} \quad (1)$$

where,  $\gamma_{lv}$  is the surface tension at the evaporating liquid-vapor interface,  $\theta$  is the contact angle of the evaporating liquid and the pore wall, and  $r_h$  is the hydraulic radius given as twice the ratio of the total specific pore volume of the wet-gel to the total specific surface area of the skeletal network of the wet-gel. It follows that for the same specific surface area, smaller pores lead to lower  $r_h$  values and higher capillary pressures. Capillary pressure around the meniscus of the evaporating solvent, and its lack thereof at other parts of the skeletal network, generates stresses throughout the gel that depend on the size of the gel, the rate of evaporation, the viscosity of the evaporating solvent and the permeability of the network [4]. At best, those stresses cause shrinkage, or when they exceed the strength of the skeletal network they cause cracks [4]. Strengthening the network to withstand the internal stresses has been considered a viable approach to minimize shrinkage and prevent

cracking. The network becomes stronger by dissolution of skeletal particles and re-precipitation of silica at the interparticle necks (Ostwald ripening) during a post-gelation stay period referred to as aging [5,6,7], or by post-gelation reinforcement with a conformal polymer coating over the entire skeletal framework (X-aerogels) [8,9,10]. The aging process has been accelerated by increasing the aging temperature [11,12]. On the other hand, in combination with or without methods to reinforce the network, shrinkage and cracking can also be prevented if stresses could be minimized by reducing –or eliminating altogether– capillary pressure. According to Eq 1, that can be accomplished either by increasing the pore size, or, for a given pore size, by reducing or eliminating  $\Delta p_{lv}$ . Thus, it has been reported that aging of silica wet-gels in TEOS-ethanol at elevated temperature (100 °C) results in larger pore sizes, which decrease the capillary pressure and reduce shrinkage [11]. In terms of reducing  $\Delta p_{lv}$ , several authors have reported on the effect of the pore-filling solvent on the drying shrinkage [4,13,14], and especially in conjunction with surface modification of silica [15]. With judicious choices of surface modification and pore-filling solvent, ambient pressure dried xerogels with aerogel-like properties have been reported [16,17,18].

Kistler's approach to *eliminate*  $\Delta p_{lv}$ , which still comprises the cornerstone in aerogel preparation, was based on taking the pore-filling liquid above its critical point. That converts the entire pore-filling liquid all at once into a supercritical fluid (SCF) that is vented off like a gas. The pore-filling liquid can be the gelation solvent itself, or another liquid, including liquid or SCF CO<sub>2</sub>. In either form, CO<sub>2</sub> is introduced in the pores via an extraction process (solvent exchange). Methods involving liquid or SCF CO<sub>2</sub> are high-pressure processes and are carried out in autoclaves. Despite high pressures, drying

methods involving the CO<sub>2</sub> route are near-ambient temperature process and are considered safe –in case of leakage– and thereby they are the most popular ones by far.

By converting the pore-filling liquid into a supercritical fluid all at once, a liquid/vapor interface is never created inside the pores, so no capillary pressure is ever exerted on the pore walls. Thereby, drying silica wet-gels with SCF CO<sub>2</sub> should cause no shrinkage, yet, as has been reported by several authors, it does [12,19]. Understanding the cause of drying shrinkage has enormous technological implications. For example, while thick wet silica gels can be made to stick on two glass facers with strong silica-to-silica adhesion forces (Figure 1A) [20], differential shrinkage during drying with SCF CO<sub>2</sub> causes delamination (Figure 1B), and poses severe restrictions to processing such facer/wet-gel assemblies into aerogels toward, for example, thermally insulating windows [21].

Either by direct observation of the gels during drying,[19] or by attaching sensors on the wet-gels,[12] several authors have traced most of the shrinkage during drying with SCF CO<sub>2</sub> to the depressurization stage of the drying process, a fact that, based on the above, is rather surprising. Possible causes of shrinkage along depressurization include [19]: (a) Accelerated syneresis due to heating during the conversion of liquid CO<sub>2</sub> to SCF CO<sub>2</sub>. Based on results presented herewith, this route to drying shrinkage is considered unlikely in the model system studied here. (b) Relaxation of the network caused by interfacial stresses when the pore-filling solvent is exchanged with much lower-viscosity liquid CO<sub>2</sub> or SCF CO<sub>2</sub>. Interfacial stresses develop at solid/liquid/liquid interfaces, and are analogous to the surface tension stresses developing at solid/liquid/liquid interfaces. The importance of those interfacial stresses has been rather downplayed based on the timing of the major

shrinkage event, that is during depressurization of the autoclave rather than during replacement of the pore-filling solvent with liquid or SCF CO<sub>2</sub>. Nevertheless, such shrinkage due to interfacial stresses is clearly evident in literature data, and amounts to about 29% of the total shrinkage [12]. (c) Incomplete washing off the pore filling solvent during solvent-exchange with liquid CO<sub>2</sub> that would cause a surface tension-induced shrinkage like that observed during ambient pressure drying; experimental evidence, however, points away from that explanation. Finally, (d) Depressurization shrinkage has been attributed to compression forces created upon desorption of CO<sub>2</sub> from molecular-distance gaps (i.e., in micropores) [22,23,24]. That model fits well with the timing of the depressurization shrinkage. However, data here and elsewhere show that drying shrinkage is not coupled strongly to microporosity. Indeed, several authors have noted that shrinkage causes silica particles to come closer together compared to the wet-gel precursors [25], and have discussed shrinkage in terms of condensation reactions between particles or clusters causing a network rearrangement [26]. Along these lines we have observed that shrinkage and extreme deformation of aerogels monoliths noted during SCF CO<sub>2</sub> drying of polydicyclopentadiene wet-gels can be halted completely if particle aggregates along the skeletal framework are rigidized by filling with polymethylmethacrylate (PMMA) [27].

Based on the above, shrinkage during drying of silica aerogels with SCF CO<sub>2</sub> has a major contributor due to particle merging during depressurization and a lesser one due to interfacial stresses during exchange of the pore-filling solvent with liquid of SCF CO<sub>2</sub>. The goal of this work was to deconvolute those two contributors and transfer the major contributor (depressurization shrinkage) out of the autoclave. The major hypothesis behind our experimental design was that once all pore-filling fluids have been removed, the

driving force that brings nanoparticles together is hydrogen bonding between –OH groups on the surfaces of primary silica nanoparticles, with the underlying assumption being that before all fluids are removed, SCF CO<sub>2</sub> included, those surface –OH groups are not available for H-bonding to one another. Since primary silica particles form secondary particles, for primary particles to be able to come closer together, the space between secondary particles should be able to accommodate primary particles from adjacent aggregates. It follows that if primary particles and assemblies thereof are closed-packed they will not be able to merge and therefore aerogels will not shrink; for the latter to take place assemblies of primary particles must be mass fractals.

Experimental work was carried out with silica wet-gels prepared via a one-step base-catalyzed (NH<sub>4</sub>OH) hydrolysis and polycondensation of tetramethylorthosilicate (TMOS) [12, 19,28]. The gelation process was monitored with liquid <sup>29</sup>Si NMR. Shrinkage studies started after all TMOS had been incorporated in the gels (2h). Most studies focused on 2h- and 24h-aged wet-gels. Based on our main hypothesis, depressurization shrinkage was deconvoluted from the total drying shrinkage, and was transferred to the wet-gel state by exchanging pore-filling gelation solvents with non-H-bonding toluene or xylene. The spatial requirement for rearrangement of skeletal nanostructures was satisfied by the fact that primary skeletal particles do form mass fractal secondary particles with sufficient empty space to accommodate primary particles from neighboring clusters. Merging of particles was supported by small angle X-ray scattering experiments conducted with wet-gels just before drying and aerogels after drying.

## 2. RESULTS

### 2.1. PREPARATION AND PROCESSING OF SILICA WET-GEL AND AEROGELS

Wet-gels were prepared at room temperature from sols consisting of TMOS:H<sub>2</sub>O:CH<sub>3</sub>OH in 1.00:3.19:8.52 mol ratio catalyzed with NH<sub>4</sub>OH in 1:25 mol ratio relative to TMOS. The sol, in 4 mL portions, was poured into cylindrical polypropylene molds, 12.5 mm in diameter.

The gelation process was monitored by following the rheological properties of the sol. The storage ( $G'$ ) and the loss ( $G''$ ) moduli of the sol cross near the gelation point (Figure 2A) [38]. The actual gelation point ( $t_{\text{gel}} = 482$  s) was found at the common inflection point of all  $\tan \delta (= G''/G')$  versus time curves obtained at different oscillation frequencies of the spindle of the rheometer. The common inflection point of all  $\tan \delta$  plots is identified more easily from the plot of the standard deviation of the  $\tan \delta$  from all five frequencies at every point in time, as shown in Figure 2B [39]. The rheological gelation point was near the phenomenological gelation point (the point where the sol stopped flowing: 540 s) consistent with absence of thixotropic phases. At  $t_{\text{gel}}$ , the value of  $\tan \delta$  is related to the gel relaxation exponent “ $n$ ” via Eq 2 [8,40].

$$\tan \delta = \tan (n\pi/2) \quad (2)$$

In turn, considering the excluded volume of the primary particles forming the clusters, “ $n$ ” is related via Eq 3 to the fractal dimension,  $D_f$ , of the clusters forming the gel network (for three-dimensional nonfractal clusters,  $D_f = D = 3$ ) [41]. The  $D_f$  value of those clusters was found equal to 2.15. Rheological data are shown in Table 1.

The chemical composition of the sols during gelation was followed with liquid  $^{29}\text{Si}$  NMR (Figure 3). The resonance at -78.30 ppm vs TMS came from unreacted TMOS.

$$n = \frac{D(D+2-2D_f)}{2(D+2-D_f)} \quad (3)$$

The peak at -76.09 ppm was assigned to partially hydrolyzed  $Q_0$  type of silicon (i.e.,  $(\text{CH}_3\text{O})_{4-x}\text{Si}(\text{OH})_x$ ,  $1 \leq x \leq 4$  [42]). The resonance at -85.78 ppm was assigned to  $Q_1$  type of silicon, as for example in the dimer  $(\text{CH}_3\text{O})_3\text{Si}-\text{O}-\text{Si}(\text{OCH}_3)_2(\text{OH})$  [43]. Unreacted TMOS was still present in the pores of the newly formed gels well beyond the gel point (8-9 min – Table 1). No TMOS, or any other solution species containing silicon was detectable in the pore-filling solvent 2h after mixing the sol. Liquid  $^{29}\text{Si}$  NMR experiments were repeated with several relaxation delays (up to 5 s) to confirm that 2h was a sufficient period for all TMOS to be incorporated in the solid network.

Right after gelation, wet-gels were very delicate, slippery and difficult to handle. Only gels after complete incorporation of TMOS into the solid framework were considered for further study of shrinkage. Wet-gels were removed from their molds at 2h, 4h, 8h, 12h, 16h, 20h and 24h after gelation, their dimensions were recorded, and they were washed with methanol, then with acetone, and finally they were loaded in an autoclave, continuously submerged in acetone as described in the Experimental section. Acetone was first extracted with liquid  $\text{CO}_2$  at 14 °C, and then the autoclave was heated to 40 °C (that is sufficiently above the critical temperature of  $\text{CO}_2$ ). After a 2h stay at that temperature, the autoclave was depressurized slowly over a period of 6 h. As shown in Figure 4A, shrinkage after aging was within error equal for all samples and did not exceed 1%. Similarly, at all stages of solvent exchange, irrespective of aging time, shrinkage never exceeded 2%, with most probable value near zero percent. After drying with  $\text{CO}_2$ , all gels, irrespective of aging

time, shrunk between 7.5% and 9.0% (Figure 4B). No identifiable trends were noted in the shrinkage of the final aerogels as a function of the aging time. Thus, owing to the similar behavior in terms of shrinkage, only the 2h and 24 h samples were chosen for further study.

The 2h- and 24h-aged wet-gels were divided into three parts that were solvent-exchanged with acetone, toluene and xylene, respectively, as described in Scheme 1. Toluene and xylene processed samples were also subjected to 24h-long Soxhlet extractions in order to assess the effect of an elevated temperature environment on shrinkage. The Soxhlet apparatus was modified with a dean stark (see Figure S.1 in Supporting Information) in order to trap water. No water was collected in the dean stark.  $^1\text{H}$  NMR analysis of the solvent used in the Soxhlet apparatus did not show any water above background either. It seems that all gelation water had already been removed during the room-temperature solvent exchanges with toluene and xylene. (More on water in the discussion of the infrared spectra in Section 3.2.1.) Wet-gels in their final solvents (acetone after solvent-exchanges, toluene or xylene after Soxhlet extraction) were loaded to the autoclave. Terminal aerogel samples are referred to by their aging time (i.e., as 2h- or 24h-) and the last solvent they were processed and loaded in the autoclave with.

In terms of shrinkage, samples aged for 2h and 24h showed the same general dimensional changes along processing (Figure 5). Samples aged for 2h swelled slightly in methanol, for a zero overall shrinkage relative to the molds. Subsequently, in acetone those samples swelled back to about the same volume they came out of the molds. Samples aged for 24h did not show those variations in shrinkage and were insensitive to methanol and acetone solvent exchanges. Both 2h- and 24h-aged gels showed a major shrinkage (5-6%) after solvent-exchange with toluene or xylene. The 2h-aged gels showed a 2% difference

in shrinkage after solvent-exchange with toluene (5%) and xylene (7%); that difference persisted through Soxhlet extraction, but became narrower (about 1%) as the samples went through drying with SCF CO<sub>2</sub>.

The 24h-aged gels shrunk by the same amount in toluene and xylene (about 5%). Soxhlet extraction did not add any new amount of shrinkage. Irrespective of the final solvent –acetone, toluene or xylene–, or whether any shrinkage was observed in it –cases of toluene or xylene–, all 24h-aged aerogels showed the same amount of shrinkage 8%–9%. However, Figure 5 shows clearly that toluene and xylene solvent-exchanges brought about 74% of the total shrinkage that was observed after SCF CO<sub>2</sub> drying of acetone-filled wet-gels, with the remainder (26%) observed after the samples came out of the autoclave. The shrinkage ratio observed after toluene and xylene solvent-exchanges matched the depressurization shrinkage ratio noted during drying of similar base-catalyzed silica wet-gels in the literature [12], as discussed in the Introduction.

## **2.2. CHARACTERIZATION OF AEROGELS FROM THE DIFFERENT PROCESSING ROUTES**

All aerogels retained the shape of their molds and were free of cracks. Basic material properties of the 2h- and 24h-aged aerogels are summarized in Table 2. Small variations in bulk densities (all in the range of 0.175–0.194 g cm<sup>-3</sup>) were attributed to the small variations in shrinkage. Skeletal densities were in the range of 1.93–2.03 g cm<sup>-3</sup>, with no identifiable trends in terms of aging time or processing solvent. All porosities were in the 90-91% v/v range.

**2.2.1. Chemical Characterization.** ATR-IR spectra of 24h-aged wet-gels just before they were loaded in the autoclave, and of the corresponding aerogels were obtained.

Typical data are exemplified in Figure 6 with the 24h-toluene samples. (Similar data for the corresponding 24h-acetone and 24h-xylene samples are given in Appendix II of the Supporting Information.) Of course, spectra of wet-gels included absorptions from the solvent, however analysis was straightforward, because there is no essential overlap with the absorptions of interest. The top row of Figure 6 shows the entire range from  $400\text{ cm}^{-1}$  to  $4000\text{ cm}^{-1}$ , while the bottom frames focus on the range between  $2500\text{ cm}^{-1}$  and  $4000\text{ cm}^{-1}$ . The overarching observation is that the 24h-toluene and the 24h-xylene wet-gels did not contain water, while the corresponding aerogels did contain water, which, presumably, was picked up as soon as aerogels were exposed to the open air. Absence of water from 24h-toluene and 24h-xylene wet-gels was further supported by the fact that attempts to cross-link those silica gels with triisocyanates did not yield any higher-density samples; on the contrary, 24h-acetone wet-gels could be cross-linked with polyurea easily [8,9,10].

In both the wet-gels and aerogels the absorption at  $455\text{ cm}^{-1}$  was due to out-of-plane rocking vibrations of the Si–O–Si bonds of silica. The absorption at  $809\text{ cm}^{-1}$  corresponds to symmetric in-plane stretching of the Si–O–Si system, while the peak at  $954\text{ cm}^{-1}$  could be associated with stretching vibrations of  $-\text{Si}-\text{O}^-$  [44,45,46]. The strongest absorption at  $1083\text{ cm}^{-1}$  (with a shoulder at  $1187\text{ cm}^{-1}$ ) was assigned to in-plane antisymmetric stretching of the Si–O–Si system (one Si–O bond gets longer, the other one shorter). The low intensity peak at  $1640\text{ cm}^{-1}$  was present *only* in the aerogel samples and is due to O–H bending from adsorbed water [44].

The absorption profile of the 24h-toluene wet-gels was markedly different from that of the corresponding aerogels in the  $3000\text{--}3800\text{ cm}^{-1}$  range (compare bottom-row spectra in Figure 6).

That range includes the O–H stretching vibrations of different kinds of OH groups from silica, water and all combinations of hydrogen-bonded OH groups. The weak, yet sharper absorption of the wet-gel at  $3599\text{ cm}^{-1}$  was attributed to O-H stretches in terminal silanols with limited H-bonding with their immediate neighbors. The broad shoulder at  $3392\text{ cm}^{-1}$  was assigned to chains of hydrogen-bonded silanols [44]. The broad absorption of the aerogel in the O-H stretch region was deconvoluted and fitted by several Gaussians. The most intense broad Gaussian from  $3000\text{ cm}^{-1}$  to  $3400\text{ cm}^{-1}$  with a maximum at  $3266\text{ cm}^{-1}$  corresponds to O-H stretching on H-bonded water (confirmed by the weak peak at  $1640\text{ cm}^{-1}$ , as discussed above). The second broad peak from  $3250\text{ cm}^{-1}$  to  $3650\text{ cm}^{-1}$  with a maximum at  $3488\text{ cm}^{-1}$  corresponds to overlapping vibration bands of –SiOH groups that are H-bonded among themselves in chains and to physically adsorbed water [44,47]. The third broad band from  $3500\text{ cm}^{-1}$  to  $3750\text{ cm}^{-1}$  with a maximum at  $3645\text{ cm}^{-1}$  corresponds to the OH stretching modes of terminal silanol groups with some isolated pairwise H-bonding to each other. Interestingly, despite adsorbed water, we can still clearly see a sharp absorption at  $3744\text{ cm}^{-1}$  in all three types of aerogels, which is assigned to isolated silanol groups [48]. The presence of that peak implies some condensation of adjacent H-bonded –SiOH groups upon drying. Finally, the weak sharp peaks at  $2958\text{ cm}^{-1}$  and at  $2858\text{ cm}^{-1}$  were attributed to C–H stretches from some residual unhydrolyzed –SiOCH<sub>3</sub> groups.

Direct-polarization solid-state <sup>29</sup>Si NMR spectra of all 2h- and 24h-aged aerogels from acetone-, toluene- and xylene-filled wet-gels are shown in Figure 7. Fitting the spectra to Gaussian profiles revealed a variation of the relative areas under the Q<sub>2</sub>:Q<sub>3</sub>:Q<sub>4</sub> peaks. Data are summarized in Table 3. In 2h-aged aerogels there is a clear increasing trend of Q<sub>2</sub> and Q<sub>3</sub>, and a decrease of Q<sub>4</sub> from acetone to toluene to xylene. In 24h-aged aerogels the

Q<sub>4</sub> silicon was about equal in samples coming from acetone and toluene wet-gels, but it was higher in aerogels from xylene wet-gels, at the expense of Q<sub>2</sub> and Q<sub>3</sub>. In 24h-toluene aerogels the Q<sub>3</sub> peak was higher than in 24h-acetone aerogels, at the expense of Q<sub>2</sub>. It is speculated that the trend of increasing Q<sub>2</sub> and Q<sub>3</sub> in 2h-aged samples as we go from acetone to toluene to xylene is related to a metastable framework whose Ostwald ripening is accelerated as the treatment temperature increased [11,12]. At any rate, that trend in Q<sub>2</sub> and Q<sub>3</sub> parallels the trend noted in shrinkage (Figure 5) and the two phenomena are considered related. On the other hand, 24h-aged samples are more “settled” chemically, yet it is considered possible that the increased intensity of Q<sub>4</sub> in the 24h-xylene samples could be again related to the higher temperature treatment and the slightly higher shrinkage of those samples after drying (Figure 5).

**2.2.2. Structural Characterization.** Microscopically (Figure 8) all aerogels consisted of virtually indistinguishable 3D networks of nm-size particles that aggregated to larger assemblies (see dashed circles, pointed by arrows in Figure 8). Interestingly, the network includes voids that fall under the definition of macropores (>50 nm). The pore structure was probed with N<sub>2</sub>-sorption and Hg-intrusion porosimetry. The solid framework was probed with small angle X-ray scattering.

The N<sub>2</sub>-sorption isotherms of all 2h- and 24h-aged aerogels from all three solvents were classified as Type IV and were practically identical to one another (Figures 9A and 9B). Specifically, all isotherms: (a) lacked a sharp rise at low  $P/P_0$  values that would indicate microporosity; (b) started rising above  $P/P_0 \sim 0.8$ , indicating presence of macroporosity; and, (c) reached about the same, albeit narrow, saturation plateaus, as the partial pressure approached unity ( $P/P_0 \rightarrow 1$ ), and showed hysteresis loops indicating

mesoporosity. Pore size distributions by the BJH equation were narrow with essentially common maxima for all samples (see insets in Figures 9A and 9B). For all samples, the specific pore volume in the range of 1.7-300 nm ( $V_{1.7-300\text{-nm}}$ , Table 2) was less than the total specific pore volume calculated from bulk and skeletal density data (via  $V_{\text{Total}} = (1/\rho_b) - (1/\rho_s)$ ) confirming presence of macroporosity. BET surface areas,  $\rho$ , were in the range of 723 m<sup>2</sup> g<sup>-1</sup> to 875 m<sup>2</sup> g<sup>-1</sup>; the surface area ranges of all samples overlapped except that of 2h-acetone ( $723 \pm 77$  m<sup>2</sup> g<sup>-1</sup>). The latter aerogels had a statistically lower surface area than the rest of the samples. The primary particle radii,  $r$ , were calculated from skeletal density and surface area via  $r = 3/(\rho_s \times \rho)$ , and were found at around 4.0 nm in all samples (see Table 2).

The surface fractal dimensions of the pores formed by primary particles,  $D_{s,N_2}$ , were calculated from the N<sub>2</sub>-sorption data and were given by the slopes of the  $\text{Ln}(V_{\text{adsorbed}})$  versus  $\text{Ln}[\text{Ln}(P_0/P)]$  plots according to Eq 4 [49], where,  $V_{\text{adsorbed}}$  is the volume of N<sub>2</sub> adsorbed at each

$$\text{Ln}(V_{\text{adsorbed}}) = \text{Ln}V_m + (D_{s,N_2} - 3) \left[ \text{Ln} \left\{ \text{Ln} \left( \frac{P_0}{P} \right) \right\} \right] \quad (4)$$

equilibrium pressure  $P$ ,  $V_m$  is the volume of N<sub>2</sub> adsorbed in a monolayer, and  $P_0$  is the saturation pressure (Figure 9C). The values of  $D_{s,N_2}$  of all samples ranged from 2.61 to 2.64 in no particular order (Table 2).

The porous structure at the macroporous level of the silica aerogels of this study was probed further with Hg-intrusion porosimetry. Figure 10A shows the data for the 24h-aged samples. (For similar data from the 2h-aged aerogels see Appendix III in Supporting Information.) The cumulative Hg intruded was about equal in all samples. Pore size

distributions (PSD) are shown in Figure 10B. The maxima of the PSD curves and the average pore diameters are tabulated in Table 4. The latter were all in the range of 1.4  $\mu\text{m}$  to 1.7  $\mu\text{m}$ .

Surface fractal dimensions of the pores in the range shown in Figure 10B were calculated from the Hg-intrusion data via Eq. 5 [50,51]:

$$\text{Ln}\left(-\frac{dV_{\text{cumulative}}}{dR}\right) = \text{Ln}K + (2 - D_{s,\text{Hg}})\text{Ln}R \quad (5)$$

where  $K$  is a constant,  $dV_{\text{cumulative}}/dR$  is the differential intrusion,  $R$  is the pore radius, and  $D_{s,\text{Hg}}$  is the surface fractal dimension. The plots of  $\text{Ln}(-dV_{\text{cumulative}}/dR)$  vs  $\text{Ln} R$  for all samples were linear (see Figure 10C) from about 400 psi to 30,000 psi. The values of  $D_{s,\text{Hg}}$  were calculated from the slopes, and were found in the range of 2.53 to 2.55. (Table 4). The  $D_{s,\text{Hg}}$  and  $D_{s,\text{N}_2}$  values considered together are consistent with a self-similar nanostructure that is extended over length scales covering several orders of magnitude.

The skeletal framework of all aerogels was probed with SAXS. Representative X-ray scattering profiles for the 24-aged aerogels processed in the three solvents of this study are shown in Figure 11. Data were analyzed using the Beaucage unified model [32,33,34]. Scattering profiles would be best fitted in four regions (Figure 11). Results are summarized in Table 5.

The slopes of the high- $Q$  power law region (Region I) were equal to -4.2 indicating primary particles with density-gradient interfaces [8]. The radii of the primary particles,  $R_1$ , were calculated through the radii of gyration ( $R_g$ ) from the curvature of the scattering profiles in Region II. All  $R_1$  values were in the range of 2-3 nm, however, with a clear increase in size from 24h-acetone to 24h-toluene and 24h-xylene samples. Overall, the

primary particle radii from SAXS were somewhat lower than the primary particle radii from gas sorption (3.6-4.2 nm), but accounting for their density gradient regions on their surfaces, the sizes by the two methods can be considered as approximately equal.

The slopes of the second, lower- $Q$  power-law regions (Region III) were lower than 3, showing that primary particles aggregated into mass-fractal secondary particles. The mass-fractal dimensions,  $D_m$ , of the second particles are equal to the slopes of Region III. The radii of the secondary particles,  $R_2$ , were calculated from the second radius of gyration obtained from the second low- $Q$  curvature of the scattering profile (Region IV). The radii of the secondary particles in aerogels processed through the three different routes ranged from 9.1 to 10.6 nm

The  $N_2$ -sorption isotherms of all 2h and 24h samples from all three solvents were classified as Type IV and were very similar, basically identical to one another (Figure 6). All isotherms reached about the same, albeit narrow, saturation plateaus, as the partial pressure approached unity ( $P/P_o \rightarrow 1$ ), and then showed hysteresis loops indicative of mesoporosity. Pore size distributions by the BJH equation were narrow with essentially common maxima for all samples (see insets in Figure 6). Nevertheless, it is also noted that all isotherms started rising above  $P/P_o \sim 0.8$ , indicating presence of macroporosity. Indeed, the specific pore volumes in the range of 1.7-300 nm ( $V_{1.7-300\text{-nm}}$ , Table 3) of all samples was less than the total specific pore volume calculated from bulk and skeletal density data (via  $V_{\text{Total}} = (1/\rho_b) - (1/\rho_s)$ ) confirming presence of macroporosity. BET surface areas were in the range of 723  $\text{m}^2 \text{g}^{-1}$  to 875  $\text{m}^2 \text{g}^{-1}$  and the individual ranges overlapped significantly. The primary particle radii,  $r$ , were calculated from skeletal density and surface area via  $r = 3/(\rho_s \times \sigma)$ , and were found around 4.0 nm in all samples.

The surface fractal dimensions of the pores formed by primary particles,  $D_{s,N_2}$ , were calculated from the  $N_2$ -sorption data and were given by the slopes of the  $\text{Ln}(V_{\text{adsorbed}})$  versus  $\text{Ln}\{\text{Ln}(P_0/P)\}$  plots according to Eq 4<sup>43</sup>

$$\text{Ln}(V_{\text{adsorbed}}) = \text{Ln}V_m + (D_{s,N_2} - 3) \left[ \text{Ln} \left\{ \text{Ln} \left( \frac{P_0}{P} \right) \right\} \right] \quad (4)$$

where,  $V_{\text{adsorbed}}$  is the volume of  $N_2$  adsorbed at each equilibrium pressure  $P$ ,  $V_m$  is the volume of  $N_2$  adsorbed in a monolayer, and  $P_0$  is the saturation pressure (Figure 6C). The  $D_{s,N_2}$  values of all samples ranged from 2.61 to 2.64 in no particular order (Table 3). The porous structure at the macroporous level of all 24h-aged aerogels was probed further with Hg-intrusion porosimetry. The Hg-intrusion isotherms of the samples processed in different solvents are shown in Figure 7. The cumulative Hg intrusion for all samples aged either for 2h or 24h, and in different solvents was about equal. Pore size distributions (see Inset in Figure 7) and average pore diameters were calculated and are tabulated in Table 4. Similarly, pore size distributions were also similar for all samples aerogels with average pore diameter in the range of 1620 nm to 2536 nm.

Fractal dimensions were calculated from the Hg-intrusion data using Eq. 5:<sup>44,45</sup>

$$\text{Ln} \left( \frac{dV_{\text{incremental}}}{dR} \right) = \text{Ln}K + (2 - D_{s,Hg}) \text{Ln}R \quad (5)$$

Where,  $dV_{\text{cumulative}}/dR$  is the differential intrusion,  $R$  is the pore radius, and  $D_{s,Hg}$  is the surface fractal dimension of the pores in the range shown in the inset of Figure 7. The plots of  $\text{Ln}(dV_{\text{cumulative}}/dR)$  vs  $\text{Ln} R$  for all samples were linear from about 400 psi to 30,000 psi. The surface fractal dimensions of the macropores,  $D_{s,Hg}$ , were calculated from the slopes, and were found in the range of 2.68 to 2.72. (Table 4). Considering those  $D_{s,Hg}$  values together with the surface fractal dimension of the pores probed with  $N_2$ -sorption, ( $D_{s,N_2}$  –

Table 3) supports the self-similarity of the silica aerogels of this study in length scales extending over several orders of magnitude.

The skeletal framework of all aerogels was probed with SAXS. Representative X-ray scattering profiles for the 24-aged aerogels processed in the three-solvents of this study is shown in Figure 13. Data were analyzed using the Beaucage unified model<sup>46,47</sup> Scattering profiles would be best-fitted in four regions as shown in Figure 13. Results are summarized in Table 5.

The slopes of the high- $Q$  power law region (Region I) were equal to -4.2 indicating primary particles with density-gradient interfaces.<sup>17</sup> The radii of the primary particles,  $R_1$ , were calculated through the radii of gyration ( $R_g$ ) from the curvature of the scattering profiles in Region II. All  $R_1$  values were in the range of 2-3 nm, however, with a clear increase in size from 24h-acetone to 24h-toluene and xylene samples. Overall, the primary particle radii from SAXS were somewhat lower than the primary particle radii from gas sorption (3.6-4.2 nm), but accounting for their density gradient regions on their surfaces, the sizes by the two methods can be considered as approximately equal.

The slopes of the second, lower- $Q$  power-law regions (Region III) were less than 3, showing that primary particles aggregated into mass-fractal secondary particles. The mass-fractal dimensions,  $D_m$ , of the second particles are equal to the slopes of Region III. The rather higher error in those values, compared to the surface fractal dimensions from  $N_2$ -sorption and Hg-intrusion was attributed to the narrow range of Region III. The radii of the secondary particles,  $R_2$ , were calculated from the second radius of gyration obtained from the second low- $Q$  curvature of the scattering profile (Region IV). The radii of the

secondary particles in aerogels processed through the three different routes ranged from 9.1 to 10.6 nm.

Finally, SAXS data were also analyzed in terms of particle size distribution (see Experimental section). Figure 12 shows and compares the volume distribution of particles vs the particle size of all 24h-aged aerogels and of the corresponding wet-gels, that is, just before they were loaded to the autoclave. The data were deconvoluted into multiple Gaussians thus giving a more detailed view of the particle present in the wet-gels and their aerogels. Table 6 lists the peak maxima of all Gaussians and their weights. In general, the number of Gaussian needed to fit the wet-gels and the corresponding aerogels are not equal; to facilitate inspection, in each wet-gel/aerogel pair, peak maxima of the partner with the lower number of Gaussians have been offset horizontally to match the nearest maximum of the partner with more Gaussians. Thus, either by inspection of Figure 12, or via closer scrutiny of the data in Table 6, we see a tendency toward larger particles as each type of 24h-wet-gels (in acetone, toluene or xylene) were dried to the corresponding aerogels. Reasoning that primary particle sizes would not change in the various solvents, and guided by the primary particle sizes via N<sub>2</sub>-sorption (Table 2) and SAXS (Table 5), we set a cutoff for the primary particle diameters at 7.0 nm (see Table 6) and we attempted a calculation of the average sizes of secondary aggregates for all wet-gels and the corresponding aerogels from the deconvoluted particle size distributions (for particles with diameters >7 nm) using Eq 6, where “i” represents the peak number.

$$Average\_Particle\_Diameter = \frac{\sum_i (Area_i \times Particle\_diameter\_@max)_i}{\sum_i Area_i} \quad (6)$$

It is noted that the average size of particles with diameters above 7.0 nm of aerogels coming from acetone-filled wet gels was 23% higher than the same value in the wet-gels (12.8 nm vs 10.4 nm, respectively). On the contrary, the average size of particles with diameters above 7.0 nm of aerogels coming from toluene- or xylene-filled wet gels was 5.5% and 7.6% apart of the same values in the corresponding wet-gels, respectively. Those trends parallel the drying shrinkage in those solvents, and support associating the depressurization part of the drying shrinkage of gels from acetone with the shrinkage observed in toluene and xylene wet-gels, both being traceable to a structural reorganization at the primary/secondary particle level.

### 3. EXPERIMENTAL

#### 3.1. MATERIALS

All reagents and solvents were used as received, unless noted otherwise. Tetramethylorthosilicate (TMOS), acetone (HPLC, >99.9), anhydrous toluene and *p*-xylene (referred to herewith as xylene) were purchased from Sigma Aldrich. Ammonium hydroxide, ACS reagent, 28-30% w/w solution in water, was purchased from Acros Organics. Anhydrous methanol (>99.8%) was purchased from Alfa Aesar. Syphon grade CO<sub>2</sub> was purchased from Ozark Gas Co.

**3.1.1. Preparation of Silica Aerogels.** Base catalyzed silica gels were prepared by mixing two solutions: one containing TMOS (3.85 mL, 3.973 g, 0.026 mol) in methanol (4.5 mL, 3.564 g, 0.111 mol), and a second solution consisting of distilled water (1.5 mL, 1.5 g, 0.083 mol) and 40  $\mu$ L of NH<sub>4</sub>OH (1.04 mol) in methanol (4.5 mL, 3.564 g 0.111

mol). After mixing, the resulting sol was poured into plastic cylindrical molds (Polypropylene Scintillation Vials, 6.5 mL, Sigma-Aldrich Catalog No. Z376825, inner diameter of 12.25 mm) and kept at room temperature (23 °C) for gelation. After gelation (in about 10 min), gels were aged at room temperature in their molds for various time periods. The aging period was selected as 2h, 4h, 8h, 12h, 16h, 20 h and 24h. At the end of each aging period, gels were removed from the molds and were washed first with methanol (2×, 4h each time, using 4× the volume of the gel for each wash). Wet-gels aged for 4h, 8h, 12h, 16h and 20h were solvent-exchanged with acetone (4×, 8h each time, using 4× the volume of the gel for each wash) and were dried in an autoclave with CO<sub>2</sub> (see Section 2.2 below). Wet-gels aged for 2h and 24h were divided into three groups (Scheme 1): (a) Gels in the first group were solvent-exchanged with acetone (4×, 8h each time, using 4× the volume of the gel for each wash) and then were dried with CO<sub>2</sub> as described in Section 2.2 below; (b) Gels in the second group first were solvent-exchanged with a 1:1 v/v mixture of methanol:toluene (1×, 8h, 4× the volume of each gel) followed by four toluene washes (8h each time, using 4× the volume of the gel for each wash). Subsequently, gels were subjected to Soxhlet extraction with toluene for 24h and finally they were dried from toluene with CO<sub>2</sub> in an autoclave (see Section 2.2); and, (c) Gels in the third group first were solvent-exchanged with a 1:1 v/v mixture of methanol:xylene (1×, 8h, using 4× the volume of the gel) followed by four xylene washes (8h each time, using 4× the volume of the gel for each wash). Subsequently, gels were subjected to Soxhlet extraction with xylene for 24h and finally they were dried from xylene with CO<sub>2</sub> in an autoclave (see Section 2.2). Shrinkage was measured at every stage along each processing route as described in Section 2.2.2 below.

### 3.2. METHODS

Drying of wet-gels was carried out in an autoclave (SPIDRY Jumbo Supercritical Point Dryer, SPI Supplies, Inc. West Chester, PA). Samples were loaded into the autoclave at room temperature and were covered with solvent (acetone, toluene or xylene). The pressure vessel was closed, and liquid CO<sub>2</sub> was allowed in while the temperature of chamber was maintained at 14 °C. Samples were kept under liquid CO<sub>2</sub> for 20 min, then liquid CO<sub>2</sub> was drained out while more liquid CO<sub>2</sub> was allowed in. That cycle was repeated three more times after all solvents had been extracted out of the pores of the samples. The criterion for the latter was that CO<sub>2</sub> released out of the autoclave formed dry ice. Subsequently, the temperature of the autoclave was raised to 40 °C and that condition was maintained for two hours. Finally, supercritical fluid (SCF) CO<sub>2</sub> was vented off like a gas over a period of 6h.

**3.2.1. Chemical Characterization of Wet-gels and Aerogels.** Gelation of TMOS was followed with liquid <sup>29</sup>Si NMR on the 400 MHz Varian Unity Inova NMR instrument. At first, a blank run without sample was performed in order to record and subtract the background due to the borosilicate glass of the NMR tube. Sols were prepared using methanol-d<sub>4</sub> and the field-frequency was locked to the deuterium of CD<sub>3</sub>OD. Broad-band proton decoupling was applied to suppress the possible nuclear Overhauser effects. Chromium acetylacetonate (0.015 M) and tetramethylsilane (TMS) were added to the sol to reduce the spin–lattice relaxation time, and as internal standard, respectively. Spectra were collected in regular intervals during gelation and beyond, using 256 scans and a relaxation delay of 1 s and 5 s. Solid-state <sup>29</sup>Si NMR spectra of all aerogels were obtained on a Bruker Avance III 400 MHz spectrometer with a silicon frequency of 52.624 MHz

using a 7 mm Bruker MAS probe and magic-angle spinning at 5 kHz.  $^{29}\text{Si}$  NMR spectra of all samples were first obtained using cross-polarization (CPMAS pulse sequence) with a contact time of 2000  $\mu\text{s}$ , a relaxation delay of 5 s, and number of scans equal to 16384. For reasons discussed elsewhere [29], CP spectra do not represent the real distribution of the various type of silicon atoms, thus spectra were also recorded with direct polarization (ZG pulse sequence) using a relaxation delay of 10 s and a number of scans equal to 8192. All  $^{29}\text{Si}$  NMR spectra were referenced externally with neat tetramethylsilane (TMS, 0 ppm), and patterns were fitted with Gaussians [30], using the Origin 8.5 software package.

Attenuated total reflectance (ATR) spectroscopy was carried out with a Nicolet-ATR spectrometer model iS50. Samples were powdered and added to the ATR crystal (diamond crystal), and ATR spectra were obtained by pressing them against the crystal with the ATR unit's pressure device. Maximum throughput of the infrared beam to the detector was achieved via optical alignment that was performed with no sample on the crystal. Data were collected at an incident beam angle of  $45^\circ$  over 32 scans with a resolution of  $4\text{ cm}^{-1}$ . In order to evaluate H-bonding, the  $\nu(\text{O-H})$  bands were deconvoluted into Gaussian-shaped peaks using the Origin 8.5 software package.

**3.2.2. Physical Characterization of Wet-gels and Aerogels.** The linear shrinkage of all aerogels as well as of their wet-gel precursors at different processing stages were calculated from the sample diameters. For wet-gels in particular, diameters were measured while samples remained submerged in the corresponding solvents. Bulk densities ( $\rho_b$ ) were calculated from the weight and the physical dimensions of the samples. Skeletal densities ( $\rho_s$ ) were determined with helium pycnometry using a Micromeritics AccuPyc II 1340 instrument.

**3.2.3. Structural Characterization of Wet-gels and Aerogels.** Rheology during gelation of TMOS was conducted using a AR 2000ex Rheometer. A small amount of sol (see Section 2.1.1 above) was placed between an aluminum cone (60 mm diameter, 2° angle) and a Peltier plate with a 500  $\mu$ m gap between the two. A multi-wave oscillation consisting of five superimposed harmonics with frequencies of 1, 2, 4, 8, and 16 rad s<sup>-1</sup> was applied to the sol using a fixed strain amplitude of 5%. The sol was mixed for 30 s and then it was placed on the rheometer. The timer was started from the moment of mixing the two solutions to make the sol. Rheological data were collected for 40 min (phenomenological gelation occurred in 8 min).

BET surface areas, pore size distributions and surface fractal dimensions of all aerogels were determined with N<sub>2</sub>-sorption porosimetry at 77 K using a Micromeritics ASAP 2020 surface area and porosity analyzer. The reported values were averages of three samples from three different batches. Pore size distributions and fractal dimensions for aerogels were also determined with Hg-intrusion porosimetry using a Micromeritics AutoPore IV 9500 instrument.

Scanning electron microscopy (SEM) of all aerogels was conducted with Au/Pd (80/20) coated samples on a Hitachi Model S-4700 field-emission microscope. A double-sided sticky carbon dot was placed on the stub. A single-sided Cu-tape was placed on top of the carbon-dot. The aerogel sample was stuck on the sticky side of the Cu-tape. To minimize charging, thin Cu-strips were also cut and placed on the top of the samples leaving a small opening for observation.

Small-angle X-ray scattering (SAXS) was carried out with a PANalytical X'PertPro Multipurpose Diffractometer (MPD) configured for SAXS, using Cu K $\alpha$  radiation ( $\lambda = 1.54$

Å), a  $1/32^\circ$  SAXS slit together with a  $1/16^\circ$  antiscatter slit on the incident beam side, and a 0.1 mm antiscatter slit and a Ni 0.125 mm automatic beam attenuator on the diffracted beam side. Wet-gels and aerogels were placed in circular holders between thin Mylar sheets, and the scattering intensities were measured with a point detector in the transmission geometry using  $2\theta$  scans ranging from  $-0.1^\circ$  up to  $5^\circ$ . SAXS intensity ( $I$ ) data are reported in arbitrary units as a function of  $Q$ , the momentum transferred during a scattering event ( $Q = 4\pi \times n \times \sin \theta / \lambda$ , where  $n$  is the refractive index of the medium for X-rays and was considered equal to unity in both xerogels and wet-gels. Data analysis was conducted with the Irena SAS tool for modeling and analysis of small-angle scattering within the commercial Igor Pro software package (WaveMetrics, Inc. Lake Oswego, OR) [31]. For this, first the  $I$  vs  $Q$  data from the Mylar sheets was subtracted from the scattering data of the samples as a background correction. Then data were desmeared using 5 iterations. Desmeared data were fitted into different levels, where each level consisted of a power-law and a Guinier knee region using the Beaucage Unified Model [32,33,34]. Particle size distributions were calculated by fitting the desmeared  $I$  vs  $Q$  data using the maximum entropy method as applied through the Irena tool [35,36,37].

#### 4. DISCUSSION

Mass fractal dimensions are a fingerprint property of assemblies of nanoparticles. The  $D_f$  value (rheology) of the assemblies that formed the primary network upon gelation was lower than the  $D_m$  value (SAXS) of the secondary particles in the aerogel network, pointing to post-gelation “ripening” processes during aging and perhaps throughout

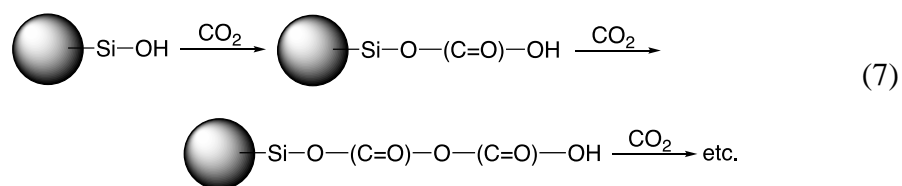
solvent-exchange. Thus, although the goal of this work was to obtain insight into the drying process, it became imperative early on to decide for how long should we let gels to age, or in other words at what stage of aging should we proceed with further processing. Thus, it turned out that although in terms of material properties viable aerogels could be obtained from wet-gels processed immediately after all TMOS had been incorporated in the gels (2h), the resulting materials showed evidence (shrinkage – Figure 5; solid-state NMR – Figure 7) that they had not “settled” yet (in spite of possible continued aging during solvent exchanges). Thus, a 24h-aging period was deemed necessary.

As summarized in Scheme 2, the major finding here was that the same amount of depressurization shrinkage reported in the literature, was transferred into the wet-gel stage by solvent-exchange of gelation solvents with non-hydrogen bonding solvents (toluene and xylene). With no H-bonding solvents in the narrow pores, H-bonding started developing between  $-\text{Si}-\text{OH}$  groups on the surface of adjacent primary nanoparticles pulling them together; that caused merging of secondary particles and moved their average particle size to larger values. That process accounted for the major part of drying shrinkage (~74%).

The remaining shrinkage (~26%) is attributed to interfacial tension forces appearing when the pore-filling solvent is replaced with  $\text{CO}_2$ . The surface tension values of acetone, toluene and *p*-xylene are 25.20, 28.40, 28.31  $\text{mN m}^{-1}$ , respectively, while that of liquid  $\text{CO}_2$  is only 0.96  $\text{mN m}^{-1}$  [52,53,54]. Thereby, replacing any pore-filling solvent of this study with liquid  $\text{CO}_2$  will generate similar capillary pressures, and therefore shrinkage due to interfacial tension should be also similar for all three solvents. Data concerning SCF  $\text{CO}_2$  drying of toluene and xylene-filled wet-gels (Figure 5B) support this

view. It is speculated that interfacial tension shrinkage takes place somewhere above the secondary particle level.

Now, our overall model dictates that depressurization shrinkage is caused by development of hydrogen bonding among surface silanol groups, and therefore it should be unconnected to what prevents H-bonding to occur in the first place. For this H-bonding based model to be internally consistent with the literature [12,19], namely, that silica wet-gels filled with acetone should not undergo all their shrinkage as soon as the pore-filling H-bonding solvent is removed, but instead they should wait until depressurization for the major part of the shrinkage to take place, one must assume that SCF CO<sub>2</sub>, albeit a non-hydrogen bonding solvent, is still able to halt shrinkage. That could be attributed to a reaction of CO<sub>2</sub> with surface silanols (Eq 7) that



continues until pores are filled. In that regard, it is noted that Eq 7 is isoenthalpic ( $\Delta H \sim 0$ ) and nearly energy-neutral ( $\Delta G \sim 0$ ), because pressurized CO<sub>2</sub> in small pores along the skeletal framework has given up its translational degrees of freedom and therefore has already paid the entropic penalty required by Eq 7 [55,56].

## 5. CONCLUSION

Despite elimination of surface tension forces on the skeletal framework of silica wet-gels during drying with SCF CO<sub>2</sub>, shrinkage is still observed. A major part of that shrinkage (~74%) has been transferred to the wet-gel stage by solvent exchange with non-hydrogen bonding solvents (toluene or *p*-xylene), and has been attributed to a merging of secondary particles driven by hydrogen bonding between surface silanol groups. The remaining drying shrinkage (~26%) was attributed to interfacial tension forces when pore-filling solvent is replaced by low-surface tension CO<sub>2</sub>. Being able to move the major part of drying shrinkage of silica aerogels to the wet-gel stage provides opportunities for better control of the shrinking process with important technological implications in applications where no shrinkage can be tolerated (e.g., see Figure 1). In addition, in recent years efforts to improve the economic efficiency of silica aerogels have been focusing on simulations of the SCF CO<sub>2</sub> drying process, with an increasing level of sophistication [57,58,59]. Current models consider and incorporate spillage and suction effects at the surface of wet-gel monoliths in contact with SCF CO<sub>2</sub> [60], however, ultimately those models will have to consider that the drying process is a two-stage moving boundary problem due to capillary and depressurization shrinkage.

## ACKNOWLEDGEMENTS

We thank the NSF under Award No. 1530603 for financial support. We also thank Professor Marc Hodes of Tufts University for fruitful discussions and the Materials

Research Center of the Missouri University of Science and Technology for support with materials characterization.

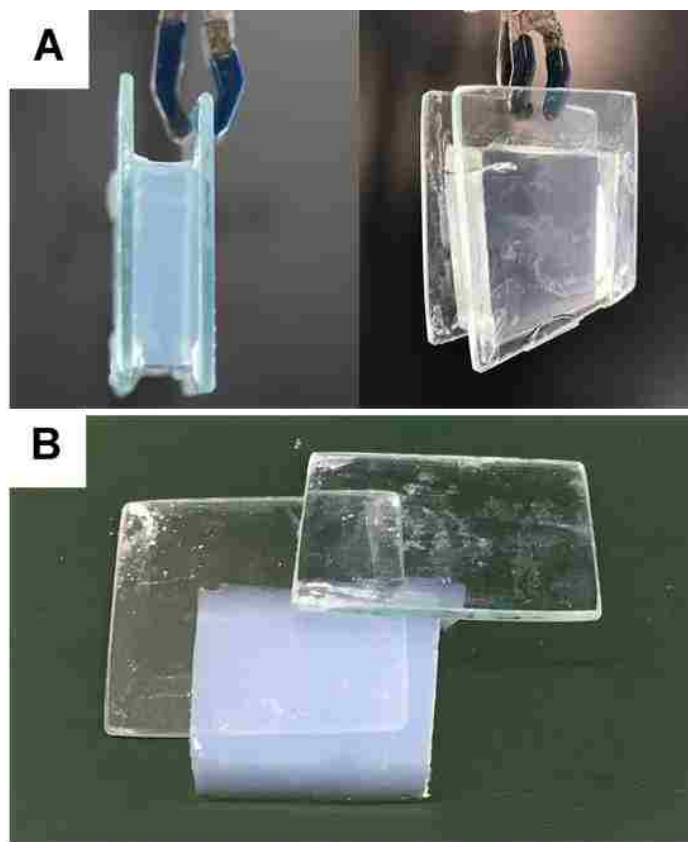


Figure 1. (A) Photograph from two perspectives of an aged and acetone-washed silica wet-gel cast between two glass plates (glass side-spacers had been removed). The surfaces of the glass plates had been modified with thin transparent xerogel films [20]. Note that the wet-gel adheres well to the two glass plates. (B) After drying with SCF CO<sub>2</sub> the aerogel delaminated from both glass facers

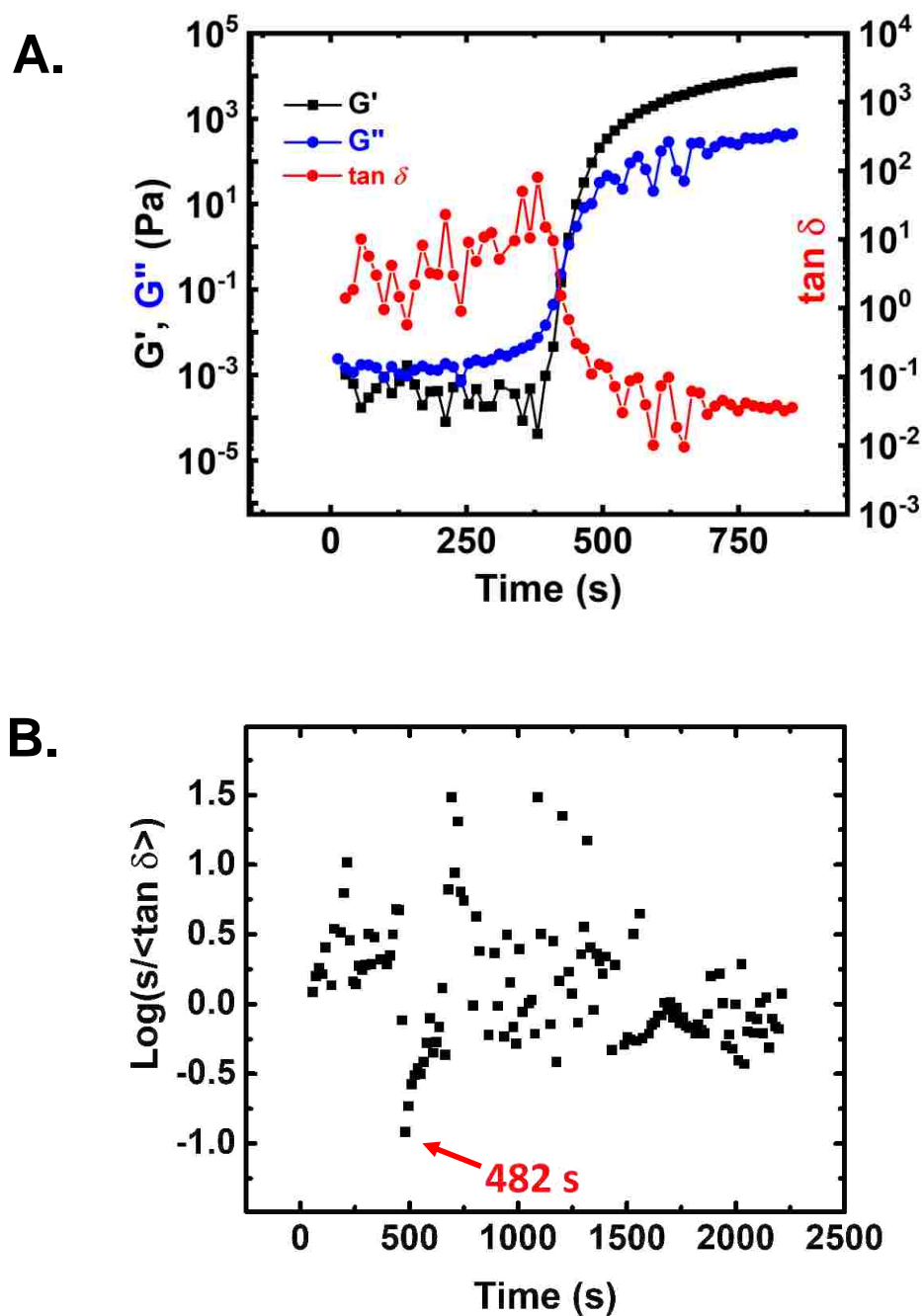


Figure 2. Rheology of a TMOS sol during gelation at 23°C, according to the procedure described in the experimental section. A. Evolution of the storage ( $G'$ ) and loss ( $G''$ ) moduli as well as of  $\tan \delta$  from mixing the sol. Data shown at 1.0  $\text{rad s}^{-1}$  oscillation frequency. (For other parameters, see Experimental Section) B. Statistical variable of  $\tan \delta$  considering all superimposed oscillation frequencies at any point in time, versus time (see text). The gelation point is defined at the minimum

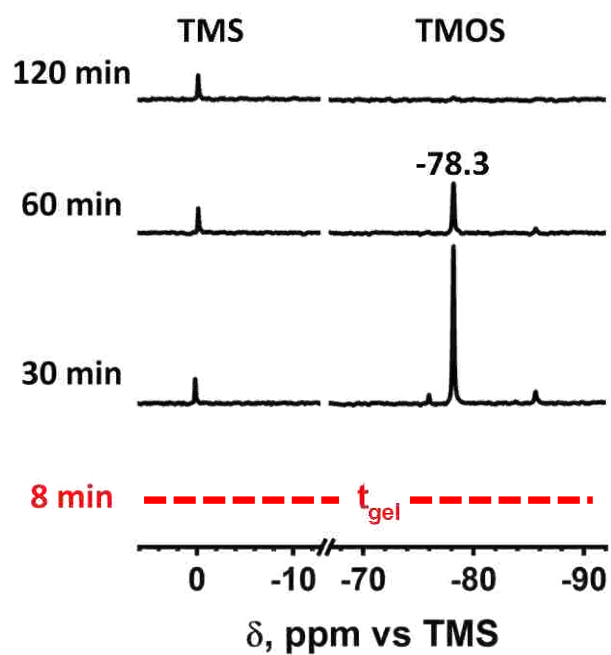


Figure 3. Liquid  $^{29}\text{Si}$  NMR of a TMOS sol up to two hours after mixing the sol. (Sol was prepared in  $\text{CD}_3\text{OD}$  – see experimental section)

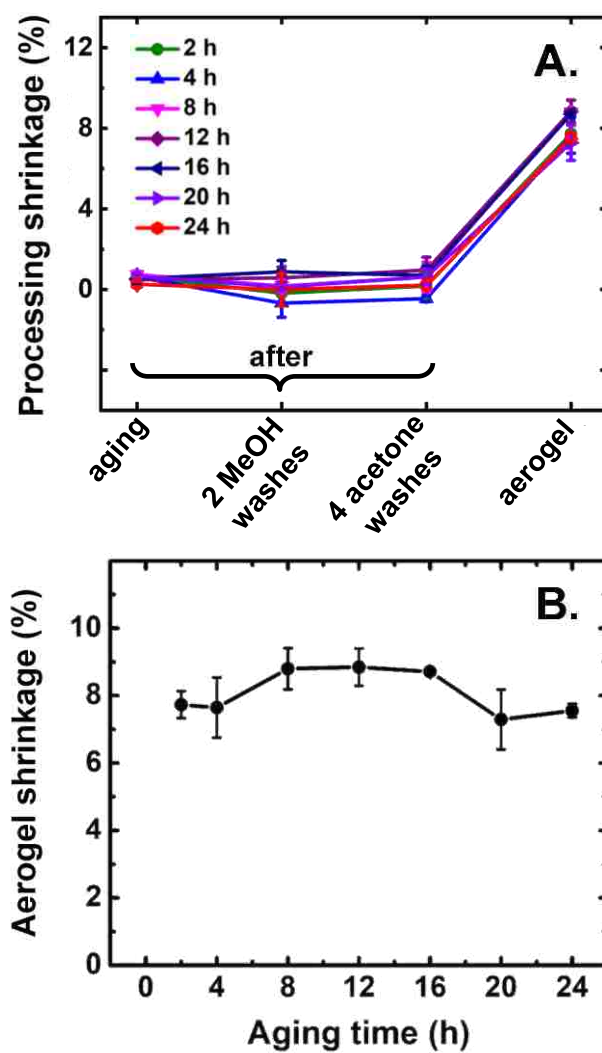


Figure 4. (A) Linear shrinkages of wet-gels and aerogels along processing. (B) Linear shrinkage of aerogels obtained by drying acetone wet-gels aged for different time periods as shown

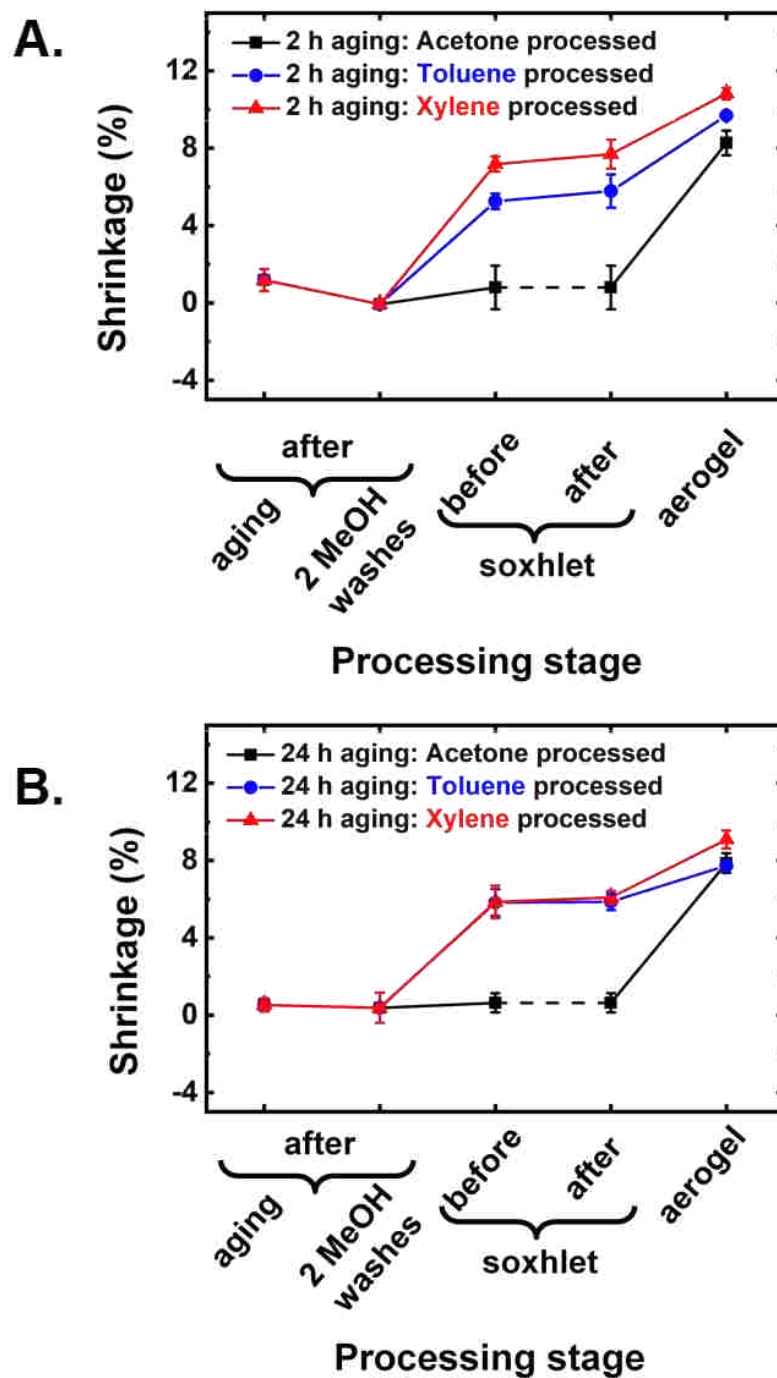


Figure 5. Linear shrinkages of wet-gels and aerogels at different processing stages for (A) 2h-aged, (B) 24h-aged samples. Dashed lines along processing of acetone-filled wet gels indicates that Soxhlet extraction was bypassed

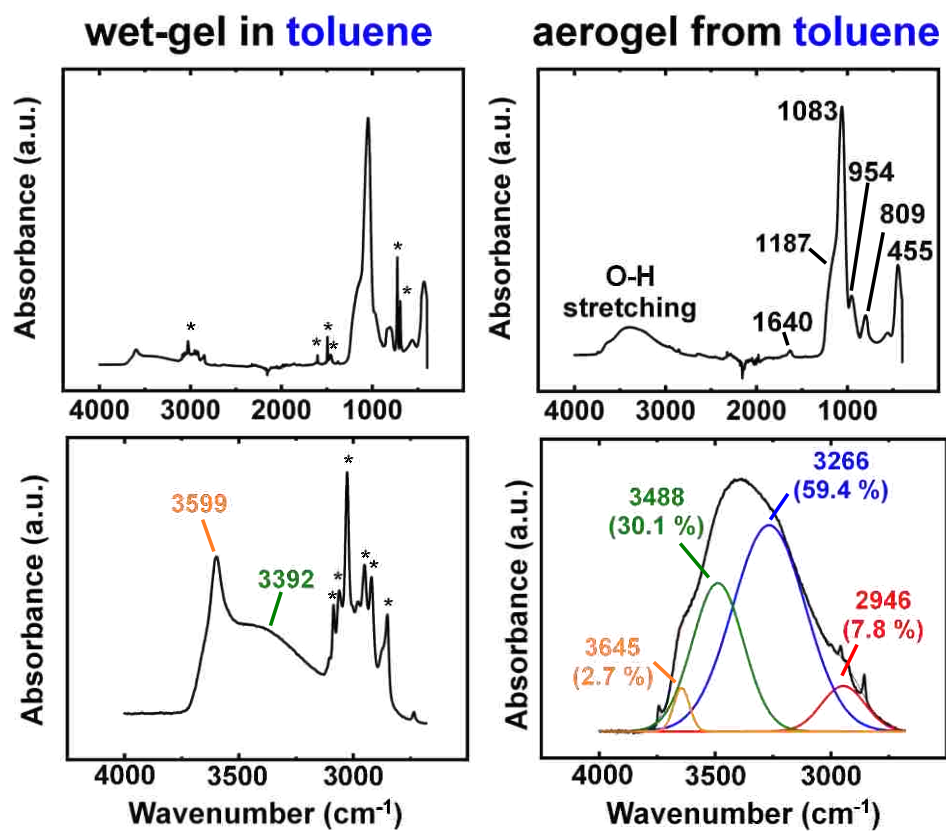


Figure 6. Top: Representative ATR-FTIR spectra of 24h-aged wet-gel and aerogel samples solvent-exchanged with toluene as shown. Bottom: The 2500  $\text{cm}^{-1}$  to 4000  $\text{cm}^{-1}$  region of the spectra shown on top. (Asterisks denote the absorptions of toluene)

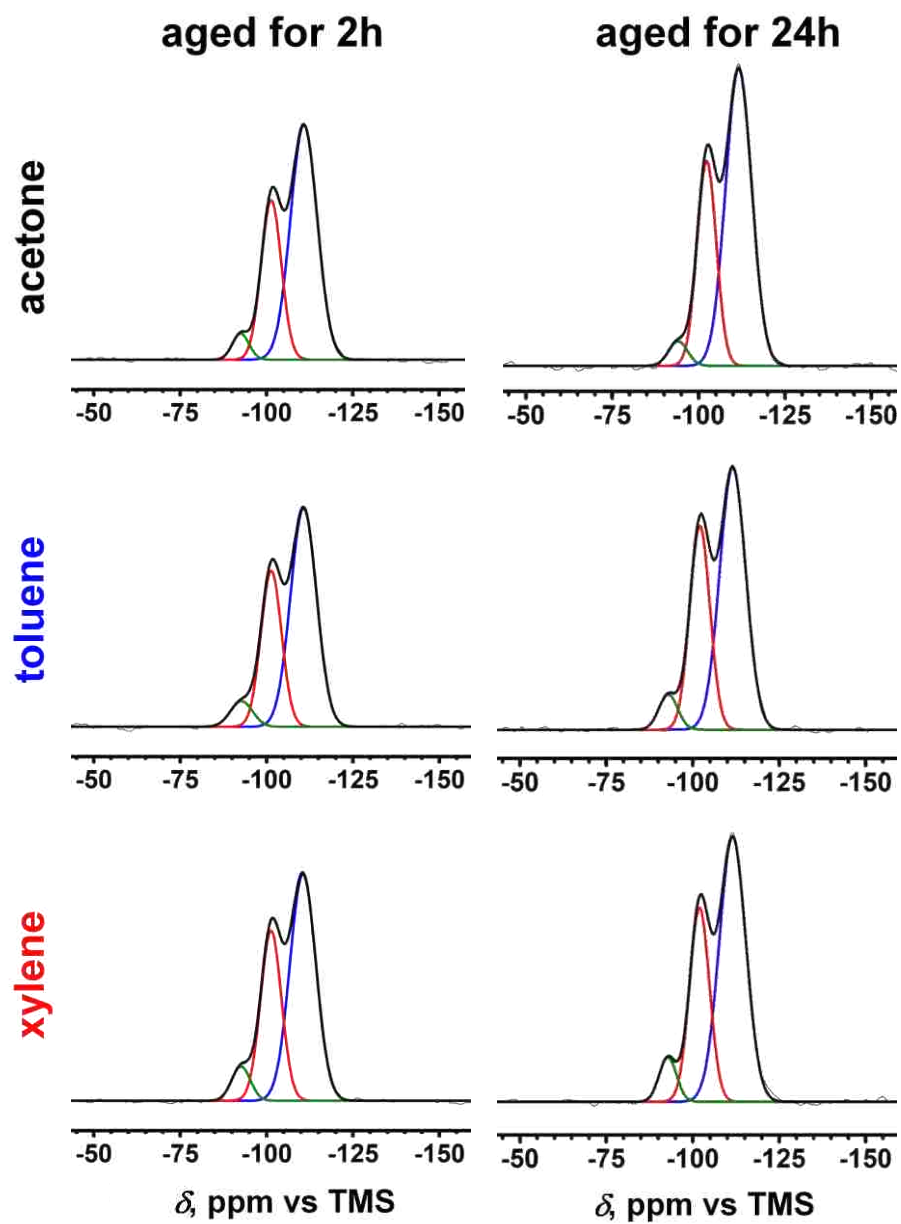


Figure 7. Direct polarization solid-state  $^{29}\text{Si}$  NMR data of aerogels prepared from wet-gels aged for 2h or 24h as shown on top, and solvent-exchanged prior to drying with the solvents shown on the left

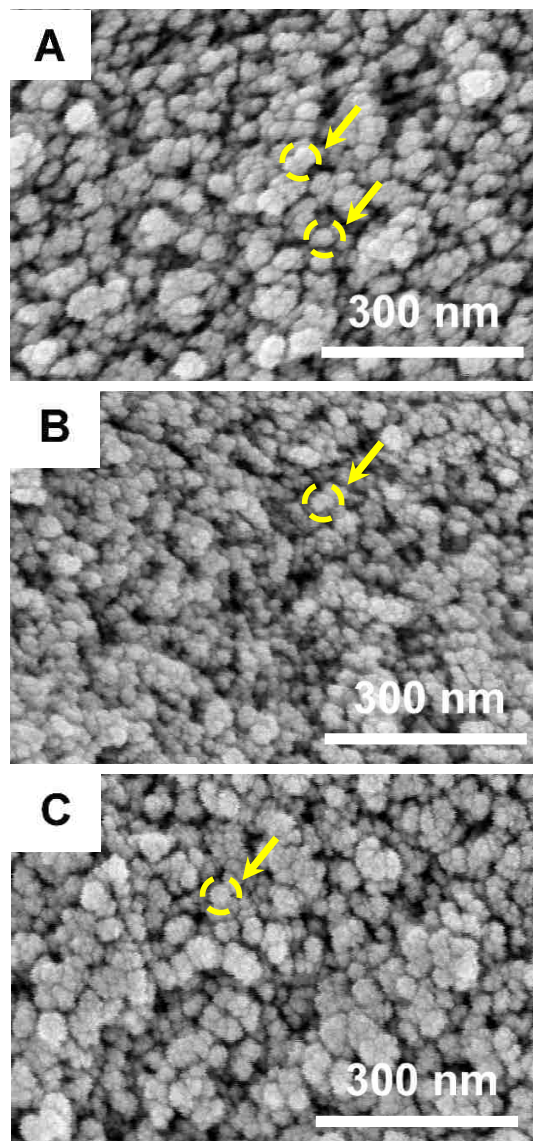


Figure 8. SEM images of 24h-aged aerogel samples processed from (A) acetone, (B) toluene, and (C) xylene. Dashed circles pointed with arrows identify aggregates of smaller particles

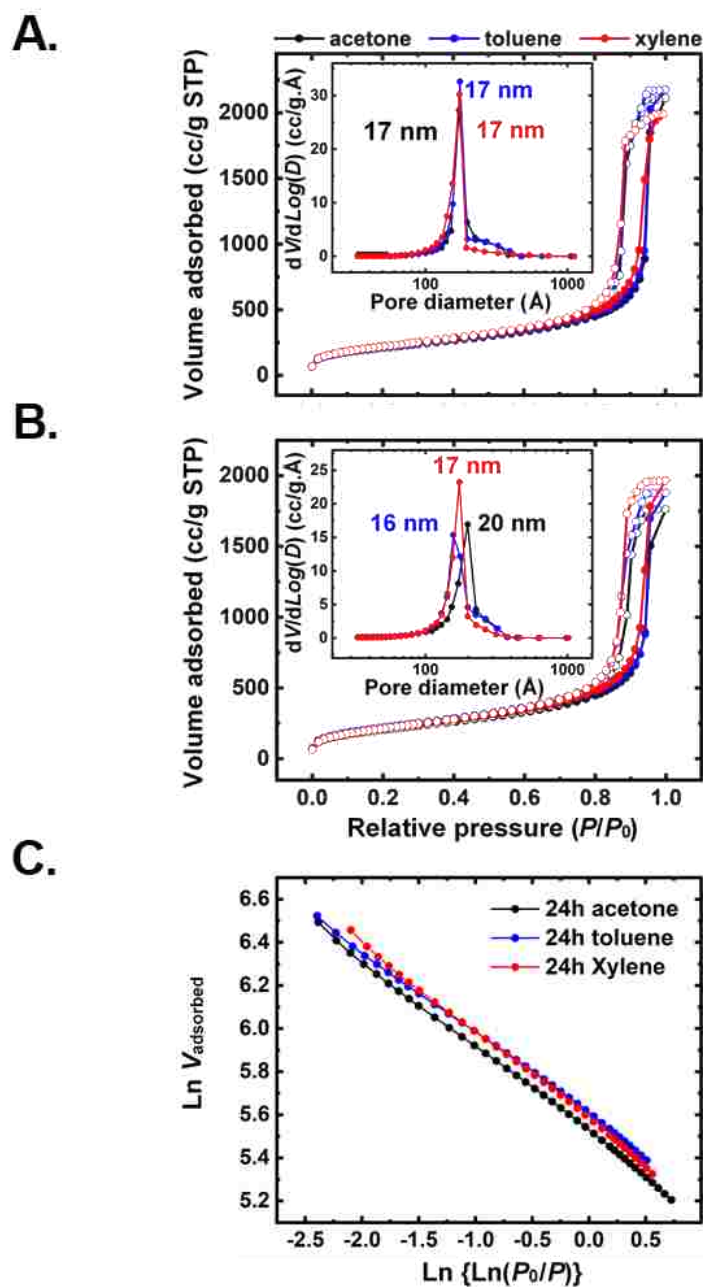


Figure 9.  $\text{N}_2$ -sorption data of aerogel samples solvent-exchanged prior to drying as shown. (A) 2h-aged aerogels. (B) 24h-aged aerogels. Insets: Corresponding pore size distributions by the BJH desorption method. (C) Plots of  $\text{Ln}(V_{\text{adsorbed}})$  vs  $\text{Ln}[\text{Ln}(P_0/P)]$  used for the determination of the surface fractal dimensions of the porous networks probed by  $\text{N}_2$ -sorption. All color-coding according to the legend within frame C

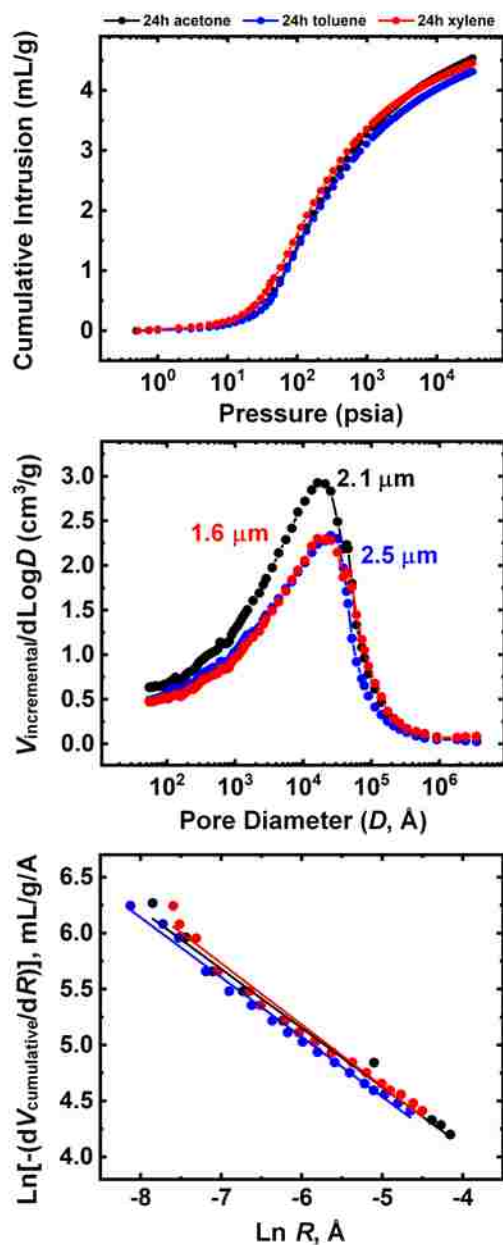


Figure 10. (A) Hg-intrusion porosimetry data of 24h-aged aerogels. (B) Pore size distributions. (C) Plots of  $\text{Ln}[-(dV_{\text{cumulative}}/dR)]$  vs  $\text{Ln } R$  used for the determination of the fractal dimensions of the porous networks probed by Hg-intrusion

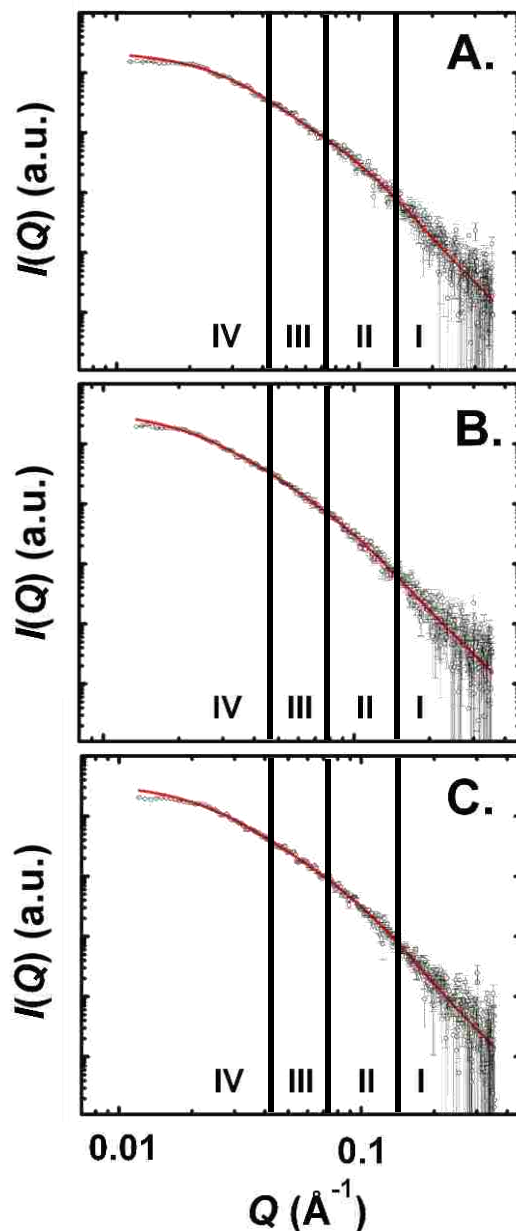


Figure 11. Small angle X-ray scattering (SAXS) data for 24h-aged aerogel samples solvent-exchanged prior to drying in acetone (A), toluene (B), and xylene (C). Primary particle radii were extracted from the first Guinier-knee (Region II); secondary particle radii from the second Guinier-knee (Region IV); Fractal dimensions of secondary particles from power-law Region III. Data are summarized in Table 5

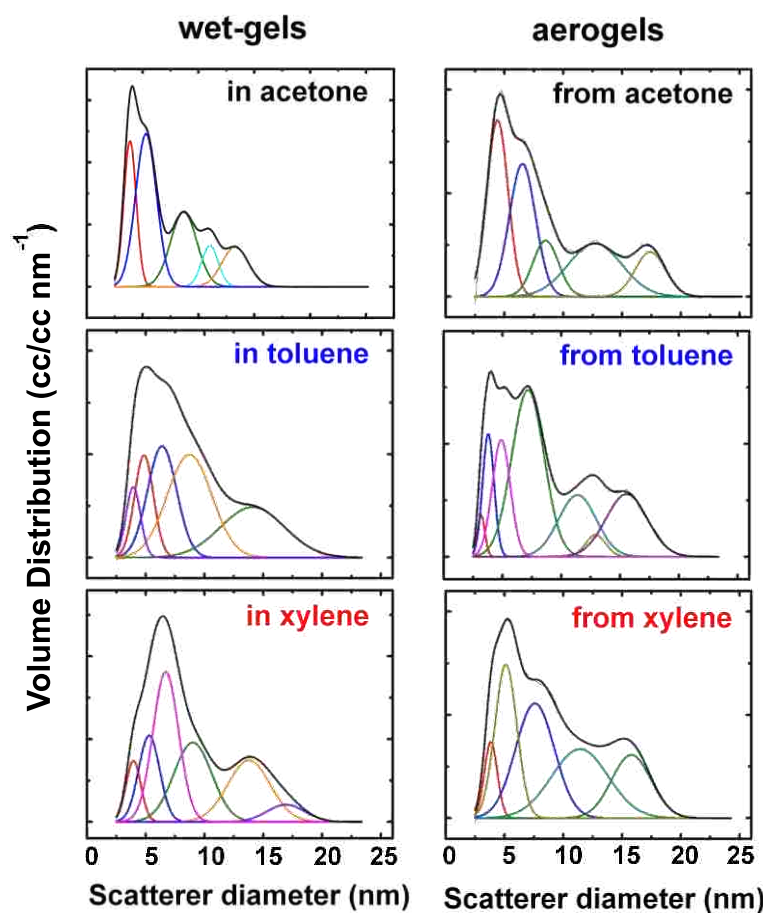
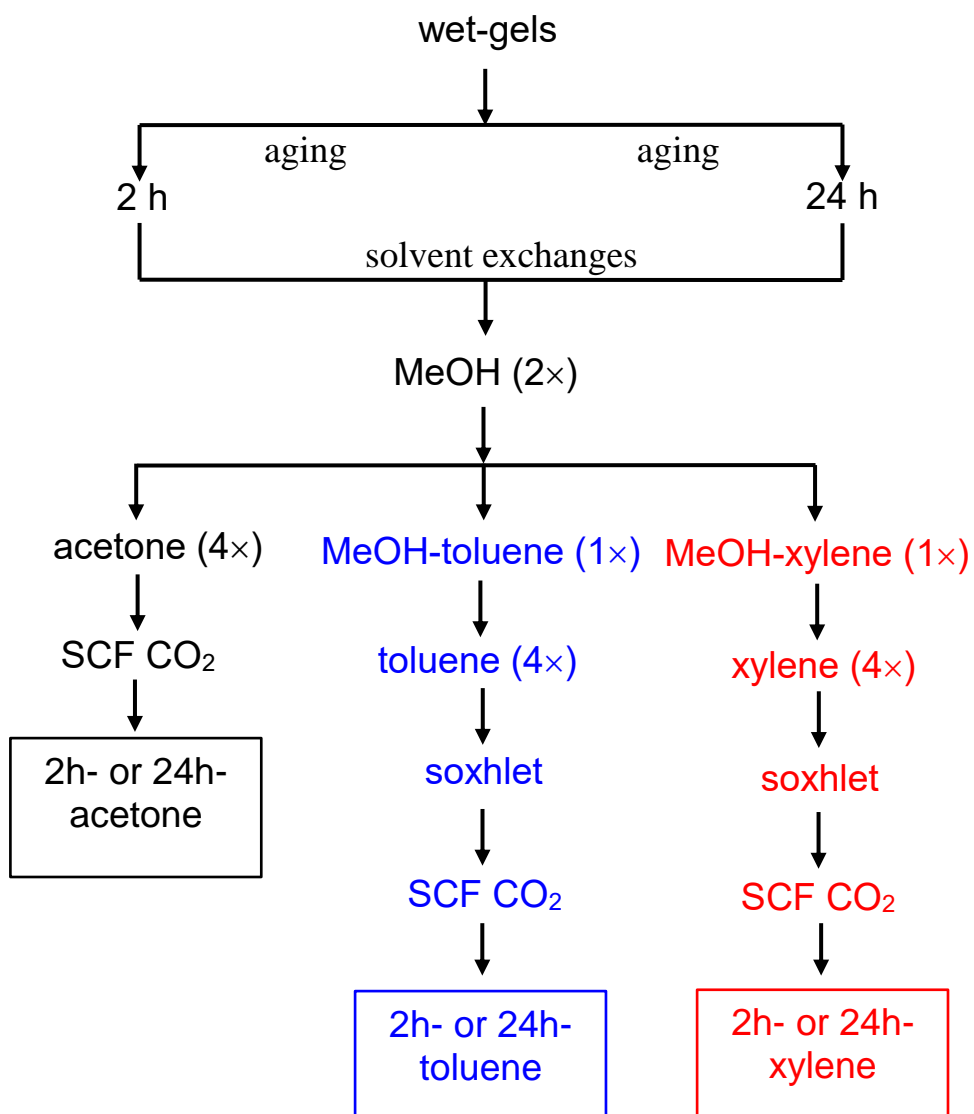
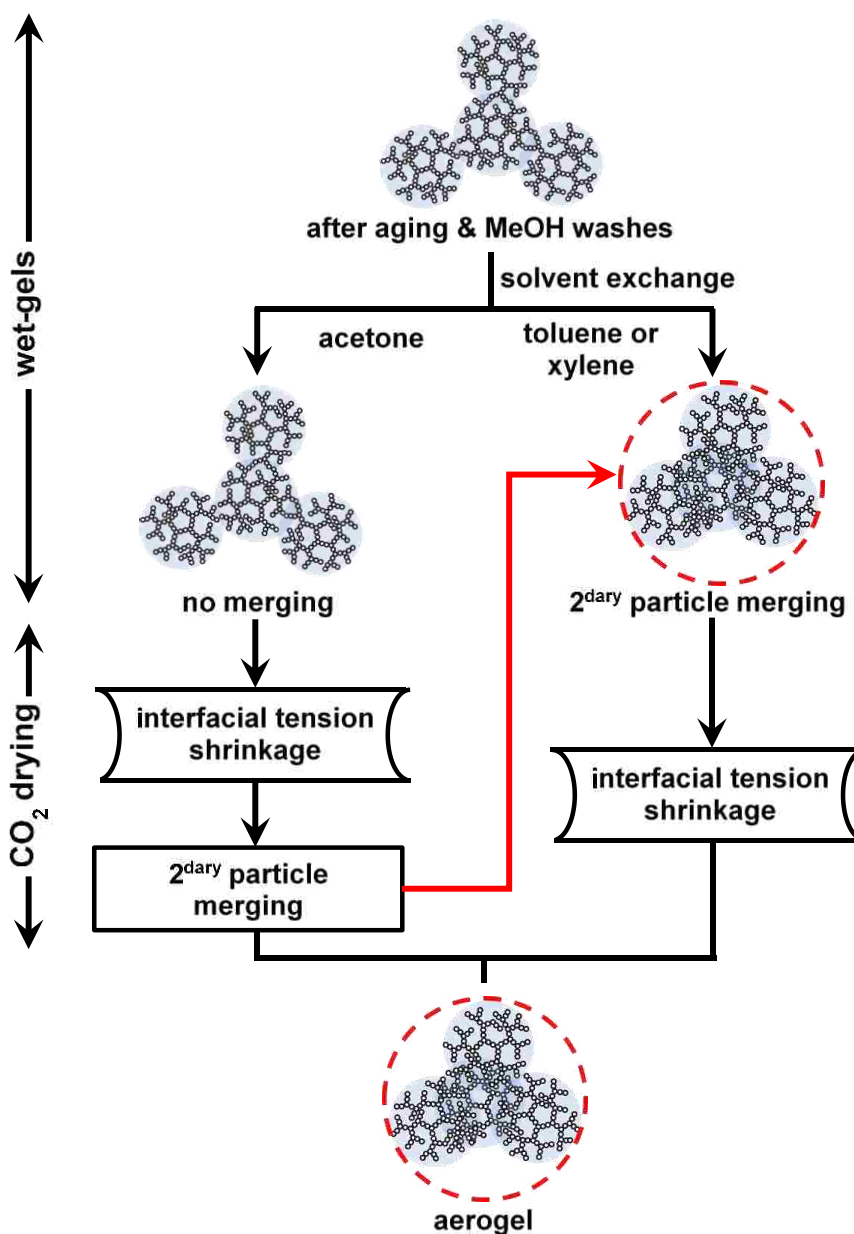


Figure 12. Deconvoluted particle-size distribution curves by fitting into Gaussians the volume distribution functions obtained from SAXS data of 24h-aged wet-gels and of the corresponding aerogels in acetone, toluene, and xylene as shown. Data are summarized in Table 6



Scheme 1. Processing of 2h- and 24h-aged wet-gels in different solvents



Scheme 2. Summary of processes that lead to shrinkage of silica wet-gels

Table 1. Rheology data during base-catalyzed gelation of TMOS sols in methanol

Phenomenological gelation time, $t_p$ (s)	Rheological gelation time, $t_r^a$ (s)	$\tan \delta$ at $t_r$	$n^b$	$Df^c$
540	482	0.36	0.22	2.15

Table 2. General materials characterization data for silica aerogels

sample	shrinkage (%) <sup>a,b</sup>	bulk density ( $\rho_b$ , g cm <sup>-3</sup> ) <sub>b</sub>	skeletal density ( $\rho_s$ , g cm <sup>-3</sup> ) <sub>c</sub>	$\Pi$ (% v/v) <sup>d</sup>	specific pore volume (cm <sup>3</sup> g <sup>-1</sup> )			BET surface area ( $\sigma$ , m <sup>2</sup> g <sup>-1</sup> )	average pore diameter (4V/ $\sigma$ , nm) <sub>h</sub>	particle radius (r, nm) <sup>i</sup>	surface fractal dimension ( $D_{s,N_2}$ ) <sup>j</sup>
					$V_{\text{Total}}$ <sub>e</sub>	$V_{1.7-300 \text{ nm}}$ <sub>f</sub>	$V_{>300 \text{ nm}}$ <sub>g</sub>				
2 h Acetone	7.73 ± 0.40	0.175 ± 0.002	1.961 ± 0.010	91.08 ± 0.70	5.20 ± 0.07	1.34 ± 0.02	3.86 ± 0.07	722.83 ± 77.01	28.80 ± 3.09 [7.88 ± 0.84]	4.23 ± 0.45	2.624 ± 0.013
2 h Toluene	9.69 ± 0.15	0.183 ± 0.001	1.940 ± 0.006	90.57 ± 0.42	4.95 ± 0.03	1.6 ± 0.33	3.34 ± 0.34	860.96 ± 29.74	22.99 ± 0.81 [7.71 ± 0.92]	3.59 ± 0.12	2.629 ± 0.007
2 h Xylene	10.82 ± 0.30	0.182 ± 0.001	1.928 ± 0.027	90.56 ± 1.89	4.98 ± 0.03	2.77 ± 0.02	2.21 ± 0.04	874.99 ± 69.13	22.75 ± 1.80 [12.81 ± 1.01]	3.56 ± 0.29	2.606 ± 0.007
24 h Acetone	7.56 ± 0.20	0.187 ± 0.014	2.025 ± 0.013	90.77 ± 1.11	4.85 ± 0.40	1.61 ± 0.06	3.24 ± 0.41	825.74 ± 86.59	23.51 ± 3.14 [8.19 ± 0.92]	3.59 ± 0.38	2.618 ± 0.014
24 h Toluene	7.73 ± 0.13	0.189 ± 0.002	1.980 ± 0.010	90.45 ± 0.69	4.79 ± 0.06	1.26 ± 0.02	3.52 ± 0.06	828.57 ± 7.37	23.10 ± 0.34 [6.85 ± 0.09]	3.66 ± 0.04	2.635 ± 0.006
24 h Xylene	9.09 ± 0.46	0.194 ± 0.014	1.916 ± 0.039	89.87 ± 2.83	4.63 ± 0.37	1.56 ± 0.14	3.07 ± 0.40	834.22 ± 50.66	22.21 ± 2.24 [7.10 ± 0.44]	3.75 ± 0.24	2.609 ± 0.016

<sup>a</sup> Shrinkage = 100 × (mold diameter – sample diameter)/(mold diameter). <sup>b</sup> Average of 3 samples. <sup>c</sup> Single sample, average of 50 measurements. <sup>d</sup> Percent porosity,  $\Pi = 100 \times (\rho_s - \rho_b)/\rho_s$ . <sup>e</sup> Calculated via  $V_{\text{Total}} = (1/\rho_b) - (1/\rho_s)$ . <sup>f</sup> Cumulative volume of pores between 1.7 and 300 nm from N<sub>2</sub>-sorption data and the BJH desorption method. <sup>g</sup>  $V_{>300 \text{ nm}} = V_{\text{Total}} - V_{1.7-300 \text{ nm}}$ . <sup>h</sup> For the first number, V was taken equal to  $V_{\text{Total}} = (1/\rho_b) - (1/\rho_s)$ ; for the number in [brackets], V was set equal to the total volume probed by N<sub>2</sub>-sorption (=  $V_{1.7-300 \text{ nm}}$ ) up to  $P/P_0 \rightarrow 1.0$ . <sup>i</sup>  $r = 3/(\rho_s \times \sigma)$ . <sup>j</sup> Calculated using Eq 4.

Table 3. Data from deconvolution of direct-polarization solid-state  $^{29}\text{Si}$  NMR spectra of aerogels as shown. chemical shifts are reported vs TMS

sample	Q <sub>2</sub> (ppm)	Area (%)	Q <sub>3</sub> (ppm)	Area (%)	Q <sub>4</sub> (ppm)	Area (%)
2h-acetone	-92.5	4.39	-101.4	32.48	-110.8	63.13
2h-toluene	-92.7	5.96	-101.3	33.93	-110.7	60.11
2h-xylene	-92.6	6.34	-101.3	35.28	-110.5	58.37
24h-acetone	-92.8	6.40	-102.0	33.29	-111.5	60.31
24h-toluene	-92.9	5.68	-102.0	35.40	-111.6	58.92
24h-xylene	-94.0	3.82	-102.3	32.32	-111.6	63.86

Table 4. Data from Hg-intrusion porosimetry

sample	peak max (nm)	average pore diameter (nm)	surface fractal dimension, $D_{s,\text{Hg}}$ <sup>c</sup>
24h-acetone	2083	1284	$2.71 \pm 0.01$
24h-toluene	2536	1190	$2.72 \pm 0.00$
24h-xylene	1620	1536	$2.68 \pm 0.02$

Table 5. SAXS data for 24h-aged silica aerogels, and processed in three different solvents

Sample	Primary particles			Secondary particles		
	high- $Q$ slope <sup>a</sup>	$R_g(1)$ <sup>b</sup> (nm)	$R_1$ <sup>c</sup> (nm)	$D_m$ <sup>d</sup>	$R_g(2)$ <sup>e</sup> (nm)	$R_2$ <sup>f</sup> (nm)
24h-acetone	$-4.20 \pm 0.46$	$1.68 \pm 0.08$	$2.18 \pm 0.10$	$2.19 \pm 0.13$	$8.17 \pm 0.36$	$10.61 \pm 0.35$
24h-toluene	$-4.20 \pm 0.22$	$2.14 \pm 0.21$	$2.78 \pm 0.27$	$2.79 \pm 0.33$	$7.83 \pm 0.19$	$10.17 \pm 0.25$
24h-xylene	$-4.21 \pm 0.19$	$2.15 \pm 0.19$	$2.79 \pm 0.25$	$2.33 \pm 0.49$	$7.04 \pm 0.12$	$9.14 \pm 0.15$

Referring to Figure 13: <sup>a</sup> From power-law Region I. <sup>b</sup> From Guinier Region II. <sup>c</sup> Particle radius  $R_1 = R_g(1)/0.77$ . <sup>d</sup> From power-law Region III. <sup>e</sup> From Guinier Region IV. <sup>f</sup> Particle radius  $R_2 = R_g(2)/0.77$ .

Table 6. Particle size distribution of 24h aged gels from SAXS

Sample		Peak-1	Peak-2	Peak-3	Peak-4	Peak-5	Peak-6	Peak-7	Avg Particle Diameter (nm)
24h acetone	wet-gel	3.88 (15.7 %)	5.29 (31.2 %)	8.71 (26.3 %)	11.04 (5.9 %)	13.25 (15.4 %)	15.78 (2.5 %)	17.50 (3.1 %)	7.17
	aerogel	4.41 (28.6 %)	6.53 (27.3 %)	8.51 (11.3 %)	-	12.70 (22.3 %)	-	17.40 (10.6 %)	8.67
24h toluene	wet-gel	3.94 (7.3 %)	4.86 (13.9 %)	6.40 (23.1)	8.73 (32.8)	-	-	14.09 (23.0 %)	8.54
	aerogel	3.18 (2.1 %)	3.79 (9.6 %)	4.89 (14.6 %)	7.17 (37.0 %)	11.38 (16.0 %)	12.92 (3.0 %)	15.56 (17.8 %)	8.76
24h xylene	wet-gel	3.96 (7.0 %)	5.29 (14.1 %)	6.71 (30.0 %)	9.01 (23.5 %)	13.78 (20.4 %)	16.92 (5.0 %)	-	8.81
	aerogel	3.84 (6.5 %)	5.12 (22.2 %)	7.59 (29.3 %)	-	11.42 (25.7 %)	15.79 (16.4 %)	-	9.13

## SUPPORTING INFORMATION

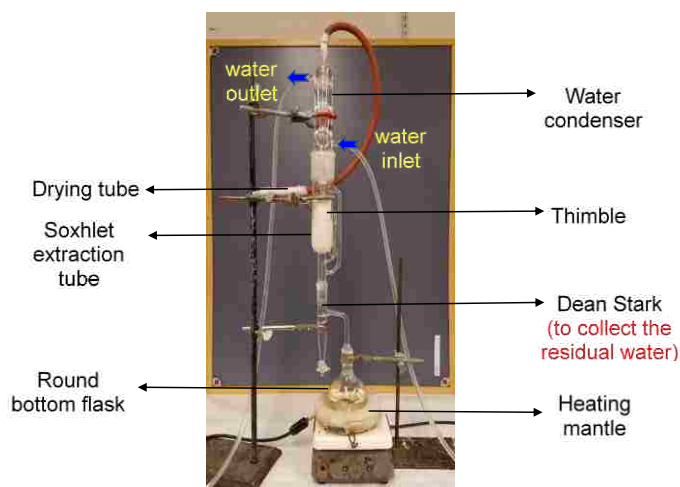


Figure S1. Soxhlet extraction set up for removal of residual water from toluene and xylene processed wet-gels

**REFERENCES**

1. Pierre AC, Pajonk GM (2012) *Chem Rev* 102:4243–4265.
2. Kistler SS (1931) *Nature* 127:741–741.
3. Smith DM, Scherer GW, Anderson JM (1995) *J Non-Cryst Solids* 188:191–206.
4. Kirkbir F, Murata H, Meyers D, Chaudhuri SR (1998) *J Non-Cryst Solids* 225:14–18.
5. Iswar S, Malfait WJ, Balog S, Winnefeld F, Lattuada M, Koebel MM (2017) *Microporous Mesoporous Mater* 241:293–302.
6. Satha H, Atamnia K, Despetis F (2013) *J Biomater Nanobiotechnol* 4:17–21.
7. Hæreid S, Nilsen, E, Ranum V, Einarsrud MA (1997) *J Sol-gel Sci Technol* 8:153–157.
8. Mohite DP, Larimore ZJ, Lu H, Mang JT, Sotiriou-Leventis C, Leventis N (2012) *Chem Mater* 24:3434–3448.
9. Leventis N (2007) *Acc Chem Res* 40:874–884.
10. Leventis N, Sotiriou-Leventis C, Zhang G, Rawashdeh A-MM (2002) *Nano Lett* 2:957–960.
11. He F, Zhao H, Qu X, Zhang C, Qiu W (2009) *J Mater Process Tech* 209:1621–1626.
12. Reichenauer G (2004) *J Non-Cryst Solids* 350:189–195.
13. Mitsiuk BM, Vysotsky ZZ, Polyakov MV (1964) *Dokl Akad Nauk SSSR* 155:1404–1406.
14. Stein DJ, Maskara A, Hæreid S, Anderson J, Smith DM (1994) In: Cheetham AK, Brinker CJ, Mecartney MA, Sanchez C (eds) *Better Ceramics Through Chemistry VI*, Materials Research Society: Pittsburgh, PA, pp 643–648.
15. Rao AV, Bhagat SD, Hirashima H, Pajonk GM (2006) *J Colloid Interf Sci* 300:279–285.
16. Kanamori K, Aizawa M, Nakanishi K, Hanada T (2007) *Adv Mater* 19:1589–1593.
17. Prakash SS, Brinker CJ, Hurd AJ, Rao SM (1995) *Nature* 374:439–443.

18. A more subtle approach to eliminate  $P_c$  would be to use a combination of a skeletal framework, solvent and/or surfactants that would yield  $\alpha=90^\circ$ . To our knowledge that has not been attempted deliberately.
19. Rangarajan B, Lira CT (1992) *Mat Res Soc Symp Proc* 271:559–566.
20. The surfaces of the glass facers had been modified with thin transparent xerogel films by spin-coating a base-catalyzed sol of TMOS similar to the one implemented in this work. See: Bohannan EW, Gao X, Gaston KR, Doss CD, Sotiriou-Leventis C, Leventis N (2002) *J Sol-gel Sci Technol* 23:235–245.
21. Mandal C, Donthula S, Soni R, Bertino M, Sotiriou-Leventis C, Leventis N (2019) *J Sol-gel Sci Technol* 90:127–139.
22. Snook IK, van Megan W (1981) *J Chem Soc Faraday Trans 2* 77:181–190.
23. van Megan W, Snook IK (1979) *J Chem Soc Faraday Trans 2* 75:1095–1102.
24. Ash SG, Everett DH, Radke C (1973) *J Chem Soc Faraday Trans 2* 69:1256–1277.
25. Dahmouche K, Santilli CV, Chaker JA, Pulcinelli SH, Craievich AF (1999) *J Appl Phys* 38:172–175.
26. Kawaguchi T, Hishikura H, Iura J (1988) *J Non-Cryst Solids* 100:220–225.
27. Mohite DP, Mahadik-Khanolkar S, Luo H, Lu H, Sotiriou-Leventis C, Leventis N (2013) *Soft Matter* 9:1531–1539.
28. Leventis N, Elder IA, Rolison DR, Anderson ML, Merzbacher CI (1999) *Chem Mater* 11:2837–2845.
29. Rewatkar PM, Taghvaei T, Saeed AM, Donthula S, Mandal C, Chandrasekaran N, Leventis T, Shruthi TK, Sotiriou-Leventis C, Leventis N (2018) *Chem Mater* 30:1635–1647.
30. See for example: Cabrera Y, Cabrera A, Larsen FH, Felby C (2016) *Holzforschung* 70:709–718.
31. Ilavsky J, Jemian PR (2009) *J Appl Cryst* 42:347–353.
32. Beaucage G (1995) *J Appl Crystallogr* 28:717–728.
33. Beaucage G (1996) *J Appl Crystallogr* 29:134–146.
34. Mang JT, Son SF, Hjelm RP, Peterson PD, Jorgensen BS (2007) *J Mater Res* 22:1907–1920.

35. Agbabiaka A, Wiltfong M, Park C (2013) *J Nanomater* Article ID 640436, <http://dx.doi.org/10.1155/2013/640436>.
36. Potton JA, Daniell GJ, Rainford BD (1998) *J Appl Cryst* 21:891–897.
37. Tatchev D, Kranold R (2004) *J Appl Crystallogr* 37:32–39.
38. Winter HH (1987) *Polym Eng Sci* 27:1698–1702.
39. Kim S-Y, Choi D-G, Yang S-M (2002) *Korean J Chem Eng* 19:190–196.
40. Raghavan SR, Chen LA, McDowell C, Khan SA, Hwang R, White S (1996) *Polymer* 37:5869–5875.
41. Muthukumar M (1989) *Macromolecules* 22:4656–4658.
42. Borba A, Vareda JP, Durães L, Portugal A, Simões PN (2017) *New J Chem* 41:6742–6759.
43. Brinker CJ, Scherer GW (1990) *Sol-gel science: The physics and chemistry of sol-gel processing*, Chap 3. Academic Press Inc, San Diego, CA, pp 97–233.
44. Innocenzi P (2003) *J Non-Cryst Solids* 316: 309–319.
45. Bertoluzza A, Fagnano C, Morelli MA, Gottardi V, Guglielmi M (1982) *J Non-Cryst Solids* 48: 117–128.
46. Almeida RM, Pantano CG (1990) *J Appl Phys* 68: 4225–4232.
47. Chen J, Li T, Li X, Chou K, Hou X (2017) *High Temp Mater Proc* 36: 607–613.
48. McDonald RS (1958) *J Am Chem Soc* 62:1168–1178.
49. Wu MK (1996) *Aerosol Sci Technol* 25:392–398.
50. Pfeifer P, Avnir D (1983) *J Chem Phys* 79:3558–3565.
51. Celis R, Cornejo J, Hermosin MC (1996) *Clay Miner* 31:355–363.
52. <https://www.dataphysics-instruments.com/Downloads/Surface-Tensions-Energies.pdf> Accessed 16 May 2019.
53. [http://www.ddbst.com/en/EED/PCP/SFT\\_C176.php](http://www.ddbst.com/en/EED/PCP/SFT_C176.php) Accessed 16 May 2019.
54. [http://www.ddbst.com/en/EED/PCP/SFT\\_C1050.php](http://www.ddbst.com/en/EED/PCP/SFT_C1050.php) Accessed 16 May 2019.
55. Majedi Far H, Rewatkar PM, Donthula S, Taghvaei T, Saeed AM, Sotiriou-Leventis C, Leventis N (2019) *Macromol Chem Phys* 220:1800333.

56. Saeed AM, Rewatkar PM, Majedi Far H, Taghvaei T, Donthula S, Mandal C, Sotiriou-Leventis C, Leventis N (2017) ACS Appl Mater Interfaces 9:13520–13536.
57. García-González CA, Camino-Reva MC, Alnaief M, Zetzl C, Smirnova I (2012) J Supercritical Fluids 66: 297–306.
58. Ozbakr Y, Erkey C (2015) J Supercritical Fluids 98:153–166.
59. Lebedev AE, Katalevich AM, Menshutina NV (2015) J Supercritical Fluids 105: 122–132.
60. Karamanis G, Dinh H, Waisbord N, Hodes M (2018) Proceedings of the 16th International Heat Transfer Conference, IHTC16-24239.

#### IV. NANOMORPHOLOGY DEPENDENT MECHANICAL PROPERTIES: A CASE STUDY BASED ON POLYURETHANE AEROGELS

Chandana Mandal<sup>1</sup>, Hojat Majedi Far, Suraj Donthula<sup>1</sup>, A B M Shaheen Ud Doulah, Chariklia Sotiriou-Leventis<sup>1</sup>, Nicholas Leventis<sup>\*,1</sup>

<sup>1</sup>Department of Chemistry, Missouri University of Science and Technology, Rolla, MO 65409, U.S.A.

Intended to submit in *ACS Nano*

#### ABSTRACT

This paper is a spin-off of our work on shape-memory polyurethane aerogels prepared from an aliphatic triisocyanate and several short diol derivatives of ethylene glycol.<sup>1</sup> First, we report that metal chlorides from Fe to Zn catalyze formation of polyurethane from 1,3,5-tris(6-isocyanatohexyl)-1,3,5-triazinane-2,4,6-trione (Desmodur N3300A from Covestro LLC) and triethylene diol at 20% w/w monomer concentration in acetonitrile. The gelation rate was followed with rheometry, and first increased from Fe to Cu, and then declined from Cu to Zn. The gelation rate was also higher with higher oxidation states (e.g., Fe<sup>3+</sup> vs Fe<sup>2+</sup> or Cu<sup>2+</sup> vs Cu<sup>+</sup>). For equal catalyst concentrations, the fastest gelation (13 min) was observed with Cu<sup>2+</sup>, and the slowest one with Fe<sup>2+</sup> (about 5.75 h). For comparison, using an equal concentration of DBTDL (dibutyltindilaurate: a well-known polyurethane catalyst), gelation was observed in 1 h 24 min. Subsequently, we studied the morphology of polyurethane aerogels obtained with different concentrations of CuCl<sub>2</sub> relative to DBTDL (4×, 1×, 1/8×, 1/10×, 1/16×, and 1/20×), and we compared their mechanical properties. The gelation time varied from 4 min (4×) to 3 h (1/20×).

Concentrations of  $\text{CuCl}_2$  less than  $1/20\times$  did not induce gelation. As the  $\text{CuCl}_2$  concentration decreased (and the gelation time increased), the morphology of the samples changed from bicontinuous networks to ever-larger fused microspheres. With the lowest catalyst concentration of this study ( $1/20\times$ ), the nanostructure consisted of interconnected particles with diameters in the range of  $40\ \mu\text{m}$ . The glass transition temperature of all samples was  $T_g = 33 \pm 1\ ^\circ\text{C}$ . The elastic modulus above glass transition ( $T_g + 10\ ^\circ\text{C}$ ) depended strongly on the nanomorphology, ranging from  $0.272\ \text{MPa}$  for bicontinuous samples ( $[\text{CuCl}_2]$  at  $4\times$ ) to  $0.033\ \text{MPa}$  for spheroidal samples ( $[\text{CuCl}_2]$  at  $4\times$ , and at  $1/16\times$  the standard concentration of DBTDL, respectively).

## 1. INTRODUCTION

Aerogels are lightweight bulk nanoporous materials made of hierarchical 3D assemblies of nanoparticles.<sup>1</sup> Shape memory materials (SMM) remember and revert back to their original shape. The two main classes of SMMs are shape memory alloys (SMAs) and shape memory polymers (SMPs). The only shape memory aerogels that were reported recently in literature were of thiol-ene based and polyurethane based (SMPU). SMPU are generally catalyzed by tin based DBTDL. But, lately, many researchers tried to replace the DBTDL catalyst with other possible catalysts. Metal ion catalysis of isocyanate-butanol reaction was studied back in 1965 by Robins, Janis.<sup>2</sup> The catalysts were divided in to two categories based on whether their effect changes based on the steric factors of the isocyanate or not. It was proposed that the metal ions help in increasing the electrophilic character of the isocyanate by coordinating to oxygen or nitrogen and in turn bring the

isocyanate and alcohol together. Activating groups on alcohols help in increasing the nucleophilicity and therefore, react with isocyanates to form urethanes.

A vast area of literature shows the use of organotin catalysts for the polymerization of isocyanate-alcohol reaction. Among organotin catalysts, diorganotin (IV) ester compounds (DBTDL and dibutyltin bis(2-ethylhexanoate)) showed high catalytic activity for the urethane formation. Those tin catalysts are sensitive to moisture where they hydrolyze and in turn reducing the catalytic activity.<sup>3</sup> The other disadvantage of using tin catalysts is because of their toxicity. Other toxic compounds that also catalyze the formation of urethane are organo-mercuric compounds such as mercuric octoate and phenyl mercuric acetate<sup>4</sup> The toxic exposure of these compounds to workers in production and to consumers directed to the use of alternative catalysts such as mixtures of bismuth and zinc carboxylates in urethane elastomers production.<sup>5</sup> Several other attempts were also made to replace tin with environment friendly organometallic catalysts consisting of bismuth, zirconium, and aluminum.<sup>6</sup> Recently, Cramail et al. reported the synthesis of polyurethane from polyols and IPDI catalyzed by penta-alkylated guanidine that led to high molecular weight and dispersity as that observed with tin catalysis.<sup>7</sup> Other non-tin based catalysts included acetyl acetonate salts of  $\text{Cr}^{+3}$ ,  $\text{Fe}^{+3}$ ,  $\text{Cu}^{+2}$ ,  $\text{Sn}^{+2}$ ,  $\text{Mn}^{+2}$ ,  $\text{Zr}^{+4}$ ,  $\text{Hf}^{+4}$ ,  $\text{In}^{+3}$ , and  $\text{Zn}^{+2}$  that were reported to catalyze the urethane formation.<sup>8</sup>

Other famous catalysts for the polyurethane formation are amine catalysts. They are generally efficient in catalyzing isocyanate-water reaction to form polyureas. Tertiary amines are considered most common organic base catalysts in the synthesis of polyurethanes. One among that class is 1,4-diazobicyclo[2,2,2]octane (DABCO). The disadvantage of using those tertiary amines is their high volatility, fish-like odor and those

environmental issues to decrease emissions from high volatile organic compounds led to the development of other catalysts. Two mechanisms were proposed for the synthesis of polyurethanes catalyzed by amines. Baker suggested a complex formation between the catalyst and isocyanate that is followed by the attack of nucleophile (alcohol). The other mechanism was suggested by Farka through protonation of the catalyst by the alcohol to form a complex that in turn reacts with isocyanate to form the urethane linkage.<sup>9</sup>

Lima, V. D. et. al. reported the comparative kinetic study of polyurethane synthesis using FTIR data between alternative catalytic systems, metal- $\beta$ -diketone complexes (iron, copper, chromium, and tin) and commercially used DBTDL. The monomers used were isophorone diisocyanate (IPDI) and polyols (polypropyleneglycol/diethyleneglycol/1,6-hexanediol polyadipate). They observed that, DBTDL was effective in reactions with polyethers while metal- $\beta$ -diketone complexes were effective in reactions with polyesters.<sup>10</sup>

Later, Sardon et al. demonstrated the use of organic acid catalysts for the synthesis of polyurethanes.<sup>11</sup> Sulfonic acids were found to be the most efficient catalysts that was proposed to be through a dual activation (hydrogen-bonding) mechanism. That involved electrophilic activation of the isocyanate through isocyanate nitrogen and nucleophilic activation of the alcohol.

Knowing the importance of organocatalysis in the polymer synthesis, Sardon et al. published a review on the perspective of synthesis of isocyanate-based polyurethanes using organocatalysis.<sup>12</sup> That article also describes the synthesis of sustainable polyurethanes using greener approaches such as: (a) isocyanate free routes; (b) replacing petroleum-based reagents with bio based reagents; and (c) organic solvent based PU to water based PU's.

In this paper, polyurethanes were synthesized using different metal salts as catalysts and the effect of catalyst concentration on the morphology and mechanical properties of the resulting aerogels was studied. The kinetics of the reaction that is the gelation time using metal salts was compared with the standard DBTDL catalyst. Furthermore, the different morphologies at different catalyst concentrations were reported.

## **2. RESULTS AND DISCUSSION**

### **2.1. SYNTHESIS**

Polyurethane aerogels were synthesized using different metal ion salts. The catalyst stock solution and TEG were mixed in acetonitrile and the triisocyanate solution in acetonitrile was added to the mixture of TEG and catalyst as shown in Scheme 1. Adding the catalyst to the TEG first increased the solubility of the catalyst. The gelation time was noted from the time of addition of the triisocyanate. The metal ion salts highlighted in blue showed the catalytic activity. While the metal salts highlighted in red were soluble in acetonitrile but didn't induce gelation. The green highlights on the metal salts corresponded to those that are insoluble in acetonitrile and therefore can't be tested as catalysts. The catalytic activity was studied based on gelation time. The yellow highlight corresponded to the metal from DBTDL. The sols prepared from triisocyanate, alcohol and different catalysts were added in molds and parafilmmed. The wet-gels were aged for 24 h and then solvent exchanged for 4x using acetone. Those solvent filled wet-gels were then dried from supercritical CO<sub>2</sub> by exchanging the pore filled solvent with liquid CO<sub>2</sub> and then later vented off as a gas at high temperature to result in final aerogels.

## 2.2. CHARACTERIZATION OF PU WET-GEL

The gelation time of all the PU sol was monitored by two ways, one by noting the phenomenological gelation time and another was by rheometry. In order to calculate the rheological gelation time, the storage modulus ( $G'$ ) and loss modulus ( $G''$ ) was measured as a function of time as shown in Figure 1A. That time was monitored after the triisocyanate was added to the mixture of TEG and catalyst to form a sol. Around the gelation point, those two curves cross as the storage modulus of the newly formed sturdy gel prevail over the loss modulus.  $\tan \delta (=G''/G')$  was plotted versus time at a given frequency and the inflection point in the  $\tan \delta$  curve defines the actual gelation point (Figure 1A). On the other hand, that gelation point can be identified as the crossing point of all  $\tan \delta$  curves at different frequencies. More precisely, that point is also obtained at the minimum of the statistical variable  $\log (s/(\tan \delta))$  versus time plot. (see in Figure 1B;  $s$  is the standard deviation of the five  $\tan \delta$  obtained at different times during gelation, at five different oscillatory frequencies of the cone, operated in the multiwave mode). Results of one of the PU wet-gel are summarized in Table 1. Rheological gelation time for all the PU gels are shown in the supporting information (S1).

At the gelation point, the  $\tan \delta$  value was related to the gel relaxation exponent “ $n$ ” via eq 1.

$$\tan \delta = \tan(n\pi/2) \quad (1)$$

In turn, considering the excluded volume of the primary particles forming the clusters, “ $n$ ” was related via eq 2 to the fractal dimension,  $D_f$ , of the clusters existing at the gel point (for three-dimensional nonfractal clusters,  $D = 3$ ).

The rheological and phenomenological gelation time for all samples were close demonstrating the absence of thixotropic phases.

$$n = \frac{D(D + 2 - 2D_f)}{2(D + 2 - D_f)} \quad (2)$$

The catalytic activity was compared for different catalysts at fixed catalyst concentration that was w.r.t.  $1 \times$  DBTDL (Figure 2). The catalytic activity first increased from Fe to Cu, and then declined from Cu to Zn. On moving to the p-block, Ga didn't form any gel at the given concentration however higher concentration of Ga induced gelation indicating that it is less active catalyst compared to Fe. However, going down the group from Ga to In, the catalytic activity increased, and it further increased on moving to Bi. The increase in that catalytic activity might be due to the increase in the complex formation ability of the metal ions. Moreover, increasing the charge in the metal ion, decreases the gelation time. It was observed that  $\text{Cu}^{2+}$  showed faster gelation compared to  $\text{Cu}^+$ . That increase is due to the increase in the electropositive character of the metal ion. As the positive charge density on the metal ion increases, it can act as better electrophile thereby more prone to accept the electron pairs from the alcohol or the isocyanate. Among all those catalysts, the fastest gelation (6 min) was observed with  $\text{Cu}^{2+}$ , and the slowest one with  $\text{Fe}^{3+}$  (about 3 h) at the given concentration. For comparison, using an equal concentration of DBTDL, gelation was observed in 31 min. Five different catalyst concentrations were tested for the study of gelation time. The gelation time of all polyurethane aerogels catalyzed using different metal ion salts are shown in Table S1. In addition to that, the gelation time decreased with increase in the catalyst concentration.

**2.2.1. Material Characterization of PU Aerogels.** All the PU aerogels were characterized for their material properties like linear shrinkage, bulk density, skeletal density and porosity (Table 1). The linear shrinkages of all samples were between 21.9 – 31.8 %. The bulk densities of all aerogels varied from 0.309 – 0.379 g cm<sup>-3</sup>. The skeletal densities of all the samples were in the range between 1.203 – 1.220 g cm<sup>-3</sup> suggesting absence of any closed pores. Porosities of all the aerogels ranged from 69-73 %. Since the monomer concentration was kept constant therefore, similar material properties were obtained for all the samples.

**2.2.2. Chemical Characterization of PU Aerogels.** All the samples were chemically characterized using <sup>13</sup>C solid-state NMR. The spectra of all the metal-catalyzed PU aerogels were similar to the spectrum of DBTDL catalyzed PU aerogel as shown in Figure 3. Peaks below 50 ppm corresponded to the aliphatic carbons of the triisocyanate. Peaks between 60 to 80 ppm corresponded to the aliphatic carbons of TEG. A sharp peak at around 148 ppm corresponded to the carbonyl carbon of the isocyanurate ring of the triisocyanate. The peak at 155 ppm corresponded to the carbonyl carbon of the polyurethane linkage. From Figure 3, all the spectra were identical indicating the formation of polyurethane aerogel similar to the polyurethane aerogel prepared using DBTDL as reported in the literature. Therefore, the final PU aerogels obtained using different catalysts are chemically similar.

**2.2.3. Structural Characterization of PU Aerogels.** The 3D arrangement of the skeletal framework in the porous space of all aerogels were studied under scanning electron microscope. In order to study the change in morphology with the change in catalyst type, the SEM images of PU aerogels with similar gelation times catalyzed by different catalysts

were compared. In order to achieve similar gelation times with different catalysts, catalyst concentration was varied as shown in Table S1. It was observed that samples with similar gelation times showed similar morphologies despite of different catalysts used. All the samples with gelation time of around 30 min showed spheroidal morphology. The spheroidal morphology consisted of individual spheres for  $\text{Co}^{2+}$  and  $\text{Zn}^{2+}$ , while  $\text{Cu}^{2+}$ ,  $\text{Cu}^+$ , and DBTDL showed spheroidal morphology with fused spheres. All the samples with similar gelation times had similar particle size indicating that the morphology of PU aerogels does not depend on the catalyst type.

Moreover, when the gelation time was varied for fixed catalyst type (e.g.,  $\text{CuCl}_2$ ), with increase in catalyst concentration from  $1/24\times$  to  $1/8\times$ , spheroidal morphologies with fused spheres were obtained. The size of the spheres for  $1/24\times$  was around 20  $\mu\text{m}$  which decreased as the gelation time increased due to decrease in the catalyst concentration. With decrease in gelation time, the morphology changed from large spheres to small spheres with fused spheroidal morphology. Upon further decrease in gelation time, the morphology changed from fused spheres to bicontinuous structures at high catalyst concentrations. Therefore, different morphologies can be obtained with same monomer type and concentration by varying the catalyst concentration. Moreover, due to low solubility of DBTDL in acetonitrile, higher catalyst concentration was not possible to use and therefore it was not possible to obtain bicontinuous structure using the above-mentioned formulation with DBTDL.

**2.2.4. Thermomechanical Characterization of PU Aerogels.** Mechanical properties like elastic modulus and shape memory properties are discussed in this part.

Glass transition temperatures were measured using temperature scans in tensile mode as explained in the Experimental Section. Representative DMA data is shown in Figure 6 for sample catalyzed with DBTDL. During the experiment, loss modulus and elastic modulus were recorded as a function of temperature. At low temperatures, samples were stiff with high elastic modulus ( $E'$ ) that was approximately 10 times higher than the loss modulus ( $E''$ ).  $\tan \delta (= E''/E')$  was also plotted in the same graph that showed a peak as temperature increased from  $-150\text{ }^{\circ}\text{C}$  to  $150\text{ }^{\circ}\text{C}$ . The maxima of  $\tan \delta$  was defined as the glass transition temperature. That temperature for all the samples prepared from different catalysts were in the range of  $31\text{-}38\text{ }^{\circ}\text{C}$ .

The shape memory experiment is visually represented in the Figure 7 by plotting stress, strain and temperature in a 3D graph. The sample's stress increases linearly with strain in the first step showing elastic behavior. That elastic property of the samples was studied from the elastic modulus calculated from the first step of every cycle. For samples catalyzed by  $\text{CuCl}_2$ , the elastic modulus remained almost constant in lower most concentration of catalyst and increased as the catalyst concentration increases. That increase in elastic modulus was observed with the change in morphology from spheroidal to bicontinuous structure. Increase in the elastic modulus of those samples could be reasoned based on the high interconnectivity between particles in the bicontinuous structure.

Shape memory properties like strain fixity and strain recovery were measured for all samples. Strain fixity was calculated using Eq 1.

$$R_f (N) = \frac{\varepsilon_u (N)}{\varepsilon_m (N)} \times 100 \quad (1)$$

Where,  $\varepsilon_u (N)$  is the strain in the sample after the stress is released at low temperature;  $\varepsilon_m (N)$  is the maximum strain achieved by the sample. It was observed that strain fixity in all cycles of all samples was greater than 97%. Strain recovery was calculated using Eq. 2.

$$R_r (N) = \frac{\varepsilon_m (N) - \varepsilon_p (N)}{\varepsilon_m (N)} \times 100 \quad (2)$$

where  $\varepsilon_p (N)$  is the residual strain left in the sample after the completion of 1 cycle. Strain recovery was lower in the first cycle and increased to greater than 98% in all the rest of the cycles for all samples. Upon closer observation, in the first cycle, there is some settling in the sample, that was explained based on the maximization of H- bonding to achieve energy minima.<sup>13</sup> That also provides an explanatory reason for the increase in the stiffness during the first cycle of tensile testing and small amount of creep afterwards. Interestingly, the elastic modulus (a thermodynamic quantity) had an inverse relationship with gelation time (a kinetic quantity) that was shown in Figure 8. Hence, from the same formulation, aerogels can be prepared with different morphologies that in turn show different mechanical properties.

### 3. EXPERIMENTAL

#### 3.1. MATERIALS

All reagents and solvents were used as received unless noted otherwise. The triisocyanate (N3300A) was obtained as a courtesy of Covestro LLC (Pittsburgh, PA) under the trade name Desmodur N3300A. Triethylene glycol (TEG), catalysts (dibutyltin dilaurate (DBTDL), anhydrous metal salts ( $\text{FeCl}_3$ ,  $\text{CoCl}_2$ ,  $\text{Ni}(\text{ClO}_4)_2$ ,  $\text{CuCl}$ ,  $\text{CuCl}_2$ ,  $\text{ZnCl}_2$ ,  $\text{InCl}_3$ ,  $\text{BiCl}_3$ , and  $\text{SnCl}_4 \cdot 5\text{H}_2\text{O}$ ), and solvents (anhydrous acetonitrile and anhydrous

acetone) were purchased from Sigma-Aldrich. Siphon-grade CO<sub>2</sub> was purchased from Ozark Gas Co.

### **3.2. PREPARATION OF THE CATALYST STOCK SOLUTIONS**

Various metal ion salts from the periodic table were tested for the catalytic activity of the polyurethane synthesis as a replacement of Sn-based DBTDL. To prepare the stock solutions, the metal salts were weighed inside a glove box and were added to the volumetric flask. Anhydrous acetonitrile was added to the volumetric flask to dissolve the metal salts. Once the salt dissolved completely, volume make up was done using acetonitrile. After the volume make up, the volumetric flask was parafilmmed and the stock solution was stored at room temperature that was used as catalyst. The concentration of the catalyst stock solution was made based upon the solubility of the catalyst in acetonitrile. The salts that were not soluble in anhydrous acetonitrile were not tested for gelation. Apart from the metal ion salts, HCl gas was also used as a catalyst.

### **3.3. SYNTHESIS OF SHAPE MEMORY POLY(ISOCYANURATE-URETHANE) AEROGELS**

As received N3300A (Desmodur N3300A, 0.504 g, 1.00 mmol) was dissolved in anhydrous acetonitrile. Triethylene glycol (TEG, 1.50 mmol), and the catalyst were dissolved in anhydrous acetonitrile in a round bottomed flask. The isocyanate solution was added to the mixture of TEG and catalyst solution. The resulting sol was stirred at 23 °C under N<sub>2</sub> for 2 min and poured into molds. Smaller rectangular specimens for dynamic mechanical analysis were cut from cylindrical samples prepared using syringes as molds (All Plastic Norm-Ject Syringes, 20 mL, Fisher Scientific Catalogue No. 14-817-32, 2.53

cm i.d.). The gelation time varied from 2 min to 4 h depending on the type of catalyst and its concentration. The resulting wet-gels were aged in their molds at room temperature for 24 h. After aging, the wet-gels were removed from the molds, washed with acetonitrile ( $2 \times 8$  h, using  $4 \times$  the volume of the gel each time) followed by acetone washes ( $4 \times 8$  h, using  $4 \times$  the volume of the gel each time) and then were dried supercritically using supercritical fluid (SCF) CO<sub>2</sub>. Samples were referred to as Cat. Type-Cat. Conc., where Cat. Type stands for the abbreviation of the catalyst type and Cat. Conc. denotes the concentration of the catalyst w.r.t. DBTDL. The concentration of DBTDL catalyst was considered as  $1 \times$  [Ref] and the catalyst concentrations for the metal salts were varied w.r.t. the DBTDL.

### 3.4. METHODS

**3.4.1. Drying.** Drying of wet-gels was carried out in an autoclave (SPIDRY Jumbo Supercritical Point Dryer, SPI Supplies, Inc. West Chester, PA, or a Spe-edSFE system, Applied Separations, Allentown, PA). Samples were loaded into the autoclave that was filled with acetone at room temperature. The pressure vessel was closed, and liquid CO<sub>2</sub> was allowed in at room temperature. Acetone was drained out from the pressure vessel while more liquid CO<sub>2</sub> was allowed in. Samples were kept under liquid CO<sub>2</sub> for 30 min. Then liquid CO<sub>2</sub> was drained out while more liquid CO<sub>2</sub> was allowed in. The cycle was repeated several times until all acetone had been extracted out of the pores of the samples. Subsequently, the temperature of the autoclave was raised to 40 °C, and that condition was maintained for 1 h. Finally, supercritical fluid (SCF) CO<sub>2</sub> was vented off as a gas.

**3.4.2. Chemical Characterization.** Solid-state <sup>13</sup>C NMR spectra were obtained with samples cut into small pieces on a Bruker Avance III 400 MHz spectrometer with a

carbon frequency of 100 MHz using a 7 mm Bruker MAS probe at a magic angle spinning rate of 5 kHz with broad-band proton suppression and the CP TOSS pulse sequence. The Total Suppression of Spinning Sidebands (TOSS) pulse sequence was applied by using a series of four properly timed 180° pulses on the carbon channel at different points of a cycle before acquisition of the FID, after an initial excitation with a 90° pulse on the proton channel. The 90° excitation pulse on the proton and the 180° excitation pulse on carbon were set to 4.2 and 10  $\mu$ s, respectively. A contact time of 2 ms was used for cross-polarization. Solid-state <sup>13</sup>C NMR spectra were referenced externally to glycine (carbonyl carbon at 176.03 ppm). Chemical shifts are reported versus TMS (0 ppm). Solid-state CPMAS <sup>15</sup>N NMR spectra were also obtained on the same Bruker Avance III 400 MHz Spectrometer with a nitrogen frequency of 40.557 MHz using a 7 mm Bruker MAS probe with broad-band proton suppression and magic angle spinning rate of 5 kHz. For crosspolarization, a 90° proton excitation pulse was set to 4.2  $\mu$ s with 2 ms contact time. Chemical shifts are reported versus liquid ammonia (0 ppm) and were externally referenced to glycine (amine nitrogen at 33.40 ppm). In all solid-state NMR experiments the relaxation delay was set at 5 s.

**3.4.3. Physical Characterization.** Bulk densities ( $\rho_b$ ) were calculated from the weight and the physical dimensions of the samples measured using a Vernier caliper. Skeletal densities ( $\rho_s$ ) were determined with helium pycnometry using a Micromeritics AccuPyc II 1340 instrument. Porosities were calculated from the bulk and skeletal densities.

**3.4.4. Structural Characterization.** Rheological gelation times for all the polyurethane gels were calculated using rheology that was conducted using AR 2000ex

Rheometer. An aluminum cone (60 mm diameter,  $2^\circ$  angle) and a peltier plate with a truncation gap of 500  $\mu\text{m}$  was used in the setup. A multi-wave oscillation consisting of five super imposed harmonics with frequencies of 1, 2, 4, 8, and 16  $\text{rad s}^{-1}$  were applied with a fixed strain amplitude of 2% on the sol. That sol was prepared as mentioned in the experimental (Section 2.1.1). Timer was started from the moment of mixing the two solutions A and B. The sol was mixed for 30 seconds and then added to the rheometer.

Structural characterization of all aerogels was carried out using scanning electron microscopy (SEM) on a Hitachi model S-4700 field-emission microscope. Small chunks of the samples were taken and placed on the C-dot pasted on the SEM stub. Thin Cu-strips were applied around the sample leaving some open area for observation. The samples were then coated with Au/Pd (60/40).

**3.4.5. Thermomechanical Characterization.** Thermomechanical characterization was performed using TA Instruments Q800 Dynamic Mechanical Analyzer (DMA). A tension clamp (TA Instruments part no. 984016.901) was used for sample testing in tension mode. All the specimens required for the testing were cut from large cylindrical samples (cooled in liquid  $\text{N}_2$ ) into rectangular shape (Length 20mm; width 15 mm; thickness 3-4 mm) in the spirit of ATM D790-10 and ASTM D065 (Ref.) using a knife under  $\text{N}_2$  in a glove box. The samples were smoothed to downsize the thickness to 3-4 mm using 3M sand paper (320 grit, part no. 98401) while it was still frozen. The clamp was calibrated in three steps sequentially: mass calibration, length calibration, and compliance calibration. Mass calibration was done by installing the stationary clamp on the movable shaft. Offset gauge was used for length measurement calibration, and compliance calibration steel shim was used for the compliance calibration. Once the clamp was calibrated, samples were

installed between the movable clamp and the fixed clamp at room temperature and the correct length of the samples was measured by the instrument by applying a small tensile force of 0.01N that prevents bending. The temperature was programmed to initial testing temperature and equilibrated at that temperature for 5 min in all the experiments.

Glass transition temperatures were determined from the viscoelastic properties of the samples that were measured by applying a sinusoidal oscillation (1 Hz) with a strain amplitude of 0.3%, while the temperature was ramped from -150 to 150 °C at 3 °C min<sup>-1</sup>.

Shape memory properties (strain fixity, strain recovery, strain recovery rate and fill factor) and mechanical properties (Elastic modulus) were extracted from the repetitive cycling experiments conducted under controlled force mode as follows: Once the samples were equilibrated at their deformation temperature ( $T_d = T_g + 10$  °C) for 5 min, the length of the sample was measured using the instrument. Then, specimens were stretched to their maximum strain (approximately 60%) at a constant force rate of 1 N min<sup>-1</sup> and then cooled to fixation temperature ( $T_f = T_g - 40$  °C) under constant stress at 5 °C min<sup>-1</sup>. That low temperature was equilibrated for 5 min and then, the stress was reduced to 0.01 N. The sample was allowed to relax for 15 min while the strain was recorded after which the temperature was ramped to their recovery temperature ( $T_r = T_d$ ) as the strain was recorded. The final temperature was equilibrated for 15 min before the next cycle was started. That complete cycle was run for 4 more times and shape memory properties were analyzed from the collected data.

#### 4. CONCLUSIONS

Shape-memory polyurethane aerogels were prepared using different metal ion catalysts that can replace DBTDL.  $\text{Cu}^{2+}$ ,  $\text{Bi}^{3+}$ , and  $\text{Cu}^+$  showed faster gelation i.e. better catalytic activity compared to DBTDL. The most active of those catalysts,  $\text{CuCl}_2$  was 6 times better catalyst than DBTDL. Bicontinuous to spheroidal morphology of PU aerogels depends on the catalyst concentration. With increase in catalyst concentration, gelation time decreases and polyurethanes with small particles were formed. Further increase in the catalyst concentration results in bicontinuous structure. Irrespective of the catalyst type, morphologies were similar for similar gelation times. The elastic modulus was directly related to the morphology: It was higher when gelation time was shorter (bicontinuous morphology). A thermodynamic kinetic relationship was observed for these polyurethane aerogels.

												Solvent: Acetonitrile					He		
H												B	C	N	O	F	Ne		
Li	Be	DBTDL										Didn't Gel		Al	Si	P	S	Cl	Ar
Na	Mg	Gelled										Insoluble							
K	Ca	Sc	Ti	V	Cr	Mn	Fe	Co	Ni	Cu	Zn	Ga	Ge	As	Se	Br	Kr		
Rb	Sr	Y	Zr	Nb	Mo	Te	Ru	Rh	Pd	Ag	Cd	In	Sn	Sb	Te	I	Xe		
Cs	Ba	La	Hf	Ta	W	Re	Os	Ir	Pt	Au	Hg	Tl	Pb	Bi	Po	At	Rn		
Fr	Ra	Ac	Rf	Db	Sg	Bh	Hs	Mt	Ds	Rg	Sn								

Figure 1. Different metal salts used as catalysts for the synthesis of shape memory polyurethane aerogels

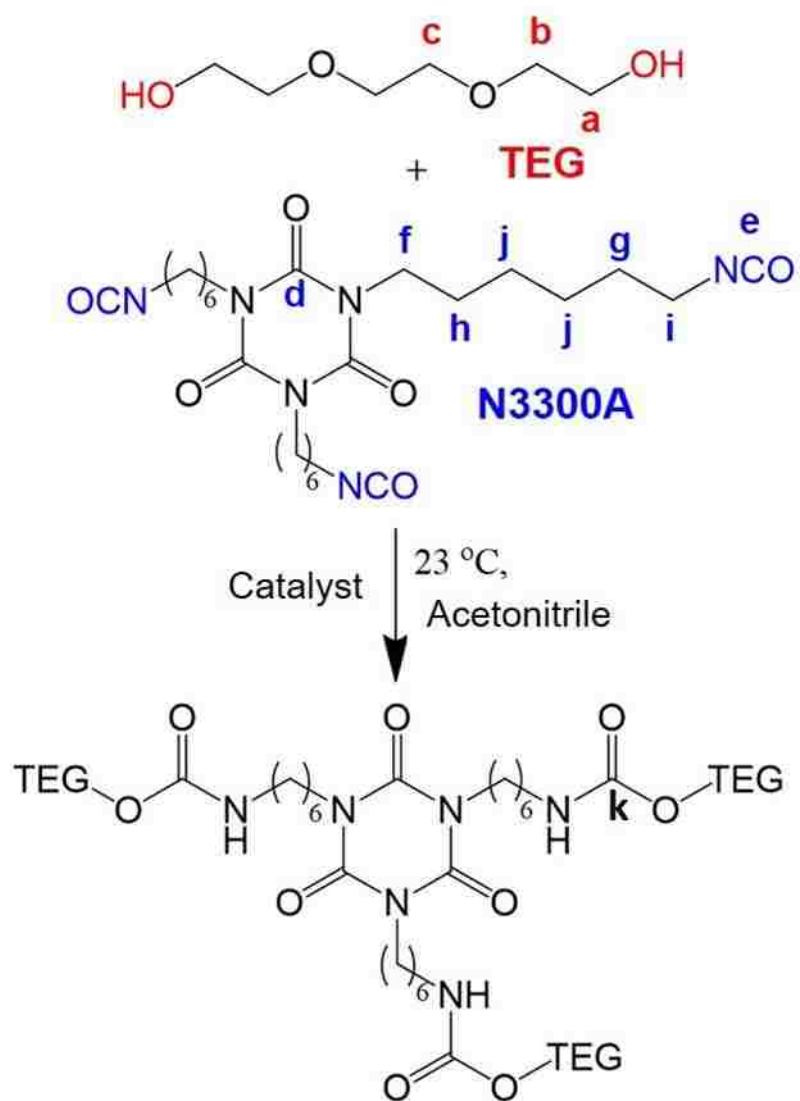


Figure 2. Reaction for the synthesis of PU aerogel

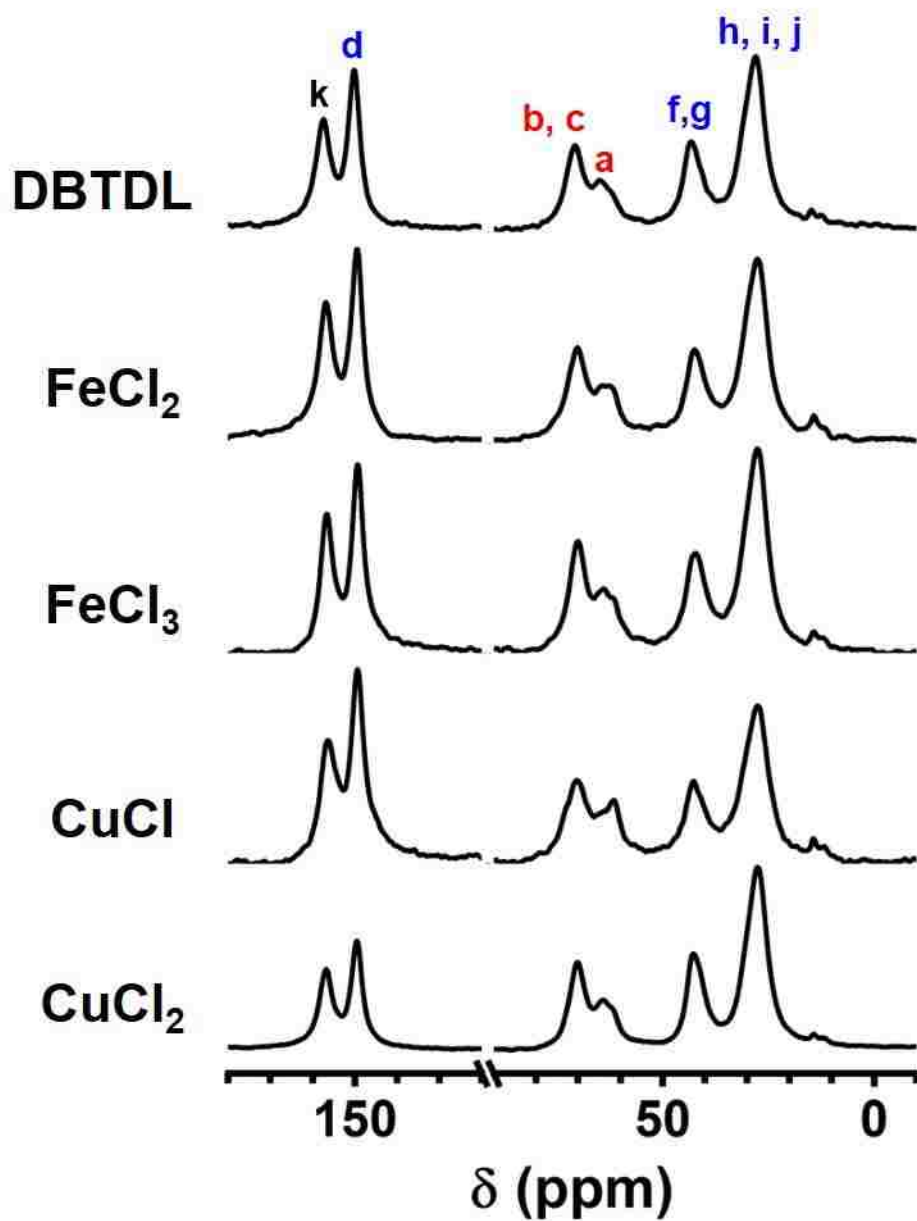


Figure 3. Solid-state  $^{13}\text{C}$  NMR of PU aerogels catalyzed by different metal salts

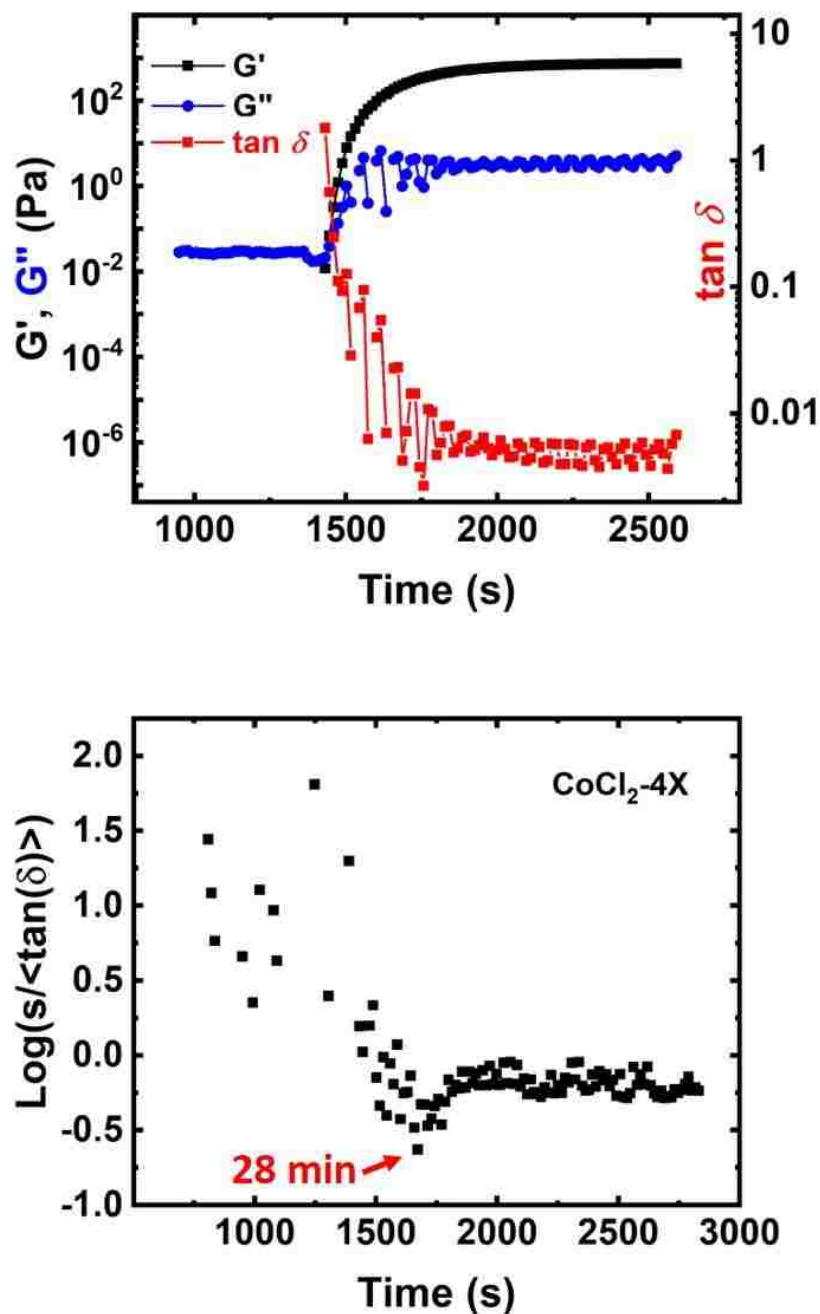


Figure 4. Rheology of the PU sol at 23°C, according to the procedure described in the experimental section. (A) Top figure. Evolution of the storage ( $G'$ ) and loss ( $G''$ ) moduli as well as of  $\tan \delta$  versus time from mixing the sol. Data shown at  $1 \text{ rad s}^{-1}$  oscillation frequency. (For other parameters, see experimental section) (B) Bottom figure. Statistical variable ( $\tan \delta$  at different oscillation frequencies) versus time (see text). The gelation point is defined at the minimum

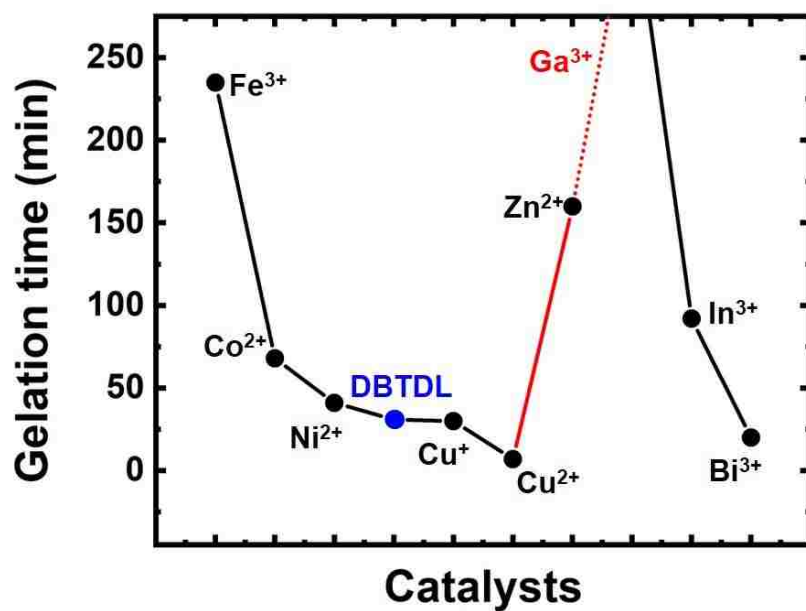


Figure 5. Gelation times for different metal salts that catalyze PU reaction

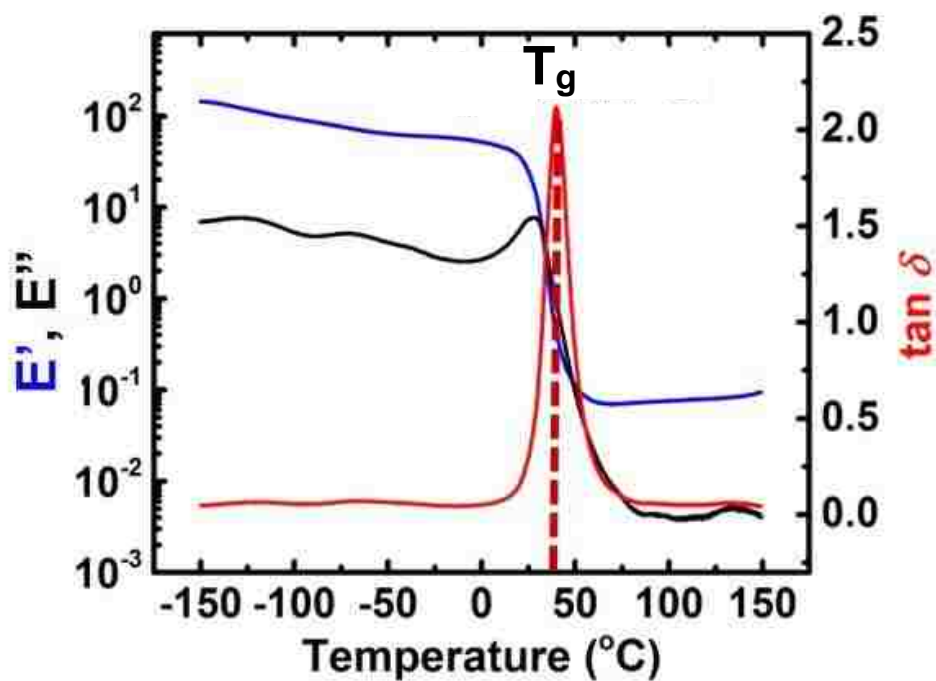


Figure 6. Storage ( $G'$ ), loss ( $G''$ ) moduli and  $\tan \delta (=G''/G')$  curves of a representative sample catalyzed by DBTDL as a function of temperature

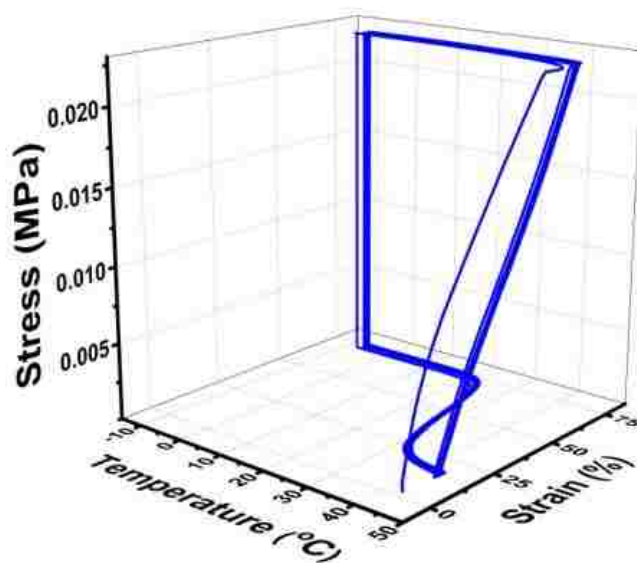


Figure 7. Typical 3D representation of shape memory experiment with temperature, strain, and stress on X, Y, and Z axes respectively

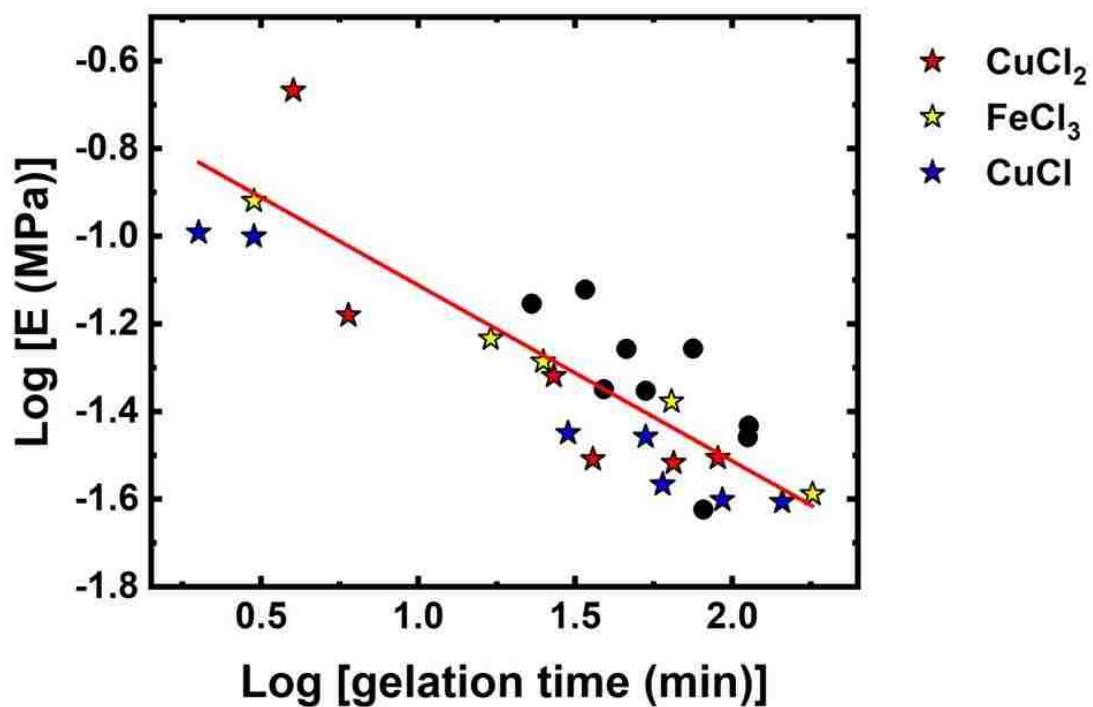
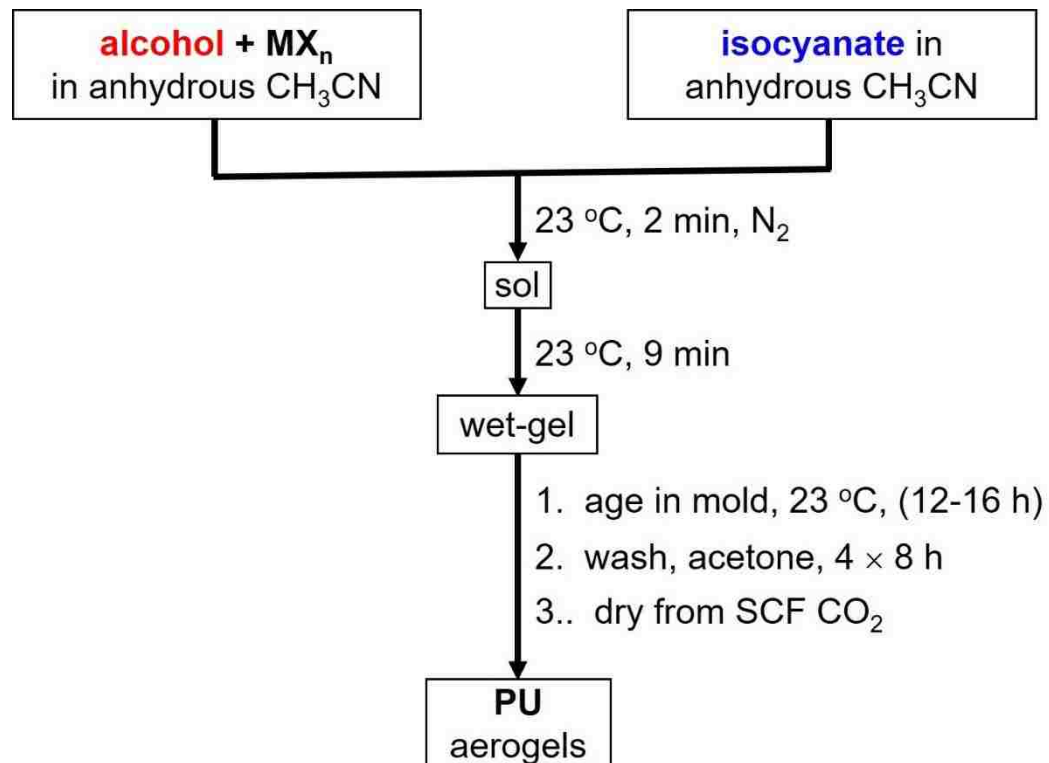


Figure 8. Relationship between  $\text{Log [E]}$  and  $\text{Log [gelation time]}$  for different samples



Scheme 1. Synthesis of SMPU aerogels using different catalysts

Table 1. Rheology data for the gelation of polyurethane sol

alkoxide	Phenomenological gelation time, $t_p$ (s)	Rheological gelation time, $t_r^a$ (s)	$\tan \delta$ at $t_r$	$n^b$	$D_f^c$
CoCl <sub>2</sub> -4×	1380	1680	0.03	0.02	2.45

## SUPPORTING INFORMATION

Table S1. Gelation time for polyurethane aerogels catalyzed using different metal ion salts.

sample	phenomenological gelation time
<b>DBTDL</b>	
1×	36 min
<b>CoCl<sub>2</sub></b>	
16×	10 min, 36 sec
8×	18 min, 15 sec
4×	23 min
2×	34 min
1×	46 min
1/2×	1hr, 15 sec
1/3×	1hr, 31 min
<b>GaCl<sub>3</sub></b>	
16×	1 min, 12 sec
10×	7 min
9×	11 min
8×	18 min
7×	37 min
6×	39 min
5.5×	1hr, 12 min
<b>CuCl</b>	
4×	1 min, 45 sec
2×	2 min, 20 sec
1×	30 min
1/2×	53 min
1/3×	1hr, 3 min
1/4×	1hr, 29 min
1/5×	1hr, 42 min
1/6×	2hr, 24 min
1/8×	3hr, 37 min
<b>CuCl<sub>2</sub></b>	
6×	4 min
5×	4 min
4×	4 min, 30 sec
2×	5 min
1×	6 min
1/8×	17 min
1/13×	23 min
1/16×	30 min
1/20×	46 min
1/26×	1hr, 17 min
1/32×	2hr
<b>ZnCl<sub>2</sub></b>	
16×	39
8×	53
4×	1hr, 21 min
2×	1hr, 52 min
1×	2hr, 35 min
<b>FeCl<sub>3</sub></b>	
16×	3 min
10×	16 min
8×	25 min
5×	43 min
4×	1hr, 5 min
2×	1hr, 44 min
1.5×	2hr, 40 min
1×	3hr, 52 min
<b>Ni(ClO<sub>4</sub>)<sub>2</sub>·6H<sub>2</sub>O</b>	
16×	35 min
4×	24 min
2×	24 min
1×	23 min

## REFERENCES

1. Pierre, A. C.; Pajonk, G. M. *Chem. Rev.* **2002**, *102*, 4243-4265.
2. Structural Effects in Metal Ion Catalysis of Isocyanate-Hydroxyl Reactions, Robins, J., *J. Appl. Poly. Sci.* **1965**, *9*, 821-838
3. Mullender, C.S. Properties of auxiliary organo-tin catalysts in polyurethane foams. In *Catalysis in Polyurethane Foams; Proceedings of the Seminar, Shrewsbury, UK, Nov 6, 1997; Rapra Technology Limited: UK, 1997; 8/1-8/4*
4. Christman, D.L.; Merkl, B.A. Trimerization Catalysts and Organomercury Compounds as Co-catalysts for the Preparation of Non-Cellular Polyurethane Elastomers. US Patent 4,438,248, March 20, 1984.
5. Ref. Arenivar, J.D.; Frish, K.C.; Wong, S.; Wang, S.; Klempner, D. Metal carboxylates for urethanes, UTECH 92, Conference Paper Abstracts, The Hague, The Netherlands, Mar 31-Apr 2, 1992; Crain Communications Ltd.: London, 1992; 161-165.
6. (a) Sardon, H.; Irusta, L.; Fernández-Berridi, M. J. *Prog. Org. Coat.* **2009**, *66*, 291-295. Ref. Blank, W. J. *Macromol. Symp.* **2002**, *187*, 261-270. (b) Blank, W. J.; He, Z. A.; Hessell, E. T. *Prog. Org. Coat.* **1999**, *35*, 19-29.
7. Alsarraf, J.; Ammar, Y. A.; Robert, F.; Cloutet, E.; Cramail, H.; Landais, Y. *Macromolecules* **2012**, *45*, 2249-2256.
8. Tin-free catalysts for the production of aliphatic thermoplastic polyurethanes Yves Schellekens, Bert Van Trimpont, Pieter-Jan Goelen, Koen Binnemans, Mario Smet, Marie-Anne Persoons and Dirk De Vos. *Green Chem.* **2014**, *16*, 4401-4407.
9. Ana L. Silva & João C. Bordado (2004) Recent Developments in Polyurethane Catalysis: Catalytic Mechanisms Review, *Catalysis Reviews*, **2004**, *46*, 31-51.
10. Kinetic Study of Polyurethane Synthesis Using Different Catalytic Systems of Fe, Cu, Sn, and Cr. Viviane de Lima, Nicole da Silva Pelissoli, Jeane Dullius, Rosane Ligabue, Sandra Einloft. *J. Appl. Poly. Sci.* **2010**, *115*, 1797-1802.
11. Organic Acid-Catalyzed Polyurethane Formation via a Dual-Activated Mechanism: Unexpected Preference of N-Activation over O-Activation of Isocyanates. Haritz Sardon, Amanda C. Engler, Julian M. W. Chan, Jeannette M. García, Daniel J. Coady, Ana Pascual, David Mecerreyes, Gavin O. Jones, Julia E. Rice, Hans W. Horn, and James L. Hedrick *J. Am. Chem. Soc.* **2013**, *135*, 16235-16241.

12. Synthesis of Polyurethanes Using Organocatalysis: A Perspective Haritz Sardon, Ana Pascual, David Mecerreyes, Daniel Taton, Henri Cramail, and James L. Hedrick. *Macromolecules*, **2015**, *48*, 3153–3165.
13. Donthula, S.; Mandal, C.; Leventis, T.; Schisler, J.; Saeed, A. M.; Sotiriou-Leventis, C.; Leventis, N. Shape Memory Superelastic Poly(isocyanurate-urethane) Aerogels (PIR-PUR) for Deployable Panels and Biomimetic Applications *Chem. Mater.* **2017**, *29*, 4461-4477

## SECTION

### 2. CONCLUSIONS

Aerogels with varying morphology and interparticle connectivity were synthesized and studied for their optical and mechanical properties. Nanomorphology dependent optical properties were studied by studying haze in silica wet-gels and aerogels as a function of silica aerogel density obtained by varying the total silane concentration. Due to the change in morphology upon crosslinking, mechanically strong and transparent crosslinked silica aerogels were prepared with low thermal conductivities by optimizing the degree of crosslinking. Cause of shrinkage was deconvoluted as a function of H-bonding interaction. Shape memory aerogels with different morphologies were prepared using different catalysts, and the effect of catalyst on the morphology was studied. In addition to that nanomorphology dependent mechanical properties of those shape memory aerogels were studied.

In paper I, haze in silica aerogels was studied as a function of silane concentration. Haze increases with decrease in the silane concentration. That was due to scattering caused either by Rayleigh scattering or Mie scattering. From the nanomorphology it was observed that particle size didn't change much with decrease in silane concentration however, the pore sizes increases along with the increase in haze. Silica aerogels, with silane concentration from K to K/16 showed Rayleigh's scattering and scatterer size was calculated from the slope. It was concluded that haze in silica aerogel for samples from k to K/16 was due to Rayleigh scattering from the secondary particles that matches the

scatterer size. Moreover, the K/32 aerogel looked opaque white indicating that it doesn't follow Rayleigh's scattering. That sample showed Mie scattering from the pores since the pores are large enough that falls in the visible part of the electromagnetic spectrum and therefore scattering increases. Apart from Rayleigh and Mie scattering, surface scattering also induce haze in silica aerogels, and it increase with decrease in aerogel density due to the fragility of silica aerogels.

In paper II, the fragility of silica aerogels was addressed in order to use them for applications in thermally insulating windows. Different silane concentrations were used to prepare silica wet-gels. All the wet-gels were crosslinked with Desmodur N3200 with different crosslinking concentrations using a design of experiment. Upon crosslinking, the mechanical properties increased due to thickening of the interparticle neck. Thermal conductivity increased with increase in crosslinking due to the increase in through solid conduction. Minimum thermal conductivity obtained was  $12.7 \text{ mW m}^{-1} \text{ K}^{-1}$  and maximum thermal conductivity was  $29.9 \text{ mW m}^{-1} \text{ K}^{-1}$ . Haze measurements of all native and crosslinked samples were done using UV-visible spectrophotometer with an integrating sphere. Haze increased with increase in crosslinking due to increase in the particle size. The particle size increased upon crosslinking due to formation of a conformal coating of polymer around the silica particle. These particles act as scatterer and upon increase in scatterer size, scattering increases increasing haze. The optimum sample had elastic modulus of  $70.29 \pm 2.94 \text{ MPa}$ , thermal conductivity of  $22.5 \pm 0.8 \text{ mW m}^{-1} \text{ K}^{-1}$  and haze of 10.5 % for 3 mm thick samples after correcting for their surface haze.

In paper III, the cause of shrinkage of silica wet-gels during supercritical drying was studied. The wet-gels were solvent exchanged with acetone, toluene, and xylene in

order to see the effect of H-bonding. It was concluded that shrinkage during drying was due to two factors. First is due to the capillary forces exerted on the walls of the silica gel due to the change in surface tension from the pore filling solvent (acetone or toluene or xylene) with liquid CO<sub>2</sub>. Second factor is due to the merging of particles into one another. The driving force for that is the loss of H-bonding interaction of the surface silanol groups of particles with the pore filling solvent and therefore particles come closer to establish H-bonding with each other. During this rearrangement, the gel shrinks. All the silica particles were mass fractals with plenty of empty space inside them to accommodate the adjacent neighboring particle during shrinkage.

In paper IV, nanomorphology dependent mechanical properties were studied for shape memory polyurethane aerogels. Shape-memory aerogels were prepared using different metal chloride salts as catalyst that can also replace DBTDL. The gelation time was dependent on the catalytic activity of the metal salts. Aerogels with similar gelation time was obtained with different types of catalyst with different catalyst concentration. Morphology was dependent on the gelation time and not on the type of catalyst. Different morphologies were obtained from spheroidal to bicontinuous structures by varying the catalyst concentration. Elastic modulus increased as the morphology changes from spheroidal to bicontinuous structures. A thermodynamic-kinetic relation was established between the gelation time and elastic modulus.

**BIBLIOGRAPHY**

1. Slater, A. G.; Cooper, A. I. Function-led design of new porous materials. *Science*. **2015**, *348*, aaa8075-1-10
2. Jiao, X.; Batchelor-McAuley, C.; Lin, C.; Katelhon, E.; Tanner, E. E. L.; Young, N. P.; Compton, R. G. Role of Nanomorphology and Interfacial Structure of Platinum Nanoparticles in Catalyzing the Hydrogen Oxidation Reaction. *ACS Catal.* **2018**, *8*, 6192-6202
3. Wang, M.; Cai, Y.; Zhao, B. Zhu, P. Time-Resolved Study of Nanomorphology and Nanomechanic Change of Early-Stage Mineralized Electrospun Poly(lactic acid) Fiber by Scanning Electron Microscopy, Raman Spectroscopy and Atomic Force Microscopy. *Nanomaterials* **2017**, *7*, 223
4. Pakdel, A.; Bando, Y.; Golberg, D. Morphology-Driven Non-wettability of Nanostructured BN Surfaces. *Langmuir*, **2013**, *29*, 7529-7533
5. Taghvaei, T.; Donthula, S.; Rewatkar, P. M.; Far, H. M.; Sotiriou-Leventis, C.; Leventis, N. K-Index: A Descriptor, Predictor, and Correlator of Complex Nanomorphology to Other Material Properties. *ACS Nano*, **2019**, *13*, 3677-3690]
6. Kim, J.; Noh, J.; Choi, H.; Lee, J.; Kim, T. Mechanical Properties of Polymer–Fullerene Bulk Heterojunction Films: Role of Nanomorphology of Composite Films. *Chem. Mater.* **2017**, *29*, 3954-3961
7. Liao, S. H.; Jhuo, H. J.; Cheng, Y. S.; Chen, S. A. Fullerene Derivative-Doped Zinc Oxide Nanofilm as the Cathode of Inverted Polymer Solar Cells with Low-Bandgap Polymer (PTB7-Th) for High Performance. *Adv. Mater.* **2013**, *25*, 4766–4771
8. He, Z.; Zhong, C.; Su, S.; Xu, M.; Wu, H.; Cao, Y. Enhanced Power-Conversion Efficiency in Polymer Solar Cells Using an Inverted Device Structure. *Nat. Photonics* **2012**, *6*, 591–595
9. Zhao, J.; Li, Y.; Yang, G.; Jiang, K.; Lin, H.; Ade, H.; Ma, W.; Yan, H. Efficient Organic Solar Cells Processed from Hydrocarbon Solvents. *Nat. Energy* **2016**, *1*, 15027
10. Creton, C. 50th Anniversary Perspective: Networks and Gels: Soft but Dynamic and Tough. *Macromolecules* **2017**, *50*, 8297-8316.
11. Chen, J.; Jin, Y.; Zhang, J.; Wu, Y.; Meng, C. Study on nanomorphology of high-structure carbon black and its bound rubber by AFM. *Surf. Rev. Lett.* **2012**, *19*, 1250003-1-10

12. Motahari, A.; Hu, N.; Vahid, A.; Omrani, A.; Rostami, A. A.; Schaefer, D. W. Multilevel Morphology of Complex Nanoporous Materials. *Langmuir* **2018**, *34*, 6719–6726]
13. Rizvi, A.; Chu, R. k. M.; Park, C. B. Scalable Fabrication of Thermally Insulating Mechanically Resilient Hierarchically Porous Polymer Foams. *ACS Appl. Mater. Interfaces* **2018**, *10*, 38410-39417
14. Donthula, S.; Mandal, C.; Leventis, T.; Schisler, J.; Saeed, A. M.; Sotiriou-Leventis, C.; Leventis, N. Shape Memory Superelastic Poly(isocyanurate-urethane) Aerogels (PIR-PUR) for Deployable Panels and Biomimetic Applications *Chem. Mater.* **2017**, *29*, 4461-4477
15. IUPAC, Compendium of Chemical Terminology (the "Gold Book"), second ed., Blackwell Scientific Publications, Oxford, **1997**
16. L. L. Hench, J. K. West. The Sol-Gel Process. *Chem. Rev.* **1990**, *90*, 33–72
17. (a) Rao, A. V.; Hegde, N. D.; Hirashima, H. Absorption and Desorption of Organic Liquids in Elastic Superhydrophobic Silica Aerogels. *J. Colloid Interface Sci.* **2007**, *305*, 124–132. (b) Rao, A. V.; Bhagat, S. D.; Hirashima, H.; Pajonk, G. M. Synthesis of Flexible Silica Aerogels Using Methyltrimethoxysilane (MTMS) Precursor. *J. Colloid Interface Sci.* **2006**, *300*, 279–285
18. Anandan, S.; Hebalkar, N.; Sarada, B. V.; Rao, T. N. In *Aerospace Materials and Material Technologies*; Prasad, N. E., Wanhill, R. J. H., Eds.; Springer: Singapore, **2017**; Chapter 5, pp 85-101
19. Wang, C. T.; Wu, C. L.; Chen, I. C.; Huang, Y. H. Humidity Sensors Based on Silica Nanoparticle Aerogel Thin Films. *Sens. Actuators, B* **2005**, *107*, 402–410
20. Li, Y. K.; Yang, D. K.; Chen, Y. C.; Su, H. J.; Wu, J. C.; Chen-Yang, Y. W. A Novel Three-Dimensional Aerogel Biochip for Molecular Recognition of Nucleotide Acids. *Acta Biomater.* **2010**, *6*, 1462–1470
21. Hong, J.; Wie, J. J.; Xu, Y.; Park, H. S. Chemical Modification of Graphene Aerogels for Electrochemical Capacitor Applications. *Phys. Chem. Chem. Phys.* **2015**, *17*, 30946-30962
22. Rousset, J. L.; Boukenter, A.; Champagnon, B.; Dumas, J.; Duval, E.; Quison, J. F.; Serughetti, J. Granular Structure and Fractal Domains of Silica Aerogels. *J. Phys.* **1990**, *2*, 8445–8455.
23. Pajonk, G. M.; Manzalji, T. Synthesis of Acrylonitrile from Propylene and Nitric Oxide Mixtures on Pbo<sub>2</sub>-Zro<sub>2</sub> Aerogel Catalyst. *Catal. Lett.* **1993**, *21*, 361–369

24. Sayari, A.; Ghorbel, A.; Pajonk, G. M.; Teichner, S. J. Kinetics of The Catalytic Transformation of Isobutene into Methacrylonitrile with NO on Supported Nickel Oxide Aerogel. *React. Kinet. Catal. Lett.* **1981**, *15*, 459–465.
25. Saeed, A. M.; Wisner, C. A.; Donthula, S.; Majedi Far, H.; Sotiriou-Leventis, C.; Leventis, N. Reuseable Monolithic Nanoporous Graphite-Supported Nanocatalysts (Fe, Au, Pt, Pd, Ni, and Rh) from Pyrolysis and Galvanic Transmetalation of Ferrocene-Based Polyamide Aerogels. *Chem. Mater.* **2016**, *28*, 4867–4877.
26. Meador, M. A. B.; Wright, S.; Sandberg, A.; Nguyen, B. N.; Keuls, F. W. V.; Mueller, C. H. Rodriguez-Solis, R.; Miranda, F. A. Low Dielectric Polyimide Aerogels as Substrates for Lightweight Patch Antennas. *ACS Appl. Mater. Interfaces* **2012**, *4*, 6346–6353.
27. Meador, M. A. B.; McMillon, E. Sandberg, A.; Barrios, E.; Wilmoth, N. G.; Mueller, C. H.; Miranda, F. A. Dielectric and Other Properties of Polyimide Aerogels Containing Fluorinated Blocks. *ACS Appl. Mater. Interfaces* **2014**, *6*, 6062–6068.
28. Xia, W.; Qu, C.; Liang, Z.; Zhao, B.; Dai, S.; Qiu, B.; Jiao, Y.; Zhang, Q.; Huang, X.; Guo, W.; Dang, D.; Zou, R.; Xia, R.; Xu, R.; Liu, M. High-Performance Energy Storage and Conversion Materials Derived from a Single Metal–Organic Framework/Graphene Aerogel Composite. *Nano Lett.* **2017**, *17*, 2788–2795.
29. Beiner, J.; Stadermann, M.; Suss, M.; Worsley, M. A.; Beiner, M. M.; Rose, K. A.; Baumann, T. F. Advanced Carbon Aerogels for Energy Applications. *Energy Environ. Sci.* **2011**, *4*, 656–667.
30. Thapliyal, P. C.; Singh, K. Aerogels as Promising Thermal Insulating Materials: An Overview. *J. Mater.* **2014**, 127049-1-10.
31. Hamann, T. W.; Martinson, A. B. F.; Elam, J. W.; Pellin, M. J.; Hupp, J. T. Atomic Layer Deposition of TiO<sub>2</sub> on Aerogel Templates: New Photoanodes for Dye-Sensitized Solar Cells. *J. Phys. Chem. C* **2008**, *112*, 10303–10307.
32. Kistler, S. S. Coherent Expanded Aerogels and Jellies. *Nature* **1931**, *127*, 741.
33. Vareda, J. P.; Lamy-Mendes, A.; Durães, L. A Reconsideration on the Definition of the Term Aerogel Based on Current Drying Trends. *Microporous Mesoporous Mater.* **2018**, *258*, 211–216.
34. Leventis, N.; Sadekar, A.; Chandrasekaran, N.; Sotiriou-Leventis, C. Click Synthesis of Monolithic Silicon Carbide Aerogels from Polyacrylonitrile-Coated 3D Silica Networks. *Chem. Mater.* **2010**, *22*, 2790–2803.
35. <http://www.aerogeltechnologies.com/silica-aerogel-samples>.

36. Lofgreen, J. E.; Ozin, G. A. Controlling morphology and porosity to improve performance of molecularly imprinted sol-gel silica. *Chem. Soc. Rev.* **2014**, *43*, 911-933.
37. Pierre, A. C.; Pajonk, G. M. Chemistry of Aerogels and Their Applications. *Chem. Rev.* **2002**, *102*, 4243-4265.
38. Gould, G. L.; Lee, J. K.; Stepanian, C. J.; Lee, K. P. High Strength, Nanoporous Bodies Reinforced with Fibrous Materials. U. S. Patent Application 20070222116, **2007**.
39. Ryu, J. Flexible Aerogel Superinsulation and its Manufacture. U. S. Patent 6068882A, **2000**.
40. Harasim, S. Building Envelope Applications for Reinforced Flexible Aerogel Insulation Blankets. Aspen Aerogels Inc. **2011**.
41. Wittwer, V. Development of Aerogel Windows. *J. Non-Cryst. Solids* **1992**, *145*, 233-236.
42. Gerlach, R.; Kraus, O.; Fricke, J.; Eccardt, P. C.; Kroemer, N.; Magori, V. Modified SiO<sub>2</sub> Aerogels as Acoustic Impedance Matching Layers in Ultrasonic devices. *J. Non-Cryst. Solids* **1992**, *145*, 227-232.
43. Cantin, M.; Casse, M.; Koch, L.; Jouan, R.; Mestreau, P.; Roussel, D.; Saclay, C.; Bonnin, F.; Moutel, J.; Teichner, S. J. Silica aerogels used as Cherenkov radiators. *Nucl. Instrum. Meth.* **1974**, *118*, 177-182.
44. Lagamba, L.; Cisbani, E.; Colilli, S.; Crateri, R.; Leo, R. D.; Frullani, S.; Garibaldi, F.; Giuliani, F.; Gricia, M.; Iodice, M.; Iommi, R.; Leone, A.; Lucentini, M.; Mostarda, A.; Nappi, E.; Perrino, R.; Pierangili, L.; Santavenere, F.; Urciuoli, G. M. Silica Aerogel Threshold Cherenkov Counters for the Jlab Hall A Spectrometers: Improvements and Proposed Modifications. *Nucl. Instr. Meth. Phys. Res. A* **2001**, *471*, 325-332.
45. Fricke J, Arduini-Schuster MC, Buttner D, Ebert H-P, Heinemann U, Hetfleisch J, Hummer E, Kuhn J, Lu X (1990) In: Cremers CJ, Fine HA (eds) Thermal Conductivity 21. Plenum Press, New York, pp 235-245.
46. Pierre AC, Rigacci A (2011) In: Aegerter M, Leventis N, Koebel M, (eds) Aerogels Handbook - Advances in Sol-Gel Derived Materials and Technologies. Springer, New York , Chapter 2, pp 21-45, DOI: 10.1007/978-1-4419-7589-8\_2.
47. <http://www.aerogel.com/products-and-solutions/all-insulation-products/> (Accessed 28 May 2018).
48. Zhao L, Yang S, Bhatia B, Strobach E, Wang EN (2016) AIP Adv 6:025123-1-8.

49. Rubin M, Lampert CM (1983) *Sol Energy Mater* 7:393-400.
50. Pajonk G (1998) *J Non-Cryst Solids* 225:307-314.
51. ASTM D1003-13, Standard Test Method for Haze and Luminous Transmittance of Transparent Plastics, ASTM International, West Conshohocken, PA, 2013, [www.astm.org](http://www.astm.org)
52. Kerker, M. The scattering of the light and other electromagnetic radiation, Chapter 3; Clarkson College of Technology: Potsdam, NY, 1969.
53. Ogawa, S.  $1/\lambda^4$  scattering of light during the drying process in porous Vycor glass with nano-sized pores. *J. Opt. Soc. Am. A.* 2013, 30, 154-159.
54. <http://faculty.fortlewis.edu/mepaciaroni/scattering.html>
55. Wang P, Korner W, Emmerling A, Beck A, Kuhn J, Fricke J (1992) *J Non-Cryst Solids* 145:141-145.
56. Beck A, Gelsen O, Wang P, Fricke J (1989) *J Phys Colloques* 50:C4-203-C4-208.
57. Leventis, N. Three-Dimensional Core-Shell Superstructures: Mechanically Strong Aerogels. *Acc. Chem. Res.* 2007, 40, 874-884.
58. Leventis, N.; Mulik, S.; Wang, X.; Dass, A.; Sotiriou-Leventis, C.; Lu, H. Stresses at the Interface of Micro with nano. *J. Am. Chem. Soc.* 2007, 129, 10660-10661.
59. Leventis, N.; Sotiriou-Leventis, C.; Zhang, G.; Rawashdeh, A.-M. M. Nano Engineering Strong Silica Aerogels. *Nano Lett.* 2002, 2, 957-960.
60. Yang, H.; Kong, X.; Zhang, Y.; Wu, C.; Cao, E. Mechanical Properties of Polymer-Modified Silica Aerogels dried Under Ambient Pressure. *J. Non-Cryst. Solids* 2011, 357, 3447-3453.
61. Maleki, H.; Duraes, L.; Portugal, A. Development of Mechanically Strong Ambient Pressure Dried Silica Aerogels with Optimized Properties. *J. Phys. Chem.* 2015, 119, 7689-7703.
62. Wang, Q.; Feng, J.; Wei, W.; Xie, J.; Xia, C.; Zhu, J.; Jiang, D. Synthesis, Characterization, and Adsorption Properties of Silica Aerogels Crosslinked with Diisocyanate under Ambient Drying. *J. Mater. Sci.* 2016, 51, 9472-9483.
63. Yang, H.; Kong, X.; Zhang, Y.; Wu, C.; Cao, E. Mechanical Properties of Polymer-Modified Silica Aerogels dried Under Ambient Pressure. *J. Non-Cryst. Solids.* 2011, 357, 3447-3453.

64. Nguyen, B. N.; Meador, M. A. B.; Medoro, A.; Arendt, V.; Randall, J.; McCorkle, L.; Shonkwiler, B. Elastic Behavior of Methyltrimethoxysilane Based Aerogels Reinforced with Tri-Isocyanate. *Appl. Mater. Interfaces* **2010**, *2*, 1430-1443.
65. Chen, K.; Bao, Z.; Du, Ai; Zhu, X.; Shen, J.; Wu, G.; Zhang, Z.; Zhou, B. One-pot Synthesis, Characterization and Properties of Acid-Catalyzed RF Crosslinked Silica Aerogels and Their Conversion to Hierarchical Porous Carbon Monoliths. *J. Sol-Gel Sci. Technol.* **2012**, *62*, 294-303.
66. Duan, Y.; Jana, S. C.; Lama, B.; Espe, M. P Self-Crosslinkable Poly(Urethane Urea)-Reinforced Silica Aerogels. *RSC Adv.* **2015**, *5*, 71551-71558.
67. Guo, H.; Meador, M. A. B.; McCorkle, L.; Quade, D. J.; Guo, J.; Hamilton, B.; Cakmak, M.; Sprowl, G. Polyimide Aerogels Crosslinked Through Amine Functionalized Polyoligomeric Silsesquioxane. *Appl. Mater. Interfaces.* **2011**, *3*, 546-552.
68. Yan, P.; Zhou, B.; Du, A. Synthesis of Polyimide Crosslinked Silica Aerogels with Good Acoustic Performance. *RSC Adv.* **2014**, *4*, 58252-58259.
69. Fei, Z.; Yang, Z.; Chen, G. Li, K. Preparation of Tetraethoxysilane-Based Silica Aerogels with Polyimide Crosslinking From 3, 3', 4, 4'-biphenyl tetracarboxylic dianhydride and 4, 4'-oxydianiline. *J. Sol-Gel Sci. Technol.* **2018**, *85*, 506-513.
70. Saeed, S.; Al-Sobaihi, R. M.; Bertino, m. F.; White, L. S. Saoud, K. M. Laser Induced Instantaneous Gelation: Aerogels for 3D Printing. *J. Mater. Chem. A* **2015**, *3*, 17606-17611.
71. Rewatkar, P. M.; Taghvaei, T.; Saeed, A. M.; Donthula, S.; Mandal, C., Chandrasekaran, N.; Leventis, T.; Shruthi, T. K.; Sotiriou-Leventis, C.; Leventis, N. Sturdy, Monolithic SiC and Si<sub>3</sub>N<sub>4</sub> Aerogels from Compressed Polymer-Crosslinked Silica Xerogel Powders. *Chem. Mater.* **2018**, *30*, 1635-1647.
72. Maleki, H.; Duraes, L.; Portugal, A. Development of Mechanically Strong Ambient Pressure Dried Silica Aerogels with Optimized Properties. *J. Phys. Chem.* **2015**, *119*, 7689-7703.
73. Shao, Z.; Wu, G.; Cheng, X.; Zhang, Y. Rapid Synthesis of Amine Crosslinked Epoxy and Methyl co-Modified Silica Aerogels by Ambient Pressure Drying. *J. Non-Cryst. Solids.* **2012**, *358*, 2612-2615.
74. Smith, D. M.; Scherer, G. W.; Anderson, J. M. Shrinkage During Drying of Silica Gel. *J. Non-Cryst. Solids* **1995**, *188*, 191-206.
75. Kirkbir, F.; Murata, H.; Meyers, D.; Chaudhuri, S. R. Drying of Aerogels in Different Solvents between Atmospheric and Supercritical Pressures. *J. Non-Cryst. Solids* **1998**, *225*, 14-18.

76. Hæreid, H.; Nilsen, E.; Ranum, V.; Einarsrud, M. A. Thermal and Temporal Aging of Two Step Acid-Base Catalyzed Silica Gels in Water/Ethanol Solutions. *J. Sol-gel Sci. & Technol.* **1957**, *8*, 153-157.
77. Dahmouche, K.; Santilli, C. V.; Chaker, J. A.; Pulcinelli, S. H.; Craievich, A. F. SAXS Study of Gelation, Aging and Drying of Silica-Polypropyleneglycol. *J. Appl. Phys.* **1999**, *38*, 172-175.
78. Satha, H.; Atamnia, K.; Despetis, F. Effect of Drying Processes on the Texture of Silica Gels. *J. Biomaterials and Nanobiotechnology*, **2013**, *4*, 17-21.
79. Yoda, S.; Ohshima, S.; Ikazaki, F. Supercritical Drying with Zeolite for the Preparation of Silica aerogels. *J. Non-Cryst. Solids* **1998**, *231*, 41-48.
80. Iswar, S.; Malfait, W. J.; Balog, S.; Winnefeld, F.; Lattuada, M.; Koebel, M. M. Effect of Aging on Silica Aerogel Properties. *Microporous and Mesoporous Materials* **2017**, *241*, 293-302.
81. He, F.; Zhao, H.; Qu, X.; Zhang, C.; Qiu, W. Modified Aging Process for Silica Aerogel. *J. Materials Processing Tech.* **2009**, *209*, 1621-1626.
82. Zhang, G.; Dass, A.; Rawashdeh, A-M. M.; Thomas, J.; Council, J. A.; Sotiriou-Leventis, C.; Fabrizio, E. F.; Ilhan, F.; Vassilaras, P.; Scheiman, D. A.; McCorkle, L.; Palczer, A.; Johnston, J. C.; Meador, M. A. B.; Leventis, N. Isocyanate-Crosslinked Silica Aerogel Monoliths: Preparation and Characterization. *J. Non-Cryst. Solids*, **2004**, *350*, 152-164.
83. Han, Q.; Urban, M. W. J. Kinetics and Mechanisms of Catalyzed and Noncatalyzed Reactions of OH and NCO in Acrylic Polyol-1,6-Hexamethylene Diisocyanate (HDI) Polyurethanes. VI. *Appl. Polym. Sci.* **2002**, *86*, 2322-2329.
84. Han, J. L.; Yu, C. H.; Lin, Y. H.; Hsieh, K. H. Kinetic Study of the Urethane and Urea Reactions of Isophorone Diisocyanate. *J. Appl. Polym. Sci.* **2008**, *107*, 3891-3902.
85. Chang, M. C.; Chen, S. A. Kinetics and Mechanism of Urethane Reactions: Phenyls Isocyanate-Alcohol Systems. *J. Polym. Sci. Part A: Polym. Chem.* **1987**, *25*, 2543-2559.
86. Donohoe, G.; Satchell, D. P. N.; Satchell, R. S. The Kinetics and Mechanism of Addition of Bulky Alcohols to Dimethyl Ketene and P-Nitrophenyl Isocyanate in Iso-Octane and Carbon Tetrachloride Solutions. *J. Chem. Soc. Perkin Trans.* **1990**, *210*, 1671-1674.
87. Bayer, O. Das Di-Isocyanat-Polyadditionsverfahren (Polyurethane). *Angew. Chem.* **1947**, *59*, 257-272.

88. Rausch, K.W.; Sayigh, A. A. R. Structure Property Relationships in Polyurethane Elastomers Prepared by One-Step Reaction. *Ind. Eng. Chem. Prod. Res. Dev.* **1965**, *4*, 92-98.
89. Islam, M. R.; Beg, M. D. H.; Jamari, S. S. Development of Vegetable-Oil-Based Polymers, *J. Appl. Polym. Sci.* **2014**, *131*, 40787–40790.
90. Delebecq, E.; Pascault, J.-P.; Boutevin, B.; Ganachaud, F. O. On the Versatility of Urethane/Urea Bonds: Reversibility, Blocked Isocyanate, and Nonisocyanate Polyurethane. *Chem. Rev.* **2012**, *113*, 80–118.
91. Pigott, K.A. Polyurethanes, in Encyclopedia of Polymer Science and Technology, Vol. 11.; John Wiley & Sons, Inc.: New York, NY, 1989; pp 506–563.
92. Wilkes, G.L.; Dziemianowicz, T.S.; Ophir, Z.H.; and Wildnauer, R. Thermally Induced Time Dependence of Mechanical Properties in Biomedical Grade Polyurethanes. *J. Biomed. Mater. Res.* **1979**, *13*, 189–206.
93. Dzierza, W. Stress-Relaxation Properties of Segmented Polyurethane Rubbers. *J. Appl. Polym. Sci.* **1982**, *27*, 1487–1499.
94. Wong, E.W.C. Development of a biomedical polyurethane. In Urethane Chemistry and Applications, *ACS Series*, **1981**; pp 489–504.
95. Engels, H. W.; Pirkl, H. G.; Albers, R.; Albach, R. W.; Krause, J.; Hoffmann, A.; Casselmann, H.; Dormish, J. Polyurethanes: Versatile Materials and Sustainable Problem Solvers for Today's Challenges. *Angew. Chem. Int. Ed.* **2013**, *52*, 9422-9441.
96. Claeys, B.; Vervaeck, A.; Hillewaere, X. K.; Possemiers, S.; Hansen, L.; Beer, T.D. Thermoplastic polyurethanes for the manufacturing of highly dosed oral sustained release matrices via hot melt extrusion and injection molding, *Eur. J. Pharm. Biopharm.* **2015**, *90*, 44–52.
97. Unverferth, M.; Kreye, O.; Prohammer, V.; Meier, M. A. Renewable Non-Isocyanate Based Thermoplastic Polyurethanes via Polycondensation of Dimethyl Carbamate Monomers with Diols. *Macromol. Rapid Commun.* **2013**, *34*, 1569–1574.
98. More, A. S.; Lebarb´e, T.; Maisonneuve, L.; Gadenne, B.; Alfos, C.; Cramail, H. Novel fatty acid based diisocyanates towards the synthesis of thermoplastic polyurethanes, *Eur. Polym. J.* **2013**, *49*, 823–833.
99. Palaskar, D. V.; Boyer, A.; Cloutet, E.; Alfos, C.; Cramail, H. Synthesis of biobased polyurethane from oleic and ricinoleic acids as the renewable resources via the AB-type self-condensation approach. *Biomacromolecules* **2010**, *11*, 1202–1211.

100. Anisur, M. R.; Kibria, M. A.; Mahfuz, M. H.; Saidur, R. Metselaar, I. H. S. C. In *Energy Sustainability Through Green Energy*; Sharma, A., Kar, S. K., Eds.; Springer: New York, NY, **2015**; Chapter 10, pp 245–263.
101. Heinen, M.; Gerbase, A. E.; Petzhold, C. L. Vegetable Oil Based Rigid Polyurethanes and Phosphorylated Flame Retardants Derived from Epoxydized Soybean Oil. *Polym. Degrad. Stab.* **2014**, *108*, 76–86.
102. Zhang, M.; Luo, Z.; Zhang, J.; Chen, S.; Zhou, Y. Effects of a Novel Phosphorus–Nitrogen Flame Retardant on Rosin Based Rigid Polyurethane Foams. *Polym. Degrad. Stab.* **2015**, *120*, 427–434.
103. Kordomenos, P. I.; Kresta, J. E. Thermal Stability of Isocyanate-Based Polymers. 1. Kinetics of the Thermal Dissociation of Urethane, Oxazolidone, and Isocyanurate Groups. *Macromolecules* **1981**, *14*, 1434–1437.
104. Liszkowska, J.; Czuprynski, B.; Paciorek-Sadowska, J. Thermal Properties of Polyurethane-Polyisocyanurate (PUR-PIR) Foams Modified with Tris(5-hydroxypentyl) Citrate. *J. Adv. Chem. Eng.* **2016**, *6*, 1000148.
105. Factsheet PU-Europe, Applications for polyurethane insulation-today’s solution for tomorrow’s needs, **2011**, <http://www.pu-europe.eu>.
106. Singhal, P.; Small, W.; Cosgriff-Hernandez, E.; Maitland D. J.; Wilson, T. S. Low Density Biodegradable Shape Memory Polyurethane Foams for Embolic Biomedical Applications. *Acta Biomater.* **2014**, *10*, 67–76.
107. Hodlur, R.; Rabinal, M. Self Assembled Graphene Layers on Polyurethane Foam as a Highly Pressure Sensitive Conducting Composite. *Compos. Sci. Technol.* **2014**, *90*, 160–165.
108. Kang, S.; Kwon, S.; Park, J.; Kim, B. Carbon Nanotube Reinforced Shape Memory Polyurethane Foam. *Polym. Bull.* **2013**, *70*, 885–893.
109. Liu, H. D.; Liu, Z. Y.; Yang, M. B.; He, Q. Superhydrophobic Polyurethane Foam Modified by Graphene Oxide. *J. Appl. Polym. Sci.* **2013**, *130*, 3530–3536.
110. Chen, T.; Qiu, J.; Zhu, K.; Li, J. Electro-Mechanical Performance of Polyurethane Dielectric Elastomer Flexible Micro-Actuator Composite Modified with Titanium Dioxide–Graphene Hybrid Fillers. *Mater. Des.* **2016**, *90*, 1069–1076.
111. Yan, R.; Wang, R.; Lou, C. W.; Huang, S. Y.; Lin, J. H. Quasi-Static and Dynamic Mechanical Responses of Hybrid Laminated Composites Based on High-Density Flexible Polyurethane Foam. *Composites Part B*, **2015**, *83*, 253–263.

112. P. Singhal, W. Small, E. Cosgriff-Hernandez, D. J. Maitland and T. S. Wilson, Low density biodegradable shape memory polyurethane foams for embolic biomedical applications, *Acta Biomater.*, **2014**, *10*, 67–76.
113. Jaudouin, O.; Robin, J. J.; Lopez-Cuesta, J. M.; Perrin, D.; Imbert, C. Ionomer-based polyurethanes: a comparative study of properties and applications. *Polym. Int.* **2012**, *61*, 495–510.
114. Fragiadakis, D.; Dou, S.; Colby, R. H.; Runt, J. Molecular mobility, ion mobility, and mobile ion concentration in poly(ethylene oxide)-based polyurethane ionomers. *Macromolecules* **2008**, *41*(15), 5723–5728, DOI: 10.1021/ma800263b.
115. Buruiana, T.; Airinei, A.; Buruiana, E. C.; Robila, G. Polyurethane cationomers containing anthryl and nitroaromatic chromophores. *Eur. Polym. J.* **1997**, *33*(6), 877–880.
116. Charnetskaya, A.G.; Polizos, G.; Shtompel, V. I.; Privalko, E. G.; Kercha, Y. Y.; Pissis, P. Phase morphology and molecular dynamics of a polyurethane ionomer reinforced with a liquid crystalline filler. *Eur. Polym. J.* **2003**, *39*(11), 2167–2174.
117. Zhu, Y.; Hu, J. L.; Choi, K. F.; Meng, Q. H.; Chen, S. J.; Yeung, K. W. Shape memory effect and reversible phase crystallization process in SMPU ionomer. *Polym. Adv. Technol.* **2008**, *19*(4), 328–333.
118. Zhu, Y.; Hu, J. L.; Lu, J.; Yeung, L. Y.; Yeung, K. W. Shape memory fiber spun with segmented polyurethane ionomer. *Polym. Adv. Technol.* **2008**, *19*(12), 1745–1753.
119. Raasch, J.; Ivey, M.; Aldrich, D.; Nobes, D. S.; Ayranci, C. Characterization of polyurethane shape memory polymer processed by material extrusion additive manufacturing. *Additive Manufacturing* **2015**, *8*, 132–141.
120. Wang, C. C.; Zhao, Y.; Purnawali, H.; Huang, W. M.; Sun, L. Chemically induced morphing in polyurethane shape memory polymer micro fibers/springs, *React. Funct. Polym.* **2012**, *72*, 757–764.
121. Casado, U. M.; Quintanilla, R. M.; Aranguren, M. I.; Marcovich, N. E. Composite films based on shape memory polyurethanes and nanostructured, polyaniline or cellulose polyaniline particles. *Synth. Met.*, **2012**, *162*, 1654–1664.
122. Chen, J.; Zhang, Z. X.; Huang, W. B.; Li, J. L.; Yang, J. H.; Wang, Y.; Zhou, Z. W.; Zhang, J. H. Carbon nanotube network structure induced strain sensitivity and shape memory behavior changes of thermoplastic polyurethane. *Mater. Des.*, **2015**, *69*, 105–113.
123. Gu, S.; Yan, B.; Liu, L.; Ren, J. Carbon nanotube– polyurethane shape memory nanocomposites with low trigger temperature. *Eur. Polym. J.* **2013**, *49*, 3867–3877.

124. Peponi, L.; Navarro-Baena, I.; Sonseca, A.; Gimenez, E.; Marcos-Fernandez, A.; Kenny, J. M. Synthesis and characterization of PCL–PLLA polyurethane with shape memory behavior. *Eur. Polym. J.* **2013**, *49*, 893–903.
125. Takahashi, T.; Hayashi, N.; Hayashi, S. Structure and properties of shape-memory polyurethane block copolymers. *J. Appl. Polym. Sci.* **1996**, *60*, 1061–1069.
126. Takahara, A.; Hergenrother, R.W.; Coury, A. J.; Cooper, S. L. *J. Biomed. Mater. Res.* **1992**, *26*, 801–818.
127. Yamada, M.; Li, Y. J.; Nakaya, T. *Macromol. Rapid Commun.* **1995**, *16*, 25–30.
128. Li, Y. J.; Nakamura, N.; Wang, Y. F.; Kodama, M.; Nakaya, T. *Chem. Mater.* **1997**, *9*, 1570–1577.
129. Zhang, L.; Brostowitz, N. R.; Cavicchi, K. R.; Weiss, R. A. Perspective: Ionomer Research and Applications. *Macromol. React. Eng.* **2014**, *8*, 81–99.
130. Petrović, Z. S.; Wan, X.; Bilić, O.; Zlatanić, A.; Hong, J.; Javni, I. Polyols and polyurethanes from crude algal oil. *J. Am. Oil Chem. Soc.* **2013**, *90*, 1073–1078.
131. Rajput, S.D.; Hundiware, D. G.; Mahulikar, P. P.; Gite, V. V. Fatty acids based transparent polyurethane films and coatings. *Prog. Org. Coat.* **2014**, *77*, 1360–1368.
132. Szycher, M. Basic concepts in polyurethane chemistry and technology. Szycher's handbook of polyurethanes, *CRC Press*, Taylor & Francis, Boca Raton, FL, **1999**.
133. Xu, Y.; Petrovic, Z.; Das, S.; Wilkes, G. L. Morphology and properties of thermoplastic polyurethanes with dangling chains in ricinoleate-based soft segments, *Polymer.* **2008**, *49*, 4248–4258.
134. Aung, M. M.; Yaakob, Z.; Kamarudin, S.; Abdullah, L. C. Synthesis and characterization of Jatropha (*Jatropha curcas* L.) oil-based polyurethane wood adhesive, *Ind. Crops Prod.*, **2014**, *60*, 177–185.
135. Saalah, S.; Abdullah, L. C.; Aung, M. M.; Salleh, M. Z.; Biak, D. R. A.; Basri, M. Waterborne polyurethane dispersions synthesized from jatropha oil, *Ind. Crops Prod.* **2015**, *64*, 194–200.
136. Rosu, D.; Rosu, L.; Cascaval, C. N. IR-change and yellowing of polyurethane as a result of UV irradiation. *Polym. Degrad. Stab.* **2009**, *94*, 591–596.
137. Davies, P.; Evrard, G. Accelerated ageing of polyurethanes for marine applications. *Polym. Degrad. Stab.* **2007**, *92*, 1455–1464.

138. Yang, X. F.; Li, J.; Croll, S.; Tallman, D.; Bierwagen, G. Degradation of low gloss polyurethane aircraft coatings under UV and prohesion alternating exposures. *Polym. Degrad. Stab.* **2003**, *80*, 51–58.
139. Gite, V.; Mahulikar, P.; Hundiwale, D. Preparation and properties of polyurethane coatings based on acrylic polyols and trimer of isophorone diisocyanate, *Prog. Org. Coat.* **2010**, *68*, 307–312.
140. Zia, K.M.; Bhatti, H. N.; Bhatti, I.A. Methods for polyurethane and polyurethane composites, recycling and recovery: A review. *React. Funct. Polym.* **2007**, *67*, 675–692.
141. Chattopadhyay, D.; Webster, D. C. Thermal stability and flame retardancy of polyurethanes. *Prog. Polym. Sci.* **2009**, *34*, 1068–1133.
142. Takahashi, T.; Hayashi, N.; Hayashi, S. Structure and properties of shape-memory polyurethane block copolymers. *J. Appl. Polym. Sci.* **1996**, *60*, 1061–1069
143. Jaudouin, O.; Robin, J. J.; Lopez-Cuesta, J. M.; Perrin, D.; Imbert, C. Ionomer-based polyurethanes: a comparative study of properties and applications. *Polym. Int.* **2012**, *61*, 495–510.
144. (a) Baker, J. W.; Bailey, D. N. *J. Chem. Soc.* **1957**, 4652-4662.] [Baker, J. W.; Davies, M. M.; Gaunt, J. *J. Chem. Soc.* **1949**, 24-27. (b) Baker, J. W.; Holdsworth, B. *J. Chem. Soc.* **1947**, 713-726.] [ Farkas, A.; Flynn, K. G. *J. Am. Chem. Soc.* **1960**, *82*, 642-645. (c) Farkas, A.; Mills, G. A.; Erner, W. E.; Maerker, J. B. *Ind. Eng. Chem.* **1959**, *51*, 1299-1300.
145. Schwetlick, K.; Noack, R.; Stebner, F. *J. Chem. Soc. Perkin Trans.* **1994**, *2*, 599-608.
146. Borkent, G.; Van Aartsen, J. J. In *Polymerization Kinetics and Technology*; 1973, pp 274-280.
147. Britain, J. W.; Gemeinhardt, P. G. *J. Appl. Polym. Sci.* **1960**, *4*, 207-211.
148. Smith, H. A. *J. Appl. Polymer Sci.* **1963**, *7*, 85-95.
149. Houghton, R. P.; Mulvaney, A. W. *Journal of Organometallic Chemistry* **1996**, *518*, 21-27.
150. Heinen, M.; Gerbase, A. E.; Petzhold, C. L. Vegetable oil-based rigid polyurethanes and phosphorylated flame-retardants derived from epoxydized soybean oil. *Polym. Degrad. Stab.* **2014**, *108*, 76–86.

## VITA

Chandana Mandal, a native of India, received her Master of Science degree in Chemistry from Indian Institute of Technology (Indian School of Mines) (IIT-ISM), Dhanbad, India in 2012 and Bachelor of Science degree in Chemistry (Honors) from Bethune College, Kolkata, India in 2010. In December 2010, she worked as project assistant under Department of Atomic Energy in Uranium Corporation of India Limited, Jaduguda, Jharkhand under Dr. P. K. Tamrakar. In the summer of 2011, she worked as a research assistant at Jadavpur University, Kolkata, India under Prof. Rina Ghosh. After her Masters, she worked in CSIR-National Metallurgical Laboratory, Jamshedpur, Jharkhand, India for 2 years under Dr. Vinay Kumar. She came to Missouri University of Science and Technology to pursue her Ph.D. degree in Chemistry in the spring of 2015. She joined the Prof. Nicholas Leventis group and her research work focused on polymeric and silica aerogels for optical and material properties. During the course of her Ph.D., she coauthored seven (7) journal articles, submitted one (1) article for publishing, and has contributed to 14 national and regional ACS meetings. She received the Chemistry Department's Outstanding Research Assistant Award in 2018. In July 2019, she received her Ph.D. in Chemistry from Missouri University of Science & Technology.